Effective Mechanical Properties of Material Models with Random Heterogeneities

by

Leon Sokratis Scheie Dimas

S.M., Massachusetts Institute of Technology (2013)
M.S., Norwegian University of Science and Technology (2013)

Submitted to the Department of Civil and Environmental Engineering in Partial Fulfillment of the Requirements for the Degree of

Doctor of Philosophy

at the

MASSACHUSETTS INSTITUTE OF TECHNOLOGY

MASSACHUSETTS INSTITUTE OF TECHNOLOGY
JUN 07 2016
LIBRARIES
ARCHIVES

February 2016

© 2016 Massachusetts Institute of Technology. All rights reserved.

Author: Signature redacted
Department of Civil and Environmental Engineering
September 25, 2015

Certified by: Signature redacted
Markus J. Buehler
Professor of Civil and Environmental Engineering
Thesis Supervisor

Accepted by: Signature redacted
Heidi Nepf
Chair, Departmental Committee for Graduate Students

Effective Mechanical Properties of Material Models with Random Heterogeneities

by

Leon Sokratis Scheie Dimas

S.M, Massachusetts Institute of Technology (2013)
M.S., Norwegian University of Science and Technology (2013)

Submitted to the Department of Civil and Environmental Engineering on September 25th, 2015, in partial fulfillment of the requirements for the degree of
Doctor of Philosophy

Abstract

In this thesis we obtain analytical approximations to the probability distribution of the elastic tensor and fracture strengths of material models with random heterogeneities. We start by investigating the effective elastic properties of one-, two-, and three-dimensional rectangular blocks whose Young's modulus varies spatially as a lognormal random field. We decompose the spatial fluctuations of the Young's log-modulus $F = \ln E$ into first- and higher-order terms and find the joint distribution of the effective elastic tensor by multiplicatively combining the term-specific effects. Through parametric analysis of the analytical solutions, we gain insight into the effective elastic properties of this class of heterogeneous materials.

Building on this analysis we find analytical approximations to the probability distribution of fracture properties of one-dimensional rods and thin two-dimensional plates for systems in which: only the Young's modulus varies spatially as an isotropic lognormal field and more generally, both the Young's modulus and the local material strength vary spatially as possibly correlated lognormal fields. The properties considered are the elongation, strength, and toughness modulus at fracture initiation and at ultimate failure. For all quantities at fracture initiation our approach is analytical in 1D and semi-analytical in 2D. For ultimate failure, we quantify the random effects of fracture propagation and crack arrest by fitting regression models to simulation data and combine the regressions with the distributions at fracture initiation. Through parametric analysis, we gain insight into the strengthening/weakening roles of the Euclidean dimension, size of the specimen, and the correlation, variance and correlation function of the random fields.

Finally, we extend the approach to investigate the elasticity of non-lognormal random heterogeneous materials. First we investigate the elastic bulk stiffness of two-dimensional checkerboard specimens in which square tiles are randomly assigned to one of two

component phases. This is a model system for multi-phase polycrystalline materials such as granitic rocks and many ceramics. We study how the bulk stiffness is affected by different characteristics of the specimen and obtain analytical approximations to the probability distribution of the effective stiffness. In particular we examine the role of percolation of the soft and stiff phases. In small specimens, we find that the onset of percolation causes significant discontinuities in the effective modulus, whereas in large specimens the influence of percolation is smaller and gradual. Secondly we study the effective stiffness of multi-phase composite systems in which the Young's modulus varies as a filtered Poisson point process and find that the homogenization approach initially developed for lognormal systems produces accurate results also for this class of non-lognormal systems.

Thesis Supervisor: Markus J. Buehler
Title: Professor of Civil and Environmental Engineering

Acknowledgements

I am grateful for the support and supervision of my advisor Professor Markus J. Buehler. Moreover, I am grateful for the freedom he has allowed me in my studies and the opportunity he gave me to work in a motivating and fruitful environment. I am also grateful for the advice and support of my committee members: Professor Daniele Veneziano, Professor Oral Buyukozturk, Professor Raul Radovitzky, and Professor Youssef Marzouk.

I also thank my colleagues in the Laboratory for Atomistic and Molecular Mechanics, in the Department of Civil and Environmental Engineering and in Departments across the institute for their support and friendship.

I am especially indebted to Professor Daniele Veneziano. Not only did he wisely direct and inspire this work, but also working under his guidance I have learned valuable lessons that I will carry with me far beyond the completion of my thesis. Professor, I will always be grateful for your mentorship and your time.

This work was funded by grants from BASF-NORA, ARO and ONR- PECASE. Their support is greatly appreciated.

Cambridge, United States, September 2015

List of Journal Publications:

I am the author of all the work presented in this thesis. Research was conducted in the Department of Civil and Environmental Engineering at the Massachusetts Institute of Technology. Part of the work presented here has been published in peer-reviewed journal papers and book chapters (chronological):

1. **L.S. Dimas**, M.J. Buehler, "Influence of geometry on mechanical properties of bio-inspired silica-based hierarchical materials,"*Bioinspiration & Biomimetics*, Vol. 7, paper # 036024, 2012
2. **L.S. Dimas**, M.J. Buehler, "Tough and Strong Composites with Simple Building Blocks," *J. Materials Research*, Vol. 28(10), pp. 1295-1303, 2013
3. **L.S. Dimas**, G. Bratzel, I. Eylon, M.J. Buehler, "Tough Composites Inspired by Mineralized Natural Materials: Computation, 3D printing and Testing," *Advanced Functional Materials*, Vol. 23(36), pp. 4629-4638, 2013
4. **L.S. Dimas**, T. Giesa, M.J. Buehler, "Fracture in stochastic media using discrete and continuum simulation methods," *J. Mech. Phys. Solids*, Vol 63, pp 651-673, 2014
5. A. Nair, F. Libonati, Z. Qin, **L.S. Dimas**, M.J. Buehler, "Mechanical and interface properties of biominerals: Atomistic to coarse grained modeling," In: Biomineralization Handbook: Characterization of biomineral and biomimetic materials (editor: Elaine DiMasi), CRC Press, 2014
6. Z. Qin, **L.S. Dimas**, D. Adler, G. Bratzel, M.J. Buehler, "Biological materials by design," *J. Phys. Cond. Mattter*, Vol. 26(7), article # 073101, 2014
7. **L.S. Dimas**, M.J. Buehler, "Modeling and Manufacturing of Bio-inspired Composites with Tunable Fracture Mechanical Properties," *Soft Matter*, Vol.10(25), 4436-4442, 2014
8. **L.S. Dimas**, D. Veneziano, T. Giesa, M.J. Buehler, "Random Bulk Properties of Heterogeneous Rectangular Blocks With Lognormal Young's Modulus: Effective Moduli," *Journal of Applied Mechanics ASME*, Vol. 82, paper # 011003, 2015

9. R. Mirzaeifar, **L.S. Dimas**, Q. Qin, M.J. Buehler, "Defect-tolerant Bioinspired Hierarchical Composites: Simulation and Experiment," *ACS Biomaterials Science & Engineering*, DOI: 10.1021/ab500120f, 2015
10. **L.S. Dimas**, D. Veneziano, T. Giesa, M.J. Buehler, "Probability Distribution of Fracture Elongation, Strength and Toughness of Notched Rectangular Blocks with Lognormal Young's Modulus," *J. Mech. Phys. Solids*, Vol 84, pp 116-129, 2015
11. **L. S. Dimas**, D. Veneziano, M.J. Buehler, "Effective Stiffness of Random Checkerboard Plates", *Journal of Applied Mechanics ASME*, Accepted for Publication, 2015

Journal papers in submission:

1. **L.S. Dimas**, D. Veneziano, M.J. Buehler, "Strength and Fracture Toughness of Heterogeneous Blocks with Joint Lognormal Modulus and Failure Strain", In submission, 2015

Table of Contents

Chapter 1: Introduction 12
1.1 Heterogeneity in Natural and Synthetic Materials 12
1.2 Effective Mechanical Properties of Heterogeneous Materials 15
1.3 Research Objectives 18
1.4 General Approach and Challenges 20

Chapter 2: Bulk Effective Stiffness of Rectangular Blocks With Lognormal Young's Modulus 23
2.1. Introduction 23
2.2 Probabilistic Model and ANOVA Decomposition 26
2.3 Distribution of the Bulk Moduli 29
2.3.1 n = 1 (one-dimensional bar of length L1) 30
2.3.2 n = 2 (L1 × L2 blocks) 31
2.3.3 n = 3 (L1 × L2 × L3 block) 33
2.3.4 Correlation Coefficients 34
2.4. Validation and Parametric Analysis 34
2.4.1 Example Validation Results 35
2.4.2 Parametric Analysis 38
2.5. Conclusions 44
Supporting Information 47
Part A: Derivation of Distributions 47
Part B: Distribution of Certain Random Distances 65

Chapter 3: Probability Distribution of Fracture Elongation, Strength, and Toughness of Notched Rectangular Blocks with Lognormal Young's Modulus 68
3.1. Introduction 68
3.2. Initial Fracture Strengths 73
3.2.1 1D (one-dimensional bar of length L1) 75
3.2.2 2D (two-dimensional rectangle with dimension L1 × L2) 76

3.3. Ultimate Fracture Strengths 77
3.4. Numerical Models and Validation of the Analytic Results 80
3.4.1 Numerical Models 80
3.4.2 Validation Runs 83
3.5. Parametric Analysis 84
3.5.1 Initial Fracture Strengths 84
3.5.2 Ultimate Fracture Strengths 90
3.6. Conclusions 93
Supporting Information 96
Part A: Derivation Details 96
Part B: Model Comparisons 98

Chapter 4: Strength and Fracture Toughness of Heterogeneous Blocks with Joint Lognormal Modulus and Failure Strain 100
4.1 Introduction 101
4.2 Stochastic Model and Other Assumptions 104
4.3 Initial Fracture Strengths 106
4.3.1 1D (one-dimensional rod of length L1) 106
4.3.2 2D (two-dimensional rectangle with dimensions L1 × L2) 108
4.3.3 3D Extension 110
4.4 Ultimate Fracture Strengths 110
4.5 Validation of the Analytical Results 113
4.6 Parametric Analysis 115
4.6.1 Initial Strengths 115
4.6.2 Ultimate Strengths of 2D Specimens 120
4.7 Conclusions 124
Supporting Information 127
Part A: Derivation of Covariance in Eq. 4.12 127
Part B: Crack-Arrest Effects in 2D Plates 128
Part C: Initial and Ultimate Strength Distributions 130

Chapter 5: The Effective Stiffness of Random Checkerboard Plates 132
5.1 Introduction 132

5.2 Factors that Influence the Effective Stiffness and the Role of Percolation 135
5.2.1 Components of Fx1, x2 and Their Effect on Feff 136
5.2.2 The Role of Percolation 143
5.2.3 Modeling the Exponent q12 in Eq. 5.4 146
5.3 Probability Distribution of the Effective Modulus 149
5.4 Numerical Validation 151
5.4.1 Numerical Model 151
5.4.2 Validation Runs 152
5.5 Comparison Between Checkerboard and Lognormal Materials 156
5.6 Conclusions 158
Supporting Information 162
Part A: Derivation of Eq. 5.12 162
Part B: Accuracy of Numerical Experiments 162
Part C: Numerical Validation for $\Delta = 1,3$ 163
Chapter 6: The Effective Stiffness of Multi-Phase Composites with Random Inclusions 168
6.1 Introduction 168
6.2 Stochastic Model and Probability Distribution of the Effective Modulus 171
6.2.1 Stochastic Model 171
6.2.2 Probability Distribution of the Effective Modulus 172
6.3 Numerical Model and Validation 175
6.4 Conclusions 177
Chapter 7: Summary and Outlook 179
7.1 Main Technical Findings 180
7.2 General Findings 184
7.3 Future Extensions 188
7.4 References: 191
7.2 List of Figures 199
7.3 List of Tables 205

Chapter 1: Introduction

In this chapter we discuss heterogeneity as a common trait of natural and synthetic materials, with a particular focus on materials with random heterogeneity. We further discuss the mechanical behavior of certain heterogeneous materials and present established methodologies for describing their effective mechanical properties. Then we describe the objectives of our work and the methodology we use along with some of the challenges faced.

1.1 Heterogeneity in Natural and Synthetic Materials

A heterogeneous material is one that is composed of domains of phases with different material properties or in which a single phase has mechanical properties that vary in space. Examples of such materials are cement, bone, granitic rocks, cellular solids, soils, wood, and fiber composites. Composite materials find widespread use in civil-, aero/astro-, automotive-, and electrical engineering. From an engineering standpoint it is thus critical have an in-depth understanding of the many classes of the role of different types of heterogeneity on the bulk properties of materials.

We distinguish between ordered heterogeneous materials and disordered, or random, heterogeneous materials. An ordered heterogeneous material is composed of domains of different phases arranged in a deterministic pattern. For example, a laminate composite with a given layering pattern and deterministic properties of the various phases is an ordered heterogeneous material. In this thesis we focus on the effective stiffness and strength of certain classes of random heterogeneous materials. First we classify and give some examples of random heterogeneous materials.

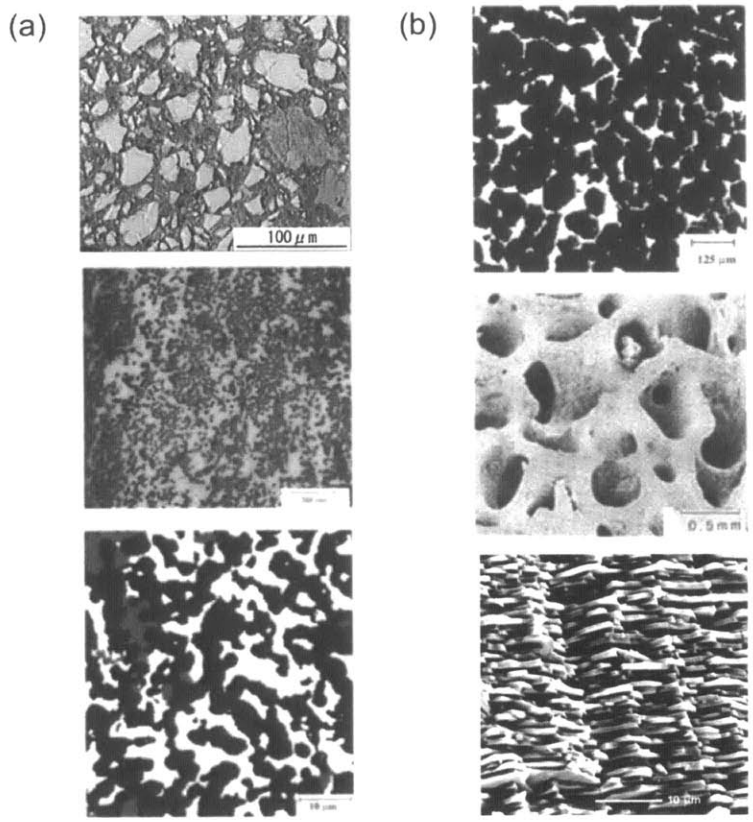

Figure 1.1: a Synthetic random heterogeneous materials. From top to bottom: Cement paste, fiber reinforced cermet, and an interpenetrating three-phase cermet composed of boron carbide (black regions), aluminum (white regions), and another ceramic phase (gray regions). **b** Natural random heterogeneous materials. From top to bottom: Fontainebleau sandstone, cellular structure of cancellous bone, and 'stack-of-coins' structure of aragonite crystals that make up gastropod nacre. Adapted and reprinted from [1-3] with permission of Springer, Elsevier and the Nature Publishing Group.

Random heterogeneous materials are materials whose microstructural characteristics can only be characterized statistically [1]. **Figures 1.1a** and **b** show examples of synthetic and natural random heterogeneous materials. **Figure 1.1a** shows from top to bottom: a backscattered electron micrograph of cement paste, an optical image of the transverse plane of a fiber-reinforced ceramic-metal (cermet) composite made of alumina fibers in an aluminum matrix, and a processed optical image of a cermet primarily composed of boron carbide and aluminum [1, 3]. Panel **b** shows, from top to bottom: a planar section of Fontainebleau sandstone obtained via X-ray microtomography, a scanning electron micrograph of the porous cellular structure of cancellous bone, and a scanning electron micrograph of a fractured nacreous shell [1-3]. The images distinguish the distinct phases in each heterogeneous system. Notably, the mechanical properties of the individual

phases may also vary randomly in space. Indeed, many material systems exhibit heterogeneity at several length scales. For example, **Figure 1.2** shows an example color plot of the spatial variation of the indentation modulus inside a sample of osteonal bone tissue (note the different length scales in the second image of **Figure 1.1b** and **Figure 1.2**) [4].

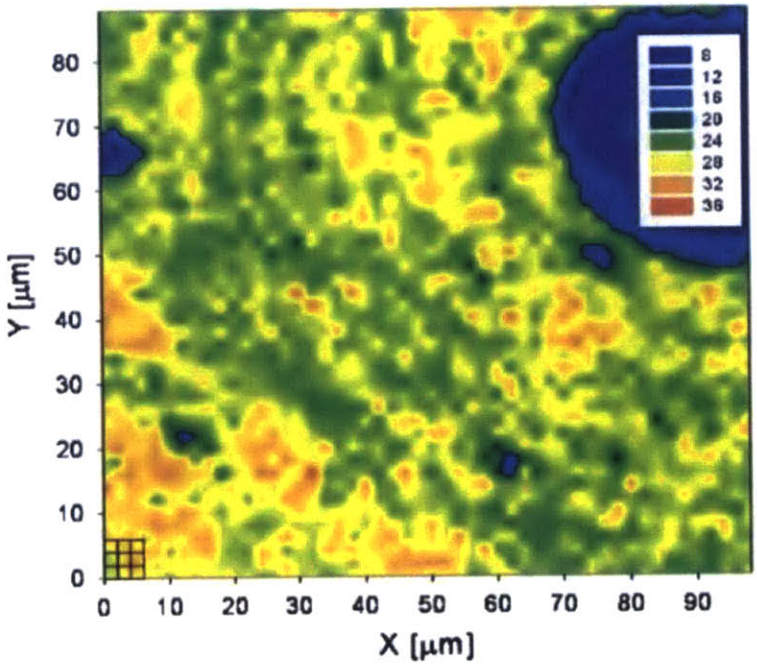

Figure 1.2: 2D interpolated color plot of the reduced indentation modulus, showing both a clear modulation along the lines of the lamellae inside an osteon, as well as regions of much lower moduli where the osteocyte lacunae and Haversian systems are present. Adapted and reprinted from [4] with permission of Cambridge University Press.

Theoretical, numerical, and experimental studies have shown that ordered heterogeneous material systems, both natural and synthetic, can exhibit mechanical performance superior to that of their elemental building blocks [5-13]. For example, reference [9] shows through theoretical analysis that in a notched laminate composite with stiff platelets embedded in a soft matrix the stress concentration at the notch tip decreases with decreasing thickness and stiffness of the matrix phase. Similarly, references [7, 14, 15] show that in materials with periodically varying material properties, crack tip stress singularities can vanish and at bi-material interfaces. Furthermore, both experimental and

numerical studies have shown that the impressive mechanical performance of biological materials is due to the intricate, hierarchical organization of building blocks with contrasting material properties [5, 16-21].

Although the mechanisms are not well understood, by analogy to ordered composites it is reasonable to assume that the fluctuations of mechanical properties in random heterogeneous systems have similar effects on their bulk mechanical characteristics. Most studies on the properties of random material systems have been numerical and experimental. For example, in reference [22] the authors conducted numerical experiments on a random material system modeled after bone and found that the effective stiffness of such systems decreases with increasing spatial variability of the local mechanical properties. Other recent numerical and experimental studies suggest that the disordered distributions of mechanical properties in natural systems can enhance their bulk mechanical fracture properties [23-30]. For example in references [23, 24, 30], motivated by experimental nano-indentation and atomic force microscopy results on bone [4, 24], the authors conducted numerical experiments to study the fracture properties of systems with randomly, and continuously, varying Young's modulus fields. These studies showed a positive correlation between heterogeneity in the Young's modulus field and improved fracture mechanical performance. In reference [25] the heterogeneous nature of nacre lamellae was studied in detail and nacre's impressive mechanical performance were attributed to microstructural characteristics such as the disordered arrangement of nano-asperities, the organic inclusions in ceramic lamellae and the locally varying Young's modulus.

1.2 Effective Mechanical Properties of Heterogeneous Materials

Depending on the length scale of the fluctuations in the microstructural characteristics, the stochastic microstructure can result in stochastic macroscopic mechanical properties. For example, it is well documented that macroscopic properties such as bulk stiffness and strength of steels, concrete, ceramics, rocks, and bone should be treated as random

variables [4, 24, 25, 31-35]. Under certain conditions, loosely speaking when the macroscopic length scale far exceeds the length scale of the random fluctuations, the effective bulk properties of random heterogeneous materials can become deterministic. These conditions are referred to as the ergodic limit. For example, in reference [36] Veneziano studied, under ergodicity conditions, the deterministic bulk effective stiffness of one-, two-, and three-dimensional blocks with a locally isotropic lognormal distribution of the Young's modulus.

In the context of structural design, it is essential to characterize the distribution of the bulk mechanical properties of engineering materials. We highlight two important reasons:

1. A detailed understanding of such distributions will lead to more accurate reliability analysis, which in turn can lead to better performing structures; and
2. In the numerical and theoretical analysis of large structural systems there is a practical limit to the resolution at which fluctuations in mechanical properties can be resolved. In order to propagate uncertainty from one length scale to the next it is thus critical to be able to obtain the effective mechanical properties.

Since the early work of Maxwell, Lord Rayleigh, and Einstein [37-39], determining the effective properties of heterogeneous material systems has been a widely studied subject; see for example [1, 40-43] for book reviews spanning several decades. When the properties of a heterogeneous system are random, the goal of homogenization is to find the joint probability distribution of the bulk properties.

Maxwell's work was concerned with the effective conductivity of a dispersion of spheres, Lord Rayleigh considered the effective conductivity of arrays of spheres, and Einstein studied the effective viscosity of a dilute dispersion of spheres. In solid mechanics, elastic homogenization is the problem of determining the bulk or effective moduli of heterogeneous elastic bodies from the geometric arrangement and properties of the component phases [1, 44-47]. The typical setup considers a homogeneous matrix in which inclusions made of one or several other phases are present. Some popular

approaches include Maxwell-type approximations, [48, 49], implicit self-consistent approximations [50-53], and differential effective-medium approximations [54, 55] based on the work of Bruggeman on conductivity approximations [56].

Maxwell-type approximations consider systems with dilute inclusions and find the effective elasticity tensor by approximating the stress/strain field as the superposition of the stress/strain field due to each individual inclusion. Implicit self-consistent approximations determine the effective elasticity tensor such that the incremental elasticity contribution of each individual phase averages to zero. Finally, differential effective-medium approximations describe the effective elasticity of heterogeneous systems by considering the differential contribution of each individual phase sequentially in the dilute inclusion limit.

The approaches listed above approximate the effective elasticity of systems with deterministic heterogeneity. Less *theoretical* work has been devoted to approximating the *distribution* of the effective mechanical properties of random heterogeneous materials. Popular numerical approaches are various stochastic finite element methods (SFEM) [57-62], coupled with Monte Carlo and spectral methods to derive the distribution of quantities of interest. Although computationally expensive, the distributions of effective mechanical properties are obtained in a straightforward manner through Monte Carlo methods by sampling the state space of random microstructures directly and finding numerically evaluating the system response. In the spectral approach one discretizes both stochastic and Euclidean space simultaneously and transforms the regular finite element problem for deterministic material microstructure to a larger problem that envelops the distribution of microstructural characteristics [57]. This approach is particularly powerful when the length scale of microstructural heterogeneity is comparable to the dimensions of the specimen and a coarse discretization of stochastic space is sufficient.

Other numerical approaches have focused on spring-network discretizations of the random microstructures [63-66], first and second order reliability methods commonly referred to as FORM/SORM [67, 68]. The first and second order reliability methods are

typically used to characterize the probability of failure of structures with random components by approximating their failure surface as either hyper-planes or quadratic hyper-surfaces. One interesting analytical technique is the use of variability response functions (VRF's), first introduced by Shinozuka [69]. VRF's can be used to find the analytical solutions to response variability of statically determinate beam structures [69, 70]. To analyze more general problems, generalized variability response functions (GVRF's) have been developed, however these also require Monte Carlo simulation [71, 72].

Analytical approaches have clear advantages over numerical approaches in efficiency and accuracy and for the study and control of sources of variation. A goal of this thesis is thus to develop a better understanding of the stochastic bulk mechanical properties of classes of random heterogeneous materials through analytical methods. We focus on random heterogeneous systems in which the length scale of heterogeneities is comparable to the macroscopic length scale and thus the effective mechanical properties must be treated as random variables.

In the next subsections we describe in detail the research objectives and the general approach we use.

1.3 Research Objectives

We aim at developing a fundamental understanding of the bulk mechanical properties (stiffness, strength and fracture toughness) of single- and multi-phase materials when the arrangement and micro-scale properties of the phases vary randomly in space. This understanding is especially critical for strength and toughness, as these properties are controlled by local stress/strain concentrations and defects and therefore remain highly variable also for large specimens. Novelties relative to previous work are:

1. The bulk properties are treated not as deterministic quantities but as random variables (hence in essence the problem is to propagate variability from smaller to larger scales in a highly complex system); and
2. Randomness of the bulk properties is characterized analytically or semi-analytically (i.e. numerically but not simulation-based), with clear advantages over Monte Carlo approaches in efficiency and accuracy and for the study and control of sources of variation.

As already indicated there are many types of single and multi-phase random heterogeneous materials and in this work we consider only a few representative cases. Materials and properties we study ar:

- Chapter 1: The bulk stiffness of one-, two-, and three-dimensional rectangular blocks in which Young's modulus varies spatially as a lognormal field;
- Chapter 2: The bulk strength of 1 and 2-dimensional rectangular blocks in which Young's modulus varies spatially as a lognormal field;
- Chapter 3: The bulk strength of one and two-dimensional rectangular blocks in which the Young's modulus and the local strength vary spatially as lognormal fields;
- Chapter 4: The bulk stiffness of two-dimensional random checkerboard plates; and
- Chapter 5: The bulk stiffness of multi-phase composites with randomly distributed inclusions.

Illustrative examples of the mechanical property fluctuations we consider are given in **Figure 1.3**. By comparison with **Figures 1.1** and **1.2** we argue that these are simple model systems for a wide range of natural and synthetic materials. Further motivation for the chosen parametric descriptions of the modulus and strength distributions is given in the respective chapters.

Figure 1.3: Examples of random fields from the **a** lognormal, **b** checkerboard, and **c** random inclusion models considered in this thesis.

In each case (defined by a combination of material class and property of interest), we

1. Develop analytical or semi-analytical approximations to the distribution of the bulk properties; and
2. Use the results to study how the distribution depends on parameters like the Euclidean dimension and size of the specimen and the random characteristics of the heterogeneities.

1.4 General Approach and Challenges

In reference [73], Veneziano et al. analyzed the effective permeability K_{eff} of rectangular blocks with fluctuating hydraulic point conductivity $K(x)$ using an analysis of variance (ANOVA) decomposition of the log-conductivity field $\ln K(x)$. The distribution of K_{eff} was approximated for the case of isotropic lognormal $K(x)$.

In this thesis we use a similar ANOVA based approach to analyze the bulk mechanical properties of random heterogeneous rectangular blocks. The basis of the approach is to decompose the natural logarithm of a random field into individual components whose homogenized effects can be found analytically, either exactly or in approximation. The individual effects are then combined to solve the original homogenization problem. As

shown in Chapter 2, this approach works very well for the elastic homogenization of rectangular blocks with isotropic lognormal modulus $E(x)$. However, in the homogenization of strength variables and when dealing with non-lognormal Young's modulus distributions, new challenges arise. These challenges are introduced below and addressed in greater detail in the pertinent chapters.

Effective Strength under Random Modulus

The strength of elastic-brittle materials is commonly characterized by the elongation at failure U, the ultimate load L (strength), and the energy release rate $\mathcal{G}_C$ (or fracture toughness $K_{I,C}$). There are several challenges to finding the distribution of these strength parameters. One is that the energy release rate, which is typically evaluated by means of the J-Integral, is not suitable for analytical treatment. It is thus necessary to find an alternative energy metric that is well correlated with $\mathcal{G}_C$ and is more suitable for theoretical analysis. In Chapter 3 we show that the strain energy T is one such metric.

A second challenge is that the failure of heterogeneous materials involves not just fracture initiation (I) at the notch tip, but the propagation of fracture through the specimen (ultimate failure U). For different applications, one may be interested in characterizing strength under either I or U conditions. This differentiation is the basis of our proposed divide-and-conquer strategy of first obtaining the distribution of (U_I, L_I, T_I) at fracture initiation and then finding the distribution of the ultimate strengths (U_U, L_U, T_U) accounting for fracture propagation and crack arrest.

Effective Strength under Random Modulus and Strength

Analyzing materials with random but spatially uniform strength (say in terms of a failure strain ε_r) poses minimal additional complexities; an obvious approach is to condition the bulk strengths on ε_r and find their unconditional distribution through convolution with the probability density of ε_r. Notably, a similar approach also works for the fracture initiation strengths of materials with spatially varying strength as the fracture initiation

strengths depend on the random strength field only through the random strength at the crack tip. By contrast, the ultimate fracture strengths depend on the random strength field through its values along the entire crack path. The ultimate strengths thus exhibit a complex dependence on the spatially varying random strength ε_r and we use a similar approach to describe the distributions of X_U as for deterministic strength.

Effective Stiffness of Multi-Phase Materials

Finally, we consider the problem of determining the distribution of the bulk elasticity tensor when the material is a composite with randomly located single- or multi-phase inclusions. In these cases the log-modulus field $F(x)$ is not normal, which is significant because the analytical treatment devised in Chapter 2 makes assumptions and approximations that are accurate under normality. However we believe that in many cases accurate results may be obtained by the ANOVA approach, replacing $F(x)$ with a normal random field with the correct second moment properties. Indeed this is the case for the filtered Poisson point process considered in Chapter 6.

However, in the checkerboard systems of Chapter 5 higher order ANOVA terms interact with marginal fluctuation terms and influence the effective stiffness in complex ways. This effect is mainly due to percolation and as a result the approach of Chapter 2 is inadequate, specifically the effect of higher order terms cannot be considered deterministic. By investigating in detail the effects of the individual ANOVA components in checkerboard systems we find an alternate model for the second order interaction that captures the effect of percolation well for a range of system parameters.

Chapter 2: Bulk Effective Stiffness of Rectangular Blocks With Lognormal Young's Modulus

The research and review presented in this chapter has been published in:

- L. S. Dimas, D. Veneziano, T.Giesa, M.J. Buehler, *Random Bulk Properties of Heterogeneous Rectangular Blocks with Lognormal Young's Modulus: Effective Moduli*, JAM, 2015.

We investigate the effective elastic properties of disordered heterogeneous materials whose Young's modulus varies spatially as a lognormal random field. For one-, two-, and three-dimensional rectangular blocks, we decompose the spatial fluctuations of the Young's log-modulus $F = \ln E$ into first- and higher-order terms and find the joint distribution of the effective elastic tensor by multiplicatively combining the term-specific effects. The analytical results are in good agreement with Monte Carlo simulations. Through parametric analysis of the analytical solutions, we gain insight into the effective elastic properties of this class of heterogeneous materials. The results have applications to structural/mechanical reliability assessment and design.

2.1. Introduction

Elastic homogenization is the problem of determining the bulk or effective moduli of heterogeneous elastic bodies from the geometric arrangement and properties of the component phases. The literature on elastic homogenization is vast; see for example [1, 40-43] for book reviews spanning several decades. The typical setup, which is appropriate for many natural and manufactured materials, considers a homogeneous matrix in which inclusions made of one or several other phases are present. A less studied case is when the local elastic properties of a single material vary spatially in a random but continuous manner, for example due to spatial variations in material density (as in bone) or in the arrangement and properties of unresolved micro-constituents (as in cement, soils

and other geologic materials). Of course, one may combine the two sources of variability by considering multi-phase composites in which the elastic properties vary not only from phase to phase, but also spatially within each phase.

Here we address the homogenization problem for single-phase rectangular blocks of Euclidean dimension $n = 1, 2$, or 3, in which the elastic Young's modulus E varies spatially as an isotropic lognormal field. Recent experimental studies indicate that various materials exhibit similar local variations in mechanical properties [4, 13, 24, 25]. Several of these, and related, investigations suggest that the local variation in mechanical properties lead to enhanced bulk mechanical properties [23-25]. There is thus a significant interest in developing a fundamental understanding of the bulk properties of materials with such local heterogeneities. In **Figure 2.1** we present two realizations of 2D normal log-stiffness fields. The fields are simulated with a simple exponential correlation function with normalized correlation lengths of 0.125 and 0.5 for **(a)** and **(b)** respectively. When the size of the block is very large compared with the characteristic scale of the heterogeneities (a case we refer to as the ergodic limit), the effective properties become deterministic [36]. In the literature a block at this length scale is commonly referred to as a representative volume element (RVE) [74]. However, for blocks of finite size, which is the case considered here, the effective properties are stochastic and must be characterized through joint probability distributions.

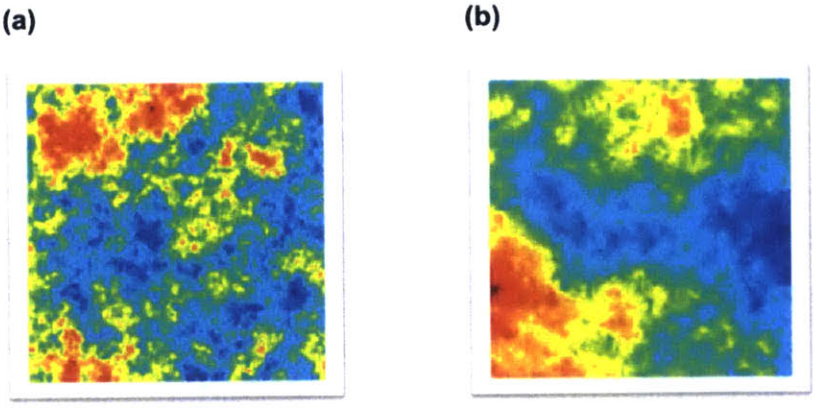

Figure 2.1: Realizations of 2D normal log-stiffness fields with a simple exponential correlation kernel for normalized correlation lengths of (a) **0.125** and (b) **0.5**.

Numerically, this problem is typically addressed through various stochastic finite element methods (SFEM) [57-62]. These studies focus on the numerical analysis of the problem, with spectral and Monte Carlo methods among the notable techniques to derive distributions of quantities of interest through numerical simulation. Other numerical approaches have focused on spring-network discretizations of the random microstructures [63, 64]. There is also significant interest in analytical solutions to the problem [69, 70, 75-77]. A particularly interesting technique is the use of variability response functions (VRF's), first introduced by Shinozuka [77]. VRF's can be used to find the analytical solutions to response variability of statically determinate beam structures [70, 77]. To analyze more general problems, generalized variability response functions (GVRF's) have been developed. These require the use of a limited number of Monte Carlo simulations and can describe the response variability of statically indeterminate beam structures and certain 2D systems [71, 72]. To the best of the authors' knowledge no studies have investigated the usefulness of GVRF's for the variable response prediction of 3D systems.

In this study we use a *full* analytical approach and develop analytical expressions for the joint distributions of the effective elastic tensor. Our approach is to make an ANOVA decomposition of the Young's log-modulus field $F(x) = \ln E(x)$ as the sum of the average value inside the block, the marginal fluctuations along the coordinate axes ("main effects"), and interactions of order $2, \ldots, n$. Then we evaluate the effect of each ANOVA term on the effective moduli in tension $E_{eff,i}$ and shear $G_{eff,ij}$. The desired distribution of the bulk moduli is the product of these term-specific effects. The term effects are obtained exactly or with high accuracy for the low-order ANOVA components and under simplifying approximations for the higher-order interactions. The most drastic approximation is that the higher-order effects are deterministic and can be estimated from the ergodic results. Since the higher-order terms make relative small contributions to the effective moduli, the resulting approximations are accurate. A similar ANOVA approach was used by Veneziano and Tabaei [73] to approximate the distribution of the effective hydraulic conductivity of heterogeneous porous blocks. Here we adapt that methodology to the elastic problem.

After validation through Monte Carlo simulation, we use the ANOVA results to analyze how the distribution of the effective moduli varies with the Euclidean dimension n, the size and shape of the block, and the variance and correlation of the $F(x)$ field. In addition to contributing to the fundamental understanding of the mechanics of disordered materials, these results can be used to assess and control the reliability of structures made of random composite materials.

2.2 Probabilistic Model and ANOVA Decomposition

We consider a rectangular n-dimensional block Ω with side lengths $L_1, \ldots, L_n$, made of linear elastic material. We assume that Poisson's ratio ν is a deterministic constant while Young's modulus varies spatially as an isotropic lognormal field $E(x)$. Hence the log-modulus $F(x) = \ln E(x)$ is isotropic normal. These fields are specified through the mean modulus m_E, the variance of the log-modulus σ_F^2, and the isotropic correlation function of the log-modulus $\rho_F(r)$. Interest is in the distribution of the full elastic tensor C_{ijkl}, which includes the normalized effective Young's moduli $E'_{eff,i} = E_{eff,i}/m_E$ and the shear moduli $G'_{eff,ij} = G_{eff,ij}/m_G$ where $m_G = \frac{1}{2(1+\nu)} m_E$. Since $E'_{eff,i}$ and $G'_{eff,ij}$ do not depend on m_E and m_G, in what follows we consider the distributions of $E_{eff,i}$ and $G_{eff,ij}$ under $m_E = m_G = 1$.

Under certain conditions ($\lim_{r\to\infty} \rho_F(r) = 0$ and $L_i \to \infty$), the effective moduli $E_{eff,i}$ and $G_{eff,ij}$ become deterministic functions of the variance σ_F^2 and the Euclidean dimension n and are independent of $\rho_F(r)$. We refer to these conditions as the ergodic limit. Using an incremental perturbation approach in which fluctuations of F in progressively higher frequency ranges $\omega < |\underline{\omega}| < \omega + \Delta\omega$ are added, Veneziano [36] found that under these ergodic conditions and for $m_E = 1$,

$$E_{eff} = \begin{cases} e^{-\sigma_F^2}, & n = 1 \\ e^{-\frac{5}{8}\sigma_F^2}, & n = 2 \\ e^{-\frac{7}{15}\sigma_F^2}, & n = 3 \end{cases} \tag{2.1}$$

The corresponding ergodic value of the shear modulus is $G_{eff} = c \cdot E_{eff}$, with E_{eff} in Eq. 2.1 and $c = \frac{1}{2(1+\nu)}$.

To study the effective Young's moduli, we subject the rectangular blocks to tension and shear. In the tension experiments we displace one block face uniformly in the direction of its normal, while fixing to 0 the corresponding displacements on the opposite face and the tractions on the rest of the boundary. In the shearing experiments, say on the (x_1, x_2)-plane, we simplify the analytical treatment by modulating the applied shear such that cross-sections at different x_3 locations undergo the same average shear deformation. This is accomplished by scaling the applied shear force by the average modulus at location x_3; see details in the supplementary material. On each given (x_1, x_2)-plane, the shear forces are applied uniformly along the boundary.

The ANOVA decomposition of the log-modulus $F(x)$ inside rectangular blocks of different Euclidean dimension n is as follows.

$n = 1$:

$$F(x_1) = \overline{F}_1 + \varepsilon_1(x_1), \tag{2.2}$$

where $\overline{F}_1$ is the average of F along the rod and $\varepsilon_1(x_1) = F(x_1) - \overline{F}_1$ is the fluctuation around that average value. $\overline{F}_1$ has mean value $-\frac{1}{2}\sigma_F^2$ and ε_1 averages to zero along the length of the rod.

$n = 2$:

$$F(x_1, x_2) = \overline{F}_{12} + \varepsilon_1(x_1) + \varepsilon_2(x_2) + \varepsilon_{12}(x_1, x_2). \tag{2.3}$$

In analogy with the one-dimensional case, the block average $\overline{F}_{12}$ has mean value $m_F = -\frac{1}{2}\sigma_F^2$ and all three ε terms have zero mean (actually, they average to zero along each coordinate direction). When (x_1, x_2) in Eq. 2.3 is considered random with uniform distribution inside the block Ω, the four components on the right hand side of Eq. 2.3 are independent normal.

n = 3:

$$\begin{aligned} F(x_1, x_2, x_3) = \overline{F}_{123} &+ \varepsilon_1(x_1) + \varepsilon_2(x_2) + \varepsilon_3(x_3) + \varepsilon_{12}(x_1, x_2) + \varepsilon_{13}(x_1, x_3) \\ &+ \varepsilon_{23}(x_2, x_3) + \varepsilon_{123}(x_1, x_2, x_3), \end{aligned} \tag{2.4}$$

Again, the block average $\overline{F}_{123}$ has mean value $m_F = -\frac{1}{2}\sigma_F^2$ and the ε terms average to zero along the coordinate directions. When (x_1, x_2, x_3) is considered random with uniform distribution in Ω, the eight components on the right hand side of Eq. 2.4 are independent normal.

For each decomposition, **Table 1** gives expressions for the individual components and their variances.

Table 2.1: ANOVA fluctuation terms and their associated variances for $\boldsymbol{n = 2}$ and $\boldsymbol{n = 3}$.

$\boldsymbol{n = 2}$
Components
$\varepsilon_1(x_1) = \overline{F}_2(x_1) - \overline{F}_{12}$
$\varepsilon_2(x_2) = \overline{F}_1(x_2) - \overline{F}_{12}$
$\varepsilon_{12}(x_1, x_2) = F(x_1, x_2) - \overline{F}_{12} - \varepsilon_1(x_1) - \varepsilon_2(x_2)$
Variances
$\sigma^2_{\overline{F}_{12}} = \overline{\rho}_{12}\sigma_F^2$
$\sigma_1^2 = Var[\varepsilon_1] = (\overline{\rho}_2 - \overline{\rho}_{12})\sigma_F^2$

$\sigma_2^2 = Var[\varepsilon_2] = (\overline{\rho}_1 - \overline{\rho}_{12})\sigma_F^2$ $\sigma_{12}^2 = Var[\varepsilon_{12}] = (1 - \overline{\rho}_1 - \overline{\rho}_2 + \overline{\rho}_{12})\sigma_F^2$
$\boldsymbol{n = 3}$
Components
$\varepsilon_1(x_1) = \overline{F}_{23}(x_1) - \overline{F}_{123}$ $\varepsilon_2(x_2) = \overline{F}_{13}(x_2) - \overline{F}_{123}$ $\varepsilon_3(x_3) = \overline{F}_{12}(x_3) - \overline{F}_{123}$ $\varepsilon_{12}(x_1, x_2) = \overline{F}_3(x_1, x_2) - \overline{F}_{123} - \varepsilon_1(x_1) - \varepsilon_2(x_2)$ $\varepsilon_{13}(x_1, x_3) = \overline{F}_2(x_1, x_3) - \overline{F}_{123} - \varepsilon_1(x_1) - \varepsilon_3(x_3)$ $\varepsilon_{23}(x_2, x_3) = \overline{F}_1(x_2, x_3) - \overline{F}_{123} - \varepsilon_2(x_2) - \varepsilon_3(x_3)$ $\varepsilon_{123}(x_1, x_2, x_3)$ $= F(x_1, x_2, x_3) - \overline{F}_{123} - \varepsilon_1(x_1) - \varepsilon_2(x_2) - \varepsilon_3(x_3) - \varepsilon_{12}(x_1, x_2)$ $- \varepsilon_{13}(x_1, x_3) - \varepsilon_{23}(x_2, x_3)$
Variances
$\sigma_{\overline{F}_{123}}^2 = \overline{\rho}_{123}\sigma_F^2$ $\sigma_1^2 = (\overline{\rho}_{23} - \overline{\rho}_{123})\sigma_F^2$ $\sigma_2^2 = (\overline{\rho}_{13} - \overline{\rho}_{123})\sigma_F^2$ $\sigma_3^2 = (\overline{\rho}_{12} - \overline{\rho}_{123})\sigma_F^2$ $\sigma_{12}^2 = (\overline{\rho}_3 - \overline{\rho}_{13} - \overline{\rho}_{23} + \overline{\rho}_{123})\sigma_F^2$ $\sigma_{13}^2 = (\overline{\rho}_2 - \overline{\rho}_{12} - \overline{\rho}_{23} + \overline{\rho}_{123})\sigma_F^2$ $\sigma_{23}^2 = (\overline{\rho}_1 - \overline{\rho}_{12} - \overline{\rho}_{13} + \overline{\rho}_{123})\sigma_F^2$ $\sigma_{123}^2 = (1 - \overline{\rho}_1 - \overline{\rho}_2 - \overline{\rho}_3 + \overline{\rho}_{12} + \overline{\rho}_{13} + \overline{\rho}_{23} - \overline{\rho}_{123})\sigma_F^2$

2.3 Distribution of the Bulk Moduli

This section summarizes our analytical results on the distribution of the effective elastic moduli. In all cases, the log-moduli $\ln E_{eff,i}$ and $\ln G_{eff,ij}$ are approximated as having

joint normal distribution with mean values, variances and correlations given below and in Supporting Information: Part A. The derivations (Supporting Information: Part A) make simplifying approximations: in some cases a distribution is assumed to be lognormal when its exact form is "between normal and lognormal" and the variance contributions from ANOVA terms of order ≥ 2 are always neglected. The accuracy of the results is assessed in Section 4 using Monte Carlo simulation.

Results for the mean values μ and variances σ^2 of the log-moduli are summarized below. Expressions for the correlation coefficients in 2D and 3D are given in Supporting Information: Part A.

2.3.1 $n = 1$ (one-dimensional bar of length L_1)

In the one-dimensional case, E_{eff} is the harmonic average of $E(x)$ along the rod and $G_{eff} = \frac{1}{2(1+\nu)} E_{eff}$. One can estimate the first two moments of $\ln E_{eff}$ by either working directly with $F(x) = \ln E(x)$ or using the ANOVA decomposition in Eq. 2.2. The results are very similar. Using the ANOVA decomposition one obtains (see Supporting Information: Part A)

$$\begin{aligned} m_{\ln E_{eff}} &= -\sigma_F^2 + \frac{1}{2}\ln\left[1 + \overline{\rho}_{e^F}\left(e^{\sigma_F^2} - 1\right)\right], \\ \sigma^2_{\ln E_{eff}} &= \ln\left[1 + \overline{\rho}_{e^F}\left(e^{\sigma_F^2} - 1\right)\right], \end{aligned} \tag{2.5}$$

and

$$\begin{aligned} m_{\ln G_{eff}} &= \ln(c) + m_{\ln E_{eff}}, \\ \sigma^2_{\ln G_{eff}} &= \sigma^2_{\ln E_{eff}}, \end{aligned} \tag{2.6}$$

where $\overline{\rho}_{e^F}$ is the average correlation of $E = e^F$ for two points uniformly and independently located along the rod. For details on the calculation of this average

correlation, see Supporting Information: Part A and Part B. Notice that, except for the term $\ln(c)$ where $c = \frac{1}{2(1+\nu)}$, the moments of $\ln E_{eff}$ and $\ln G_{eff}$ are identical. The spatial average $\overline{F}_1$ contributes additively to $\ln E_{eff}$ and $\ln G_{eff}$ and the fluctuation term $e^{\varepsilon_1(x)}$ contributes through its harmonic average.

It is interesting to compare the moments in Eq. 2.5 with those of the log average modulus $\ln(\overline{E})$. The latter is approximately normal with parameters,

$$\begin{aligned} m_{\ln \overline{E}} &= -\frac{1}{2}\sigma^2_{\ln E_{eff}}, \\ \sigma^2_{\ln \overline{E}} &= \sigma^2_{\ln E_{eff}}. \end{aligned} \tag{2.7}$$

Hence E_{eff} has the same distribution as $\left[e^{-\sigma_F^2}\left(1+\overline{\rho}_{e^F}(e^{\sigma_F^2}-1)\right)\right]\overline{E}$. The factor $\left[e^{-\sigma_F^2}\left(1+\overline{\rho}_{e^F}(e^{\sigma_F^2}-1)\right)\right]$decreases from 1 to $e^{-\sigma_F^2}$ as the average correlation $\overline{\rho}_{e^F}$ decreases from 1 (constant modulus $E = e^F$ along the rod) to 0 (ergodic limit in which the average correlation of E along the rod is zero).

2.3.2 $n = 2$ ($L_1 \times L_2$ blocks)

Using the ANOVA Decomposition in Eq. 2.3, one finds (see Supporting Information: Part A.3)

$$\begin{aligned} m_{\ln E_{eff,1}} &= -\frac{1}{8}(5-5\overline{\rho}_1+3\overline{\rho}_2+5\overline{\rho}_{12})\sigma_F^2+\frac{1}{2}\ln\left[\frac{1+\overline{\rho}_{e^{\overline{F}_2}}\left(e^{\overline{\rho}_2\sigma_F^2}-1\right)}{1+\overline{\rho}_{e^{\varepsilon_2}}\left(e^{(\overline{\rho}_1-\overline{\rho}_{12})\sigma_F^2}-1\right)}\right], \\ \sigma^2_{\ln E_{eff,1}} &= \ln\left[1+\overline{\rho}_{e^{\overline{F}_2}}\left(e^{\overline{\rho}_2\sigma_F^2}-1\right)\right]+\ln\left[1+\overline{\rho}_{e^{\varepsilon_2}}\left(e^{(\overline{\rho}_1-\overline{\rho}_{12})\sigma_F^2}-1\right)\right], \end{aligned} \tag{2.8}$$

and

$$m_{\ln G_{eff,12}} = \ln(c)-\frac{1}{8}\sigma_{12}^2-\frac{1}{2}\sigma_F^2+\frac{1}{2}\sum_{i=1}^{2}\left\{\ln\left[1+\overline{\rho}_{e^{\varepsilon_i}}\left(e^{\sigma_{\varepsilon_i}^2}-1\right)\right]-\sigma_{\varepsilon_i}^2\right\}, \tag{2.9}$$

$$\sigma^2_{\ln G_{eff,12}} = \overline{\rho}_{12}\sigma_F^2 + \sum_{i=1}^{2} \ln\left[1 + \overline{\rho}_{e^{\varepsilon_i}}\left(e^{\sigma^2_{\varepsilon_i}} - 1\right)\right],$$

where the various average correlations $\overline{\rho}$ are explained in Supporting Information: Part A. The distribution of $\ln E_{eff,2}$ is obtained by interchanging the indices 1 and 2 in Eq. 2.8.

Eq. 2.8 can be understood as follows. The contribution to $\ln E_{eff_1}$ from the first two terms in Eq. 2.3 is obtained by reference to a 1-D problem with appropriate log-modulus variance and correlation function: compare the expression $-\frac{5}{8}\sigma_F^2 + \frac{1}{2}\ln\left[1 + \overline{\rho}_{e^{\overline{F}_2}}\left(e^{\overline{\rho}_2\sigma_F^2} - 1\right)\right]$ in Eq. 2.8 with Eq. 2.5. The contribution of $\varepsilon_2(x_2)$ to $\ln E_{eff_1}$ is the arithmetic average of $e^{\varepsilon_2(x)}$, while the second-order fluctuation $\varepsilon_{12}(x_1, x_2)$ is assumed to contribute an ergodic factor to $m_{\ln E_{eff_1}}$ from Eq. 2.1. For the log-effective shear modulus, the effect of the spatial average $\overline{F}_{12}$ is as in Eq. 2.8, while the main effects $\varepsilon_1(x_1)$ and $\varepsilon_2(x_2)$ contribute through the harmonic averages of $e^{\varepsilon_1(x)}$ and $e^{\varepsilon_2(x)}$. Also in this case the second order fluctuation effect is approximated as a deterministic ergodic factor.

The following special cases of Eq. 2.8 are noted:

1. Two-dimensional ergodic case $(\overline{\rho}_1 = \overline{\rho}_2 = \overline{\rho}_{12} = 0)$. Under these conditions Eq. 2.8 gives $\left(m_{\ln E_{eff,1}} = e^{-\frac{5}{8}\sigma_F^2}, \sigma^2_{\ln E_{eff,1}} = 0\right)$, in accordance with Eq. 2.1 for $n = 2$;
2. One-dimensional case $(\overline{\rho}_2 = 1, \overline{\rho}_1 = \overline{\rho}_{12} = 0) \Rightarrow \left(m_{\ln E_{eff,1}} = \left[1 + \overline{\rho}_{e^F}\left(e^{\sigma_F^2} - 1\right)\right]e^{-\sigma_F^2}, \sigma^2_{\ln E_{eff,1}} = \ln\left[1 + \overline{\rho}_{e^F}\left(e^{\sigma_F^2} - 1\right)\right]\right)$. This coincides with Eq. 2.5;
3. One-dimensional ergodic case $(\overline{\rho}_2 = 1, \overline{\rho}_{e^F} = \overline{\rho}_1 = \overline{\rho}_{12} = 0) \Rightarrow (m_{\ln E_{eff,1}} = e^{-\sigma_F^2}, \sigma^2_{\ln E_{eff,1}} = 0)$, in accordance with Eq. 2.1 for $n = 1$.

Case 2 above is significant as it shows that the one-dimensional parameters in Eq. 2.5 are recovered in the limit $L_1/L_2 \to \infty$; hence the 2D results are consistent with the 1D analysis. Similar special cases apply to the shear modulus in Eq. 2.9.

2.3.3 $n = 3$ ($L_1 \times L_2 \times L_3$ block)

Using the ANOVA Decomposition in Eq. 2.4, the following expressions are derived in Supporting Information: Part A.4:

$$\begin{aligned} m_{\ln E_{eff,1}} &= -\frac{1}{2}(1-\overline{\rho}_1+\overline{\rho}_{23}+\overline{\rho}_{123})\sigma_F^2-\frac{1}{8}(\sigma_{12}^2+\sigma_{13}^2)+\frac{1}{30}\sigma_{123}^2 \\ &\quad +\frac{1}{2}\ln\left[1+\overline{\rho}_{e^{\overline{F}_{23}}}\left(e^{\overline{\rho}_{23}\sigma_F^2}-1\right)\right] \\ &\quad -\frac{1}{2}\ln\left[1+\overline{\rho}_{e^{\overline{F}_1-\overline{F}_{123}}}\left(e^{(\overline{\rho}_1-\overline{\rho}_{123})\sigma_F^2}-1\right)\right] \\ \sigma_{\ln E_{eff,1}}^2 &= \ln\left[1+\overline{\rho}_{e^{\overline{F}_{23}}}\left(e^{\overline{\rho}_{23}\sigma_F^2}-1\right)\right]+\ln\left[1+\overline{\rho}_{e^{\overline{F}_1-\overline{F}_{123}}}\left(e^{(\overline{\rho}_1-\overline{\rho}_{123})\sigma_F^2}-1\right)\right] \end{aligned} \tag{2.10}$$

$$\begin{aligned} m_{\ln G_{eff,12}} &= \ln(c)-\frac{1}{8}\sigma_{12}^2+\frac{1}{15}\sigma_{123}^2-\frac{1}{2}\sigma_F^2 \\ &\quad +\frac{1}{2}\sum_{i=1}^{2}\left\{\ln\left[1+\overline{\rho}_{e^{\varepsilon_i}}\left(e^{\sigma_{\varepsilon_i}^2}-1\right)\right]-\sigma_{\varepsilon_i}^2\right\} \\ \sigma_{\ln G_{eff,12}}^2 &= \overline{\rho}_{123}\sigma_F^2+\sum_{i=1}^{2}\ln\left[1+\overline{\rho}_{e^{\varepsilon_i}}\left(e^{\sigma_{\varepsilon_i}^2}-1\right)\right] \end{aligned} \tag{2.11}$$

where $\sigma_{12}^2, \sigma_{13}^2$ and σ_{123}^2 are given in Table 2.1 and the average correlations $\overline{\rho}_J$ for any given index list $J$are found using the distribution of R_J in Supporting Information: Part B.

In analogy to the $n = 2$ case, for E_{eff_1}we find the contribution from $\overline{F}_{123} + \varepsilon_1(x_1)$ by using the 1-D results with an appropriate variance and correlation function. The remaining main effects $\varepsilon_2(x)$ and $\varepsilon_3(x)$ contribute through the arithmetic averages of $e^{\varepsilon_2(x)}$ and $e^{\varepsilon_3(x)}$, as in the two-dimensional case. Finally, we use deterministic ergodic

approximations for the effects of $\varepsilon_{12}(x_1, x_2)$, $\varepsilon_{23}(x_2, x_3)$, $\varepsilon_{13}(x_1, x_3)$, and $\varepsilon_{123}(x_1, x_2, x_3)$.

The distribution of the effective shear modulus $G_{eff_{12}}$ is found in a way similar to the $n = 2$ case. This includes the effect of the spatial average $\overline{F}_{123}$ and the effects of the two in-plane fluctuations $\varepsilon_1(x)$ and $\varepsilon_2(x)$, which contribute through the harmonic averages of $e^{\varepsilon_1(x)}$ and $e^{\varepsilon_2(x)}$. We eliminate the influence of the third main effect, $\varepsilon_3(x)$, by scaling the shear stresses by $e^{\varepsilon_3(x_3)}$ along the x_3-direction, as previously explained. The average shear strain is thus the same in each (x_1, x_2)-plane through the block. Again, we use ergodic approximations to account for $\varepsilon_{12}(x_1, x_2)$ and $\varepsilon_{123}(x_1, x_2, x_3)$, while $\varepsilon_{13}(x_1, x_3)$ and $\varepsilon_{23}(x_2, x_3)$ are assumed to have no influence on $G_{eff_{12}}$.

The remaining three-dimensional elastic moduli are obtained by permuting the indices in Eqs. 2.10 and 2.11.

2.3.4 Correlation Coefficients

Expressions and derivations for the correlation coefficients for all pairs of log-moduli are presented in Supporting Information: Part A. In total there are three correlation coefficients in 2D and fifteen correlation coefficients in 3D.

The variance of the spatial average $\overline{F}_{12}$ in 2D and $\overline{F}_{123}$ in 3D is an important common contributor to the variance of all log-moduli. This is why the correlation coefficient tends to be large for all pairs of log-moduli (see Section 2.4). Pairs of log-moduli that depend on main effects in the same way (through either arithmetic or harmonic averaging) are especially highly correlated.

2.4. Validation and Parametric Analysis

To validate the analytical approximations, we use Monte Carlo simulation. For each simulation of the modulus field, the elastic problem is solved directly in 1D and through a finite element model in 2D and 3D, with linear four- and eight-node elements, respectively. The system is resolved on an 80x80 grid (6,400 elements) in 2D and a 20x20x20 grid (8,000 elements) in 3D.

We simulate the Gaussian process $F(x)$ with a Karhunen-Loève expansion, with 80, 6400, and 8000 modes for the one-, two- and three-dimensional system, respectively. This is more than sufficient to accurately describe F-fields with the minimum correlation lengths used ($L_1/8$ for $n = 1$ and 2, $L_1/4$ for $n = 3$). The Karhunen-Loève expansion of the Gaussian process is a singular value decomposition of the covariance kernel [78]. All reported numerical distributions are based on 10,000 Monte Carlo simulations.

2.4.1 Example Validation Results

To illustrate, we present a few comparisons between numerical and analytical results involving different space dimensions n, specimen sizes, and parameters of the normal log-modulus $F = \ln E$. For $n = 1$, we consider a bar of unit length L, correlation distance $r_0 = 0.125$, standard devation $\sigma_F = 0.3$ and two alternative correlation functions, $\rho_F(r) = e^{-r/r_0}$ and $\rho_F(r) = e^{-(r/r_0)^2}$. In 2D, we analyze a rectangular specimen with side lengths $L_1 = 1$ and $L_2 = 100$, correlation length $r_0 = 2$, standard deviation $\sigma_F = 0.5$ and correlation function $\rho_F(r) = e^{-r/r_0}$. In 3D, we analyze a cubic specimen with $L = 1$, $r_0 = 0.25$, $\sigma_F = 0.3$ and correlation function $\rho_F(r) = e^{-r/r_0}$.

The results are summarized in **Figure 2.2** through a comparison of the marginal and bivariate distributions of the effective log moduli $F_i = \ln E_{eff_i}$ and $\Gamma_{ij} = \ln G_{eff_{ij}}$. For $n = 1$, we show only the distribution of the effective Young's modulus since E_{eff} and G_{eff} are deterministically related. The red ellipses are theoretical 2-sigma dispersion ellipses (consider that for a sample size of 10,000, simulations from the normal distribution should be approximately enveloped by the 3-sigma dispersion ellipse). In all

cases there is good agreement between analytical approximations and simulation results. Discrepancies, which are minor and limited to blocks with high aspect ratios, largely originate from the assumption of joint normality of the effective log-moduli: for highly elongated 2D specimens (see **Figure 2.2b**), the transversal modulus is an upper-bound to the longitudinal modulus and this condition is inconsistent with joint normality. For $n = 3$ the correlation coefficients range between $R = 0.9941$ and $R = 0.9996$ and the difference between the analytical predictions and the numerical results is never more than 0.5% of R. Similarly good agreement between analytical and simulation results have been obtained for different block geometries and stochastic properties of the log-modulus.

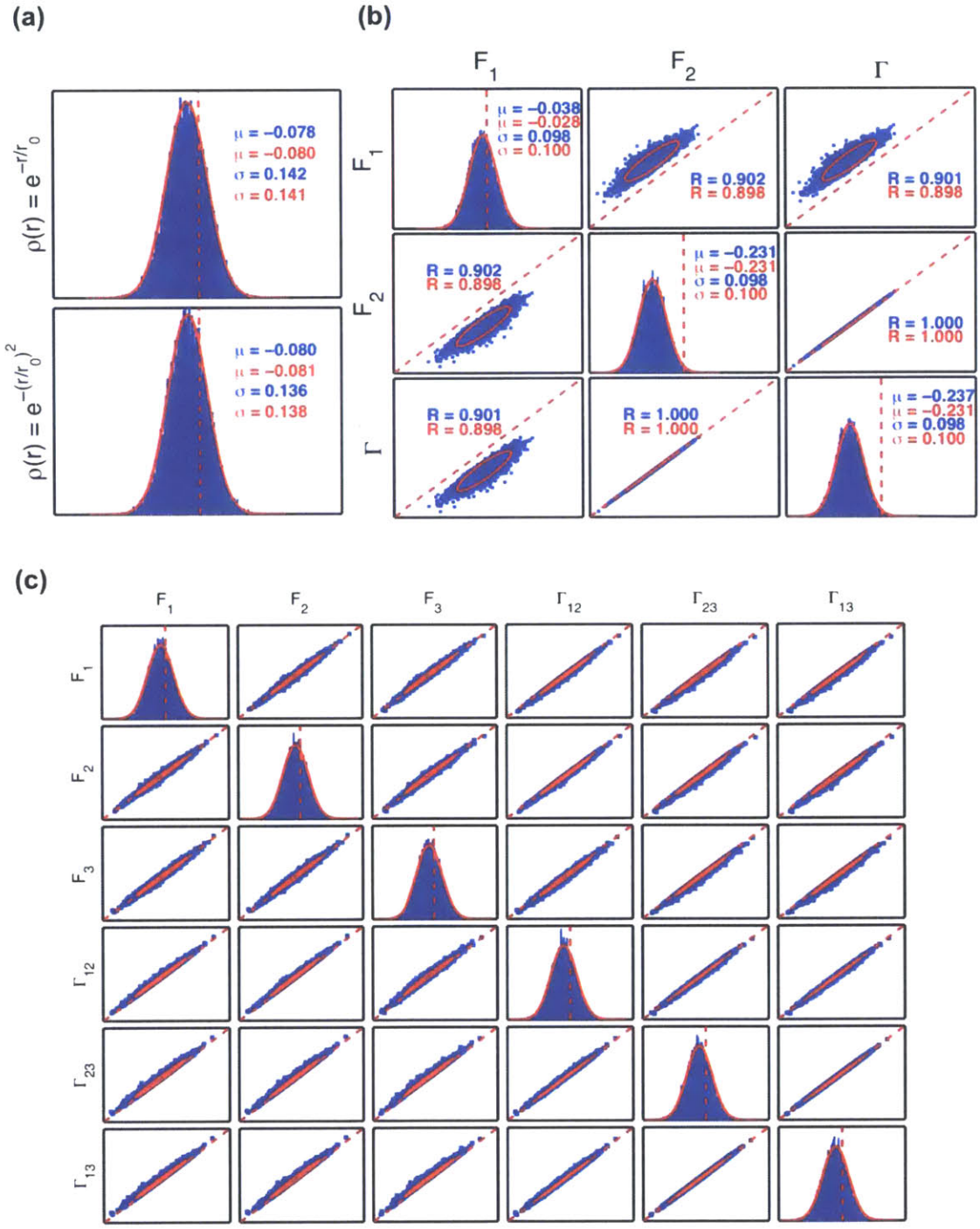

Figure 2.2: **(a)** 1D rod. Comparison of theoretical (red) and numerically predicted distributions (blue) of $\boldsymbol{F_1}$ for $\boldsymbol{r_0/L = 0.125}$, $\boldsymbol{\sigma_F = 0.3}$ and correlation function $\boldsymbol{e^{-r/r_0}}$ or $\boldsymbol{e^{-(r/r_0)\wedge 2}}$. **(b)** Comparison of theoretical and simulated distributions of the 2D elastic tensor for a rectangular block with parameters $\boldsymbol{L_2/L_1 = 100}$, $\boldsymbol{r_0/L_1 = 2}$, $\boldsymbol{\sigma_F = 0.5}$ and correlation function $\boldsymbol{e^{-r/r_0}}$. **(c)** Similar comparison for a cubic specimen with $\boldsymbol{r_0/L = 0.25}$, $\boldsymbol{\sigma_F = 0.3}$ and correlation function $\boldsymbol{e^{-r/r_0}}$.

As a benchmark of the efficacy of standard homogenization rules we also compute the Voigt and Reuss bounds for specimens with lognormal Young's modulus distributions. We find that for a 2D square specimen with lognormal stiffness, and exponential correlation kernel with parameters $r_0 = 0.125$ and $\sigma_F = 0.8$ the average Voigt estimate is almost a factor 2 larger than the average Reuss estimate. The discrepancy between the estimates depends on the parameters of the stochastic Young's modulus field. In future work we will present simple rules for the point estimates of effective stiffnesses based on the methodology developed here.

2.4.2 Parametric Analysis

Having found that the ANOVA approach produces accurate results, we use the analytical formulas to investigate how the distribution of the effective moduli varies with different controlling factors. In all cases (for $n = 1$, 2, and 3) the mean value of the log effective moduli is bound from above by zero meaning that heterogeneity always has a softening effect (see also **Figure 2.2**).

$n = 1$

Figure 2.3 shows the first two moments (mean m and standard deviation σ) of $\ln E_{eff}$ for 1D specimens. The moments are displayed for two different correlation functions $\rho(r)$ and a range of effective specimen lengths L/r_0, where r_0 is the correlation distance. Since the mean values are very nearly proportional to σ_F^2 and the standard deviations are very nearly proportional to σ_F, we calculate these moments under the reference condition $\sigma_F = 0.5$ and divide them by 0.25 and 0.5, respectively, to produce the standardized quantities m/σ_F^2 and σ/σ_F that are plotted in the figure. The effective shear modulus is deterministically related to the effective tensile modulus and is not shown. Interpretation of the plots is made easier by considering two extreme conditions:

1. In the low correlation limit $L/r_0 \gg 1$, E_{eff} approaches the 1D ergodic value with $m = -\sigma_F^2$ (see Eq. 2.1) and $\sigma = 0$;
2. In the high correlation limit $L/r_0 \ll 1$, E_{eff} equals the random but nearly uniform value of E inside the rod; hence $m = -0.5\sigma_F^2$ and $\sigma = \sigma_F$.

As the effective rod length L/r_0 varies from 0 to infinity, μ and □ vary smoothly between these two limits. The different exponents of the radii in the correlation functions lead to different decay rates of μ and □, the Gaussian correlation function exhibits significantly faster decay.

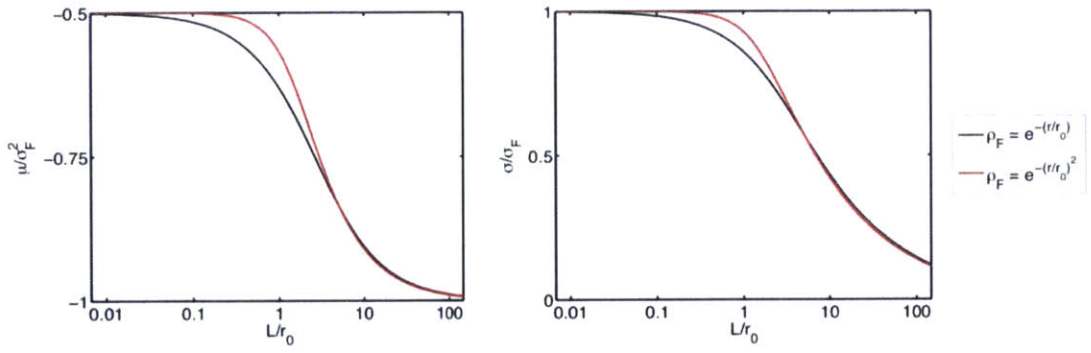

Figure 2.3: Normalized mean and standard deviation of the effective Young's modulus of a 1D rod as a function of the dimensionless specimen length $\boldsymbol{L/r_0}$, for correlation functions $\boldsymbol{e^{-(r/r_0)}}$ and $\boldsymbol{e^{-(r/r_0)^2}}$. As $\boldsymbol{L/r_0 \to \infty}$ the mean value tends to the deterministic ergodic limit, while the standard deviation tends to **0**.

$n = 2$

Figure 2.4 shows the first two moments (through the mean values □, standard deviations □, and correlation coefficients R) of the log effective moduli $F_i = \ln E_{eff,i}$ and $\Gamma = \ln G_{eff}$ for 2D blocks. The plots cover a wide range of aspect ratios L_2/L_1 and normalized correlation lengths r_0/L_1. As for $n = 1$, we calculate the mean values and standard deviations for $\sigma_F = 0.5$ and normalize them by 0.5 and 0.25 to obtain the normalized moments plotted in the figure. The correlation coefficients do not display a simple dependence on σ_F, but to avoid cluttering we show them only for $\sigma_F = 0.5$ (in

other work, not presented here, we have calculated R for different values of σ_F and observed similar trends).

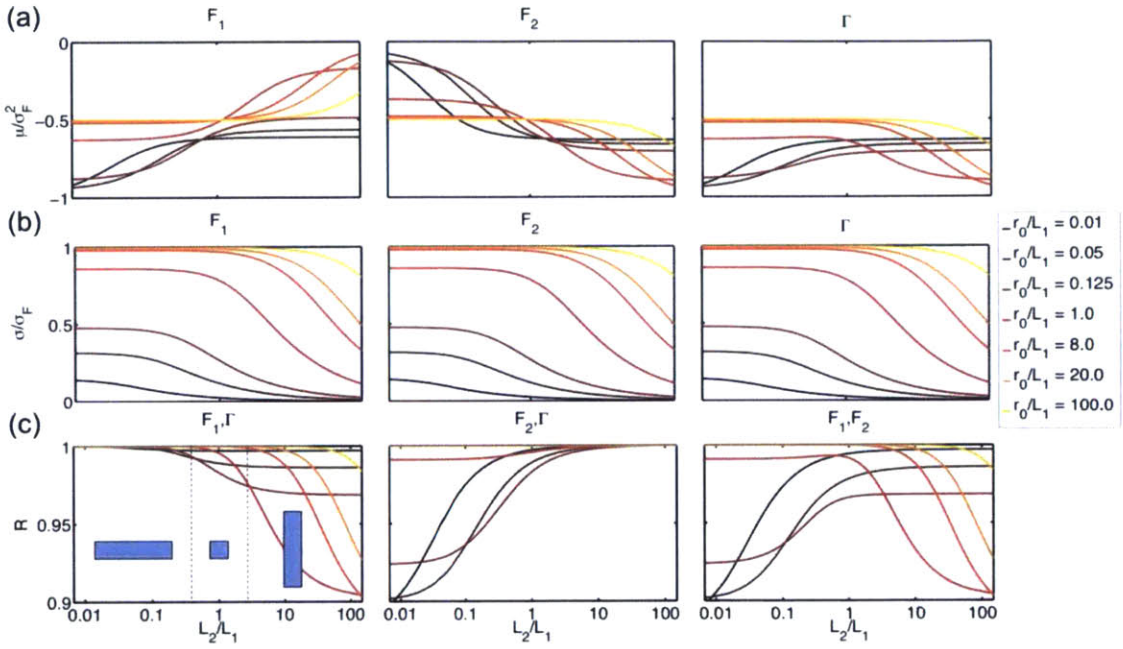

Figure 2.4: Parameters of the effective elastic tensor of a 2D rectangular block as a function of the aspect ratio L_2/L_1 and the normalized correlation distance r_0/L_1. The correlation function is e^{-r/r_0}. The correlation coefficients are shown for $\sigma_F = 0.5$. The longitudinal, square-like and transversal regimes are indicated in the lower left panel.

To understand **Figure 2.4**, it is useful to think of three reference regimes: the longitudinal regime when the specimen is highly elongated in the stretching direction (hence when $L_2/L_1 \ll 1$ for F_1 and $L_2/L_1 \gg 1$ for F_2), the square-like regime $L_2/L_1 \approx 1$, and the transversal regime when the specimen is much thinner in the stretching direction. We denote by $L_{min} = \min\{L_1, L_2\}$ and $L_{max} = \max\{L_1, L_2\}$ the minimum and maximum side lengths of the specimen; hence when $L_{min} \ll r_0 \ll L_{max}$, the 2D specimen behaves like a 1D rod. Properties of the effective moduli under limiting conditions involving the above regimes are:

1. When $L_{min} \ll r_0 \ll L_{max}$, the modulus E varies longitudinally along the rod but not transversally. The effective longitudinal modulus equals the harmonic average

of E with $m/\sigma_F^2 = -1$, whereas the effective transversal modulus equals the arithmetic average of E with $m/\sigma_F^2 = 0$;

2. Irrespective of the aspect ratio L_2/L_1, in the low correlation limit $r_0 \ll L_{min}$, E_{eff_1} and E_{eff_2} approach the 2D ergodic value with $m/\sigma_F^2 = -5/8$;
3. When $r_0 \gg L_{max}$, E_{eff_1} and E_{eff_2} equal the random but nearly uniform value of E inside the specimen. Therefore $m/\sigma_F^2 = -0.5$ for both moduli.

In Cases 1 and 2 the effective moduli are deterministic (therefore $\sigma/\sigma_F = 0$), whereas in Case 3 the effective moduli are maximally uncertain with $\sigma/\sigma_F = 1$. Many of the plots in **Figure 2.4** display transitions between two or more of the above limiting cases (of course the limiting cases themselves are never exactly realized due to finite range of the parameter values considered). Next we point at some such transitions and at general features of the results.

m_{F_1}

First consider the mean value of the effective log-modulus F_1 in the case of low correlation ($r_0/L_1 = 0.01$, black curve). As L_2/L_1 increases, one observes a transition from the first (longitudinal) to the second (ergodic) limiting condition. By the time the specimen is square, the transition is essentially complete and m_{F_1} remains nearly constant in the transversal regime. At the other correlation extreme (highest correlation with $r_0/L_1 = 100$, yellow curve), all modulus fluctuations are negligible for longitudinal and square-like specimens. Hence in these cases the third limiting condition is met and $m_{F_1}/\sigma_F^2 = -0.5$. As the ratio L_2/L_1 becomes very large, the transversal limit is approached and the first limiting condition is met. The behavior of m_{F_1} in other correlation cases can be understood by considering that values of m/σ_F^2 close to 0, -0.5, $-5/8$ and -1 are respectively associated with arithmetic averaging, no averaging, ergodic conditions, and harmonic averaging of the modulus field.

m_{F_2}

The plots of m_{F_2} are similar but inverted relative to those of m_{F_1}. The transitions between different regimes occur at the same aspect ratios L_2/L_1, but since stretching is now in the x_2 direction, the longitudinal and transversal regimes are interchanged.

m_Γ

Apart from the factor $c = \frac{1}{2(1+\nu)}$, the main difference between the effective shear and longitudinal moduli is that the main-effect fluctuations of F have a harmonic exponentiated-averaging effect in shear and a harmonic or arithmetic exponentiated-averaging effect in tension. Under ergodic conditions, these main effects are negligible and the $-5/8$ rule applies to all moduli, in shear and tension. In combination, these considerations lead to the approximate rule $m_\Gamma = \ln(c) + \min\{m_{F_1}, m_{F_2}\}$.

σ

The normalized standard deviations in **Figure 2.4b** are identical for all three log-moduli. The reason is that the variance of the log arithmetic average of a lognormal field is very nearly the same as the variance of its log harmonic average. In general, for a given correlation length r_0, σ decreases as the specimen size increases. This is why, for any given dimensionless correlation distance r_0/L_1, σ decreases as the aspect ratio L_2/L_1 increases. The highest values of σ, close to σ_F, are found when the log modulus F has near-perfect correlation inside the specimen.

Correlations

Figure 2.4c shows the correlation coefficients R for the three pairs of log-moduli. A general observation is that in all cases R is above 0.9. The highest values, close to 1, are obtained in the ergodic and high-spatial-correlation regimes. The lowest values are between moduli that depend significantly on the first-order fluctuations of the log-modulus, but are obtained through different averaging operations (arithmetic or harmonic) of E. Examples for F_1 and F_2 are cases with low correlation and small L_2/L_1 or high correlation and large L_2/L_1. Relatively low correlations are also seen between F_1

or F_2 and □ when one of the F moduli is close to the arithmetic average of E (stretching in the transversal direction).

$n = 3$

Figure 2.5 uses a format similar to **Figure 2.4** to show results for a 3-D rectangular block with $L_1 = L_2 = L = 1$ and different normalized correlation lengths r_0/L and box heights L_3/L. Since we have set $L_1 = L_2$, the log Young's moduli F_1 and F_2 and the log shear moduli Γ_{13} and Γ_{23} have identical distributions. As for $n = 1$and $n = 2$, we calculate all parameters for $\sigma_F = 0.5$ and divide the mean values and standard deviations by 0.5 and 0.25, respectively. Also like for $n = 2$, the correlation coefficients are shown for $\sigma_F = 0.5$. Of the eight unique correlation coefficients (R_{F_1,F_2}, R_{F_1,F_3}, $R_{F_1,\Gamma_{12}}$, $R_{F_1,\Gamma_{13}}$, $R_{F_3,\Gamma_{12}}$, $R_{F_3,\Gamma_{13}}$, $R_{\Gamma_{12},\Gamma_{13}}$, $R_{\Gamma_{13},\Gamma_{23}}$), we display three representative ones ($R_{F_1,\Gamma_{13}}$, $R_{F_3,\Gamma_{13}}$, R_{F_1,F_3}).

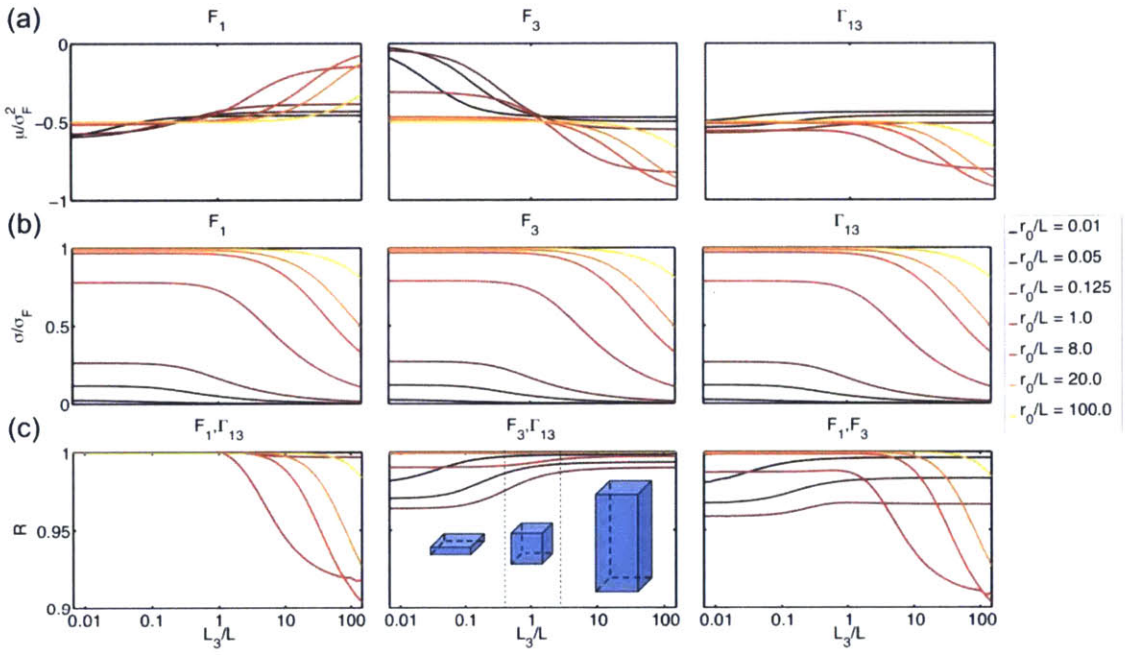

Figure 2.5: Parameters of the effective tensor for a 3D rectangular block with side lengths $L_1 = L_2 = L$ and L_3 as a function of the aspect ratio L_3/L and the normalized correlation distance r_0/L_1. The correlation function is e^{-r/r_0}. The correlation coefficients are for $\sigma_F = 0.5$. The plate-like, cube-like, and elongated regimes are indicated in the center low panel.

Results are qualitatively similar to those for $n = 2$. In particular one may notice transitions between various regimes: the thin-plate regime when $L_3/L \ll 1$, the cube-like regime when $L_3/L \approx 1$, and the elongated regime when $L_3/L \gg 1$. The quantitative differences from the 2D case are mainly explained by the fact that, as $L_3/L \to 0$, the block in **Figure 2.5** becomes a thin square plate, whereas under $L_2/L_1 \to 0$ the block in **Figure 2.4** becomes a thin 1D rod. A closer analogy can be drawn (and much closer results are observed) between the log-moduli F_2 in **Figure 2.4** and F_3 in **Figure 2.5**.

2.5. Conclusions

We have studied the effective elastic moduli of one-, two-, and three-dimensional rectangular blocks when the log Young's modulus $F(x) = \ln E(x)$ varies spatially as a normal random field. By using an ANOVA decomposition that expresses $F(x)$ as a constant plus a number of first- and higher-order fluctuation terms and analyzing each ANOVA term in turn, we developed analytical (joint lognormal) approximations to the distribution of the effective elastic tensor. To our knowledge, this is the first time that this problem has been addressed analytically. The advantage of an analytical approach over simulation is that the results are either in closed form or computable at relatively low cost, making it possible to use them for parametric analysis and ultimately for reliability-based design and optimization.

Due to various simplifying assumptions, the results are approximate, but we have found very good correspondence with Monte Carlo simulations for a wide range of geometric and stochastic parameters. The accuracy of the first two moment predictions (mean values, variances and correlation coefficients of the log-moduli) is high. The main differences come from the fact that the assumption of joint lognormal distribution is not always verified: for certain geometric configurations and loading conditions, one modulus may be known to be larger than another, whereas under joint lognormality constraints of this type cannot be imposed.

We used the analytical results to explore the dependence of the distribution of the log effective elasticity tensor on various geometric parameters (Euclidean dimension $n = 1$, 2 or 3, specimen size, aspect ratios) and probabilistic characteristics (log-modulus variance, correlation distance, shape of the correlation function). We identified limiting conditions under which it is easy to understand the main features of the distribution of the log-effective elasticity tensor and highlighted transition regimes between these limiting conditions.

In all cases we observed a softening in the mean effective log-moduli induced by the heterogeneity. Moreover, simple approximate rules were obtained and verified through simulation. One is that the log-variances of all tensor components can be taken to be the same. Another is that in most cases the log-moduli are very strongly correlated; hence in first-order approximation one could assume perfect dependence, reducing the computational task to evaluating only the mean values and common variance of the log-moduli. Exceptions to this second rule involve moduli that depend significantly on different averages (typically arithmetic for one, harmonic for the other) of the exponentiated first-order fluctuations of $F(x)$.

Future extensions of this work include:

1. Application of the moments of the effective moduli as parameters of building blocks in larger scale structural systems;
2. Application of the ANOVA approach and the lognormal approximation to other classes of randomly heterogeneous materials, in particular materials with different types of random multi-phase inclusions and possibly random within-phase variation of the elastic modulus;
3. Development of simple rules to approximate the effective elasticity tensor given a spatial pattern of Young's modulus $E(x)$. While much work has been done on this problem in the past, we are interested in seeing whether homogenization rules based on the ANOVA/lognormal approach can outperform existing rules.
4. Application of the ANOVA approach to other effective properties, such as the effective strength and fracture toughness of randomly heterogeneous specimens.

The general aim of these extensions is to develop analytical tools to characterize and control the mechanical effects of random material heterogeneities, and make it possible to design materials with superior reliability properties.

Supporting Information

Part A: Derivation of Distributions

In the derivations below the following notation is used:

- $J = \{j_1, \ldots, j_s\}$ = set of $s \leq n$ coordinate directions in n-space
- J^c = complement of J = set of $(n - s)$ coordinate directions not in J
- $x_J, x_J^c, x_{J_1}, x_{J_2}$ = coordinate vectors associated with J, J^c, J_1, J_2
- Ω_J = s-dimensional box with side lengths $L_{j_1}, \ldots, L_{j_s}$ (for $s = n$, $\Omega_J = \Omega$; otherwise Ω_J is an s-dimensional slice of Ω)
- R_J = random distance between two points uniformly and independently distributed in Ω_J.
- $R_J(r)$ = random distance between a point uniformly distributed in Ω_J and a second point uniformly and independently distributed in a similar slice translated by r in the x_1 direction. Hence $R_J = R_J(0)$.
- $\overline{\rho}_J = E[\rho_F(R_J)]$ = average correlation of F for two points uniformly and independently distributed inside Ω_J.
- $\overline{\rho}_J(r) = E\left[\rho_F\left(R_J(r)\right)\right]$. For $r = 0, \overline{\rho}_J(0) = \overline{\rho}_J$.
- $\overline{F}_J$= average value of F inside Ω_J. $\overline{F}_J$ is a random function of $\underline{x}_{J^c}$, with variance $\sigma^2_{\overline{F}_J} = \overline{\rho}_J \sigma_F^2$.

Figure 2.A1 illustrates the distances R_J and $R_J(r)$.

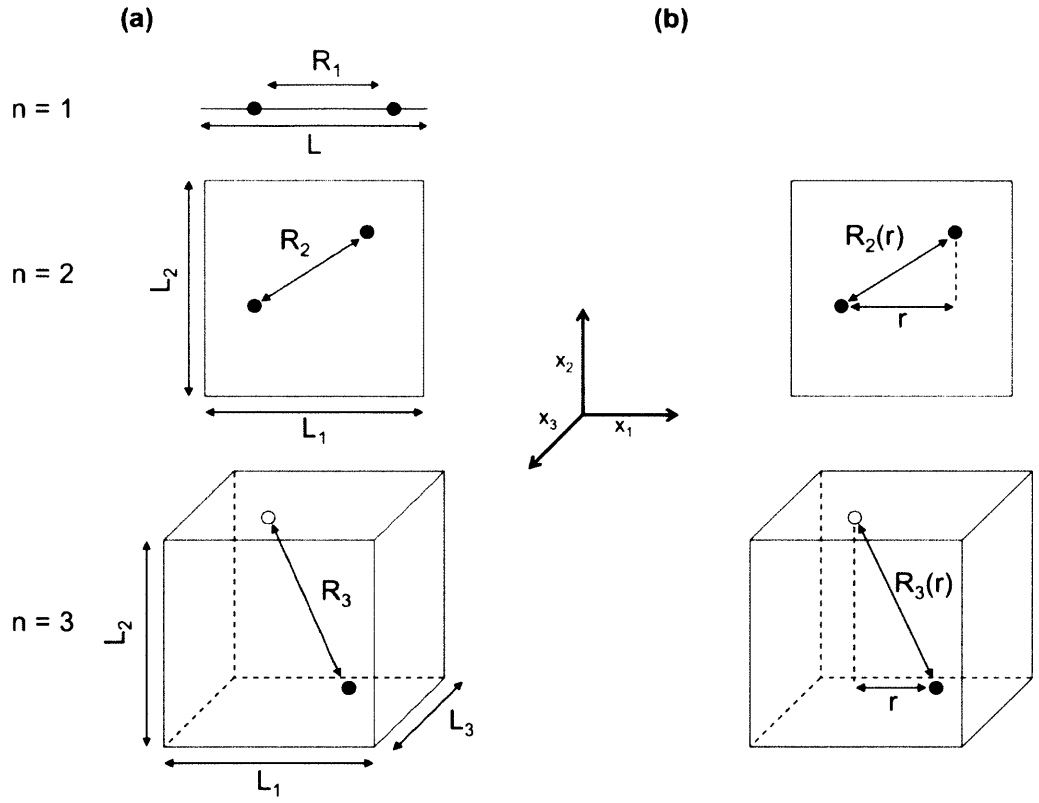

Figure 2.A1: **(a)** Block geometry for $n = 1, n = 2$, and $n = 3$ and distances R_i between random points in the blocks. **(b)** Illustration of random distances $R_i(r)$.

A.1 $n = 1$

Derivation of Eq. 2.5

For a one-dimensional bar of length L_1, the elongation u is related to the stress σ as

$$u = \sigma \int_0^{L_1} \frac{dx}{E(x)} \rightarrow E_{eff} = \frac{\sigma}{u/L_1} = \frac{1}{I} \tag{2.A1}$$

where $I = \frac{1}{L_1}\int_0^{L_1} \frac{dx}{E(x)}$. We obtain a lognormal approximation to the distribution of E_{eff} by first finding the mean value, variance, and correlation function of $1/E(x)$. Then we find the mean value and variance of I, and finally the mean value and variance of $1/I$. An approximation is made in the last step where it is assumed that I is lognormal (the exact distribution of I is neither normal nor lognormal). For each lognormal or assumed

lognormal variable, we give below the mean and variance of the variable itself and the mean and variance of its natural logarithm. For random processes, we also give the correlation and log-correlation functions, which are denoted by $\rho(r)$ and $\rho_{\ln}(r)$, respectively. We starts from the mean $m_E = 1$ and the variance σ_F^2 and correlation function $\rho_F(r)$ of the log-modulus $F(x) = \ln E(x)$. Other parameters are listed below in the order in which they are calculated:

$$E(x) \sim \begin{cases} m_E = 1;\ \sigma_{\ln E}^2 = \sigma_F^2;\ \rho_{\ln E}(r) = \rho_F(r) \\ m_{\ln E} = -\dfrac{1}{2}\sigma_F^2;\ \sigma_E^2 = e^{\sigma_F^2} - 1;\ \rho_E(r) = \rho_{e^F}(r) = \dfrac{e^{\sigma_F^2 \rho_F(r)} - 1}{e^{\sigma_F^2} - 1} \end{cases} \tag{2.A2a}$$

$$\frac{1}{E(x)} \sim \begin{cases} m_{\ln(1/E)} = \dfrac{1}{2}\sigma_F^2;\ \sigma_{\ln(1/E)}^2 = \sigma_F^2;\ \rho_{\ln(1/E)}(r) = \rho_F(r) \\ m_{1/E} = e^{\sigma_F^2};\ \sigma_{1/E}^2 = e^{2\sigma_F^2}\left(e^{\sigma_F^2} - 1\right);\ \rho_{1/E}(r) = \rho_{e^F}(r) \end{cases} \tag{2.A2b}$$

$$I \sim \begin{cases} m_I = e^{\sigma_F^2};\ \sigma_I^2 = \bar{\rho}_{e^F} e^{2\sigma_F^2}\left(e^{\sigma_F^2} - 1\right) \\ m_{\ln I} = \sigma_F^2 - \dfrac{1}{2}\ln\left[1 + \bar{\rho}_{e^F}\left(e^{\sigma_F^2} - 1\right)\right];\ \sigma_{\ln I}^2 = \ln\left[1 + \bar{\rho}_{e^F}\left(e^{\sigma_F^2} - 1\right)\right] \end{cases} \tag{2.A2c}$$

$$\bar{\rho}_{e^F} = E\left[\rho_{e^F}(R_1)\right] = \int_0^{L_1} \rho_{e^F}(r)\, f_{R_1}(r) dr \tag{2.A2d}$$

In Eq. 2.A2d $f_{R_1}(r)$ is the probability of the random distance between two points uniformly and independently distributed along the rod; see Supporting Information: Part B. Eq. 2.5 follows from Eq. 2.A2c, the assumption that I has lognormal distribution, and the relationship $E = 1/I$.

Derivation of Eq. 2.6

We write

$$\Gamma(x_1) = \overline{\Gamma}_1 + \varepsilon_1(x_1) \tag{2.A3}$$

where

$$\overline{\Gamma}_1 : N\left\{m_{\overline{\Gamma}_1} = \ln c - \frac{1}{2}\sigma_F^2; \sigma_{\overline{\Gamma}_1}^2 = \overline{\rho}_1\sigma_F^2\right\}$$

$$\varepsilon_1(x_1) : N\left\{m_{\varepsilon_1} = 0; \sigma_{\varepsilon_1}^2 = (1-\overline{\rho}_1)\sigma_F^2; \rho_{\varepsilon_1}(r) = \frac{\rho_F(r) - \overline{\rho}_1}{1-\overline{\rho}_1}\right\} \tag{A4}$$

$$e^{\varepsilon_1(x_1)} : LN\left\{m_{e^{\varepsilon_1}} = e^{\frac{1}{2}\sigma_{\varepsilon_1}^2}; \sigma_{e^{\varepsilon_1}}^2 = e^{\sigma_{\varepsilon_1}^2}\left(e^{\sigma_{\varepsilon_1}^2} - 1\right); \rho_{e^{\varepsilon_1}}(r) = \frac{e^{[\rho_F(r)-\overline{\rho}_1]\sigma_F^2} - 1}{e^{(1-\overline{\rho}_1)\sigma_F^2} - 1}\right\}$$

The log-effective modulus Γ_{eff} is given by

$$\Gamma_{eff} = \overline{\Gamma}_1 - \ln\left[\frac{1}{L_1}\int_0^{L_1} e^{-\varepsilon_1(x_1)}dx_1\right] \tag{2.A5}$$

where in good approximation $-\ln\left[\frac{1}{L_1}\int_0^{L_1} e^{-\varepsilon_1(x_1)}dx_1\right]$ has normal distribution with mean value and variance given by (see Eq. 2.A2c)

$$\begin{aligned} m &= \frac{1}{2}\left\{\ln\left[1 + \bar{\rho}_{e^{\varepsilon_1}}\left(e^{\sigma_F^2} - 1\right)\right] - \sigma_{\varepsilon_1}^2\right\}, \\ \sigma^2 &= \ln\left[1 + \bar{\rho}_{e^{\varepsilon_1}}\left(e^{\sigma_F^2} - 1\right)\right] \end{aligned} \tag{2.A6}$$

By adding the mean value and variance of $\overline{\Gamma}_1$ one obtains

$$\begin{aligned} m_{\Gamma_{eff}} &= \ln(c) - \frac{1}{2}\sigma_F^2 + \frac{1}{2}\left\{\ln\left[1 + \bar{\rho}_{e^{\varepsilon_1}}\left(e^{\sigma_{\varepsilon_1}^2} - 1\right)\right] - \sigma_{\varepsilon_1}^2\right\}, \\ \sigma_{\Gamma_{eff}}^2 &= \overline{\rho}_1\sigma_F^2 + \ln\left[1 + \bar{\rho}_{e^{\varepsilon_1}}\left(e^{\sigma_{\varepsilon_1}^2} - 1\right)\right] \end{aligned} \tag{2.A7}$$

Except for the term $\ln c$, these results are identical to those for the log-effective Young's modulus F_{eff} (notice the similarities between the terms $\overline{\rho}_{e^F}$ and $\overline{\rho}_{e^{\varepsilon_1}}$).

A.2 $n = 2$

Derivation of Eq. 2.8

Consider the ANOVA decomposition of $F(x_1, x_2)$ in Eq. 2.3. We assess the effect of different terms on E_{eff} as follows:

• *First two terms in Eq. 2.3*

If one considers only the first two terms in Eq. 2.3, the log-modulus becomes $\bar{F}_{12} + \varepsilon_1(x_1) = \bar{F}_2(x_1)$ and is a function only of x_1. To evaluate the effective modulus under these conditions, notice that

$$
\begin{aligned}
&F(x_1, x_2) \sim N\left(m_F = -\frac{1}{2}\sigma_F^2;\ \sigma_F^2;\ \rho_F(r)\right) \\
&\rightarrow \bar{F}_2(x_1) \sim N\left(m_{\bar{F}_2} = -\frac{1}{2}\sigma_F^2;\ \sigma_{\bar{F}_2}^2 = \bar{\rho}_2\sigma_F^2;\ \rho_{\bar{F}_2}(r) = \frac{\bar{\rho}_2(r)}{\bar{\rho}_2}\right) \\
&\rightarrow e^{\bar{F}_2(x_1)} \sim LN\left(m_{e^{\bar{F}_2}} = e^{-\frac{1}{2}(1-\bar{\rho}_2)\sigma_F^2};\ \sigma_{e^{\bar{F}_2}}^2 = e^{-\frac{1}{2}(1-\bar{\rho}_2)\sigma_F^2}\left(e^{\bar{\rho}_2\sigma_F^2} - 1\right);\ \rho_{e^{\bar{F}_2}}\right. \\
&\qquad\qquad \left. = \frac{e^{\bar{\rho}_2(r)\sigma_F^2} - 1}{e^{\bar{\rho}_2\sigma_F^2} - 1}\right)
\end{aligned}
\tag{2.A8}
$$

where $\bar{\rho}_2(r) = E\left[\rho_F\left(R_{2,r}\right)\right]$=(see Supporting Information: Part B). Notice that for $r = 0$, $\bar{\rho}_2(0) = \bar{\rho}_2$.

This case is analogous to the one-dimensional problem analyzed in Part A.1, except that:

1. The mean modulus is $e^{-\frac{1}{2}(1-\bar{\rho}_2)\sigma_F^2}$ not 1;
2. The log-variance is $\bar{\rho}_2\sigma_F^2$ not σ_F^2; and
3. The log-correlation function is $\rho_{\bar{F}_2}(r)$ not $\rho_F(r)$

Accounting for these differences in the results for the one-dimensional case and recalling that $\bar{F}_2(x_1) = \bar{F}_{12} + \varepsilon_1(x_1)$, one obtains that in good approximation the effective modulus has log-normal distribution with parameters

$$m = e^{-\frac{1}{2}(1+\bar{\rho}_2)\sigma_F^2}\left[1 + \bar{\rho}_{e^{\bar{F}_2}}\left(e^{\bar{\rho}_2\sigma_F^2} - 1\right)\right]$$
$$\sigma_{\ln}^2 = \ln\left[1 + \bar{\rho}_{e^{\bar{F}_2}}\left(e^{\bar{\rho}_2\sigma_F^2} - 1\right)\right] \tag{2.A9}$$

Notice that $\sigma_{\ln}^2$ in Eq. 2.A9 is the same as the first term in the log-variance in Eq. 2.8. Hence that component of variance comes from the first two terms in the ANOVA decomposition of Eq. 2.3.

• *Third term in Eq. 2.3*

Under $F(x_1, x_2) = \varepsilon_2(x_2)$, the log-modulus depends only on x_2 and

$$E_{eff} = \frac{1}{L_2}\int_0^{L_2} e^{\varepsilon_2(x_2)}dx_2 \tag{2.A10}$$

where

$$\varepsilon_2(x_2) \sim N\left(m_{\varepsilon_2} = 0;\ \sigma_{\varepsilon_2}^2 = (\bar{\rho}_1 - \bar{\rho}_{12})\sigma_F^2;\ \rho_{\varepsilon_2}(r) = \frac{\bar{\rho}_1(r) - \bar{\rho}_{12}}{\bar{\rho}_1 - \bar{\rho}_{12}}\right) \tag{2.A11}$$

The correlation function in Eq. 2.A11 is obtained from $\bar{F}_1(x_2) = \bar{F}_{12} + \varepsilon_2(x_2)$. Since for random x_2 the terms $\bar{F}_{12}$ and $\varepsilon_2(x_2)$ are uncorrelated, the covariance function of $\bar{F}_1(x_2)$ is $Cov[\bar{F}_1(x_2), \bar{F}_1(x_2 + r)] = \sigma_{\bar{F}_{12}}^2 + \sigma_{\varepsilon_2}^2\rho_{\varepsilon_2}(r)$. The correlation function $\rho_{\varepsilon_2}(r)$ in Eq. 2.A11 follows from this relationship and $Cov[\bar{F}_1(x_2), \bar{F}_1(x_2 + r)] = \rho_1(r)\sigma_F^2$ (in analogy with Eq. A8), $\sigma_{\bar{F}_{12}}^2 = \bar{\rho}_{12}(r)\sigma_F^2$ (from Table 1), and $\sigma_{\varepsilon_2}^2 = (\bar{\rho}_1 - \bar{\rho}_{12})\sigma_F^2$ from Eq. 2.A11.

It follows from Eq. 2.A11 that $e^{\varepsilon_2(x_2)}$ is a lognormal process with mean value, variance and correlation function

$$
\begin{aligned}
m_{e^{\varepsilon_2}} &= e^{\frac{1}{2}(\bar{\rho}_1-\bar{\rho}_{12})\sigma_F^2} \\
\sigma^2_{e^{\varepsilon_2}} &= e^{(\bar{\rho}_1-\bar{\rho}_{12})\sigma_F^2}\left[e^{(\bar{\rho}_1-\bar{\rho}_{12})\sigma_F^2}-1\right] \\
\rho_{e^{\varepsilon_2}}(r) &= \frac{e^{\sigma^2_{\varepsilon_2}\rho_{\varepsilon_2}(r)}-1}{e^{\sigma^2_{\varepsilon_2}}-1} = \frac{e^{[\bar{\rho}_1(r)-\bar{\rho}_{12}]\sigma_F^2}-1}{e^{(\bar{\rho}_1-\bar{\rho}_{12})\sigma_F^2}-1}
\end{aligned}
\tag{2.A12}
$$

Finally, from Eqs. 2.A10 and 2.A12, the effect on E_{eff} is a random factor with mean value, variance and log-variance (the last quantity, under the approximation of lognormal distribution)

$$
\begin{aligned}
m &= m_{e^{\varepsilon_2}} = e^{\frac{1}{2}(\bar{\rho}_1-\bar{\rho}_{12})\sigma_F^2} \\
\sigma^2 &= \bar{\rho}_{e^{\varepsilon_2}}\sigma^2_{e^{\varepsilon_2}} = \bar{\rho}_{e^{\varepsilon_2}}e^{(\bar{\rho}_1-\bar{\rho}_{12})\sigma_F^2}\left[e^{(\bar{\rho}_1-\bar{\rho}_{12})\sigma_F^2}-1\right] \\
\sigma^2_{\ln} &= -\ln(m^2)+\ln(m^2+\sigma^2) = \ln\left[1+\bar{\rho}_{e^{\varepsilon_2}}\left(e^{(\bar{\rho}_1-\bar{\rho}_{12})\sigma_F^2}-1\right)\right]
\end{aligned}
\tag{2.A13}
$$

• *Fourth term in Eq. 2.3*

In the ergodic case, the effect of $\left[\varepsilon_{12}(x_1,x_2)-\frac{1}{2}\sigma^2_{12}\right]$ on E_{eff} is a factor $e^{-\frac{1}{2}\sigma^2_{12}}$; see Eq. 2.1 for $n=2$. Therefore the ergodic approximation to the effect of $\varepsilon_{12}(x_1,x_2)$ on E_{eff} is the deterministic factor

$$
e^{\frac{1}{2}\sigma^2_{12}}e^{-\frac{5}{8}\sigma^2_{12}} = e^{-\frac{1}{8}\sigma^2_{12}} = e^{-\frac{1}{8}(1-\bar{\rho}_1-\bar{\rho}_2+\bar{\rho}_{12})\sigma_F^2} \tag{2.A14}
$$

where we have used $\sigma^2_{12} = (1-\bar{\rho}_1-\bar{\rho}_2+\bar{\rho}_{12})\sigma_F^2$ from Table 2.1.

Equation 2.8 follows from multiplicatively combining the effects in Eqs. 2.A9, 2.A13 and 2.A14.

Derivation of Eq. 2.9

The ANOVA decomposition of $\Gamma(x_1, x_2)$ is

$$\Gamma(x_1, x_2) = \overline{\Gamma}_{12} + \varepsilon_1(x_1) + \varepsilon_2(x_2) + \varepsilon_{12}(x_1, x_2) \tag{2..A15}$$

where

$$\begin{aligned}
&\overline{\Gamma}_{12}: N\left\{m_{\overline{\Gamma}_{12}} = \ln(c) - \frac{1}{2}\sigma_F^2; \sigma_{\overline{\Gamma}_{12}}^2 = \overline{\rho}_{12}\sigma_F^2\right\} \\
&\varepsilon_1(x_1): N\left\{m_{\varepsilon_1} = 0, \sigma_{\varepsilon_1}^2 = (\overline{\rho}_2 - \overline{\rho}_{12})\sigma_F^2, \rho_{\varepsilon_1}(r) = \frac{\overline{\rho}_2(r) - \overline{\rho}_{12}}{\overline{\rho}_2 - \overline{\rho}_{12}}\right\} \\
&e^{\varepsilon_1(x_1)}: LN\left\{m_{e^{\varepsilon_1}} = e^{\frac{1}{2}\sigma_{\varepsilon_1}^2}, \sigma_{e^{\varepsilon_1}}^2 = e^{\sigma_{\varepsilon_1}^2}\left(e^{\sigma_{\varepsilon_1}^2} - 1\right), \rho_{e^{\varepsilon_1}}(r)\right. \\
&\qquad\qquad \left. = \frac{e^{[\overline{\rho}_2(r) - \overline{\rho}_{12}]\sigma_F^2} - 1}{e^{(\overline{\rho}_2 - \overline{\rho}_{12})\sigma_F^2} - 1}\right\}
\end{aligned} \tag{2.A16}$$

The properties of $\varepsilon_2(x_2)$ in Eq. 2.A15 are similar to those of $\varepsilon_1(x_1)$ (interchange the indices 1 and 2) and the second-order interaction field $\varepsilon_{12}(x_1, x_2)$ is normal with mean value 0 and variance $\sigma_{12}^2 = (1 - \overline{\rho}_1 - \overline{\rho}_2 + \overline{\rho}_{12})\sigma_F^2$.

The effect of $\varepsilon_1(x_1)$ on Γ_{eff} is an additive variable with mean value and variance given by Eq. 2.A6 with parameters in Eq. 2.A16. The effect of $\varepsilon_2(x_2)$ is similar (interchange 1 with 2). Finally, the effect of $\varepsilon_{12}(x_1, x_2)$ is approximated as a deterministic additive constant equal to $b\sigma_{12}^2$ where $b = \frac{1}{2} - \frac{5}{8} = -\frac{1}{8}$ (value under tension).

In summary, in the 2D case the distribution of the log-effective shear modulus $\square_{eff}$ is approximately normal with mean value and variance

$$m_{\Gamma_{eff}} = \ln(c) - \frac{1}{2}\sigma_F^2 - \frac{1}{2}\sigma_{12}^2 + \frac{1}{2}\sum_{i=1}^{2}\left\{\ln\left[1 + \bar{\rho}_{e^{\varepsilon_i}}\left(e^{\sigma_{\varepsilon_i}^2} - 1\right)\right] - \sigma_{\varepsilon_i}^2\right\},$$
$$\sigma_{\Gamma_{eff}}^2 = \bar{\rho}_{12}\sigma_F^2 + \frac{1}{2}\sum_{i=1}^{2}\ln\left[1 + \bar{\rho}_{e^{\varepsilon_i}}\left(e^{\sigma_{\varepsilon_i}^2} - 1\right)\right] \quad (2.A17)$$

Correlation Coefficients

Next we derive expressions for the correlation coefficients of different pairs of effective log-moduli in the 2D case.

$R_{F_{eff_1},F_{eff_2}}$

We start from the correlation between the log-effective moduli F_{eff_1} and F_{eff_2}. Note that $\overline{F}_{12}$ has the same random effect on F_{eff_1} and F_{eff_2} and that, in our approximate two-dimensional analysis, the effect of $\varepsilon_{12}(x_1, x_2)$ is considered determinist and is the same for F_{eff_1} and F_{eff_2}. The main issue is to determine the variances and covariance of the effects of $\varepsilon_1(x_1)$ and $\varepsilon_2(x_2)$ on the log-effective moduli. Since the reasoning on $\varepsilon_1(x_1)$ and $\varepsilon_2(x_2)$is symmetrical, it suffices to consider the effect of $\varepsilon_1(x_1)$ on F_{eff_1} and F_{eff_2}.

The processes $\varepsilon_1(x_1)$ and $e^{\varepsilon_1(x_1)}$ are respectively normal and lognormal, with parameters

$$\varepsilon_1(x_1): m_{\varepsilon_1} = 0, \sigma_{\varepsilon_1}^2 = \left(\overline{\rho}_2 - \overline{\rho}_{12}\right)\sigma_F^2, \rho_{\varepsilon_1}(r) = \frac{\overline{\rho}_2(r) - \overline{\rho}_{12}}{\overline{\rho}_2 - \overline{\rho}_{12}}$$
$$e^{\varepsilon_1(x_1)}: m_{e^{\varepsilon_1}} = e^{\frac{1}{2}\sigma_{\varepsilon_1^2}}, \sigma_{e^{\varepsilon_1}}^2 = e^{\sigma_{\varepsilon_1}^2}\left(e^{\sigma_{\varepsilon_1}^2} - 1\right), \rho_{e^{\varepsilon_1}}(r) = \frac{e^{[\overline{\rho}_2(r) - \overline{\rho}_{12}]\sigma_F^2} - 1}{e^{(\overline{\rho}_2 - \overline{\rho}_{12})\sigma_F^2} - 1} \quad (2.A18)$$

Under $F(x_1, x_2) = \varepsilon_1(x_1)$, the variables $I_1 = 1/E_{eff_1}$ and $I_1 = E_{eff_2}$ are given by

$$I_1 = \frac{1}{L_1}\int_0^{L_1} e^{-\varepsilon_1(x_1)}dx_1 \quad (2.A19)$$

$$I_2 = 1/L_1 \int_0^{L_1} e^{\varepsilon_1(x_1)} dx_1$$

Since $\varepsilon_1(x_1)$ and $-\varepsilon_1(x_1)$ are statistically equivalent, the distributions of I_1 and I_2 are the same and have the following mean value, variance, log-mean value and log-variance (the last two quantities, under the assumption of lognormality):

$$\begin{aligned} &m_I = e^{\frac{1}{2}\sigma_{\varepsilon_1}^2}, \sigma_I^2 = \overline{\rho}_{e^{\varepsilon_1}} \sigma_{e^{\varepsilon_1}}^2 \\ &m_{\ln(I)} = \frac{1}{2}\sigma_{\varepsilon_1}^2 - \frac{1}{2}\ln\left[1 + \overline{\rho}_{e^{\varepsilon_1}}\left(e^{\sigma_{\varepsilon_1}^2} - 1\right)\right], \sigma_{\ln(I)}^2 = \ln\left[1 + \overline{\rho}_{e^{\varepsilon_1}}\left(e^{\sigma_{\varepsilon_1}^2} - 1\right)\right] \end{aligned} \tag{2.A20}$$

In addition, the covariance between I_1 and I_2 is

$$Cov[I_1, I_2] = e^{\sigma_{\varepsilon_1}^2} E_{R_1}\left[e^{-\rho_{\varepsilon_1}(R_1)\sigma_{\varepsilon_1}^2} - 1\right] \tag{2.A21}$$

Equation 2.A21 is obtained by noting that $\varepsilon_1(x_1)$ and $-\varepsilon_1(x_1)$ have cross-covariance function $-\rho_{\varepsilon_1}(r)\sigma_{\varepsilon_1}^2$. It follows that the cross-covariance function of $e^{\varepsilon_1(x_1)}$ and $e^{-\varepsilon_1(x_1)}$ is

$$Cov\left[e^{\varepsilon_1(x_1)}, e^{-\varepsilon_1(x_1+r)}\right] = \sigma_{e^{\varepsilon_1}}^2 \frac{e^{-\rho_{\varepsilon_1}(r)\sigma_{\varepsilon_1}^2} - 1}{e^{\sigma_{\varepsilon_1}^2} - 1} = e^{\sigma_{\varepsilon_1}^2}\left[e^{-\rho_{\varepsilon_1}(r)\sigma_{\varepsilon_1}^2} - 1\right] \tag{2.A22}$$

where we have used the expression for $\sigma_{e^{\varepsilon_1}}^2$ in Eq. 2.A18. As stated in Eq. 2.A21, the covariance between I_1 and I_2 is the expected value of this cross-covariance for two points independently and uniformly distributed in $[0, L_1]$.

Using relations for lognormal distributions, the covariance between $F_{eff_1} = -\ln(I_1)$ and $F_{eff_2} = \ln(I_2)$ is

$$Cov[F_{eff_1}, F_{eff_2}] = -Cov[\ln(I_1), \ln(I_2)] = -\ln\left(1 + \frac{Cov[I_1, I_2]}{m_I^2}\right)$$
$$= -\ln\left(E_{R_1}\left[e^{-\rho_{\varepsilon_1}(R_1)\sigma_{\varepsilon_1}^2}\right]\right) \quad \text{(2.A23)}$$

In summary, we found that under $F(x_1, x_2) = \varepsilon_1(x_1)$ the log-moduli $F_{eff_1} = -\ln(I_1)$ and $F_{eff_2} = \ln(I_2)$ have approximate normal distribution with parameters

$$m_{F_{eff_2}} = \frac{1}{2}\sigma_{\varepsilon_1}^2 - \frac{1}{2}\ln\left[1 + \overline{\rho}_{e^{\varepsilon_1}}\left(e^{\sigma_{\varepsilon_1}^2} - 1\right)\right]; m_{F_{eff_1}} = -m_{F_{eff_2}}$$
$$\sigma_{F_{eff_1}}^2 = \sigma_{F_{eff_2}}^2 = \ln\left[1 + \overline{\rho}_{e^{\varepsilon_1}}\left(e^{\sigma_{\varepsilon_1}^2} - 1\right)\right] \quad \text{(2.A24)}$$
$$Cov[F_{eff_1}, F_{eff_2}] = -\ln\left(E_{R_1}\left[e^{-\rho_{\varepsilon_1}(R_1)\sigma_{\varepsilon_1}^2}\right]\right)$$

If now one includes all the ANOVA terms, F_{eff_1} and F_{eff_2} have common variance and covariance

$$\sigma_{F_{eff}}^2 = \overline{\rho}_{12}\sigma_F^2 + \sum_{i=1}^{2} \ln\left[1 + \overline{\rho}_{e^{\varepsilon_i}}\left(e^{\sigma_{\varepsilon_i}^2} - 1\right)\right]$$
$$Cov[F_{eff_1}, F_{eff_2}] = \overline{\rho}_{12}\sigma_F^2 - \sum_{i=1}^{2} \ln\left(E_{R_i}\left[e^{-\rho_{\varepsilon_i}(R_i)\sigma_{\varepsilon_i}^2}\right]\right) \quad \text{(2.A25)}$$

The correlation coefficient is found as the ratio $\frac{Cov[F_{eff_1}, F_{eff_2}]}{\sigma_{F_{eff}}^2}$.

$R_{F_{eff_1}, \Gamma_{eff}}$

Consider now the correlation coefficient between Γ_{eff} and $F_{eff,1}$. Notice that $\overline{F}_{12}$ and $\varepsilon_1(x_1)$ have the same random effect on Γ_{eff} and $F_{eff,1}$, whereas $\varepsilon_2(x_2)$ affects the log-moduli through the following additive random effects:

- Effect on Γ_{eff}: Additive term $-\ln(I_1)$, where $I_1 = \frac{1}{L_2}\int_0^{L_2} e^{-\varepsilon_2(x_2)}dx_2$
- Effect on F_{eff_1}: Additive term $\ln(I_2)$, where $I_2 = \frac{1}{L_2}\int_0^{L_2} e^{-\varepsilon_2(x_2)}dx_2$

Following the analysis for the correlation coefficient between F_{eff_1} and F_{eff_2}, Eqs. 2.A18-2.A23, the covariance between the additive terms $-\ln(I_1)$ and $\ln(I_2)$ is

$$-\ln\left(E_{R_2}\left[e^{-\rho_{\varepsilon_2}(R_2)\sigma^2_{\varepsilon_2}}\right]\right) \tag{2.A26}$$

When the effects of $\overline{F}_{12}$ and $\varepsilon_1(x_1)$ are included, the covariance between Γ_{eff} and $F_{eff,1}$ becomes

$$Cov\left[F_{eff,1}, \Gamma_{eff}\right] = \overline{\rho}_{12}\sigma_F^2 + \ln\left[1 + \bar{\rho}_{e^{\varepsilon_1}}\left(e^{\sigma^2_{\varepsilon_1}} - 1\right)\right] - \ln\left(E_{R_2}\left[e^{-\rho_{\varepsilon_2}(R_2)\sigma^2_{\varepsilon_2}}\right]\right) \tag{2.A27}$$

For $Cov\left[F_{eff,2}, \Gamma_{eff}\right]$, interchange 1 with 2 in Eq. 2.A27. The correlation coefficients are found as the ratios $\frac{Cov\left[F_{eff_i}, \Gamma_{eff}\right]}{\sigma^2_{F_{eff}}}$.

A.3 $n = 3$

We now consider the joint distribution of the effective Young's and shear log-moduli for a three-dimensional rectangular box.

Derivation of Eq. 2.10

• *First Two Terms in Eq. 2.4*

Considering only the first two terms in Eq. 4, the log-modulus $\bar{F}_{123} + \varepsilon_1(x_1) = \bar{F}_{23}(x_1)$ varies only with x_1. To evaluate the effective modulus under these conditions, notice that

$$\bar{F}_{23}(x_1) \approx N\left(m_{\bar{F}_{23}} = -\frac{1}{2}\sigma_F^2;\ \sigma^2_{\bar{F}_{23}} = \bar{\rho}_{23}\sigma_F^2; \rho_{\bar{F}_{23}}(r) = \frac{\bar{\rho}_{23}(r)}{\bar{\rho}_{23}}\right) \tag{2.A28}$$

$$e^{\bar{F}_{23}(x_1)} \approx LN\left(m_{e^{\bar{F}_{23}}} = e^{-\frac{1}{2}(1-\bar{\rho}_{23})\sigma_F^2};\ \sigma^2_{e^{\bar{F}_{23}}}\right.$$

$$\left. = e^{-(1-\bar{\rho}_{23})\sigma_F^2}\left(e^{\bar{\rho}_{23}\sigma_F^2} - 1\right);\ \rho_{e^{\bar{F}_{23}}}(r) = \frac{e^{\bar{\rho}_{23}(r)\sigma_F^2} - 1}{e^{\bar{\rho}_{23}\sigma_F^2} - 1}\right)$$

where $\bar{\rho}_{23}(r) = E\left[\rho_F\left(R_{23}(r)\right)\right]$ and $R_{23}(r)$ is the random distance between two points independently and uniformly distributed on two parallel $(L_2 \times L_3)$ rectangles separated by distance r. For the distribution of this distance, see Eq. 2.B8. The case $r = 0$ gives $R_{23}(0) = R_{23}$ and $\bar{\rho}_{23}(0) = \bar{\rho}_{23}$.

Evaluation of the distribution of E_{eff} is analogous to the one-dimensional problem in Section A.1, except that:

1. The mean modulus is $e^{-\frac{1}{2}(1-\bar{\rho}_{23})\sigma_F^2}$ not 1;
2. The log-variance is $\bar{\rho}_{23}\sigma_F^2$ not σ_F^2; and
3. The log-correlation function is $\rho_{\bar{F}_{23}}(r)$ not $\rho(r)$

Accounting for these differences, one obtains that in good approximation E_{eff} has lognormal distribution with parameters

$$\begin{aligned} m &= e^{-\frac{1}{2}(1-\bar{\rho}_{23})\sigma_F^2}\left[1 + \bar{\rho}_{e^{\bar{F}_{23}}}\left(e^{\bar{\rho}_{23}\sigma_F^2} - 1\right)\right] \\ \sigma^2_{\ln} &= \ln\left[1 + \bar{\rho}_{e^{\bar{F}_{23}}}\left(e^{\bar{\rho}_{23}\sigma_F^2} - 1\right)\right] \end{aligned} \tag{2.A29}$$

• *Effect of ε Terms Without 1 in the Index List*

Under

$$F(x_1, x_2, x_3) = \varepsilon_2(x_2) + \varepsilon_3(x_3) + \varepsilon_{23}(x_2, x_3) = \bar{F}_1(x_2, x_3) - \bar{F}_{123} \tag{2.A30}$$

the log-modulus F is a function only of x_2 and x_3 and

$$E_{eff} = \frac{1}{L_2 L_3}\int_0^{L_2} dx_2 \int_0^{L_3} e^{\bar{F}_1(x_2,x_3)-\bar{F}_{123}} dx_3 \tag{2.A31}$$

Using Table 2.1, $\bar{F}_1(x_2,x_3) - \bar{F}_{123}$ is a normal random field with parameters

$$\begin{aligned} m_{\bar{F}_1-\bar{F}_{123}} &= 0 \\ \sigma^2_{\bar{F}_1-\bar{F}_{123}} &= (\bar{\rho}_1 - \bar{\rho}_{123})\sigma_F^2 \\ \rho_{\bar{F}_1-\bar{F}_{123}}(r) &= \frac{\bar{\rho}_1(r) - \bar{\rho}_{123}}{\bar{\rho}_1 - \bar{\rho}_{123}} \end{aligned} \tag{2.A32}$$

Therefore $e^{\bar{F}_1(x_2,x_3)-\bar{F}_{123}}$ is a lognormal field with mean value, variance and correlation function given by

$$\begin{aligned} m_{e^{\bar{F}_1-\bar{F}_{123}}} &= e^{\frac{1}{2}(\bar{\rho}_1-\bar{\rho}_{123})\sigma_F^2} \\ \sigma^2_{e^{\bar{F}_1-\bar{F}_{123}}} &= e^{(\bar{\rho}_1-\bar{\rho}_{123})\sigma_F^2}\left[e^{(\bar{\rho}_1-\bar{\rho}_{123})\sigma_F^2} - 1\right] \\ \rho_{e^{\bar{F}_1-\bar{F}_{123}}}(r) &= \frac{e^{\sigma^2_{\bar{F}_1-\bar{F}_{123}}\rho_{\bar{F}_1-\bar{F}_{123}}(r)} - 1}{e^{\sigma^2_{\bar{F}_1-\bar{F}_{123}}} - 1} = \frac{e^{[\bar{\rho}_1(r)-\bar{\rho}_{123}]\sigma_F^2} - 1}{e^{(\bar{\rho}_1-\bar{\rho}_{123})\sigma_F^2} - 1} \end{aligned} \tag{2.A33}$$

It follows from Eqs. 2.A31 and 2.A33 that E_{eff} has mean value, variance and log-variance (the last quantity, under the approximate assumption of lognormality)

$$\begin{aligned} m &= m_{e^{\bar{F}_1-\bar{F}_{123}}} = e^{\frac{1}{2}(\bar{\rho}_1-\bar{\rho}_{123})\sigma_F^2} \\ \sigma^2 &= \bar{\rho}_{e^{\bar{F}_1-\bar{F}_{123}}}\sigma^2_{e^{\bar{F}_1-\bar{F}_{123}}} = \bar{\rho}_{e^{\bar{F}_1-\bar{F}_{123}}} e^{(\bar{\rho}_1-\bar{\rho}_{123})\sigma_F^2}\left[e^{(\bar{\rho}_1-\bar{\rho}_{123})\sigma_F^2} - 1\right] \\ \sigma^2_{\ln} &= -\ln(m^2) + \ln(m^2+\sigma^2) = \ln\left[1 + \bar{\rho}_{e^{\bar{F}_1-\bar{F}_{123}}}\left(e^{(\bar{\rho}_1-\bar{\rho}_{123})\sigma_F^2} - 1\right)\right] \end{aligned} \tag{2.A34}$$

where $\bar{\rho}_{e^{\bar{F}_1-\bar{F}_{123}}} = E\left[\rho_{e^{\bar{F}_1-\bar{F}_{123}}}(R_{23})\right]$.

• *Effects of* $\varepsilon_{12}(x_1, x_2)$ *and* $\varepsilon_{13}(x_1, x_3)$

The term $\varepsilon_{12}(x_1, x_2)$ is similar to $\varepsilon_{12}(x_1, x_2)$ in the two-dimensional problem. We show in Section 2.4 that the effect of that term on E_{eff} is accurately estimated from the ergodic result in Eq. 2.1 for $n = 2$. Considering that in the three-dimensional case $\varepsilon_{12}(x_1, x_2)$ has mean value zero and variance $\sigma_{12}^2 = (\bar{\rho}_3 - \bar{\rho}_{13} - \bar{\rho}_{23} + \bar{\rho}_{123})\sigma_F^2$, the ergodic approximation to its effect on E_{eff} is the deterministic factor

$$e^{-\frac{1}{8}\sigma_{12}^2} = e^{-\frac{1}{8}(\bar{\rho}_3 - \bar{\rho}_{23} - \bar{\rho}_{13} + \bar{\rho}_{123})\sigma_F^2} \tag{2.A35}$$

The corresponding factor for $\varepsilon_{13}(x_1, x_3)$ is

$$e^{-\frac{1}{8}\sigma_{13}^2} = e^{-\frac{1}{8}(\bar{\rho}_2 - \bar{\rho}_{12} - \bar{\rho}_{23} + \bar{\rho}_{123})\sigma_F^2} \tag{2.A36}$$

• *Effect of* $\varepsilon_{123}(x_1, x_3)$

We use the ergodic results in Eq. 2.2 for $n = 3$ to approximate the effect on E_{eff} as the deterministic factor

$$m_{e^{\varepsilon_{123}}} e^{-\frac{7}{15}\sigma_{123}^2} = e^{\left(\frac{1}{2} - \frac{7}{15}\right)\sigma_{123}^2} = e^{\frac{1}{30}\sigma_{123}^2} \tag{2.A37}$$

where $\sigma_{123}^2 = (1 - \bar{\rho}_1 - \bar{\rho}_2 - \bar{\rho}_3 + \bar{\rho}_{12} + \bar{\rho}_{13} + \bar{\rho}_{23} - \bar{\rho}_{123})\sigma_F^2$ from Table 2.1. The coefficient 1/30 in the exponent of Eq. 2.A37 makes this factor close to 1.

By multiplicatively combining the effects in Eqs. 2.A29, 2.A34, 2.A35, 2.A36 and 2.A37, one obtains that the distribution of E_{eff} in the three-dimensional case is approximately lognormal with parameters in Eq. 2.10.

Derivation of Eq. 2.11

Consider the average shear $\overline{\gamma}_{12}$ produced by shear stresses $\overline{\tau}_{12}$. To make the problem analytically tractable, we consider the case when the boundary traction τ_{12} is constant on any plane normal to x_3, but varies with x_3 as $e^{\varepsilon_3(x_3)}$, i.e. we consider shear tractions

$$\tau_{12}(x_3) = \overline{\tau}_{12} \frac{e^{\varepsilon_3(x_3)}}{\frac{1}{L_3}\int_0^{L_3} e^{\varepsilon_3(u)} du} \tag{2.A38}$$

Under the tractions in Eq. 2.A38 and $\Gamma(x_1, x_2, x_3)$, the average shear strain $\overline{\gamma}_{12}$ is independent of x_3 and the variance of $\Gamma_{eff,12} = \ln(\overline{\tau}_{12}/\overline{\gamma}_{12})$ is given by Eq. 2.A17 using parameters appropriate to the 3D case. One might further assume that the other two second-order terms, $\varepsilon_{13}(x_1, x_3)$ and $\varepsilon_{23}(x_2, x_3)$, have no effect on $\Gamma_{eff,12}$ and that the effect of the third-order term $\varepsilon_{123}(x_1, x_2, x_3)$ is a deterministic additive constant $\frac{1}{15}\sigma_{123}^2$. Under these assumptions

$$\begin{aligned} m_{\Gamma_{eff,12}} &= \ln(c) - \frac{1}{2}\sigma_F^2 - \frac{1}{2}\sigma_{12}^2 + \frac{1}{15}\sigma_{123}^2 \\ &\quad + \frac{1}{2}\sum_{i=1}^{2} \left\{ \ln\left[1 + \bar{\rho}_{e^{\varepsilon_i}}\left(e^{\sigma_{\varepsilon_i}^2} - 1\right)\right] - \sigma_{\varepsilon_i}^2 \right\}, \\ \sigma_{\Gamma_{eff,12}}^2 &= \overline{\rho}_{123}\sigma_F^2 + \frac{1}{2}\sum_{i=1}^{2} \ln\left[1 + \bar{\rho}_{e^{\varepsilon_i}}\left(e^{\sigma_{\varepsilon_i}^2} - 1\right)\right] \end{aligned} \tag{2.A39}$$

Correlation Coefficients

We derive expressions for the correlation coefficients of selected pairs of log-moduli for $n = 3$. Expressions for other pairs are found by appropriately permuting indices.

$R_{F_{eff_1}, F_{eff_2}}$

For the case of a three-dimensional rectangular block, the log-modulus may be decomposed as

$$F(x_1,x_2,x_3) = \overline{F}_3(x_1,x_2) + \varepsilon_3(x_3) + \varepsilon_{13}(x_1,x_3) + \varepsilon_{23}(x_2,x_3) + \varepsilon_{123}(x_1,x_2,x_3) \tag{2.A40}$$

where $\overline{F}_3(x_1,x_2) = \overline{F}_{123} + \varepsilon_1(x_1) + \varepsilon_2(x_2) + \varepsilon_{12}(x_1,x_2)$ is the average of the F field in the x_3 direction.

We evaluate the variances and covariance of F_{eff_1} and F_{eff_2} under the simplifying approximation that the contributions from the last 3 terms in Eq. 2.A40 are negligible. Under this condition, we estimate the variance and covariance contribution from $\overline{F}_3(x_1,x_2)$ by using the 2D results in Eq. 2.A25 (applied to $\overline{F}_3(x_1,x_2)$ rather than $F(x_1,x_2)$). The term $\varepsilon_3(x_3)$ makes an identical random contribution to the log-effective moduli. This common effect can be found by following the procedure in Eqs. 2.A10-2.A13. The final result is as follows:

The log-effective moduli F_{eff_j} have the same variance, given by

$$\sigma_{\varepsilon_1}^2 = (\overline{\rho}_{23} - \overline{\rho}_{123})\sigma_F^2$$
$$\overline{\rho}_{e^{\varepsilon_1}} = \frac{2}{L_1}\int_0^{L_1}\left(1-\frac{r}{L_1}\right)\frac{e^{[\overline{\rho}_{23}(r)-\overline{\rho}_{123}]\sigma_F^2}-1}{e^{(\overline{\rho}_{23}-\overline{\rho}_{123})}-1}dr \tag{2.A41}$$

(similarly for ε_2 and ε_3). The covariance between F_{eff_1} and F_{eff_2} is

$$Cov[F_{eff_1}, F_{eff_2}] = \overline{\rho}_{123}\sigma_F^2 + \ln[1+\overline{\rho}_{e^{\varepsilon_3}}(e^{\sigma_{\varepsilon_3}^2}-1)] - \sum_{i=1}^{2}\ln\left(E_{R_i}\left[e^{-\rho_{\varepsilon_i}(R_i)\sigma_{\varepsilon_i}^2}\right]\right) \tag{2.A42}$$

where $\rho_{\varepsilon_1}(r) = \frac{\overline{\rho}_{23}(r) - \overline{\rho}_{123}}{\overline{\rho}_{23} - \overline{\rho}_{123}}$. The correlation coefficient is found as the ratio $\frac{Cov[F_{eff_1}, F_{eff_2}]}{\sigma^2_{F_{eff}}}$.

$R_{\Gamma_{eff,12}, \Gamma_{eff,13}}$

$\overline{F}_{123}$ and $\varepsilon_1(x_1)$ have identical effects on $\Gamma_{eff,12}$ and $\Gamma_{eff,13}$. Also, under the simplifying assumptions stated above, no other ANOVA term makes positive contributions to the variances of both $\Gamma_{eff,12}$ and $\Gamma_{eff,13}$. It follows that

$$Cov[\Gamma_{eff,12}, \Gamma_{eff,13}] = \overline{\rho}_{123}\sigma_F^2 + \ln[1 + \bar{\rho}_{e^{\varepsilon_1}}(e^{\sigma^2_{\varepsilon_1}} - 1)] \tag{2.A43}$$

$R_{F_{eff_1}, \Gamma_{eff,12}}$

This is similar to the covariance between Γ_{eff} and $F_{eff,1}$ in 2D. Adaptation of Eq. 2.11 to the 3D case gives

$$\begin{aligned} &Cov[F_{eff,1}, \Gamma_{eff_{12}}] \\ &\quad = \overline{\rho}_{123}\sigma_F^2 + \ln[1 + \bar{\rho}_{e^{\varepsilon_1}}(e^{\sigma^2_{\varepsilon_1}} - 1)] - \ln(E_{R_2}[e^{-\rho_{\varepsilon_2}(R_2)\sigma^2_{\varepsilon_2}}]) \end{aligned} \tag{2.A44}$$

$R_{F_{eff_3}, \Gamma_{eff,12}}$

The effect of $\overline{F}_{123}$ is the same on both log-moduli. The first-order fluctuations $\varepsilon_1(x_1)$ and $\varepsilon_2(x_2)$ contribute to $\Gamma_{eff,12}$ through the harmonic averages of the exponentiated processes $e^{\varepsilon_1(x_1)}$ and $e^{\varepsilon_2(x_2)}$, whereas the contributions to $F_{eff,3}$ are the arithmetic averages of the same processes. All other ANOVA terms have been assumed to have no effect on the variance of $\Gamma_{eff,12}$. It follows that

$$Cov[F_{eff,3}, \Gamma_{eff,12}] = \bar{\rho}_{123}\sigma_F^2 + -\sum_{i=1}^{2} \ln\left(E_{R_i}\left[e^{-\rho_{\varepsilon_i}(R_i)\sigma_{\varepsilon_i}^2}\right]\right) \quad (2.A45)$$

Part B: Distribution of Certain Random Distances

The main task in calculating the mean value and log-variance of E_{eff} and G_{eff} in Eqs. 2.5,2.6 and 2.8-2.11 is the calculation of $\bar{\rho}$ terms, defined as the expected value of $\rho(R_J)$ or $\rho[R_J(r)]$, where $\rho(d)$ is some correlation function, R_J is the random distance between two points uniformly and independently distributed in Ω_J, and $R_J(r)$ is the random distance between a point uniformly distributed in Ω_J and a point with uniform distribution in $\Omega_{J,r}$, a region obtained by translating Ω_J by r in the x_1 direction. In the latter case, the index list J does not include 1. Ω_J is a straight line segment in one dimension, a rectangle in two dimensions, and a box in three dimensions. The distributions of R_J and $R_J(r)$ are given below.

B.1 Distribution of R_J

For a segment of length L_j the probability density function of R_J is

$$f_{R_J}(s) = \frac{2}{L_j}\left(1 - \frac{s}{L_j}\right) \quad (2.B1)$$

and for a rectangle with side lengths L_1 and L_2 the probability density $f_{R_{12}}(s)$ is (see for example [79]),

$$f_{R_{12}}(s) = \frac{1}{(L_1L_2)^{1/2}} g\left[\frac{s}{(L_1L_2)^{1/2}}, (L_1/L_2)\right] \quad (2.B2)$$

where $g(w,a) = 2w[g_1(w,a) + g_2(w,a) + g_2(w/a, 1/a)]$ and

$$g_1(w,a) = \begin{cases} \pi + w^2 - 2w(a + 1/a), & 0 < w < \sqrt{a^2 + 1/a^2} \\ 0, & otherwise \end{cases}$$

$$g_2(w,a) = \begin{cases} 2(w^2 - 1)^{1/2} - 2ar\cos\left(\frac{1}{w}\right) - a^{-2}(w-1)^2 & 0 < w < \sqrt{1 + a^4} \\ 0, & otherwise \end{cases}$$

Alternatively, using $R_{12}^2 = R_1^2 + R_2^2$, one may calculate $f_{R_{12}}$ numerically as

$$f_{R_{12}}(r) = r\int_0^{\pi/2} f_{R_1}[r\cos(\theta)] f_{R_2}[r\sin(\theta)]\, d\theta, \quad 0 \le r \le \sqrt{L_1^2 + L_2^2} \qquad \text{(B3)}$$

For a square ($a = L_1/L_2 = 1$), accurate estimates of $\bar{\rho}_{12}$ result from replacing the square by a disc having the same area. The probability density of the distance R_{12} inside a disc of radius r is (Tu and Fischbach, 2002)

$$f_{R_{12}}(s) = \frac{2s}{r^2} - \frac{s^2}{\pi r^4}\sqrt{4r^2 - s^2} - \frac{4s}{\pi r^2}\sin^{-1}\left(\frac{s}{2r}\right), \quad 0 \le s \le 2r \qquad \text{(B4)}$$

The distribution of R_{123} for a three-dimensional box has a far more complicated analytical form; see for example Philip (1991). However, in analogy with a two-dimensional rectangle one may use the relationship $R_{123}^2 = R_{12}^2 + R_3^2$ and find $f_{R_{123}}$ numerically as

$$f_{R_{123}}(r) = r\int_0^{\pi/2} f_{R_{12}}[r\cos(\theta)] f_{R_3}[r\sin(\theta)]\, d\theta, \quad 0 \le r \le \sqrt{L_1^2 + L_2^2 + L_3^2} \qquad \text{(B5)}$$

In the special case of a cube, a good approximation to $\bar{\rho}_{123}$ comes from considering the distance R_{123} within a ball of the same volume. The probability density function of R_{123} for a ball of radius r is (e.g. Tu and Fischbach, 2002)

$$f_{R_{123}}(s) = \frac{3s^2}{r^3} - \frac{9}{4}\frac{s^3}{r^4} + \frac{3}{16}\frac{s^5}{r^6}, \quad 0 \le s \le 2r \qquad \text{(B6)}$$

B.2 Distribution of $R_J(r)$

The distribution of $R_J(r)$ can be found from the relationship

$$R_J(r) = \sqrt{R_J^2 + r^2} \tag{2.B7}$$

It follows that the probability density function of $R_J(r)$ is obtained from the probability density function of R_J as

$$f_{R_J(r)}(s) = \frac{s}{\sqrt{s^2 - r^2}} f_{R_J}\left(\sqrt{s^2 - r^2}\right), \quad r \leq s \leq \sqrt{R_{J,max}^2 + r^2} \tag{2.B8}$$

where $R_{J,max}$ is the maximum possible value of R_J.

Chapter 3: Probability Distribution of Fracture Elongation, Strength, and Toughness of Notched Rectangular Blocks with Lognormal Young's Modulus

The research and review presented in this chapter has been published in:

- L. S. Dimas, D. Veneziano, T.Giesa, M.J. Buehler, *Probability Distribution of Fracture Elongation, Strength, and Toughness of Notched Rectangular Blocks with Lognormal Young's Modulus*, JMPS, 2015.

We find analytical approximations to the probability distribution of fracture properties of one-dimensional rods and thin two-dimensional plates when Young's modulus varies spatially as an isotropic lognormal field. The properties considered are the elongation, strength, and toughness modulus at fracture initiation and at ultimate failure. This is an extension of the previous chapter that, under the same conditions, dealt with the distribution of the bulk elastic moduli. For all quantities at fracture initiation our approach is analytical in 1D and semi-analytical in 2D. For ultimate failure, we quantify the random effects of fracture propagation and crack arrest by fitting regression models to simulation data and combine the regressions with the distributions at fracture initiation. The results are validated through a series of Monte Carlo simulations. Through parametric analysis, we gain insight into the strengthening/weakening roles of the Euclidean dimension and size of the specimen and the variance and correlation function of the log-modulus field.

3.1. Introduction

Experimental investigations indicate that the elastic properties of many natural and man-made materials exhibit large random-looking local fluctuations [4, 24, 25]. A

fundamental question is how these small-scale fluctuations affect the bulk strength of the material. Some studies suggest that the fluctuations enhance fracture performance in natural materials such as bone and nacre [22-29]. In layered materials it is well known that the crack driving stresses decrease when fracture propagates in the direction of increasing stiffness [14, 15, 80, 81]. Under certain conditions, the stress concentration at the crack tip completely vanishes and the uncracked part of the specimen behaves like pristine composite [9]. Qualitatively similar results have been obtained for materials with periodically but smoothly varying elastic properties [7, 82-84]. Other studies have focused on materials with random local variation of the elastic modulus, using mainly numerical tools. These include finite element formulations suited for probabilistic analysis [85-87], first and second order reliability methods commonly referred to as FORM/SORM [67, 68], and Monte Carlo simulation [65, 66]. Numerical methods are general, but they are often computationally inefficient and not well suited to systematically investigate the dependence of the bulk mechanical properties on the subscale heterogeneities, conduct parametric analyses, or optimize new materials. For the latter purposes one needs analytical or semi-analytical tools.

In Chapter 2 we reported analytical approximations for the joint distribution of the effective elastic moduli in tension and shear. That study considered n-dimensional rectangular blocks (n = 1, 2 or 3) whose Young's modulus $E(x)$ varies spatially as an isotropic lognormal field. A key step of the approach was to make an analysis-of-variance (ANOVA) decomposition of the log-modulus field by expressing $F(x) = \ln E(x)$ as the sum of the average inside the block, marginal fluctuations along the coordinate axes ("main effects"), and interactions of order 2, ..., n. Following this decomposition, the joint distribution of the bulk modulus was obtained by multiplicatively combining the effects of the individual ANOVA terms. An interesting specific finding, which is used in the present study, is that accurate results on the bulk moduli are obtained by treating the effects of the interaction terms of order 2 or higher as deterministic ("ergodicity assumption").

Here we derive the probability distribution of fracture properties of notched thin rods ($n = 1$) and thin rectangular plates ($n = 2$); see **Figure 3.1a**. Like in Chapter 2, we consider Poisson's ratio ν to be deterministic constant and the elastic modulus $E(x)$ to vary spatially as an isotropic lognormal field with mean value 1. Hence the log-modulus $F(x) = \ln E(x)$ is isotropic Gaussian with some variance σ_F^2, mean value $-0.5\sigma_F^2$, and some correlation function $\rho_F(r)$. Under these conditions the probabilistic model is completely specified by σ_F and $\rho_F(r)$.

We study the fracture properties of the blocks in tension when one face normal to the x_1 direction is displaced by an increasing amount U_1 relative to the opposite face. We fix to zero the tractions on the remaining boundary and allow Poisson contraction. We assume that a small process zone develops around the crack tip while the remaining specimen remains linear elastic. The crack propagates when a longitudinal strain at the edge of the process zone exceeds a critical value. In a homogeneous material, this is equivalent to fracture propagating when the strain intensity factor exceeds some threshold value. In a discrete lattice model, this failure criterion corresponds to using a critical failure strain that scales with the inverse square root of the discretization length.

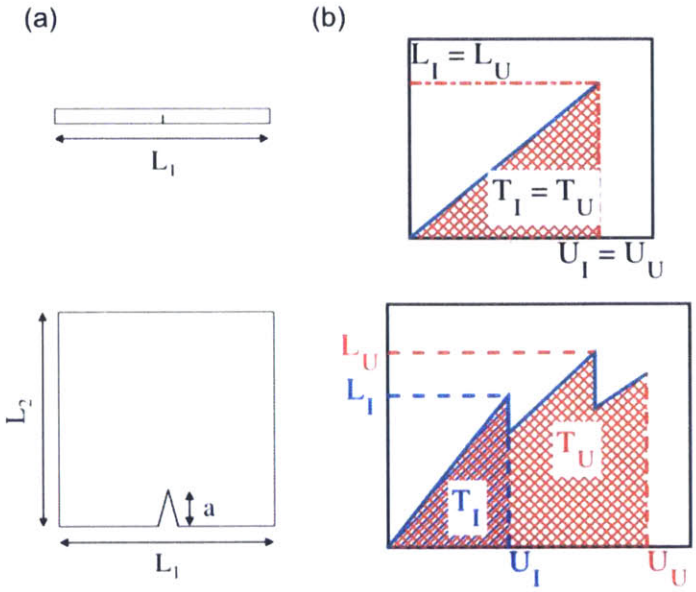

Figure 3.1: (a) Specimen geometry and **(b)** measures of fracture strength for 1D rods and 2D plates. In the 1D rods the modulus varies only in the $\boldsymbol{x_1}$-direction and in 2D plates there are modulus variations both along the $\boldsymbol{x_1}$-direction and $\boldsymbol{x_2}$-direction.

In this setting, we are after the probability distribution of six random variables: the elongation U_I, load L_I, and toughness modulus T_I when fracture initiates at the notch tip (subscript I) and the corresponding quantities U_U, L_U, and T_U which are the largest values of U, L, and T experienced by the specimen until fracture percolation occurs (ultimate failure, subscript U). We collectively refer to $\{U_I, L_I, T_I\}$ as the initial fracture strengths and to $\{U_U, L_U, T_U\}$ as the ultimate fracture strengths. These 6 quantities are schematically illustrated in **Figure 3.1b**. As shown in that figure, the toughness modulus is defined as the work done by the external forces per unit specimen length in 1D or unit specimen area in 2D [88]. A more commonly used measure of fracture toughness is the energy release rate at fracture initiation, $\mathcal{G}_c$. Here we use T_I because it has a very simple interpretation, is trivial to evaluate, and has a high correlation with $\mathcal{G}_c$. For example, **Figure 3.2** shows a scatterplot of 1000 $(T_I, \mathcal{G}_c)$ values from Monte Carlo simulation. In this case we considered a $2L \times L$ rectangular specimen with notch depth $a = L/2$ and normal log-modulus field $F(x)$ with correlation function $\rho_F(r) = e^{-2r/L}$ and standard deviation $\sigma_F = 0.3$. Values of $\mathcal{G}_c$ were obtained by numerically calculating the J-integral in a region around the notch tip. We use modified expressions for the J-integral that are path-independent also for systems with a modulus field that varies in x_1 and x_2 [89-91].

The strong linear dependence with correlation coefficient 0.92 indicates that T_I is a suitable substitute for $\mathcal{G}_c$.

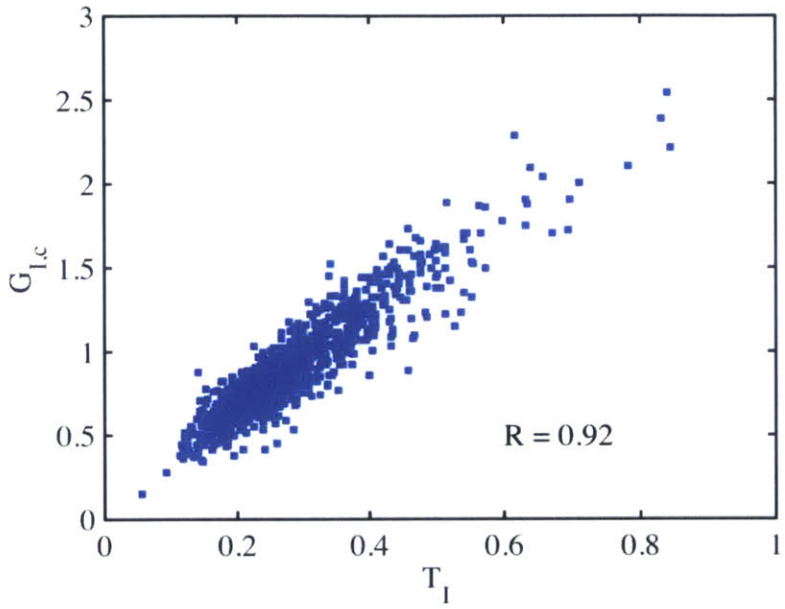

Figure 3.2: Scatterplot and correlation coefficient between strain energy release rate at fracture initiation $\boldsymbol{\mathcal{G}_{I,c}}$ and initial toughness modulus $\boldsymbol{T_I}$. One thousand Monte Carlo simulations of a $\boldsymbol{2L \times L}$ specimen in which the log-modulus field $\boldsymbol{F(x)}$ is normal with double exponential correlation function, standard deviation $\boldsymbol{\sigma_F = 0.3}$, and correlation length $\boldsymbol{r_0 = 0.5L}$.

The ultimate toughness T_U is similarly defined, as the work done by the external forces per unit specimen length or area when fracture percolates through the material. Note that a one-dimensional rod fails upon fracture initiation; hence in the 1D case $T_I = T_U$. The same is true for 2D plates with spatially uniform Young's modulus ($\sigma_F^2 = 0$ and $E(x) \equiv m_E = 1$). The fracture strengths under $E(x) \equiv 1$ are referred to here as the "uniform strengths" and are denoted by U_0, L_0, and T_0.

It is attractive to state results in terms of dimensionless quantities obtained by dividing the initial and ultimate strengths by the corresponding uniform strengths. Thus, using lower case letters for the dimensionless variables, we seek the distributions of $u_I = U_I/U_0$, $l_I = L_I/L_0$, … and $t_U = T_U/T_0$. These quantities are independent of the mean

value of the elastic modulus (which without loss of generality we have set to 1) and the strain intensity factor at which failure initiates and propagates.

The distributions of u_I, l_I and t_I are obtained in Section 3.2 and those of u_U, l_U, and t_U are derived in Section 3.3. Section 3.4 validates the analytical results through Monte Carlo simulation and Section 3.5 uses the analytical expressions to parametrically investigate how the distributions of the initial and ultimate fracture strengths depend on the geometry of the specimen and the characteristics of the random modulus fluctuations. Section 3.6 summarizes the main findings and points at future research directions.

3.2. Initial Fracture Strengths

A key problem to obtain the distributions of l_I and t_I is to find the joint distribution of the elongation at fracture initiation u_I and the effective Young's modulus in the direction of stretching E_{eff}. This is sufficient because l_I and t_I are related to E_{eff} and u_I as $l_I = \frac{E_{eff}}{m_E} u_I$ and $t_I = \frac{E_{eff}}{m_E} u_I^2$ or, since $m_E = 1$,

$$\begin{aligned} \ln l_I &= \ln E_{eff} + \ln u_I, \\ \ln t_I &= \ln E_{eff} + 2 \ln u_I. \end{aligned} \tag{3.1}$$

In our approximate analytical treatment, we assume that this joint distribution is lognormal (simulation results support this approximation, although we know that the exact distribution is not strictly lognormal). Hence we need to find the mean values, variances and covariance of $\ln E_{eff}$ and $\ln u_I$. The first two moments of $\ln E_{eff}$ for un-notched specimens were derived in Chapter 2. Here we use those results, having verified that a small notch affects minimally the bulk stiffness. We choose a notch depth of $a = L/5$. Results of numerical simulation not presented here indicate that the first and second moment properties of the normalized fracture initiation elongation $\ln u_I$ are insensitive to notch depth. The first and second moment properties of the fracture initiation load and toughness are influenced by the notch depth only through the effective stiffness.

For $n = 1$ (modulus variations are only present along the x_1-direction), we analytically derive the first two moments of $\ln u_l$ using the ANOVA decomposition of the log-modulus field $F(x) = \ln E(x)$; see Chapter 2 for such decomposition. For $n = 2$ (modulus variations are present both along the x_1-and x_2-direction), we again use the ANOVA approach for the covariance between $\ln u_l$ and $\ln E_{eff}$, but for the mean value and variance of $\ln u_l$ we use a different method. The reason is that, contrary to the log-effective modulus $\ln E_{eff}$ analyzed in Chapter 2, the second order term ε_{12} in the two-dimensional ANOVA decomposition of $F(x)$ contributes non-negligibly to the variance of $\ln u_l$. Since it is difficult to obtain that contribution analytically, we find the moments of $\ln u_l$ using the following semi-analytical sensitivity strategy.

The log elongation $\ln u_l$ is some functional $g(F(x))$ of the log-modulus field. We discretize space and use Taylor series expansion around the specimen average value $\overline{F}$ to approximate $\ln u_l$ as a linear function of the log-moduli $F_i = F(\boldsymbol{x}_i)$ at the grid points $\boldsymbol{x}_i$. This gives

$$\ln u_l = g(F(x)) \approx \sum_i b_i\left(F_i - \overline{F}\right) \tag{3.2}$$

where the sensitivity coefficients b_i are obtained by numerically calculating the change in $\ln u_l$ due to a perturbation of F_i. This is done using a finite-element model (see Section 3.4 and the Supporting Information for details). Since at large distances from the notch tip the b_i coefficients are negligible, it is sufficient to consider a limited region around the notch. The reason why the deviations of the local log-moduli F_i are from the specimen average value $\overline{F}$ not the theoretical mean μ_F is that when all the F_i equal $\overline{F}$ (this corresponds to a spatially uniform modulus), the elongation at fracture initiation equals the uniform value U_0 and the log-dimensionless displacement $\ln u_l$ is zero.

Expressions for the moments of the initial fracture strengths are given below. Detailed derivations are provided in the Supporting Information.

3.2.1 1D (one-dimensional bar of length L_1)

The normalized displacement at fracture initiation u_I equals $\varepsilon_0/\varepsilon$ where, for any given elongation U_1, ε_0 and ε are the longitudinal strains at the location of the notch under uniform and random elastic modulus, respectively. In both cases, the strain at any point along the rod is given by the (constant) longitudinal stress divided by the tensile modulus E at that location. In turn, for any given U_1 the longitudinal stress is proportional to the harmonic average of $E(x)$. These considerations give

$$\begin{aligned}
\varepsilon_0 &= \frac{U_1}{L_1}, \\
\varepsilon &= \frac{\sigma}{E(0)} = \frac{U_1}{\int \frac{E(0)}{E(x)}\,dx} = \frac{\varepsilon_0}{\langle \frac{E(0)}{E(x)} \rangle}, \\
u_I &= \frac{\varepsilon_0}{\varepsilon} = \langle \frac{E(0)}{E(x)} \rangle = \langle e^{F(0)-F(x)} \rangle.
\end{aligned} \tag{3.3}$$

where $x = 0$ is the location of the notch and $\langle h(x) \rangle = \frac{1}{L_1}\int_{-L_1/2}^{L_1/2} h(x)\,dx$ is the spatial average of a quantity h that varies along the rod.

Using Eq. 3.3, the first two moments of u_I are found as the first two moments of the spatial average $\langle e^{F(0)-F(x)} \rangle$. The results are (see Supporting Information)

$$\begin{aligned}
m_{u_I} &= \frac{2}{L_1}\int_0^{\frac{L_1}{2}} e^{[1-\rho_F(r)]\sigma_F^2}\,dr, \\
\sigma_{u_I}^2 &= \int_{-\frac{L_1}{2}}^{\frac{L_1}{2}}\int_{-\frac{L_1}{2}}^{\frac{L_1}{2}} e^{[1-\rho_F(r_1)]\sigma_F^2+[1-\rho_F(r_2)]\sigma_F^2} \\
&\qquad \cdot \left\{ e^{[1-\rho_F(r_1)-\rho_F(r_2)+\rho_F(r_1-r_2)]\sigma_F^2} - 1 \right\} dr_1 dr_2, \\
m_{\ln u_I} &= \ln(m_{u_I}) - \frac{1}{2}\sigma_{\ln u_I}^2,
\end{aligned} \tag{3.4}$$

$$\sigma^2_{\ln u_I} = -2\ln(m_{u_I}) + \ln(\sigma^2_{u_I} + m^2_{u_I}).$$

where the expressions for the log moments follow from the simplifying assumption that u_I has lognormal distribution. The Supporting Information uses the expression of $\ln u_I$ in Eq. 3.3 and results on $\ln E_{eff}$ in Chapter 2 to further show that

$$cov[\ln E_{eff}, \ln u_I] = \frac{1}{2}\left(\sigma^2_F - \sigma^2_{\ln E_{eff}} - \sigma^2_{\ln u_I}\right). \tag{3.5}$$

Finally, from Eq. 3.1 and the moments derived above, we obtain the first two moments of $\ln l_I$ and $\ln t_I$, as

$$\begin{aligned} m_{\ln l_I} &= m_{\ln E_{eff}} + m_{\ln u_I}, \\ \sigma^2_{\ln l_I} &= \sigma^2_{\ln E_{eff}} + \sigma^2_{\ln u_I} + 2 \cdot cov[\ln E_{eff}, \ln u_I], \end{aligned} \tag{3.6}$$

and

$$\begin{aligned} m_{\ln t_I} &= m_{\ln E_{eff}} + 2 \cdot m_{\ln u_I}, \\ \sigma^2_{\ln t_I} &= \sigma^2_{\ln E_{eff}} + 4 \cdot \sigma^2_{\ln u_I} + 4 \cdot cov[\ln E_{eff}, \ln u_I]. \end{aligned} \tag{3.7}$$

3.2.2 2D (two-dimensional rectangle with dimension $L_1 \times L_2$)

Equation 3.2 gives

$$\begin{aligned} m_{\ln u_I} &= 0 \\ \sigma^2_{\ln u_I} &= \sum_i \sum_j b_i b_j cov[(F_i - \bar{F})(F_j - \bar{F})] \approx \sum_i \sum_j b_i b_j \rho_F(\boldsymbol{x}_i, \boldsymbol{x}_j)(1 - \overline{\rho}_{12})\sigma^2_F \end{aligned} \tag{3.8}$$

where $\overline{\rho}_{12}$ is the average correlation of F for two points independently and uniformly distributed inside the specimen. A simplifying assumption made for the variance in Eq.

3.8 is that the non-homogeneous random field $F_i - \bar{F}$ has the same second-moment properties as the isotropic field $F_i - m_F$, except for the reduced variance $(1 - \bar{\rho}_{12})\sigma_F^2$. In Section 3.4 we evaluate the accuracy of this and other approximations.

To find an expression for the covariance between $\ln E_{eff}$ and $\ln u_l$, we consider the ANOVA decomposition of $F(x)$, which has the form $F(x_1, x_2) = \bar{F}_{12} + \varepsilon_1(x_1) + \varepsilon_2(x_2) + \varepsilon_{12}(x_1, x_2)$. The main effect ε_2 has no influence on $\ln u_l$ and the second order term ε_{12} contributes negligibly to the variance of $\ln E_{eff}$. It follows that the covariance we are seeking is the same as the covariance between $\ln E_{eff}$ and $\ln u_l$ for a 1D rod with log modulus $F'(x_1) = \bar{F}_{12} + \varepsilon_1(x_1)$. Making these changes in Eq. 3.5 gives

$$cov[F_{eff}, \ln u_l] = \frac{1}{2}\left(\sigma_F^2 - \sigma_{\ln E_{eff}}^2 - \sigma_{\ln u_{l_{F'}}}^2\right). \tag{3.9}$$

where $\sigma_{\ln u_{l_{F'}}}^2$ is the variance $\sigma_{\ln u_l}^2$ in Eq. 3.4 under the stiffness field F'.

The first two moments of $\ln l_l$ and $\ln t_l$ are given by Eqs. 3.6 and 3.7, like in the 1D case.

3.3. Ultimate Fracture Strengths

The normalized ultimate fracture strengths u_U, l_U, and t_U are bounded from below by the corresponding fracture initiation strengths. Here we seek a simple model that respects this constraint and accurately describes data generated via Monte Carlo simulation, using the discrete mechanical model described below in Section 3.4.1. Examples of simulation data are shown in **Figure 3.3a** as scatter plots of $\ln X_U$ vs $\ln X_l$ for $X = u$, l and t. All these simulation results are for a square specimen with side length L and log-modulus $F(x)$ with standard deviation $\sigma_F = 0.3$ and spatial correlation function $\rho_F(r) = e^{-8r/L}$. Hence the correlation length equals $L/8$. Ignoring for the moment the left censoring at X_l, for all three strength measures the mean value of $\ln X_U$ in an approximately linear function of $\ln X_l$. Other common features are that the distribution of $\ln X_U$ is positively skewed and

the scatter is approximately independent of X_I. Finally, one observes that in cases when the skewness is moderate the distribution of $(\ln X_U \mid \ln X_I)$ is close to normal.

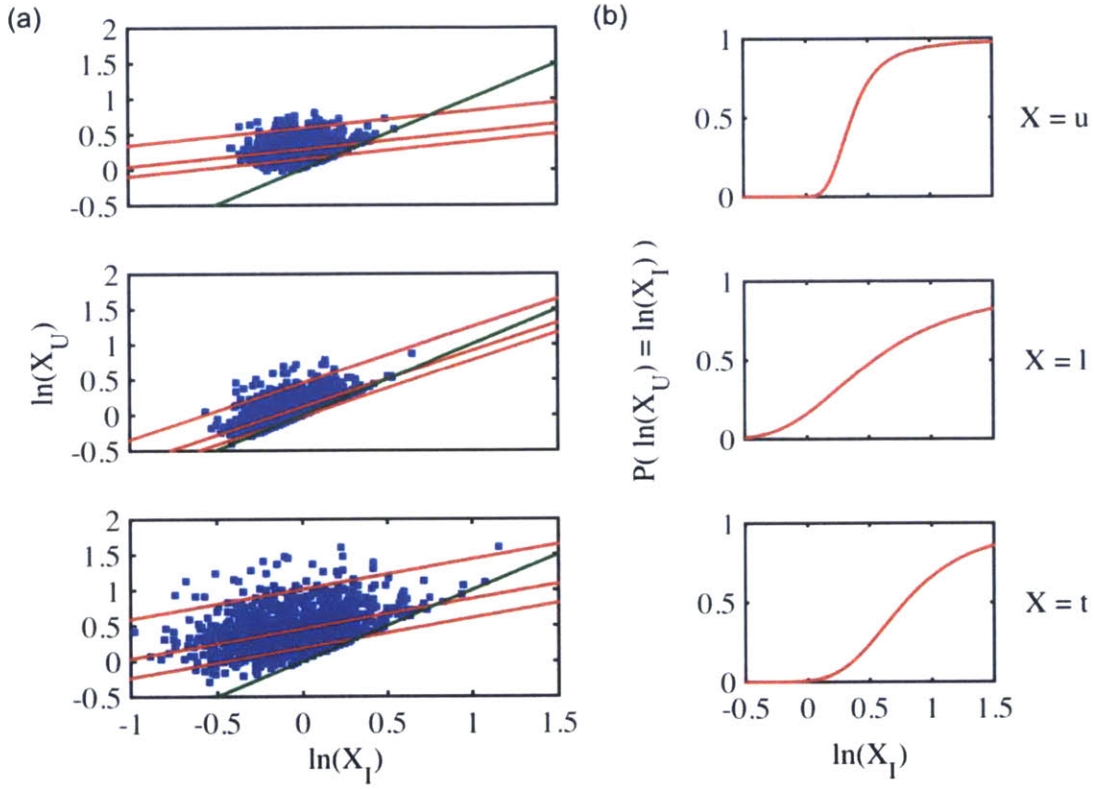

Figure 3.3: (a) Log-log scatterplots of ultimate strength $\boldsymbol{X_U}$ versus initial strength $\boldsymbol{X_I}$ for $\boldsymbol{X = u, l}$, and $\boldsymbol{t}$, 1000 Monte Carlo simulations of a square specimen with unit side length. The log-modulus $\boldsymbol{F(x)}$ is normal with simple exponential correlation function $\boldsymbol{\rho_F(r)}$, standard deviation $\boldsymbol{\sigma_F = 0.3}$ and correlation length $\boldsymbol{r_0 = 0.125}$. The red lines indicate fitted 10^{th} , 50^{th} , and 90^{th} percentiles prior to censoring. **(b)** Probability $\boldsymbol{P(\ln X_U = \ln X_I)}$ as a function of $\boldsymbol{\ln X_I}$ based on the fitted models.

To capture these features and include the normal distribution as a special case, we fit linear regression models with □-stable distribution $\mathcal{S}(\alpha, \beta, \sigma, \mu)$ of the response variable $\ln X_U$. □-stable distributions (see for example [92]) have four parameters: the so-called stability index $0 < \alpha \leq 2$ with value 2 in the normal case, the skewness parameter $-1 \leq \beta \leq 1$, the scale parameter $\sigma \geq 0$, and the location parameter $-\infty < \mu < \infty$. All parameters are assumed independent of X_I, except for μ which varies like $\mu = c_o + c_1 \ln X_I$. Hence, considering left-censoring at $\ln X_I$, the final model for $\ln X_U$ is

$$\ln X_U \sim \max\{\ln X_I, \mathcal{S}(\alpha, \beta, \sigma, c_o + c_1 \ln X_I)\}, \tag{3.10}$$

In a more complex model, one could allow the parameters of the □-stable distribution to vary with X_I. However, this would significantly increase the complexity of the model and as we show in Section 3.4.2, the model in Eq. 3.10 already produces highly accurate results.

Given a simulation set of (X_{I_i}, X_{U_i}) pairs, the regression parameters α, β, σ, c_o, and c_1 in Eq. 3.10 are found by maximizing the likelihood

$$l(\alpha, \beta, \sigma, c_o, c_1) \propto \prod_{X_{Ii}=X_{Ui}} F_{\alpha,\beta,\sigma,c_o+c_1 \ln X_{I_i}}(\ln X_{I_i}) \prod_{X_{Ii}<X_{Ui}} f_{\alpha,\beta,\sigma,c_o+c_1 \ln X_{I_i}}(\ln X_{I_i}), \quad (3.11)$$

where F and f are the □-stable cumulative distribution and density function, respectively, with parameters as given.

Once the censored regression model in Eq. 3.10 is estimated, the probability density function of $\ln X_U$ is given by

$$f_{\ln X_U}(x) = \int_{-\infty}^{x} f_{\max\{u, S(\alpha,\beta,\sigma,c_o+c_1 u)\}}(x) f_{\ln X_I}(u) du, \quad (3.12)$$

where $f_{\ln X_I}$ is a normal density and $f_{\max\{u, S(\alpha,\beta,\sigma,c_o+c_1 u)\}}(x)$ is a left-censored □-stable density, with a probability mass at u due to censoring.

As an example, the red lines in **Figure 3.3a** give the 10th, 50th, and 90th percentiles of the fitted distribution of $\ln X_U$ prior to censoring. These fitted percentiles correspond well to the scatter of the simulation values. For each strength measure $X = \{u, l, t\}$, **Figure 3.3b** uses the fitted □-stable regression models to show the probability that $X_U = X_I$ (no increase in strength from fracture initiation to ultimate failure) as a function of the strength at fracture initiation. Consistently with the scatter plots in **Figure 3.3a** and intuition, this probability increases as the strength at fracture initiation increases (because

a high fracture initiation strength implies that the region near the notch tip is relatively stiff and, after that stiff region fails, the fracture is likely to propagate through the specimen in an unstable way). It is interesting and again intuitively expected that $P(X_U = X_I)$ is more sensitive to X_I for displacement at failure ($X = u$) than for load resistance ($X = l$). The reason is that the relative stiffness at the notch tip is more highly correlated with the displacement at failure than with the initial load resistance. The sensitivity for toughness ($X = t$) is intermediate, since toughness is roughly the product of u and l.

3.4. Numerical Models and Validation of the Analytic Results

We validate the theoretical results using Monte Carlo simulation. For each simulated modulus field, we solve the 1D problem directly: we compute the effective stiffness E_{eff} as the harmonic average of $E(x)$ along the rod, obtain the initial elongation u_I from Eq. 3.4, and find l_I and t_I from Eq. 3.1. In 2D, we use a finite element model to obtain the fracture initiation strengths and a spring network model to propagate the fracture and evaluate the ultimate strengths. Section 3.4.1 describes these numerical models and shows examples of fracture simulation results for the 2D case and Section 3.4.2 presents validation results.

3.4.1 Numerical Models

The finite element model for square 2D specimens consists of an 80x80 grid of linear four node elements and is developed in MATLAB. The spring network model is composed of 80x80 FCC lattice unit cells with axial elements forming bonds between nearest neighbors and is simulated with code developed in Python. Similar spring network models have been extensively used to solve mechanical problems [65, 93-95]; they have a simple parameterization and are especially well suited to study crack propagation due to their accurate tracking of the fracture path [96]. We prefer the FEM model for the initial fracture strengths, as it is computationally more efficient. In the FEM model the strain at the notch tip is computed from the elongation of the lower boundary

of the elements immediately ahead of the notch tip. In the spring network model the same strain is found as the maximum elongation of the bonds in the immediate vicinity of the notch tip. Simulations to verify consistency between the finite element and discrete lattice models exhibit very good agreement (see Part B of the Supporting Information).

We simulate Gaussian fields $F(x)$ with a Karhunen-Loève expansion (a singular value decomposition of the covariance kernel [78]), with 80 and 6400 modes for the 1D and 2D system, respectively. The numerical distributions reported below for the fracture initiation strengths are based on 10,000 Monte Carlo simulations. As simulating the entire crack path is computationally more demanding (40 minutes per simulation on a Dell Precision T5500 with an Intel Xeon 5600 series processor), numerical distributions for the ultimate fracture strengths are based on only 1,000 Monte Carlo simulations.

To illustrate the ultimate strength calculations, **Figure 3.4** shows fracture paths and associated load-elongation relationships for unit square specimens with three simulated log-modulus fields. The log-modulus realizations are from Gaussian fields $F(x)$ with correlation function $\rho_F(r) = e^{-8r}$ and standard deviation $\sigma_F = 0.3$, 0.3 and 0.7 for panels **a**, **b** and **c**, respectively. Numbers identify peaks of the force-elongation curves and corresponding locations of the crack tip. Specifically, "1" corresponds to the location of the initial notch tip and "2" indicates the last crack arrest event, following which fracture propagates in an unstable way through the rest of the specimen. System **a** fails in an unstable way upon fracture initiation, whereas both systems **b** and **c** experience crack arrest. The fracture path is nearly straight in cases **a** and **b**, whereas it is very erratic in case **c** due to the higher spatial variation of the modulus.

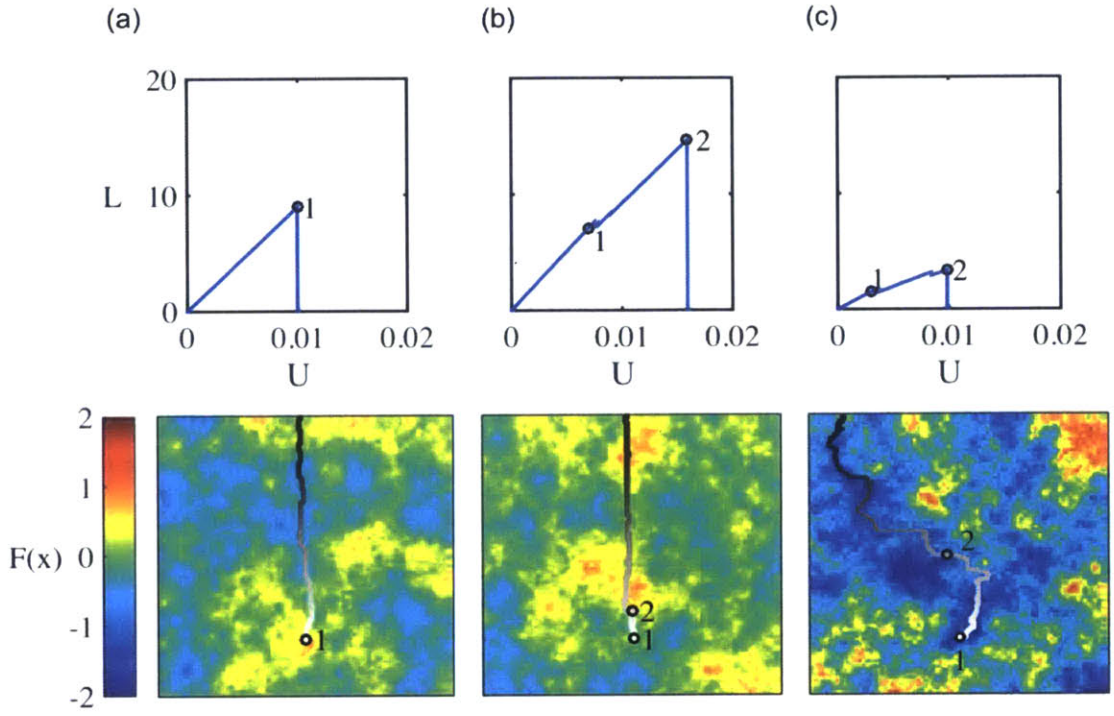

Figure 3.4: Example fracture paths and corresponding load elongation curves for notched square specimens with unit side length. The log-modulus $\boldsymbol{F(x)}$ is a normal field with simple exponential correlation function $\boldsymbol{\rho_F(r)}$, correlation length $\boldsymbol{r_0 = 0.125}$, and standard deviation **a** $\boldsymbol{\sigma_F = 0.3}$ **b** $\boldsymbol{\sigma_F = 0.3}$ **c** $\boldsymbol{\sigma_F = 0.7}$. The number '1' indicates the location of the initial crack tip and '2' indicates the last crack-arrest event. Specimen **a** fails upon initial crack propagation while both **b** and **c** exhibit crack arrest.

In case **a** the fracture initially moves towards areas with lower modulus, while in **b** it initially moves towards stiffer regions. Hence the force-displacement plots are consistent with what has been observed in layered materials when fracture propagates towards softer or stiffer layers [7, 15, 81, 82]. To verify this interpretation, we considered a bi-material specimen patterned to idealize case **b**. This is done by using for the two materials the modulus near the crack tip and the average modulus near the crack arrest location in **b**. As is shown in the Supporting Information, results for the two systems are similar, confirming that softening/stiffening environments ahead of the crack tip play a similar role in layered and the present disordered materials. However, as displayed in **Figure 3.4c**, a disordered modulus with high spatial gradients guides the fracture away from stiff regions and causes it to percolate along low-modulus valleys. This reduces the effectiveness of the crack arrest mechanism relative to layered or periodic heterogeneity.

3.4.2 Validation Runs

Next we make some comparisons between simulation and analytical results for 1D and 2D specimens. We consider rods of unit length and square plates with unit side length. In all cases, $\sigma_F = 0.3$ and $\rho_F(r) = e^{-8r}$.

Figures 3.5a and **3.5b** show the empirical (blue, from 10,000 simulations) and analytical distributions (red) of the initial log-strengths, respectively for 1D and 2D specimens. In the one-dimensional case the analytical results match the numerical results very well. In the 2D case there are small discrepancies: the sensitivity model in Eq. 3.2 underestimates the standard deviation of $\ln u_I$ by about 10% and gives $m_{\ln u_I} = 0$, whereas the mean value from simulation is slightly positive. That said, the analytical results are quite accurate and capture well the dominant features of the distributions.

Figure **3.5c** compares the empirical and model distributions of the ultimate log-strengths $\ln X_U$ in the 2D case. Again, the analytical distributions accurately fit the empirical results. In particular, the skewness and lower and upper tails of the distributions are very accurately described.

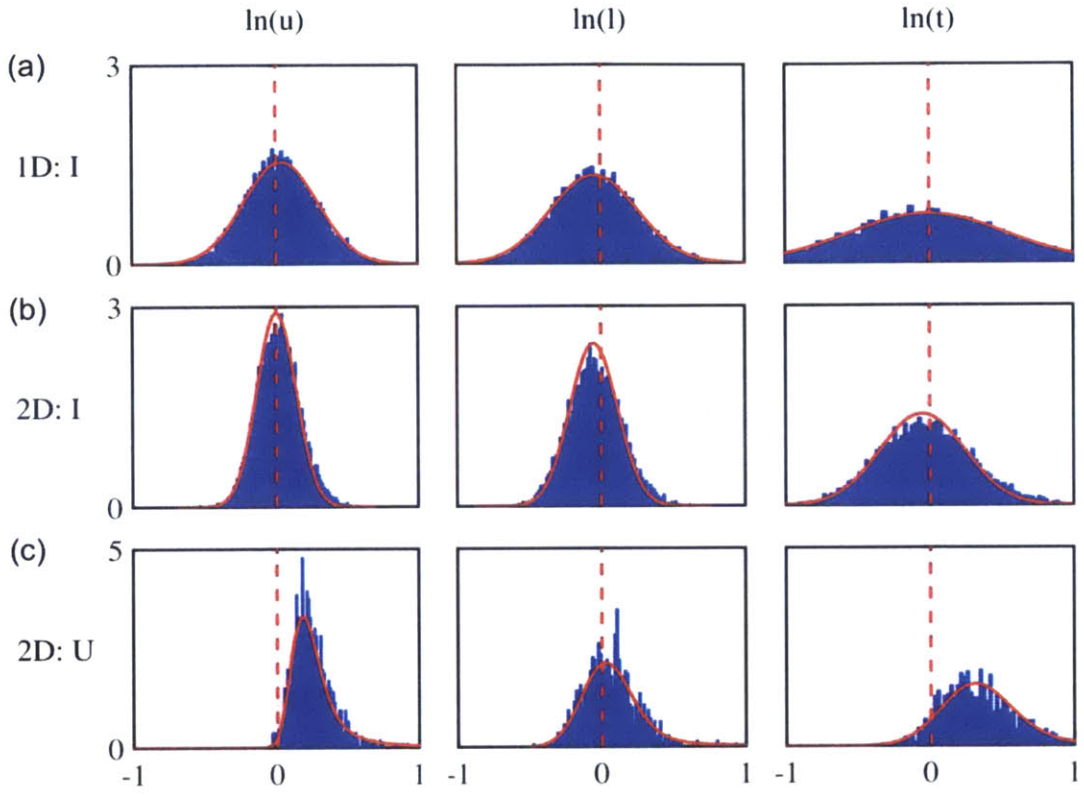

Figure 3.5: Comparison of analytical fracture strength distributions (red) with histograms from Monte Carlo simulations (blue). **a** initial strengths for a rod of unit length, and **b** initial strengths for a square plate with unit side length, and **c** ultimate strengths for a square plate of unit side length. Simulation of 10,000 samples in cases (**a**,**b**) and 1,000 samples in case **c**. In all cases the log-modulus field $\boldsymbol{F(x)}$ is normal with simple exponential correlation function $\boldsymbol{\rho_F(r)}$, standard deviation $\boldsymbol{\sigma_F = 0.3}$, and correlation length $\boldsymbol{r_0 = 0.125}$.

3.5. Parametric Analysis

As the final step, we use the analytical results to study how the distribution of the six fracture strength parameters in 1D and 2D systems depends on the Euclidean dimension and size of the specimen and the spatial fluctuations of the elastic log-modulus. To aid interpretation, we include also some results for the log-effective modulus $\ln E_{eff}$.

3.5.1 Initial Fracture Strengths

The mean value m and standard deviation σ of $\ln u_l$, $\ln E_{eff}$, $\ln l_l$ and $\ln t_l$ and the covariance between $\ln u_l$ and $\ln E_{eff}$ are shown in **Figure 3.6** for rods and **Figure 3.7** for square plates. The moments of $\ln E_{eff}$ are displayed as dashed lines. Results are shown for two correlation functions $\rho_F(r)$ (simple exponential in blue, double exponential in red) and cover a wide range of the normalized correlation length r_0/L, which varies in log scale on the horizontal axis. Since the mean values, variances and covariance are very nearly proportional to σ_F^2, the results are presented through the ratios m/σ_F^2, σ/σ_F, and $cov(\ln E_{eff}, \ln u_l)/\sigma_F^2$. Normalization facilitates the evaluation of sensitivity to the geometry of the specimen and the characteristics of the log-modulus field.

Rods

The first two moments of $\ln u_l$ and $\ln E_{eff}$ are plotted in the top row of **Figure 3.6**. It is instructive to first consider these properties under the limiting conditions of very low spatial correlation of the log-modulus ($\frac{r_0}{L} \ll 1$) and very high spatial correlation ($\frac{r_0}{L} \gg 1$):

1. In the low correlation limit the rod approaches ergodic conditions, in which the log effective modulus is deterministic and equals $-\sigma_F^2$. One can see these conditions nearly realized when $r_0/L = 0.1$. Concurrently, $m_{\ln u_l}$ and $\sigma_{\ln u_l}$ approach their maximum values, which are $m_{\ln u_l}/\sigma_F^2 = 0.5$ and $\sigma_{\ln u_l}/\sigma_F = 1$.
2. In the high correlation limit the rod has spatially uniform modulus and $\ln E_{eff}$ has the same distribution as F at any given location. Therefore $\ln E_{eff}$ has mean value $-0.5\sigma_F^2$ and variance σ_F^2. Under the same limiting conditions, $u_l \to 1$ and the mean and standard deviation of $\ln u_l$ vanish.

The next two rows of **Figure 3.6** show the normalized mean m/σ_F^2 and standard deviation σ/σ_F of the log initial strength $\ln l_l$ and toughness modulus $\ln t_l$. Since the strain field around the notch tip $x = 0$ is proportional to the applied stress divided by $E(0)$, the load when the critical strain intensity factor is reached must be proportional to $E(0)$. This is why, irrespective of the correlation model and correlation distance, the

distribution of $\ln l_I$ is identical to that of F. The toughness modulus t_I is proportional to the product of the load l_I and the elongation u_I; hence $m_{\ln t_I} = m_{\ln l_I} + m_{\ln u_I}$ and $\sigma^2_{\ln t_I} \approx \sigma^2_{\ln l_I} + \sigma^2_{\ln u_I}$, where the approximation holds exactly when $cov[\ln E_{eff}, \ln u_I] = 0$ (the covariance is indeed small; see the last panel of **Figure 3.6**).

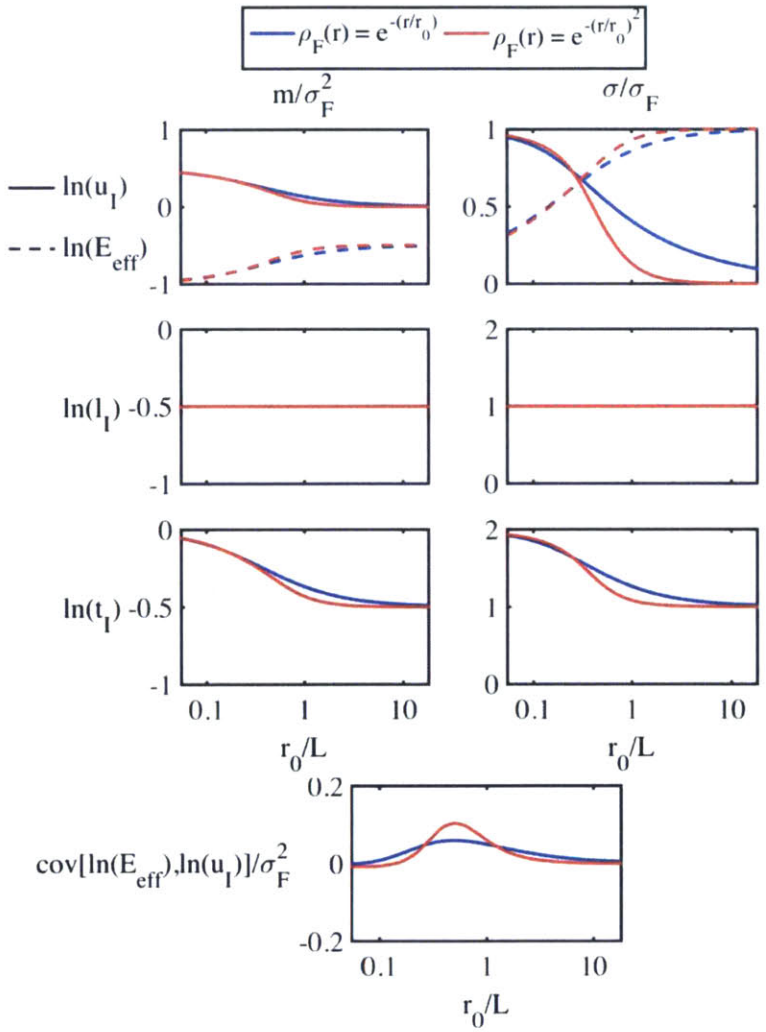

Figure 3.6: Parameters of the initial fracture strength distributions for 1D rods as a function of the normalized correlation length r_0/L. Blue and red curves show results for simple- and double-exponential correlation functions.

The asymptotic low-correlation results hold in good approximation for $\frac{r_0}{L} < 0.1$. Those for high correlation are approximately attained for $\frac{r_0}{L} > 1$ and $\frac{r_0}{L} > 10$, depending on the type of correlation function (lower convergence occurs for the simple exponential

model). Transition between the asymptotic conditions occurs more rapidly and around $\frac{r_0}{L} = 0.3$ for the double exponential correlation and more gradually and around $\frac{r_0}{L} = 0.5$ for the simple exponential correlation.

Plates

Using the same format, **Figure 3.7** shows results for square specimen with side length L. The sensitivity model in Eq. 3.2 gives $m_{\ln u_I} = 0$ for all correlation models and correlation distances (as discussed in Section 3.4.1, the true mean value is small but positive). The log displacement at fracture initiation, $\ln u_I$, depends on the contrast between the modulus in the immediate vicinity of the notch tip and the effective stiffness. Like in the 1D case, this contrast is highest in the ergodic limit $\frac{r_0}{L} \ll 1$, when the effective stiffness becomes deterministic. In the high correlation limit the modulus is uniform and $\ln u_I$ is deterministic. We conclude that the behavior of $\sigma_{\ln u_I}$ under limiting conditions is qualitatively the same as in the 1D case.

Finally we consider the log initial strength $\ln l_I$ and toughness modulus $\ln t_I$. Since $m_{\ln u_I}$ is estimated to be zero, we have $m_{\ln l_I} = m_{\ln t_I} = m_{\ln E_{eff}}$. Like in the 1D case, the fact that $cov[\ln E_{eff}, \ln u_I]$ is small implies accuracy of the relations $\sigma^2_{\ln l_I} \approx \sigma^2_{F_{eff}} + \sigma^2_{\ln u_I}$ and $\sigma^2_{\ln t_I} \approx \sigma^2_{\ln l_I} + \sigma^2_{\ln u_I}$.

In the 2D case, the distributions of the initial displacement u_I and initial toughness t_I are less sensitive to the shape of the correlation function and the correlation length than in the 1D case. The opposite is true for the distribution of $\ln l_I$ (because in the 1D case this distribution is the same irrespective of the correlation function).

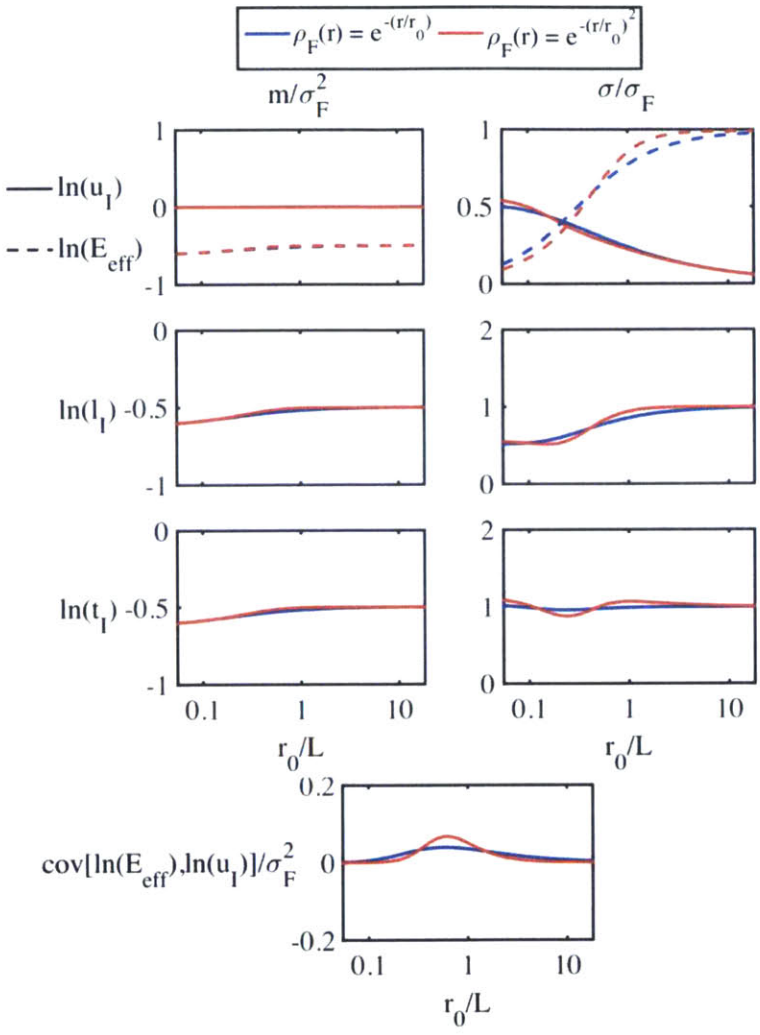

Figure 3.7: Same as **Figure 3.6** for square plates.

Overall Effect of Heterogeneity

Figures 3.6 and **3.7** show results in terms of the moments of the initial log-strengths X. To more directly understand whether the heterogeneities increase or decrease the fracture strengths, one can examine the un-logged mean and median values, $m_X = e^{m_{\ln X}+0.5\sigma^2_{lnX}}$ and $X_{0.5} = e^{m_{\ln X}}$. This is done in **Figure 3.8** for $\sigma_F = 1$, for both rods and square plates. The mean and median values for any other value of σ_F are obtained as $m_X = (m_X|\sigma_F = 1)^{\sigma_F^2}$ and $X_{0.5} = (X_{0.5}|\sigma_F = 1)^{\sigma_F^2}$. Values larger than 1 indicate increased strength and values below 1 indicate lower strength compared to the uniform case. Notice

that due to the positive skewness of the lognormal distribution, the mean values always exceed the median values.

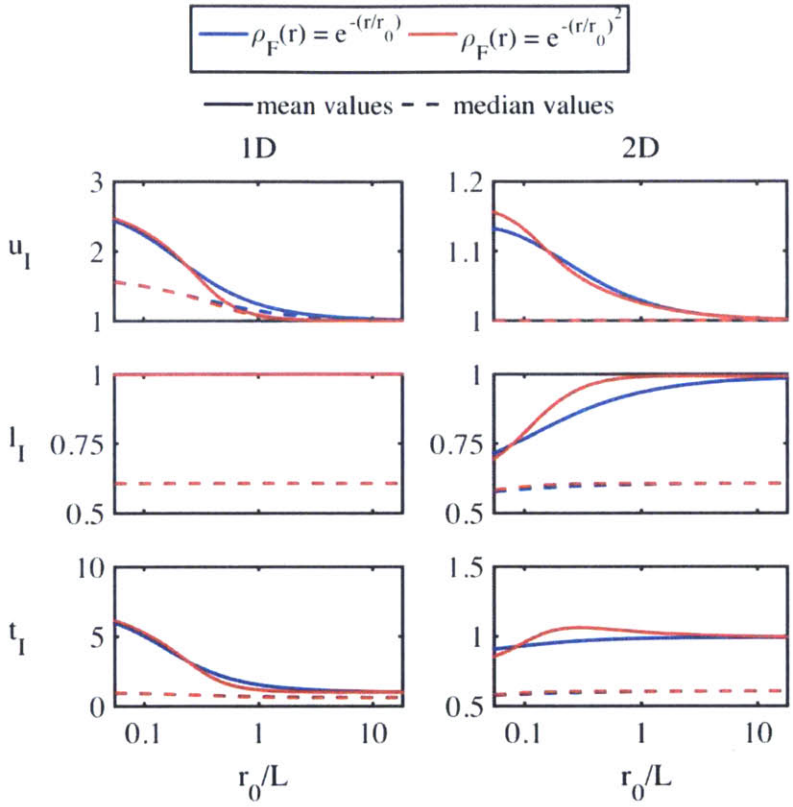

Figure 3.8: Mean (solid lines) and median values (dashed lines) of the initial fracture strengths for 1D rods and 2D squares as a function of the normalized correlation length r_0/L. Blue and red curves show results for simple- and double- exponential correlation functions.

When the correlation length r_o exceeds the size of the specimen L, the modulus field is nearly uniform and the mean and median of all the strength measures are close to the value under uniform modulus (normalized values in **Figure 3.8** close to 1). In the case of rods with low correlation, the heterogeneities increase the mean initial displacement and toughness, whereas the mean load capacity remains the same. The median value exceeds 1 for elongation at fracture initiation, is 1 for toughness, and is below 1 for load capacity. For 2D specimens, the low-correlation median values are similar to the 1D case, but the mean values are lower due to the smaller log-variances (compare the standard deviations in **Figures 3.6 and 3.7**). These results point at a complex pattern of strength enhancement

and reduction due to random spatial variation of the modulus: in general the elongation at failure initiation is enhanced, while the load at initial failure tends to be lower.

One can also examine the dispersion of the normalized (unlogged) strengths X. This is conveniently done through the coefficient of variation $V_X = \sigma_X/m_X$. Since for a lognormal distribution $V_X = \sqrt{e^{\sigma^2_{\ln X}} - 1}$, we refer to our previous discussion of σ_{lnX} in **Figures 3.6 and 3.7**.

3.5.2 Ultimate Fracture Strengths

Next we consider how various parameters affect fracture propagation and crack arrest, hence the regression model in Eq. 3.10. We consider a square specimen with unit side length and Gaussian log-modulus $F(x)$ with correlation function $\rho_F(r) = e^{-r/r_0}$ and vary the correlation length $r_0 = \{0.125,0.25,0.5,1\}$ and standard deviation $\sigma_F = \{0.3,0.5,0.7\}$. For each parameter combination (r_0, σ_F), we obtain maximum likelihood estimates of the parameters in Eq. 3.10 for $X = \{u, l, t\}$ based on 250 Monte Carlo simulations. We found that the stability index α has maximum likelihood values close to 1.3 for $X = u, l$ and 1.35 for $X = t$ and that in all cases the skewness parameter β has maximum likelihood value 1. Hence we fix α and β to these values and estimate the remaining three parameters (c_0, c_1, σ) by maximum likelihood. Results are shown in **Figure 3.9**. Noticeable features are:

- The regression intercept c_0 and residual dispersion σ increase as a function of σ_F. This is due to the fact that higher log-modulus fluctuations produce larger and more dispersed crack-arrest effects. The increase is not dramatic, due to the fact that for large σ_F the fracture tends to propagate along "valleys" of the modulus landscape (see for example the simulation in **Figure 3.4c**). When crack arrest occurs, the ultimate displacement and toughness always increase above the fracture initiation values, whereas that is not necessarily the case for the ultimate load. This is why c_0 tends to be lower for l compared with u and t;

- c_0 is larger for shorter correlation length r_0, because less correlated log-modulus fields produce larger crack-arrest effects;
- c_0 and σ^2 for $\ln(t)$ are approximately the sum of c and σ^2 for $\ln(u)$ and $\ln(l)$. This is due to the fact that the ultimate elongation and load contribute in an essentially multiplicative way to the ultimate toughness, and the present results are in terms of log-moments; and
- The regression slope c_1 has a somewhat complicated dependence on the standard deviation σ_F and correlation length r_0. Notice that $c_1 = 1$ corresponds to a regression line parallel to the lower bound $\ln X_U = \ln X_I$, hence to statistically identical crack-arrest effects for all initial strengths X_I. At the other extreme, $c_1 = 0$ indicates that the crack-arrest effects are negatively correlated with the initial strength, to the point that the distribution of X_U is the same irrespective of X_I. For highly correlated log-modulus fields (large r_0), the ultimate load and toughness approach the first condition, whereas for small r_0 and large σ_F the ultimate elongation and toughness approach the second condition.

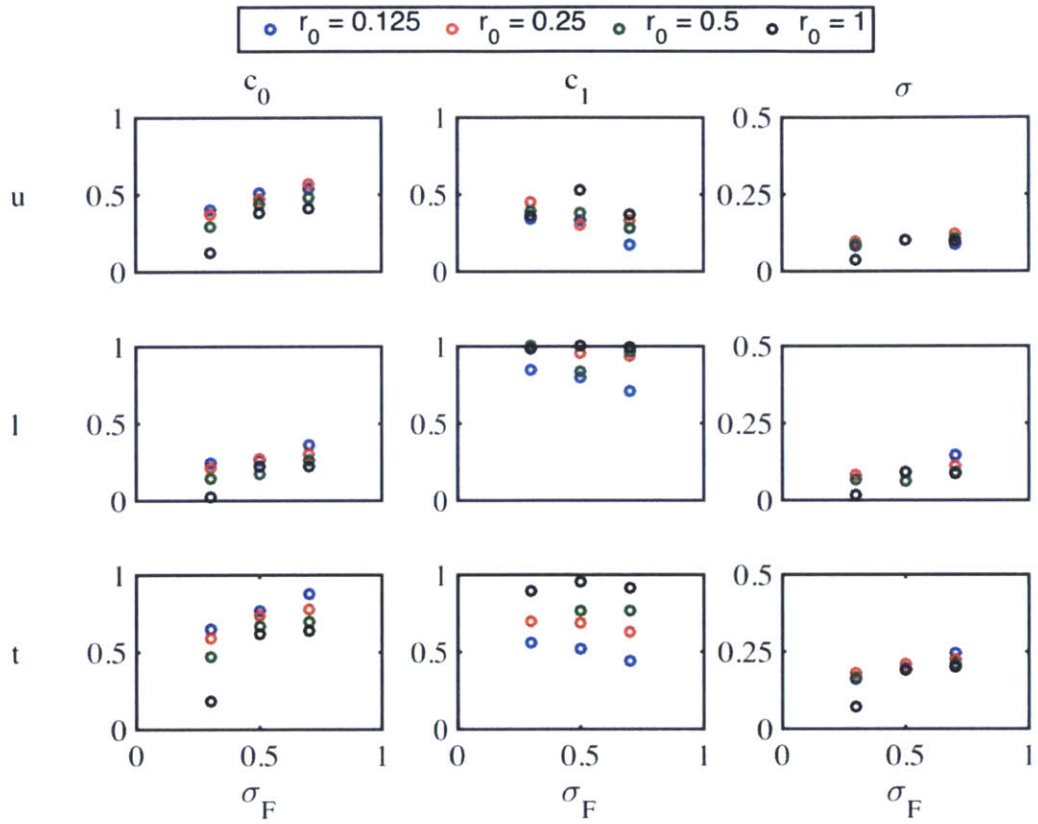

Figure 3.9: Parameters of the regression model in Eq. 3.10 for square specimens with unit side length. Normal log-modulus $\boldsymbol{F(x)}$ with simple exponential correlation function $\boldsymbol{\rho_F(r)}$, standard deviation $\boldsymbol{\sigma_F} = \{\mathbf{0.3, 0.5, 0.7}\}$ and correlation length $\boldsymbol{r_0} = \{\mathbf{0.125, 0.25, 0.5, 1}\}$. Parameters are fitted by maximum likelihood to 250 Monte Carlo simulations.

To better appreciate the effects of crack arrest and evaluate the overall strengthening or weakening brought about by the heterogeneities at ultimate failure, **Figure 3.10** compares the distributions of $\ln X_I$ and $\ln X_U$ for $X = \{u, l, t\}$ in the case of a square specimen with unit side length. The normal log-modulus $F(x)$ has simple exponential correlation function $\rho_F(r)$, standard deviation $\sigma_F = 0.5$, and correlation length $r_0 = \{0.125, 0.25, 0.5, 1\}$. The effects of crack arrest are most pronounced for displacement and toughness and are larger for less correlated log-modulus fields. For low correlation, the ultimate displacement is virtually always above the uniform value. This is largely true also for the ultimate toughness, whereas the ultimate load benefits less from crack arrest and its distribution remains centered on the value under uniform modulus. In order for crack arrest to occur, the crack must encounter a sufficiently stiff patch on its path to

overcome the increase in strain concentration. Also, as illustrated in **Figure 3.1b**, any crack arrest leads to $t_U > t_I$, but in order for $l_U > l_I$ to occur the crack must encounter such a stiff patch that the elongation required to resume crack propagation more than balances the decrease in effective stiffness due to the reduced size of the intact specimen.

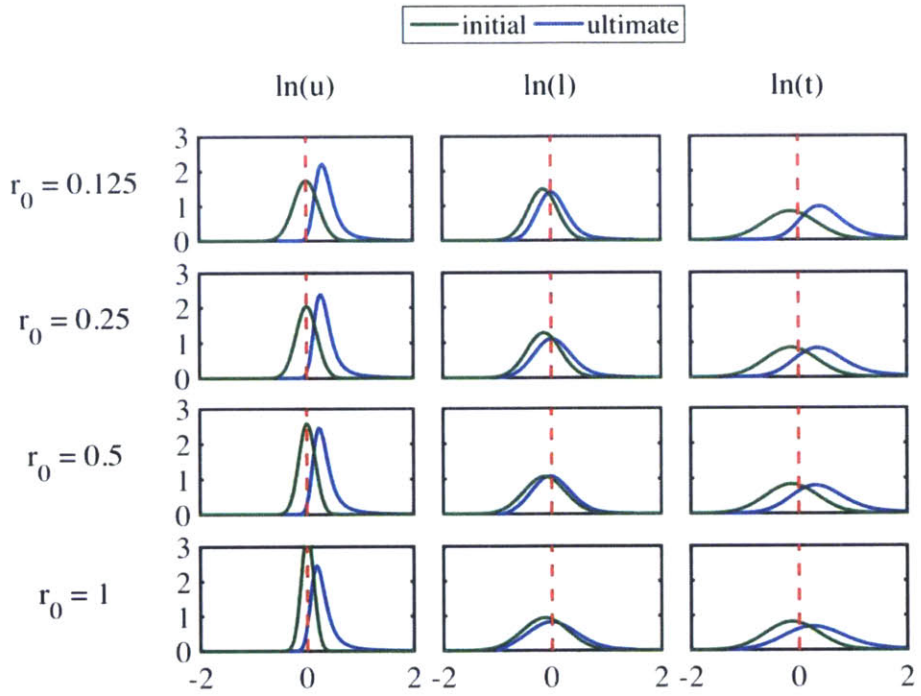

Figure 3.10: Marginal distributions of the normalized initial and ultimate log-fracture strengths for $\boldsymbol{\sigma_F = 0.5}$ and $\boldsymbol{r_0 = \{0.125, 0.25, 0.5, 1\}}$.

Interestingly, the log-dispersion tends to be smaller for the ultimate strengths than the initial strengths because the crack-arrest effects are negatively correlated with the strengths at fracture initiation. We calculated the distributions in **Figure 3.10** also for other values of σ_F and observed that the main effect of σ_F is contraction/dilation of the distributions relative to the origin.

3.6. Conclusions

We built upon the models and analysis strategy in Chapter 2 to study the distribution of fracture strength characteristics of rods and plates in which the log-Young's modulus $F(x) = \ln E(x)$ varies spatially as an isotropic normal field. We distinguished between two stages of the fracture process, fracture initiation at the notch tip and ultimate failure following fracture propagation through the specimen (the two conditions coincide in the case of 1D rods). For each stage, we developed analytical or semi-analytical approximations to the distribution of elongation U, strength L, and the toughness modulus T. Qualitatively, our results are in agreement with previous work on fracture in materials with randomly disordered Young's modulus distributions [23-25].

The methods depend to some extent on the Euclidean dimension of the specimen ($n = 1$ or 2), the quantity considered (U, L, or T), and the condition under which the probability distribution is assessed (fracture initiation I or ultimate failure U). Specifically, we obtain the distributions for rods by using an analysis-of-variance approach similar to that in Chapter 2, whereas for 2D plates we use a semi-analytical sensitivity model. For the effects of crack arrest, we fit regression models to simulation data. All results were validated through Monte Carlo simulation and then used to study the influence of various parameters on the distribution of U, L and T at fracture initiation and the effects of fracture propagation and crack arrest. To our knowledge this is the first time that these fracture strength problems are addressed analytically or semi-analytically. We are also unaware of previous studies in which the effects of crack arrest are related to the probabilistic parameters of the stiffness field.

The study has provided fundamental insights into the fracture behavior of this class of heterogeneous materials:

1. The strengths at fracture initiation display a complex behavior relative to their values under uniform modulus ($E(x) \equiv m_E$): The heterogeneities generally increase the mean values, whereas the median value is lower or higher depending on the Euclidean dimension of the specimen and the quantity considered (U, L,

and T). Specifically, gains in the median occur for elongation U and toughness T, whereas the median of the load L is lower than the uniform value;

2. In 2D specimens, crack arrest increases the strengths at ultimate failure relative to their values at fracture initiation. This effect is modest for the ultimate load, but is important for the ultimate elongation and toughness;
3. For limited variations of the modulus field we observe similar crack arrest mechanisms as in laminates and composites with periodically varying modulus: crack arrest occurs as the fracture propagates towards higher modulus regions and its effect is controlled by the modulus contrast. As the variability of the modulus field increases, low modulus valleys appear. Fracture tends to propagate along these valleys, limiting the effectiveness of crack arrest and giving rise to different fracture patterns than those observed in laminated composites; and
4. The dispersion of the fracture strength parameters is smaller in the 2D than the 1D case and for 2D specimens decreases somewhat from initial fracture to ultimate failure conditions.

Possible further extensions of this work include:

1. Study the effects of statistical anisotropy, as a way to bridge between the present isotropic materials and laminated composites;
2. Extend the methodology to random non-lognormal heterogeneous materials, for example materials with single- or multi-phase inclusions or natural and engineering materials such as bone and concrete; and
3. Study the effects of random spatially varying material strength (here the material strength is considered deterministic).

Supporting Information

Part A: Derivation Details

Equation 2.4

To find the mean value and variance of $u_I = \langle e^{F(0)-F(x)} \rangle$ in Eq. 2.3, we proceed in 3 steps:

1. Find the mean value and covariance function of the Gaussian process $\Delta F(x) = F(0) - F(x)$;
2. Find the mean value and covariance function of the lognormal process $RE(x) = \exp[F(0) - F(x)]$;
3. Find the mean value and variance of $u_I = \langle e^{RE(x)} \rangle$.

Let $\rho_Y(\tau)$ and $B_Y(x_1, x_2)$ denote the (stationary) correlation and (nonstationary) covariance function of some random field $Y(x)$ and $N\{\bullet\}$ and $LN\{\bullet\}$ be the normal and lognormal distribution with parameters $(\bullet)$. Using basic second-moment results and properties of normal and lognormal distributions, we obtain

$$\begin{aligned}
&\Delta F(x) \sim N\{m_{\Delta F} = 0, B_{\Delta F}(r_1, r_2) = [1 - \rho_F(r_1) - \rho_F(r_2) + \rho_F(r_1 - r_2)]\sigma_F^2\} \\
&RE(x) \sim LN\ \{m_{RE}(r) = e^{[1-\rho_F(r)]\sigma_F^2}, \\
&B_{RE}(x_1, x_2) = m_{RE}(r_1) m_{RE}(r_2)\left[e^{B_{\Delta F}(r_1, r_2)} - 1\right]\} \qquad (3.A1) \\
&u_I \sim LN\left\{m_{u_I} = \frac{2}{L_1}\int_0^{L_1/2} m_{RE}(r)dx\,, \sigma_{u_I}^2 = \frac{1}{L_1^2}\int_{-L_1/2}^{L_1/2} dr_1 \int_{-L_1/2}^{L_1/2} B_{RE}(r_1, r_2)dr_2\right\}.
\end{aligned}$$

Substituting the expressions for $B_{RE}(r_1, r_2)$, $m_{RE}(r_1)$, and $B_{\Delta F}(r_1, r_2)$ in the parameters of u_I gives the mean value m_{u_I} and variance $\sigma_{u_I}^2$ in Eq. 3.4.

Equation 5

To obtain the covariance between $\ln u_I$ and $\ln E_{eff}$, we observe that

$$\ln u_I = \ln \langle \frac{E(0)}{E(x)} \rangle = \ln E(0) + \ln \langle \frac{1}{E(x)} \rangle$$
$$\ln E_{eff} = -\ln \langle \frac{1}{E(x)} \rangle \tag{3.A2}$$

or, with $I = \langle \frac{1}{E(x)} \rangle$,

$$\ln u_I = \ln E(0) + \ln I$$
$$\ln E_{eff} = -\ln I \tag{3.A3}$$

Therefore

$$Cov[\ln u_I, \ln E_{eff}] = -\sigma^2_{\ln I} - Cov[\ln E(0), \ln I] \tag{3.A4}$$

To find $Cov[\ln E(0), \ln I]$, we use

$$\sigma^2_{\ln u_I} = \sigma^2_{\ln E(0)} + \sigma^2_{\ln I} + 2Cov[\ln E(0), \ln I] \tag{3.A5}$$

and $\sigma^2_{\ln E(0)} = \sigma^2_F$ to obtain

$$Cov[\ln E(0), \ln I] = \frac{1}{2}\left(\sigma^2_{\ln u_I} - \sigma^2_F - \sigma^2_{\ln I}\right) \tag{3.A6}$$

Substitution into Eq. 3.A4 gives the result in Eq. 3.5.

Coefficients of the Linear Sensitivity Model in Eq. 3.2

To calculate the sensitivity coefficients b_i in Eq. 3.2, we use a Finite Element model of a notched square specimen with 80x80 linear four node elements. We set the log-modulus of all elements to the homogeneous value F_{hom} except for one tile i in a neighborhood of the notch tip. For each i, in separate experiments we set the element log-stiffness to $F_i = F_{hom} + \ln 2$ and $F_i = F_{hom} - \ln 2$ in separate experiments and record the resulting values $u_{i,\ln 2_+}$ and $u_{i,\ln 2_-}$ of u_I. The coefficient b_i is then found as

$$b_i = \frac{\ln u_{Ii,\ln 2_+} - \ln u_{Ii,\ln 2_-}}{2 \ln 2} \tag{3.A7}$$

Part B: Model Comparisons

FEM and Spring Bead Models

Figure 3.B1 compares values of F_{eff}, $\ln u_I$, $\ln l_I$, and $\ln t_I$ generated by the finite element and spring bead models for 1000 Monte Carlo simulations of a 2D square specimen. The log- stiffness field $F(x) = \ln E(x)$ is normal with simple exponential correlation function, normalized correlation length $r_0/L = 0.125$, and standard deviation $\sigma_F = 0.3$. The log-stiffnesses predicted by the two models are virtually identical and the remaining quantities show close correspondence, with correlation $R \geq 0.95$.

2. Stochastic Lognormal System and Bi-Material Composite

Figure 3.B2 compares the load-elongation curve of the system in **Figure 3.3b** to the same curve for a bi-material composite analog, with stiffness representative of conditions at points 1 and 2. The stiffness fields are also shown. The stress strain curves display similar behavior (similar degree of crack arrest, similar ultimate elongation), indicating that the bi-material analog captures important features of the crack-arrest mechanisms in the stochastic system.

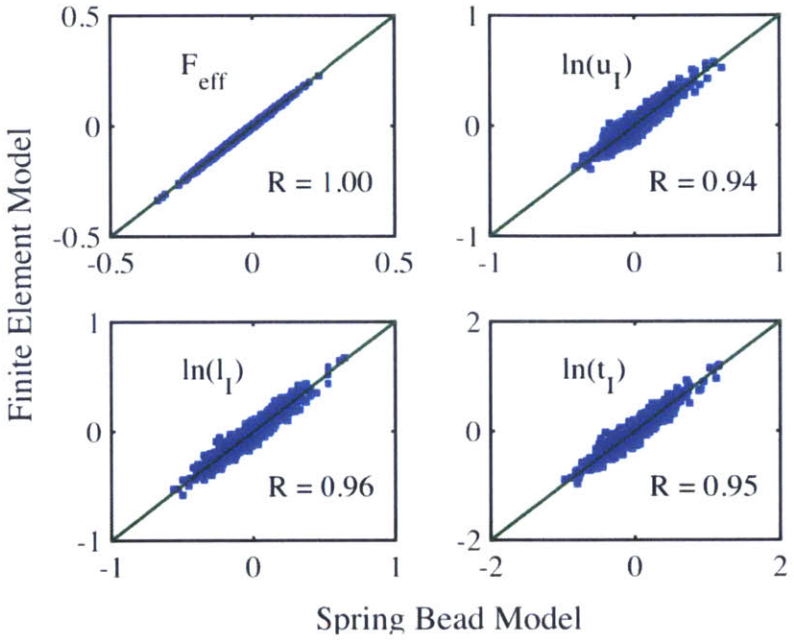

Figure 3.B1: Scatter plot and correlation coefficient of the log effective stiffness and log initial strengths calculated with the finite element and spring bead models.

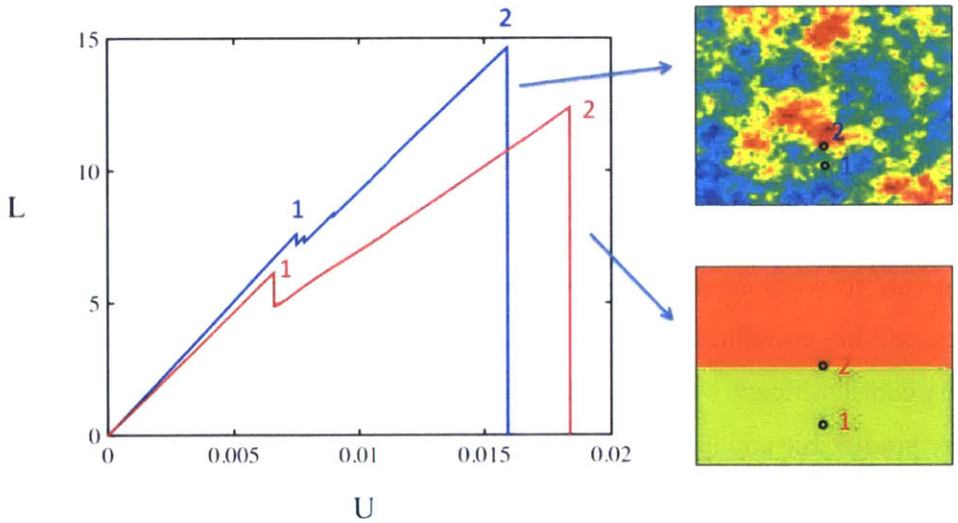

Figure 3.B2: Load-deflection curve and stiffness map of a stochastic system realization and a corresponding bi-material composite analog.

Chapter 4: Strength and Fracture Toughness of Heterogeneous Blocks with Joint Lognormal Modulus and Failure Strain

The research and review presented in this chapter will be published in:

- L. S. Dimas, D. Veneziano, M.J. Buehler, *Strength and Fracture Toughness of Heterogeneous Blocks with Joint Lognormal Modulus and Failure Strain*, In submission, 2015.

We obtain analytical approximations to the probability distribution of the fracture strengths of notched one-dimensional rods and two-dimensional plates in which the stiffness (Young's modulus) and strength (failure strain) of the material vary as jointly lognormal random fields. The fracture strength of the specimen is measured by the elongation, load, and toughness at two critical stages: when fracture initiates at the notch tip and, in the 2D case, when fracture propagates through the entire specimen. This is an extension of Chapter 3 on the elastic and fracture properties of systems with random Young's modulus and deterministic material strength. For 1D rods our approach is analytical and builds upon the ANOVA decomposition technique of Chapter 2. In 2D we use a semi-analytical model to derive the fracture initiation strengths and regressions fitted to simulation data for the effect of crack arrest during fracture propagation. Results are validated through Monte Carlo simulation. Randomness of the material strength affects in various ways the mean and median values of the initial strengths, their log-variances, and log-correlations. Under low spatial correlation, material strength variability can significantly increase the effect of crack arrest, causing ultimate failure to be a more predictable and less brittle failure mode than fracture initiation. These insights could be used to guide design of more fracture resistant composites, and add to the design features that enhance material performance.

4.1 Introduction

The initiation and propagation of fracture in notched linear elastic media is controlled by the stresses, strains and material strength around the evolving fracture tip. In turn, the stresses and strains depend on the boundary conditions, the specimen geometry (including the prior fracture path), and the stiffness tensor field over the entire body.

Natural and synthetic materials often exhibit significant stochastic-looking fluctuations in elastic modulus and strength [4, 24, 25, 31-33]. Several studies have found that fluctuations in the modulus can enhance the fracture performance of materials such as bone and nacre [22-29]. However, depending on the pattern of the fluctuations, the opposite may also be true and when the fluctuations are stochastic, various weakening and strengthening outcomes are usually possible. Understanding the influence of random material heterogeneities on the bulk mechanical properties using analytical/numerical predictive models is a critical first step for the reliability assessment and design of such materials.

Previous research has focused on cases with random spatial variation of the elastic modulus or the local strength, but not both. Studies that include fluctuations of the elastic modulus use mostly numerical tools, typically variants of finite element analysis [85-87] in combination with first and second order uncertainty propagation [67, 68] or Monte Carlo simulation [65, 66]. While these numerical methods are general, they are computationally inefficient and unsuited for parametric analysis, optimization or design.

Materials with random local variation of strength have also been analyzed. Following Weibull's pioneering work [33], several studies view the failure of initially intact specimens as a weakest-link problem, which is often amenable to analytical treatment [97-99]. Other studies consider specimens in which fracture initiates at the tip of a pre-existing notch and focus on the fracture path using numerical simulation [100-102]. We know of no analytical investigation in which randomness of the bulk fracture strength of notched specimens is related to randomness of the local strength field.

This paper is the third in a series aimed at analytically characterizing the distribution of the bulk elastic and strength properties of materials in which the elastic modulus and local strength vary randomly in space. Chapter 2 developed approximations for the joint distribution of the bulk stiffness tensor of n-dimensional rectangular blocks ($n = 1, 2,$ or 3) when Young's modulus $E(x)$ varies as an isotropic lognormal field. The approach makes use of an analysis of variance (ANOVA) decomposition of the log-modulus $F(x) = \ln E(x)$ as the sum of the average $\bar{F}$ inside the block, marginal fluctuations along the coordinate axes ("main effects"), and interactions of order $2, \ldots, n$. The joint distribution of the bulk stiffness tensor is obtained by multiplicatively combing the effects of the individual ANOVA terms.

In Chapter 3 we derived the probability distribution of various strength properties of notched thin rods ($n = 1$) and rectangular plates ($n = 2$); see **Figure 4.1a**. Also in this case Young's modulus $E(x)$ is assumed to vary as an isotropic lognormal field, but focus is on the probability distribution of six specimen strength variables: the elongation U_I, load L_I, and toughness modulus T_I when fracture initiates at the notch tip (subscript I) and corresponding quantities U_U, L_U, and T_U defined as the largest values of U, L, and T as fracture propagates through the specimen (ultimate failure, subscript U). As shown in **Figure 4.1b**, the toughness modulus is defined as the work done by the external forces, per unit specimen length in 1D and unit specimen area in 2D [88]. As was shown in Chapter 3, there is high positive correlation between the present T variable and measures of fracture toughness based on the J-integral. For thin rods our method is analytical and exploits the ANOVA decomposition of the log-modulus field mentioned above. In 2D, the method is semi-analytical in that the effect of crack arrest on the ultimate strengths is quantified by fitting regression models to simulation data.

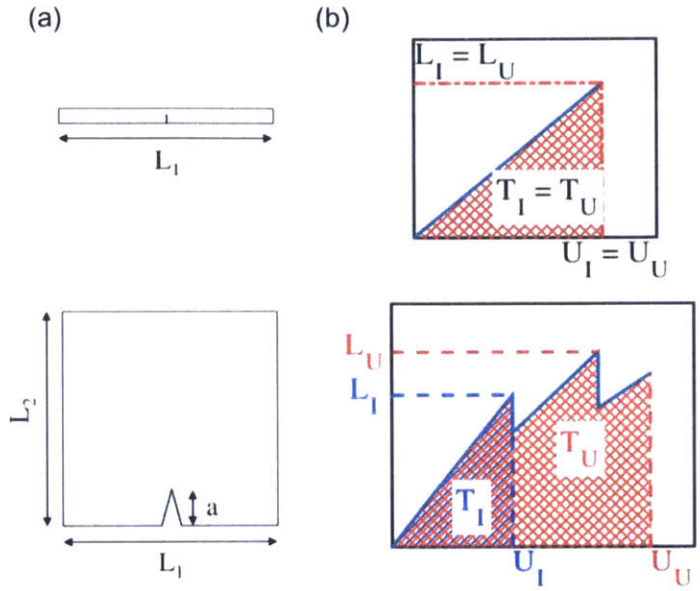

Figure 4.1: a Specimen geometry and **b** fracture strength measures for 1D rods and 2D plates. The definitions are identical to in Chapter 3.

Here we extend the work of Chapter 3 by considering cases when Young's modulus and the local strength are joint lognormal random fields. As before, we study the distribution of U, L and T under initial (I) and ultimate failure conditions (U), as one face of the block normal to the x_1-direction is incrementally displaced relative to the opposite face, with zero tractions on the rest of the boundary. A small process zone is assumed to develop around the crack tip while the rest of the specimen remains linear elastic. The crack initiates or propagates when the maximum longitudinal strain at the edge of the process zone exceeds a random critical value (the "local material strength"). In a continuous linear brittle material this is equivalent to fracture propagating when the strain intensity factor exceeds some threshold value, whereas in a discrete lattice idealization the critical failure strain should be proportional to the inverse square root of the discretization length. This is a well-established way of modeling fracture propagation and has been shown to produce results consistent with experiment [96, 103, 104].

More details on the model, in particular the representation of the stochastic modulus and local material strength, are given in Section 4.2. Sections 4.3 and 4.4 present the derivation of approximations to the distribution of the initial specimen strengths $\{U_I, L_I,$

$T_l\}$ and ultimate specimen strengths $\{U_U, L_U, T_U\}$, respectively. This is done for both 1D and 2D specimens. Section 4.5 validates the analytical approximations using Monte Carlo simulation and Section 4.6 uses the analytical results to study the sensitivity of the bulk strength distributions to various geometric and stochastic-model parameters. Conclusions and an outlook on future developments are presented in Section 4.7.

4.2 Stochastic Model and Other Assumptions

We consider Poisson's ratio ν to be deterministic constant, and both the elastic modulus $E(x)$ and failure strain $\varepsilon_r(x)$ to be isotropic lognormal fields. Without loss of generality (see below), we set the mean values of these fields to 1. Hence the log-modulus $F(x) = \ln E(x)$ and log failure strain $\ln \varepsilon_r(x)$ are isotropic Gaussian with some variances σ_F^2 and $\sigma_{\ln \varepsilon_r}^2$ and mean values $-0.5\sigma_F^2$ and $-0.5\sigma_{\ln \varepsilon_r}^2$. The two fields are assumed to have the same correlation function $\rho(r)$ where r is spatial distance.

The similarity in the stochastic models of $E(x)$ and $\varepsilon_r(x)$ makes physical sense, since the mechanisms that produce variations in Young's modulus typically control also the local strength. For example, in bone and nacre the variations in stiffness and strength are largely due to fluctuations in the mineral content of the composite [4, 24, 25, 105]. The assumption of lognormal distribution is made in part for analytical convenience and in part because the lognormal distribution has been found to accurately describe the modulus and strength of many materials [106-109]. This assumption breaks down for multi-phase composites, for which the distributions are multi-modal; see Chapters 5 and 6.

Regarding dependence between the modulus and strength fields, we assume that at any given location x_o the log-strength $\ln \varepsilon_r(x_o)$ depends on the log-modulus field $F(x)$ through only the local value $F(x_o)$. This Markov-like cross-dependence structure is motivated by the observation that fracture strength and stiffness are local material

properties. The correlation coefficient between $\ln \varepsilon_r(x_0)$ and $F(x_o)$, denoted by ρ, is allowed to vary between -1 and 1.

The previous assumptions are embedded in the representation,

$$\ln \varepsilon_r(x) = bF(x) + \eta(x) \tag{4.1}$$

where b is a constant and F and η are independent isotropic normal fields with possibly different mean values and variances, but identical correlation function $\rho(r)$. Simple second-moment analysis leads to the following relationships between the parameters of the model in Eq. 4.1 and the parameters of the $\ln \varepsilon_r$ and F fields:

$$\begin{aligned} m_\eta &= \frac{1}{2}\left(b\sigma_F^2 - \sigma_{\ln \varepsilon_r}^2\right) \\ \sigma_\eta &= \sqrt{1-\rho^2}\,\sigma_{\ln \varepsilon_r} \\ b &= \rho \frac{\sigma_{\ln \varepsilon_r}}{\sigma_F} \end{aligned} \tag{4.2}$$

The Markov-like property mentioned earlier between $\ln \varepsilon_r$ and F follows from independence between F and η in Eq. 4.1.

Notice that the initial strength, elongation, and toughness depend on the log-modulus $F(x)$ over the entire specimen, whereas the critical strain $\varepsilon_r(x)$ influences the same quantities through only the value ε_r^* at the notch tip. By contrast, the ultimate strengths depend on $F(x)$ and $\varepsilon_r(x)$ everywhere in the specimen.

Like in Chapter 3, it is convenient to make the fracture strengths (the elongation U, load L, and toughness T) dimensionless. We do so by dividing these quantities by the corresponding values U_0, L_0, and T_0 when all the stochastic fluctuations are suppressed (in the present case, when $E(x) \equiv 1$ and $\varepsilon_r(x) \equiv 1$). Hence, using lower case letters for the dimensionless variables, we seek the distributions of $u_I = U_I/U_0$, $l_I = L_I/L_0$, ... and

$t_U = T_U/T_0$. These 6 distributions are independent of the mean values of the elastic modulus and failure strain, which for simplicity we have set to 1.

4.3 Initial Fracture Strengths

We start by estimating the first and second moment properties of the initial strengths $X_I = [u_I, l_I, t_I]$ in one- and two-dimensonsal specimens. The approach is similar to in Chapter 3, but includes stochasticity of the material strength. We denote by ε_r^*, E^* and $F^* = \ln E^*$ the strength, modulus and log-modulus at the crack tip and by $\overline{F}$ the average of the log-modulus over the specimen.

4.3.1 1D (one-dimensional rod of length L_1)

In the 1D case the (constant) stress σ is related to the elongation U as $\sigma = E_{eff}U/L_1$ where $E_{eff} = \left(\frac{1}{L_1}\int_0^{L_1} e^{-F(x)}dx\right)^{-1}$. The strain at the crack tip, $\varepsilon^* = \varepsilon(L_1/2)$, is given by

$$\varepsilon^* = \frac{\sigma}{E^*} = \frac{E_{eff}}{E^*}U/L_1 \tag{4.3}$$

Setting $\varepsilon^* = \varepsilon_r^*$ in Eq. 4.3 and solving for U gives the elongation at failure $U_I = \varepsilon_r^* L_1 \frac{E^*}{E_{eff}}$. Under uniform conditions, the same elongation is $U_0 = L_1$. Therefore the dimensionless displacement at failure $u_I = U_I/U_0$ satisfies

$$\ln u_I = \ln \varepsilon_r^* + F^* - F_{eff} \tag{4.4}$$

where $F_{eff} = \ln E_{eff}$. The corresponding dimensionless failure load l_I and toughness t_I are related to u_I and F_{eff} as

$$\ln l_I = F_{eff} + \ln u_I\,, \tag{4.5}$$

$$\ln t_l = F_{eff} + 2 \cdot \ln u_l$$

Finally, substitution of $\ln u_l$ in Eq. 4.4 gives

$$\begin{aligned} \ln l_l &= \ln \varepsilon_r^* + F^*, \\ \ln t_l &= 2 \ln \varepsilon_r^* + 2F^* - F_{eff}. \end{aligned} \tag{4.6}$$

As for the case of deterministic strength, we approximate the distribution of the initial log strength vector $\ln X_l = [\ln u_l, \ln l_l, \ln t_l]$ as multivariate normal. Its first and second moments can be found by noting that $\ln X_l$ in Eqs. 4.4 and 4.6 is a linear function of the random vector $[\ln \varepsilon_r^*, F^*, F_{eff}]$, whose first two moments are obtained as follows.

The moments of the effective log stiffness $F_{eff} = \ln E_{eff}$, where E_{eff} is the harmonic average of E, do not depend on the strength model and were derived in Chapter 2 and the moments of the sub-vector $[\ln \varepsilon_r^*, F^*]$ are externally specified; see Section 4.2. To complete the second-moment characterization, one additionally needs the covariances $cov\,[\ln \varepsilon_r^*, F_{eff}]$ and $cov[F^*, F_{eff}]$. Using $\ln \varepsilon_r^* = bF^* + \eta^*$ from Eq. 4.1 and noting that $\eta^* = \eta(L_1/2)$ is independent of $F(x)$ and hence of F_{eff}, one concludes that

$$cov\,[\ln \varepsilon_r^*, F_{eff}] = b \cdot cov[F^*, F_{eff}] \tag{4.7}$$

Therefore it is sufficient to estimate only one of the above covariance terms. Our strategy is to approximate $cov[F^*, F_{eff}]$ as $cov[F^*, \overline{F}]$ (thus replacing the harmonic average of E with the geometric average), as the latter covariance is simpler to calculate. In numerical simulations using a range of realistic specifications of the random modulus field this approximation has proved accurate, although one may expect the accuracy to deteriorate for extremely large σ_F. (In 2D, E_{eff} is close to the geometric average of E and an approximation of this type is even more accurate.)

The approximating covariance is

$$cov[F^*, \overline{F}] = \sigma_F^2 E[\rho(R^*)] \tag{4.8}$$

where R^* is the random distance between the notch tip and a point uniformly distributed inside the specimen, $\rho(r)$ is the spatial correlation function of F, and $E[\,]$ denotes expectation. In the 1D case, R^* has uniform distribution between 0 and $L_1/2$.

4.3.2 2D (two-dimensional rectangle with dimensions $L_1 \times L_2$)

In the 2D case, Eqs. 4.4 and 4.6 do not hold. Specifically, $\ln u_l$ retains linearity in $\ln \varepsilon_r^*$ but has a complicated dependence on the log-modulus field $F(x)$. However, Eq. 4.5 still applies. Therefore our approach is to first develop a joint normal approximation to the distribution of $[F_{eff}, \ln u_l]$ and then find the joint distribution of the initial log-strengths $[\ln u_l, \ln l_l, \ln t_l]$ using the linear relationships in Eq. 4.5.

Analytical approximations of the first two moments of F_{eff} for 2D specimens were derived in Chapter 2. Again notice that these moments do not depend on the material strength model. All one needs additionally are the mean value and variance of $\ln u_l$ and the covariance between F_{eff} and $\ln u_l$. To approximate these moments we use a first-order second-moment (FOSM) approach similar to the one used in Chapter 3 for deterministic strength. We discretize space into a Cartesian grid of points x_i. Then we use numerical perturbation analysis around the average log-modulus $\overline{F}$ to approximate $\ln u_l$ as a linear function of the log-moduli $F_i = F(\boldsymbol{x}_i)$. This gives

$$\ln u_l \approx \ln \varepsilon_r^* + \sum_i b_i \left(F_i - \overline{F}\right), \tag{4.9}$$

where the sensitivity coefficients b_i are the same as for deterministic strength; see Eq. 3.2. Using Eq. 4.9, we set $F'_i = F_i - \overline{F}$, approximate the F' field as was done for deterministic strength, and find the mean value and variance of $\ln u_l$ as

$$m_{\ln u_I} = m_{\ln \varepsilon_r^*},$$

$$\sigma^2_{\ln u_I} = \sigma^2_{\ln \varepsilon_r^*} + \mathrm{Var}\left[\sum_i b_i F'_i\right] + \sum_i b_i \mathrm{Cov}[\ln \varepsilon_r^*, F'_i] \tag{4.10}$$

where $\mathrm{Var}[\sum_i b_i F'_i]$ is the same as for deterministic strength. In analogy to the 1D case, the covariance terms $cov[\ln \varepsilon_r^*, F'_i]$ are approximated as

$$cov[\ln \varepsilon_r^*, F'_i] \approx b\sigma^2_{F'} \rho(r_i^*) \tag{4.11}$$

where b is the coefficient in Eq. 4.1 and r_i^* is the distance of the i^{th} discretization point from the notch tip. Equation 4.11 approximates $cov[\ln \varepsilon_r^*, F'^*]$ as $b\sigma^2_{F'}$ and, like for deterministic strength, assumes in approximation that the spatial correlation function of F' is the same as the correlation function of F. In numerical implementation, one may limit the summations in Eq. 4.10 to values of i for which b_i is significantly nonzero.

Finally, one needs the covariance between F_{eff} and $\ln u_I$. As was noted in Section 4.3.1, a good approximation to E_{eff} in the 2D case is the geometric average of E. Therefore, a good approximation to F_{eff} is the average $\overline{F} = \frac{1}{n}\sum_i F_i$ where n is the number of discretization points. Using $\overline{F}$ in place of F_{eff}, the linearized expression of $\ln u_I$ in Eq. 4.9 gives

$$cov[F_{eff}, \ln u_I] \approx \sigma_F^2 \left\{ \left(\sum_i b_i \right) \left(\frac{1}{n} + b \right) E[\rho(R^*)] - E[\rho(R_{12})] \right\} \tag{4.12}$$

where the b_i are the coefficients of the linearized sensitivity model in Eq. 4.9, b is the coefficient of $F(x)$ in Eq. 4.1, R^* is the random distance between the notch tip and a point uniformly distributed inside the specimen, R_{12} is the random distance between two points uniformly distributed inside the specimen, and $E[]$ denotes expectation with

respect to these random distances. The Supporting Information includes a detailed derivation of Eq. 4.12.

4.3.3 3D Extension

The approach we have described for notched 2D specimens can be extended rather easily to 3D blocks in which an initial imperfection induces a stress singularity at a known location x^*. Here we do not pursue this extension in detail, but simply indicate how conceptually it can be made.

The reason why the extension is conceptually simple is that Eq. 4.5 still applies. Then the key step is to find the second-moment properties of $[F_{eff}, \ln u_I]$ in 3D. The second-moment properties of F_{eff} were derived in Chapter 2 and the mean and variance of $\ln u_I$ and the covariance between F_{eff} and $\ln u_I$ can be approximated using the same approach as for 2D.

4.4 Ultimate Fracture Strengths

Clearly the normalized ultimate fracture strengths u_U, l_U, and t_U are bounded from below by the corresponding initial fracture strengths. To illustrate the relationship between these two sets of quantities, **Figure 4.2a** shows scatter plots of $\ln X_U$ vs $\ln X_I$ for $X = u, l,$ and t. These simulation results are for a square specimen with side length L, spatial correlation function $\rho(r) = e^{-8r/L}$ (the same correlation function applies to the log-modulus $F(x)$ and log-strength $\ln \varepsilon(x)$), standard deviations $\sigma_F = \sigma_{\ln \varepsilon} = 0.3$, and local correlation coefficient $\rho = -1$. We choose a relatively short correlation distance $r_0 = L/8$ to promote crack arrest and $\rho = -1$ to show an extreme case: when $\rho = -1$ and $\sigma_{\ln \varepsilon_r} = \sigma_F$, the local log-strength and local log-modulus have opposite effects on local crack propagation, creating conditions furthest removed from the deterministic strength cases considered in Chapter 3. If one ignores the left censoring at $\ln X_I$, the mean value of

$\ln X_U$ varies approximately linearly with $\ln X_I$ and the scatter around the mean value may be considered constant. These features were also observed for deterministic strength and hold over a wide range of specimen size and random model parameters. However, in the case with random strength the scatter around the mean is more symmetrical and a normal regression model suffices (this is a simplification over the non-symmetrical Levy regression model used in Chapter 3). Including left-censoring and using the above observations, the final model for $\ln X_U$ is

$$\ln X_U \sim \max\{\ln X_I, \mathcal{N}(c_0 + c_1 \ln X_I, \sigma)\}. \tag{4.13}$$

where $\mathcal{N}(m, \sigma)$ is a normal random variable with mean value m and standard deviation σ. The parameters (c_0, c_1, σ) vary with the size of the specimen, the characteristics of the random modulus and strength fields, and the strength parameter considered (u, l, or t). An analysis of these dependences is made in Section 4.6.

Given a set of simulated (X_{I_i}, X_{U_i})-pairs, the parameters c_0, c_1, and σ are found by maximizing the likelihood

$$l(c_0, c_1, \sigma) \propto \prod_{X_{I_i}=X_{U_i}} F_{c_0+c_1 \ln X_{I_i},\sigma}(\ln X_{I_i}) \prod_{X_{I_i}<X_{U_i}} f_{c_0+c_1 \ln X_{I_i},\sigma}(\ln X_{U_i}), \tag{4.14}$$

where F and f are the normal cumulative distribution and density function, respectively, with parameters listed in the subscript. From the regression model in Eq. 4.13, the marginal probability density function of $\ln X_U$ is obtained as

$$f_{\ln X_U}(x) = \int_{-\infty}^{x} f_{\max\{u,\mathcal{N}(c_0+c_1 \ln X_I,\sigma)\}}(x) f_{\ln X_I}(x)\, du, \tag{4.15}$$

where $f_{\ln X_I}(x)$ is a normal density and $f_{\max\{u,\mathcal{N}(c_0+c_1 \ln X_I,\sigma)\}}(x)$ is a left-censored normal density, with a nonzero probability mass at u.

As an example, the red lines in **Figure 4.2a** give the 10th, 50th, and 90th percentiles of the fitted conditional distribution of $\ln X_U$ given $\ln X_I$, prior to censoring. **Figure 4.2b** shows the model-based probability that crack arrest contributes to the ultimate strength, $P(\ln X_U > \ln X_I)$, for $X = u, l$ and t. This probability is significantly larger than in the case of deterministic strength (dotted lines in **Figure 4.2b**). When only the modulus varies spatially, crack arrest contributes to the ultimate strength only if the fracture encounters a patch sufficiently stiff to overcome the increasing strain concentration. When also the strength is random, crack arrest will contribute to the ultimate strength both if the fracture encounters a sufficiently stiff or strong path and the probability $P(\ln X_U > \ln X_I)$ thus increases.

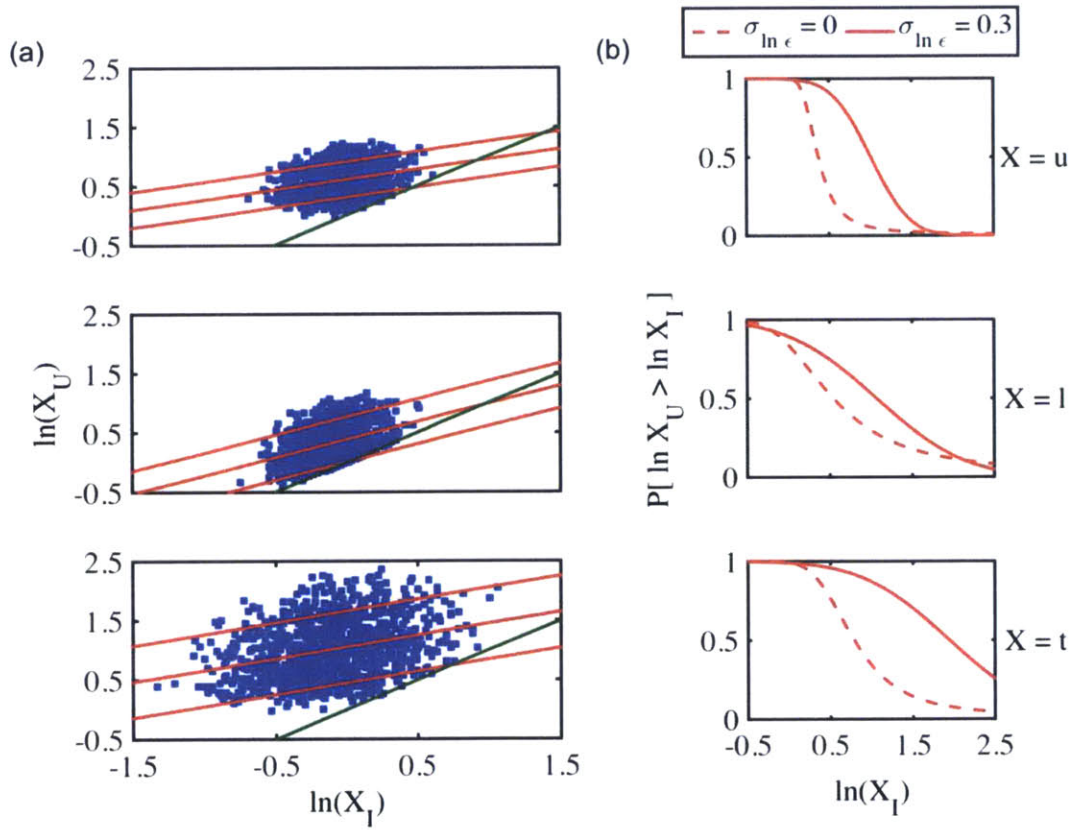

Figure 4.2: Square specimen. **a** Log-log scatterplots of the ultimate strength $\boldsymbol{X_U}$ versus the initial strength $\boldsymbol{X_I}$ for $\boldsymbol{X = u, l}$, and $\boldsymbol{t}$ from 1000 Monte Carlo simulations. The log-modulus $\boldsymbol{F(x)}$ and log-strength $\boldsymbol{\ln \varepsilon_r(x)}$ are normal with simple exponential spatial correlation function with correlation length $\boldsymbol{r_0/L = 0.125}$, standard deviations $\boldsymbol{\sigma_F = \sigma_{\ln \varepsilon_r} = 0.3}$, and correlation $\boldsymbol{\rho = -1}$ between $\boldsymbol{F(x)}$ and $\boldsymbol{\ln \varepsilon_r(x)}$ for any given $\boldsymbol{x}$. The red lines are fitted 10th, 50th, and 90th percentiles prior to censoring. **b** Probability $\boldsymbol{P(\ln X_U > \ln X_I)}$ as a function of $\boldsymbol{\ln X_I}$ based on the fitted models, for deterministic and random strength.

An important feature of **Figure 4.2** is that the slope of the regressions is below 1, indicating that crack-arrest has a compensatory effect on the ultimate strengths: the crack-arrest effect is large when the initial strength is low and essentially nil when the initial strength is high. The first condition occurs when the notch tip region is weak and fracture is likely to propagate through stronger patches of material. The second condition occurs when the notch tip region is strong and after crack initiation the fracture propagates in an unstable way through the specimen. The smaller-than-1 slope reduces the scatter of the ultimate log-strengths relative to the initial log-strengths.

Another important feature of **Figure 4.2** is that the probability $P(\ln X_U > \ln X_I)$ is more sensitive to $\ln X_I$ for the displacement at failure u_U than for the load l_U and toughness t_U. The reason is that the relative fracture resistance at the crack tip, now measured as a combination of the local stiffness and strength, is more correlated with the fracture initiation elongation u_I than with the initial load l_I or toughness t_I. For considerations on how different model parameters affect the regressions, see Section 4.6 and Part B of the Supporting Information.

4.5 Validation of the Analytical Results

The analytical results of Sections 4.3 and 4.4 use various assumptions and approximations. Here we validate them through comparison with Monte Carlo simulation. In the 1D case, following each simulation of the modulus and strength field we solve the problem directly: we compute the effective stiffness E_{eff} as the harmonic average of $E(x)$ along the rod, record the modulus E^* and strength ε_r^* at the notch tip, and obtain the initial elongation at failure u_I and the corresponding load l_I and toughness t_I from Eqs. 4.4 and 4.6. In 2D we use a finite element model to obtain the fracture initiation strengths and a spring network model to propagate the fracture and evaluate the ultimate strengths. The numerical procedure for simulation, material discretization and analysis is identical to that in Chapter 3 and is not repeated here.

To exemplify, **Figure 4.3** shows results for rods and square specimens under the same stochastic parameter setting as in **Figure 4.2**: $\sigma_F = \sigma_{\ln \varepsilon_r} = 0.3$, $\rho = -1$, and $\rho(r) = e^{-8r/L}$. Specifically, **Figures 4.3a** and **4.b** show the empirical (blue, from 10,000 Monte Carlo simulations) and analytical (red) distribution of the initial log-strengths for 1D and 2D specimens, respectively. In both cases the analytical densities match very well the histograms from simulation. Notably, the agreement in the 2D case is better than for deterministic strength (see **Figure 3.5**), as randomness of the strength makes the approximations of the linearized model in Eq. 4.8 less severe. Note that for this specific parameter combination the 1D load l is deterministic.

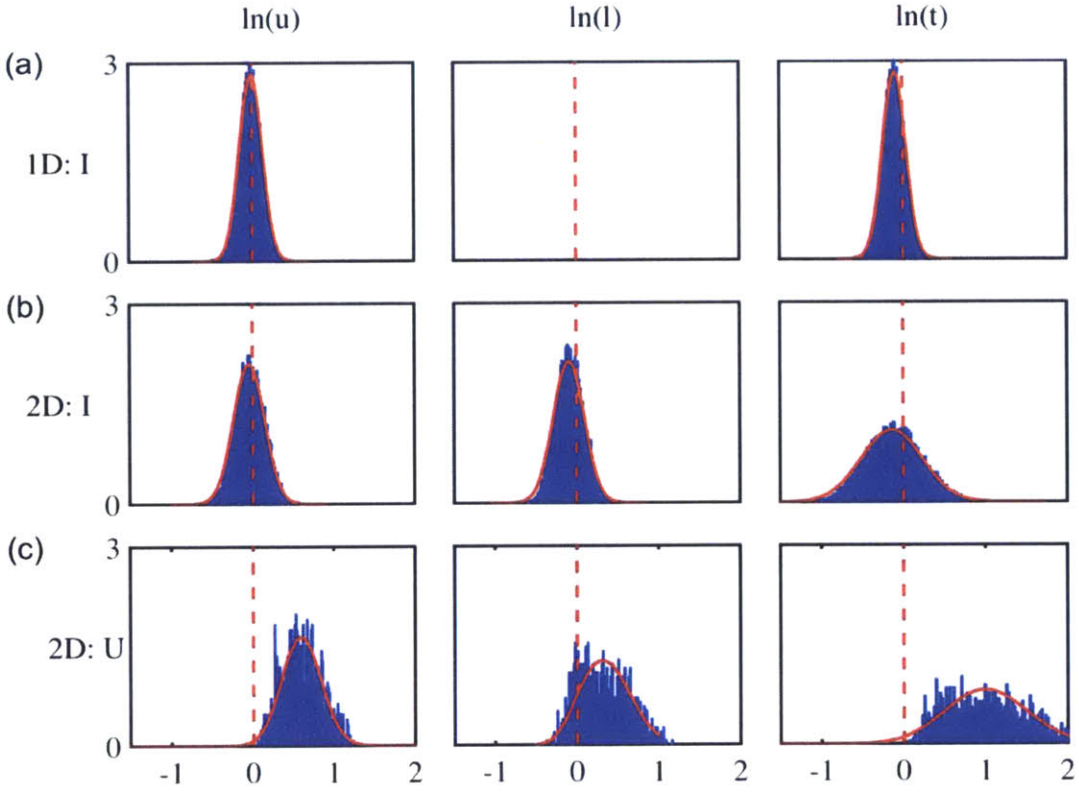

Figure 4.3: Comparison of analytical fracture strength distributions (red) with histograms from Monte Carlo simulations (blue). **a** Initial strengths for a rod, **b** initial strengths for a square plate, and **c** ultimate strengths for a square plate. Simulation of 10,000 samples in cases (**a**,**b**) and 1,000 samples in case **c**. Randomness of $\boldsymbol{F(x)}$ and $\boldsymbol{\ln \varepsilon_r(x)}$ is the same as in **Figure 4.2**.

Figure 4.3c shows similar comparisons for the ultimate strength parameters in the 2D case. Due to the higher computational demand for propagating the fracture through the specimen, the simulation sample size is reduced to 1,000. Again, the analytical

distributions fit very well the empirical results. Validation analyses under different model specifications produce qualitatively similar conclusions.

4.6 Parametric Analysis

Next we use the analytical results of Sections 4.3 and 4.4 to study how the distributions of the strength vectors X_l and X_U ($X = u, l, t$) depend on the Euclidean dimension and size of the specimen and the stochastic model of the modulus and failure strain. Since Chapter 3 already made a sensitivity study for the case of deterministic material strength, here we focus on the role of randomness of the failure strain and its correlation with the elastic modulus.

4.6.1 Initial Strengths

First we analyze in some detail the initial strengths of 1D rods and then comment on the differences in the 2D case. In all cases the spatial correlation function is assumed to be exponential, $\rho(r) = e^{-r/r_0}$, with correlation length parameter r_0.

For rods, **Table 4.1** gives ordinary and log-moments of the initial strengths under the limiting conditions of low-spatial correlation ($r_0/L \ll 1$, $F_{eff} \to -\sigma_F^2$ deterministic) and high spatial correlation ($r_0/L \gg 1$, $F_{eff} \to F^*$ random). The moments follow directly from Eqs. 4.4 and 4.6 and the limiting values of F_{eff} noted above. These limiting cases produce simple expressions and bracket results for intermediate degrees of spatial correlation. The log-mean values $E[\ln X_l]$ are not listed as they are related to the median strengths $X_{l_{0.5}}$ as $E[\ln X_l] = \ln X_{l_{0.5}}$. The symbols next to the expressions indicate the relative importance of variability in the modulus and the failure strain: $=$ indicates symmetrical effects of the two log-variances, E indicates higher sensitivity to the log-modulus variance, ε_r indicates higher sensitivity to the variance of the log-failure strain, and O denotes equal effects with opposite signs. As it is clear from Eq. 4.6, for the initial

load l_I the two effects are always symmetrical. For the other two strength measures, variability of the failure strain becomes more dominant as the spatial correlation r_0/L increases (compare right and left columns in **Table 4.1**). Below we sequentially discuss the behavior of the mean and median values, log-variances, and log-correlations of the initial strengths.

Mean and Median Values

An important question is whether, on average, the strengths and log-strengths of heterogeneous rods are above or below their homogeneous values. This corresponds to the mean and median of the dimensionless strengths X_I being above or below 1. Interestingly, the mean values tend to exceed 1 and the medians tend to be below 1. Therefore, whether randomness is on average beneficial or detrimental depends to a large extent on whether one considers the bulk strengths or their logs. Other notable features are:

- The median strengths do not depend on the correlation ρ between the log-failure strain and the log-modulus and all decrease as randomness of the failure strain increases. Therefore, as judged through the median strengths, randomness of the failure strain has a deleterious effect. Increasing the spatial correlation r_0/L does not affect the load l_I, but reduces the median values of the other two strengths;
- The behavior of the mean values is more complex: the mean strengths increase with $\sigma_{\ln \varepsilon_r}$ when $\rho > 0$ (except for $E[u_I]$ when $r_0/L \gg 1$) and decrease when $\rho < 0$ (except for $E[t_I]$, which has a minimum for some non-zero $\sigma_{\ln \varepsilon_r}$). Hence, in general, both the sign and magnitude of the correlation coefficient ρ matter for the mean strengths.

Table 4.1: Values of the first and second moments of the initial logged strengths $\ln X_I$ and initial unlogged strengths X_I under the limiting conditions of low spatial correlation $r_0/L \ll 1$ (the log-modulus and log-strength are ergodic and the log-effective stiffness F_{eff} is deterministic, $F_{eff} = -\sigma_F^2$) and high spatial correlation $r_0/L \gg 1$ (the log-modulus and log-strength are spatially uniform and $F_{eff} = F^*$).

$a = \sigma_{\ln \varepsilon_r}$ $b = \sigma_F$ $c = \sigma_F/\sigma_{\ln \varepsilon_r}$ $\rho = corr[\ln \varepsilon_r, F]$					
		$r_0/L \ll 1$		$r_0/L \gg 1$	
mean	u_I	$e^{b^2+\rho ab}$	E	1	n/a
	l_I	$e^{\rho ab}$	=	$e^{\rho ab}$	=
	t_I	$e^{a^2+2b^2+4\rho ab}$	E	$e^{a^2+2\rho ab}$	ε_r
median	u_I	$e^{-0.5a^2+0.5b^2}$	0	$e^{-0.5a^2}$	ε_r
	l_I	$e^{-0.5a^2-0.5b^2}$	=	$e^{-0.5a^2-0.5b^2}$	=
	t_I	e^{-a^2}	ε_r	$e^{-a^2-0.5b^2}$	ε_r
var	$\ln u_I$	$a^2 + b^2 + 2\rho ab$	=	a^2	ε_r
	$\ln l_I$	$a^2 + b^2 + 2\rho ab$	=	$a^2 + b^2 + 2\rho ab$	=
	$\ln t_I$	$4(a^2 + b^2 + 2\rho ab)$	=	$4a^2 + b^2 + 4\rho ab$	ε_r
corr	$\ln u_I, \ln l_I$	1	n/a	$\frac{1+\rho c}{\sqrt{1+c^2+2\rho c}}$	ε_r
	$\ln u_I, \ln t_I$	1	n/a	$\frac{2+\rho c}{\sqrt{4+c^2+4\rho c}}$	ε_r
	$\ln l_I, \ln t_I$	1	n/a	$\frac{2+c^2+3\rho c}{\sqrt{(1+c^2+2\rho c)(4+c^2+4\rho c)}}$	ε_r
	$\ln u_I, F_{eff}$	n/a		ρ	n/a
	$\ln l_I, F_{eff}$	n/a		$\frac{\rho+c}{\sqrt{1+c^2+2\rho c}}$	E
	$\ln t_I, F_{eff}$	n/a		$\frac{2\rho+c}{\sqrt{4+c^2+4\rho c}}$	ε_r

For 2D plates one cannot obtain simple analytical results. Numerical analysis shows that the dependence of the mean and median strengths on $\sigma_{\ln \varepsilon_r}$ and ρ is qualitatively similar to the 1D case. However, the quantitative effects are generally smaller. In particular, the increases of $E[X_1]$ with $\sigma_{\ln \varepsilon_r}$ for positive ρ are more modest than in 1D. For example, in the ergodic limit when $\rho = 1$ and $\sigma_F = \sigma_{\ln \varepsilon_r} = 0.5$ the value of $E[t_1]$ in 2D square specimens increases by a factor of ~2 as opposed to ~5 in 1D rods (~40% of strengthening effect in 1D is preserved in 2D). The values of $E[u_1]$ and $E[l_1]$ are $20 - 40\%$ lower in 2D. In the high-correlation limit the discrepancies between the one- and two-dimensional values are smaller.

Log-variances

A second feature of significance is the variance of the log-strengths and the contributions to it from the modulus, the critical strain, and their correlation ρ. Besides being important in their own right, the log-variances are responsible for the difference between the mean and median strengths noted above.

In the limit of very low spatial correlation, the effective stiffness becomes deterministic, the strengths depend exclusively on the elongation at fracture initiation, and $var[\ln u_1] = var[\ln l_1] = \frac{1}{4} var[\ln t_1]$. If the modulus and failure strain are positively correlated ($\rho > 0$), randomness of the failure strain increases the variance of all the log-strengths, whereas when $\rho < 0$ the log-strength variances increase or decrease depending on ρ and the ratio $\sigma_F/\sigma_{\ln \varepsilon_r}$.

Similar considerations apply under high spatial correlation, but the failure strain becomes the more dominant contributor to the log-variances of the initial strengths (except for the initial load, which does not depend on r_0/L).

The log-strength variances of 2D specimens exhibit a qualitatively similar dependence on ρ and $\sigma_F/\sigma_{\ln \varepsilon_r}$, but their values are lower than for 1D rods. For example, under very low spatial correlation with $\rho = 1$ and $\sigma_F = \sigma_{\ln \varepsilon_r} = 0.5$, the variances $var[\ln u_1]$, $var[\ln l_1]$,

and $var[\ln t_I]$ are respectively 1, 1, and 4 in 1D versus 0.75, 0.75, and 1.5 in 2D. In the very high correlation limit these variances become 0.25, 1, and 2.25 in 1D and 0.5, 0.7 and 1.2 in 2D. The variances of the three log-strengths are more similar for plates than for rods.

Log-correlations

Finally, we look at the correlation between initial log-strength pairs and between the log-strengths and the log-effective modulus F_{eff}. While Table 4.1 and the discussion below apply to 1D rods, results for 2D plates are similar.

As noted already, in the limit of no spatial correlation the effective stiffness is deterministic and $\ln u_I$ is the only source of variability for all the strengths. This is why all the log-initial strengths are perfectly correlated.

For high spatial correlation, the log-strength correlations exhibit a complex dependence on ρ and $c = \sigma_F/\sigma_{\ln \varepsilon_r}$. As **Figure 4.4a** shows, ρ is a lower bound to all the log-strength correlations. Therefore, when $\rho = 1$ all the log-strengths are perfectly correlated. When $\rho < 1$, the correlations between $\ln u_I$ and the other two initial log-strengths increase from ρ to 1 as the standard deviation ratio c decreases from ∞ (no material strength variability) to 0 (no elastic modulus variability). This behavior can be understood by considering that for high spatial correlation the initial elongation u_I depends only on the material strength while l_I and t_I depend also on the log-modulus. In order for these correlations to be significantly below 1, it must be that $\frac{r_0}{L} > 1, \sigma_F \gg \sigma_{\ln \varepsilon_r}$, and $\rho \ll 1$. For the load l_I and toughness t_I, notice that under either $c = 0$ and $c = \infty$ their uncertainty comes exclusively from the modulus or exclusively from the material strength; hence under these extreme scenarios their correlation is 1. As it is clear from Eq. 4.5, the correlation is minimum for $\sigma_F = \sigma_{\ln \varepsilon_r}$ $(c = 1)$.

Figure 4.4b shows the correlations between the log-strengths $\ln X_I$ and the log-effective modulus F_{eff} in the high spatial correlation limit (for very low-spatial correlation, F_{eff} is

deterministic). Since F is spatially constant, $corr[\ln u_l, F_{eff}] = corr[\ln u_l, F^*] = corr[\ln \varepsilon_r^*, F^*] = \rho$ for all c. The correlation of F_{eff} with either $\ln l_l$ or $\ln t_l$ approaches 1 as $c \to \infty$ and ρ as $c \to 0$. Therefore, the correlations of $\ln X_l$ with F_{eff} are significantly below 1 only if $\rho < 1$. For $\ln l_l$ and $\ln t_l$, an additional condition for low correlation is that $\sigma_F \ll \sigma_{\ln \varepsilon_r}$.

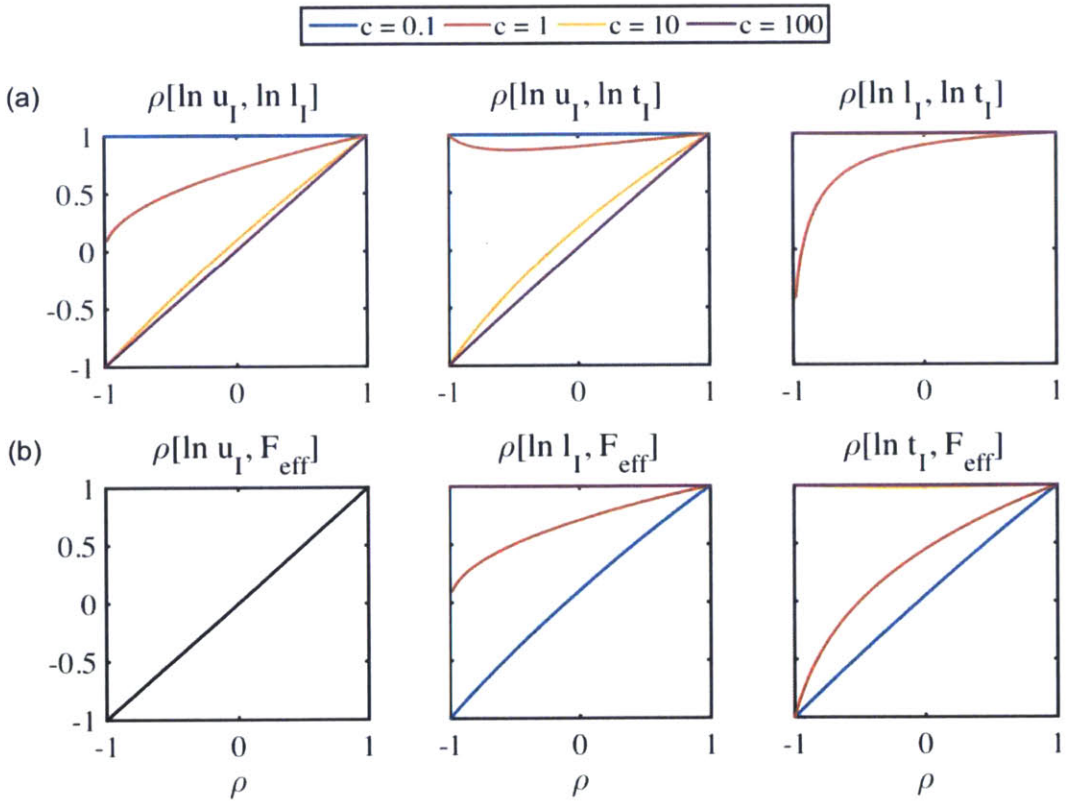

Figure 4.4: Correlation coefficients of the log-strengths and log-effective modulus in 1D rods with high spatial correlation of the modulus and failure strain ($\boldsymbol{r_0/L \gg 1}$). Correlation between **a** log-strength pairs and **b** log-strength and the log-effective modulus for different $\boldsymbol{\rho}$ and select values of $\boldsymbol{c = \sigma_F/\sigma_{\ln \varepsilon_r}}$.

4.6.2 Ultimate Strengths of 2D Specimens

A key feature of heterogeneous 2D specimens is the increase in strength from crack initiation to complete specimen severance as a result of crack arrest. As shown in **Figure 4.2**, the relationship between the initial and ultimate strengths can be quantified through censored linear regressions of the type $\ln X_U = \max\{\ln X_l, c_0 + c_1 \ln X_l + \delta\}$, where c_0

and c_1 are constants and δ is a normal random variable with zero mean and some standard deviation σ. **Figure 4.5** shows the regression parameters (c_0, c_1, σ) estimated from simulation experiments for the elongation at failure ($X = u$). Results for the other two strength measures (load l and toughness t) are given in the Supporting Information, Part B. The parameters in **Figure 4.5** are for $\sigma_F = 0.3$ and all combinations of $r_0/L = \{0.125, 0.25, 1\}$, $\sigma_{\ln \varepsilon_r} = \{0, 0.3, 0.7\}$, and $\rho = \{-1, 0, 1\}$. The case $\sigma_{\ln \varepsilon_r} = 0$ (top row), which corresponds to deterministic fracture strain, was already considered in Chapter 3. Our main interest here is the sensitivity of the parameters to $\sigma_{\ln \varepsilon_r}$ and ρ.

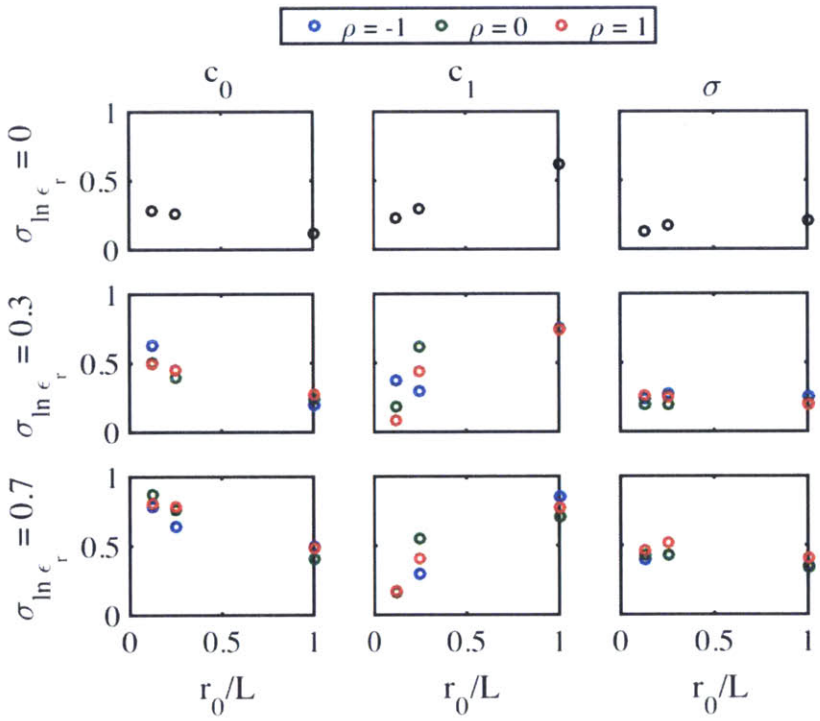

Figure 4.5: Parameters of the regression model in Eq. 4.13 for the elongation $\boldsymbol{X = u}$ of a square specimen. $\boldsymbol{F(x)}$ and $\boldsymbol{\ln \varepsilon_r(x)}$ have exponential spatial correlation function with correlation length $\boldsymbol{r_0/L} = \{\mathbf{0.125, 0.25, 1}\}$, standard deviations $\boldsymbol{\sigma_F = 0.3}$ and $\boldsymbol{\sigma_{\ln \varepsilon_r}} = \{\mathbf{0, 0.3, 0.7}\}$ and correlation $\boldsymbol{\rho} = \{\mathbf{-1, 0, 1}\}$. In each case, the parameters are fitted to 100 Monte Carlo simulations.

To interpret **Figure 4.5**, it is useful to note the effects of varying the parameters c_0, c_1 and σ one-at-a-time:

- Increasing c_0 increases the average crack-arrest effect X_U / X_I (this and other comments that follow technically apply to the log-strengths);
- Increasing c_1 makes the crack-arrest effect less dependent on the initial strength X_I. For example, when $c_1 = 0$ the ultimate strength X_U is independent of X_I (except for the constraint $X_U \geq X_I$), meaning that the initial strength X_I and crack arrest effect X_U / X_I compensate each other in determining X_U. At the other extreme, for $c_1 = 1$ the crack-arrest effect X_U / X_I is independent of X_I;
- Increasing σ increases the dispersion of X_U / X_I.

Figure 4.5 shows that, for the elongation u:

1. The dispersion σ increases with $\sigma_{\ln \varepsilon_r}$, especially when $\sigma_{\ln \varepsilon_r} > \sigma_F$. This is true for all ρ. The increase is most pronounced when the spatial correlation r_0/L is low, as this condition produces high strength gradients along the fracture path and therefore significant crack-arrest effects;
2. The slope c_1 exhibits no clear dependence on ρ and some positive association with $\sigma_{\ln \varepsilon_r}$. For large $\sigma_{\ln \varepsilon_r}$, c_1 is quite sensitive to the spatial correlation. Specifically, for low r_0/L the ultimate displacement u_U and u_I are nearly independent, whereas for large r_0/L the crack-arrest effect u_U / u_I is nearly independent of u_I.
3. The regression parameter that is most affected by randomness of the failure strain is the intercept c_0, which controls the average crack-arrest effect. Like for σ, dependence of c_0 on $\sigma_{\ln \varepsilon_r}$ is strongest for low spatial correlation (small r_0/L). The correlation between the log-modulus and log-failure strain, ρ, has a secondary effect on c_0.

In the Supporting Information we show the regression parameters of the strengths $X = l$, and t obtained by fitting the model in Eq. 13 to the same 100 Monte Carlo simulations used for $X = u$ in **Figure 4.5**. Qualitatively the regression parameters for $X = l$, and t exhibit the same dependencies on $\sigma_{\ln \varepsilon_r}$ and ρ as for $X = u$. As for deterministic strength,

the regression intercept c_0 is significantly smaller for $X = l$ than for $X = u$ and $X = t$, indicating that also when the material strength is random, crack arrest has more significant strengthening effects on the displacement and toughness than on the failure load. Moreover, the regression slope c_1 is larger for $X = l$ than for $X = u$ and $X = t$, indicating a stronger negative correlation between $\ln(X_U/X_I)$ and $\ln X_I$ for u and t than for l.

Low spatial correlation of the material properties has interesting strength implications. It produces ultimate strengths X_U that are nearly independent of the strength at fracture initiation X_I (see low values of c_1). Also notice that, when the spatial correlation is low and $\sigma_{\ln \varepsilon_r}$ is increased, the increase of the crack-arrest dispersion σ is more than compensated for by a large increase of the intercept c_0. The net effect is an apparent healing induced by crack arrest, whereby ultimate failure is a less brittle and more predictable failure mode than fracture initiation.

To better appreciate the effect of random failure strain on the ultimate strengths, **Figure 4.6** compares the distributions of the normalized initial and ultimate log-elongation for $r_0/L = 0.125$, $\sigma_F = 0.3$, $\rho = \{-1, 0, 1\}$, and $\sigma_{\ln \varepsilon_r} = \{0, 0.3, 0.7\}$ in square specimens. The ultimate log-elongation is almost always above the homogeneous value and the mean value of $\ln u_U$ increases with increasing $\sigma_{\ln \varepsilon_r}$. Notice that the correlation ρ has more influence on the dispersion at initial than ultimate failure and that the log-dispersion at ultimate failure is typically smaller than at fracture initiation (except for $\rho = -1$, $\sigma_{\ln \varepsilon_r} = 0.3$). In general, **Figure 4.6** confirms that crack arrest is a significant strengthening mechanism for $\ln u_U$ and that the ultimate elongation is more predictable than the elongation at fracture initiation. In Part C of the Supporting Information we make similar comparisons for $X = l$ and $X = t$. Those distributions exhibit similar qualitative characteristics as for $X = u$. As for the case of deterministic strength, crack arrest has a more pronounced strengthening effect on fracture elongation u and fracture toughness t than on the fracture load l.

The results presented here are for square specimens. In rectangular specimens the crack-arrest effect depends on the aspect ratio L_1/L_2 and displays continuous variation between the (zero) effect for rods and the effects noted above for square specimens.

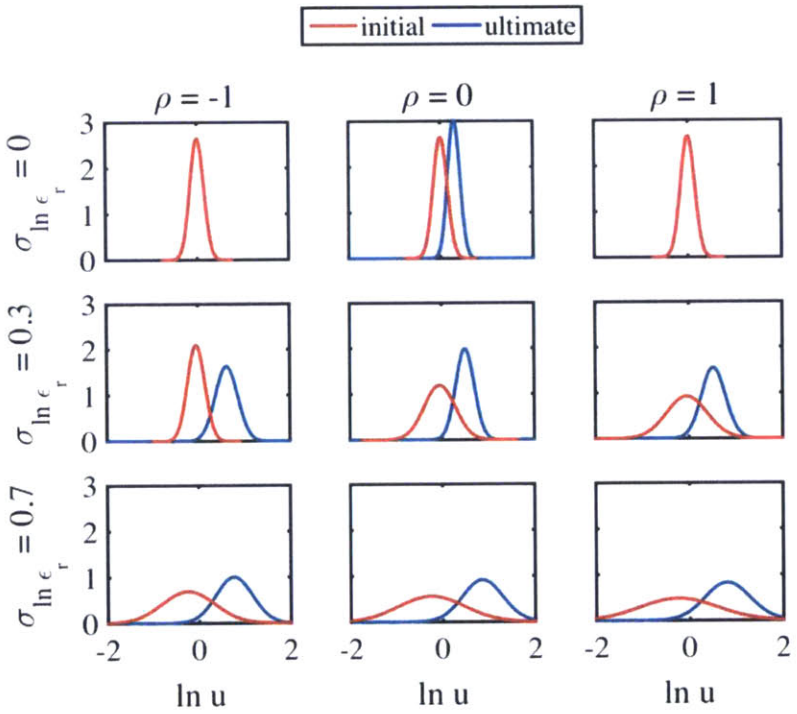

Figure 4.6: Marginal distributions of the normalized initial and ultimate log elongation $\ln u$ for $r_0/L = 0.125$, $\sigma_F = 0.3$, $\rho = \{-1, 0, 1\}$, and $\sigma_{\ln \varepsilon_r} = \{0, 0.3, 0.7\}$.

4.7 Conclusions

Here we have extended the probabilistic analysis of fracture strength to include the effect of random fracture strain. Specifically, we have analyzed the distribution of the elongation, load and toughness at fracture initiation and ultimate failure for notched 1D rods and 2D plates when Young's modulus E (stiffness) and the local fracture strain ε_r (material strength) vary as isotropic lognormal fields. Since Chapter 3 considered the case of random Young's modulus, emphasis here is on the role of randomness of the material strength (measured by the log-variance $\sigma^2_{\ln \varepsilon_r}$ and the standard deviation ratio

$c = \sigma_{\ln E}/\sigma_{\ln \varepsilon_r}$) and the dependence between stiffness and material strength (measured by $\rho = corr[\ln \varepsilon_r, \ln E]$). The approach is analytical or semi-analytical. This has distinct advantages over purely numerical simulation, which is not suitable for sensitivity analysis, reliability analysis or material design.

The main conclusions on the normalized fracture strengths (the fracture strengths divided by their values when the modulus and failure strain are spatially homogeneous and equal to their respective mean values) are as follows:

1. The median normalized strengths at fracture initiation are generally smaller than 1, decrease with increasing $\sigma^2_{\ln \varepsilon_r}$, and are not affected by ρ. By contrast, the mean values are generally above 1. Therefore, whether on average a specimen is weakened or strengthened by failure strain heterogeneity largely depends on whether one reasons in arithmetic or log scale. The mean values depend on both $\sigma^2_{\ln \varepsilon_r}$ and ρ. When $\rho > 1$, heterogeneity of the material strength tends to increase the mean values at fracture initiation. The opposite is true when $\rho < 0$;
2. Like the mean values, the log-variances of the initial strengths vary with $\sigma_{\ln \varepsilon_r}$, ρ, and the specific initial strength considered (u_I, l_I, or t_I). Similar trends apply to 2D plates, but the log-variances are smaller than for 1D specimens.
3. The correlation coefficients between log-strength pairs and between the log-strengths and the log-effective modulus are generally close to 1. These correlation coefficients can be significantly below 1 only when $\rho \ll 1$. Additional conditions for low correlation depend on the pair of variables considered; see for example Section 4.6.1 for 1D rods.
4. In 2D specimens, increasing the randomness of the material strength makes crack-arrest events more frequent and increases the ratio X_U / X_I between ultimate and initial strengths.
5. When the modulus and material strength have low spatial correlation, randomness of the material strength can significantly increase the effect of crack arrest, causing ultimate failure to be a more predictable and less brittle failure mode than fracture initiation.

Based on these results, one can suggest guidelines for material design that depend on the specific design objectives. For example, if there is concern with the reliability and median value of the initial strengths, the heterogeneity in strength should be minimized and, when it cannot be avoided, should be negatively correlated with the local modulus. On the other hand, if the ultimate strengths are the main concern, randomness of the strength is beneficial and the correlation ρ with the local modulus is less important. Moreover, high spatial correlation of the local strength and modulus is deleterious to the ultimate strengths, whereas low spatial correlation can be used to promote crack arrest.

In bone, the local heterogeneity due to the variable degree of mineralization is widely recognized as being a key contributor to its remarkable fracture mechanical properties. Notably, the degree of mineralization is highly correlated with both local strength and stiffness and varies spatially over very short length scales (on the order of nano- and micrometers). These characteristics of the bone microstructure are consistent with what we have highlighted as favorable design specifications for the ultimate strengths.

An important future extension is to consider materials with non-lognormal heterogeneity, in particular materials composed of a matrix and single or multi-phase inclusions. Materials in this broad class differ by the geometry of the inclusions (laminae, filaments, etc.), the mechanical properties of the matrix and the inclusions, and the possible presence of interface weaknesses. We are currently expanding our theoretical analysis to materials with some of these characteristics.

Supporting Information

Part A: Derivation of Covariance in Eq. 4.12

To obtain the covariance in Eq. 4.12, we use the linearized model in Eq. 9 to obtain

$$cov[\ln E_{eff}, \ln u_l] \approx cov\left[\overline{F}, \sum_i b_i \left(F_i - \overline{F}\right)\right] + cov[\overline{F}, \ln \varepsilon_r^*] \tag{4.A1}$$

The first term in Eq. 4.A1 is

$$cov\left[\overline{F}, \sum_i b_i \left(F_i - \overline{F}\right)\right] = \sum_i b_i \, cov[\overline{F}, F_i] - \left(\sum_i b_i\right)\sigma_{\overline{F}}^2. \tag{4.A2}$$

The covariance $cov[\overline{F}, F_i]$ on the right hand side of Eq. 4.A2 is given by $\frac{\sigma_F^2}{n} E[\rho(R_i)]$, where $\rho(r)$ is the spatial correlation function of F and R_i is the random distance of the i^{th} discretization point from a point uniformly distributed inside the specimen. Since the coefficient b_i is significantly nonzero only for points close to the notch tip x^*, one may simplify the calculations by replacing $E[\rho(R_i)]$ with $E[\rho(R^*)]$, where R^* is the random distance of a uniformly distributed point from the notch tip. The variance $\sigma_{\overline{F}}^2$ in Eq. 4.A2 is given by $\sigma_{\overline{F}}^2 E[\rho(R_{12})]$, where R_{12} is the random distance between two points uniformly and independently distributed inside the specimen.

The term $cov[\overline{F}, \ln(\varepsilon_r^*)]$ in Eq. 4.A1 is given by

$$cov[\overline{F}, \ln \varepsilon_r^*] = b cov[F^*, \overline{F}] = b\sigma_{\overline{F}}^2 E[\rho(R^*)]. \tag{4.A3}$$

Substitution into Eq. 4.A1 gives the expression in Eq. 4.12.

Part B: Crack-Arrest Effects in 2D Plates

In the paper, we found that each log-ultimate strength $\ln X_U$ can be related to the corresponding log-initial strength $\ln X_I$ through a censored linear regression model with normal residuals; see Eq. 4.13. **Figure 4.2** gives example regressions and **Figure 4.5** shows how for a square specimen the regression parameters for the failure elongation $X = u$ vary with selected parameters of the stochastic model (the log-strength standard deviation $\sigma_{\ln \varepsilon_r}$, the correlation ρ between the log-modulus and log-material strength, and the spatial correlation distance r_0/L).

Figures B1 and **B2** show similar regression parameter plots for the other two measures of fracture strength, the load at failure $X = l$ and the fracture toughness $X = t$. The parameters are obtained by fitting the regression in Eq. 13 to the same 100 Monte Carlo simulations that were used for the elongation $X = u$. Qualitatively the regression parameters for $X = l$ and t exhibit the same dependencies on $\sigma_{\ln \varepsilon_r}$ and ρ as for $X = u$. Notably, as was the case for deterministic strength, the regression intercept c_0 is significantly smaller for $X = l$ than for $X = u$ and $X = t$, indicating that also for random strength crack arrest has less of a strengthening effect on the failure load than it does on elongation and toughness. Moreover, the regression slope c_1 is larger for $X = l$ than for $X = u$ and $X = t$. This indicates that for the latter strengths there is a stronger negative correlation between the crack-arrest effect $\ln(X_U/X_I)$ and the initial strength $\ln X_I$.

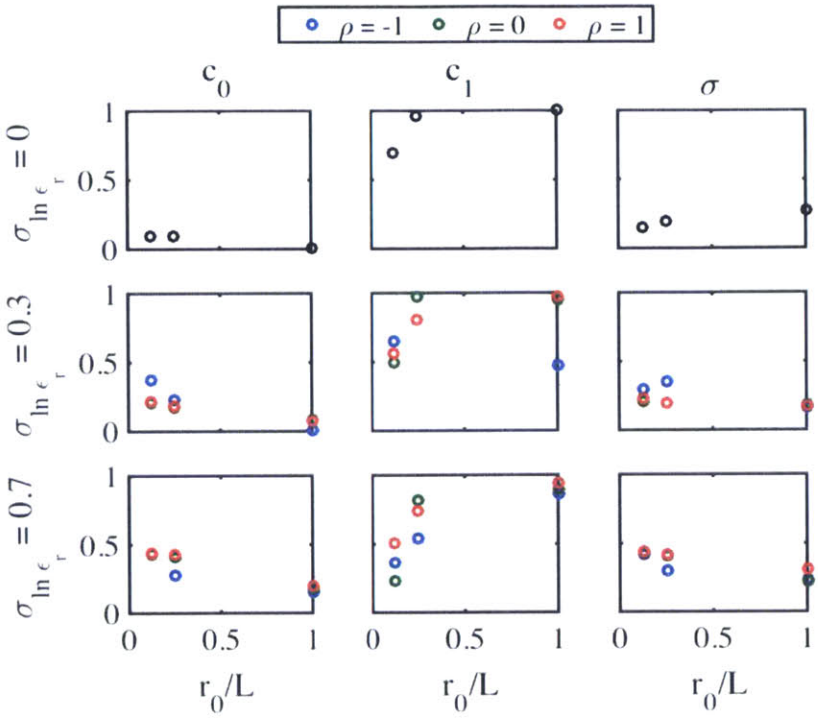

Figure B1: Parameters of the regression model in Eq. 4.13 for the load $X = l$ of a square specimen. The stochastic model of $F(x)$ and $\ln \varepsilon_r(x)$ is the same as in **Figure 4.5**. In each case, the parameters are fitted to 100 Monte Carlo simulations.

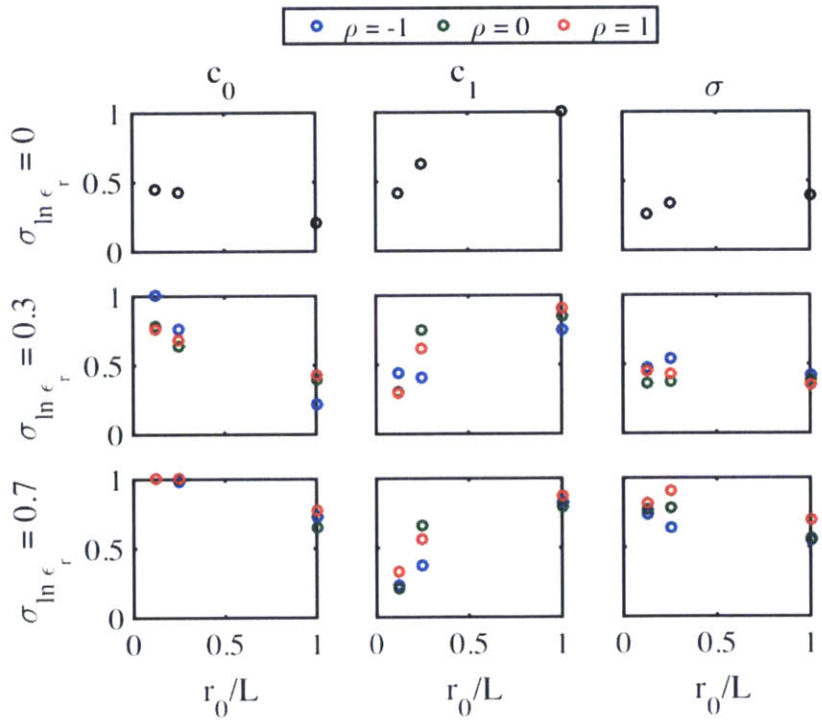

Figure B2: Same as **Figure B1** for the toughness $X = t$.

Part C: Initial and Ultimate Strength Distributions

Figures C1 and **C2** compare marginal distributions of the normalized initial and ultimate log-load and log-toughness for $r_0/L = 0.125$, $\sigma_F = 0.3$, $\rho = \{-1, 0, 1\}$, and $\sigma_{\ln \varepsilon_r} = \{0, 0.3, 0.7\}$ in a square specimen. These distributions exhibit similar qualitative characteristics as for the fracture elongation $X = u$ in **Figure 4.6**. As in the case of deterministic strength Chapter 3, crack arrest has a more pronounced strengthening effect for the elongation u and toughness t than for the load l. Also note that, like for $X = u$, the log-distributions at ultimate failure are less dispersed than the log-distributions at initial failure.

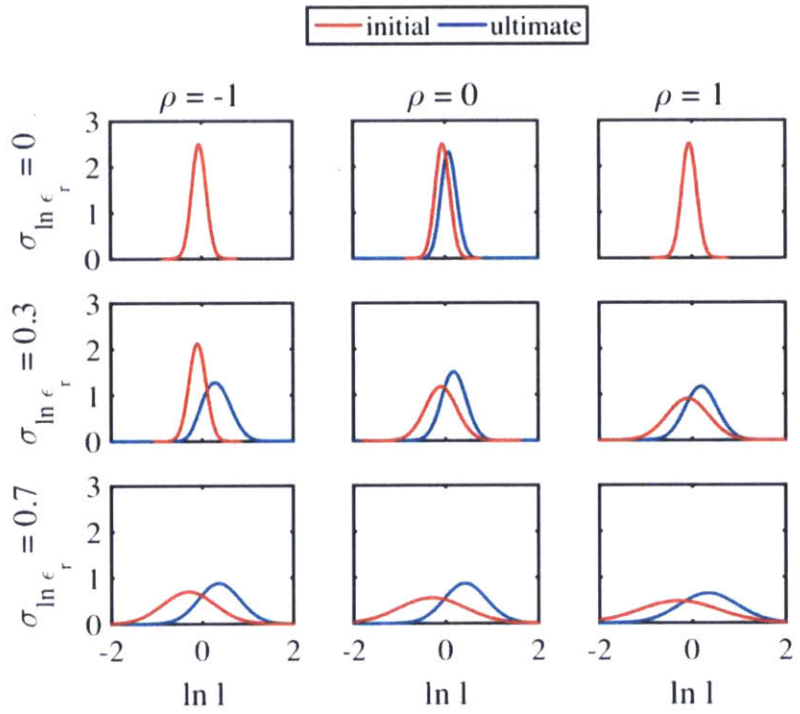

Figure C1: Distributions of the normalized initial and ultimate log-failure load $\ln l$ for $r_0/L = 0.125$, $\sigma_F = 0.3$, $\rho = \{-1, 0, 1\}$, and $\sigma_{\ln \varepsilon_r} = \{0, 0.3, 0.7\}$.

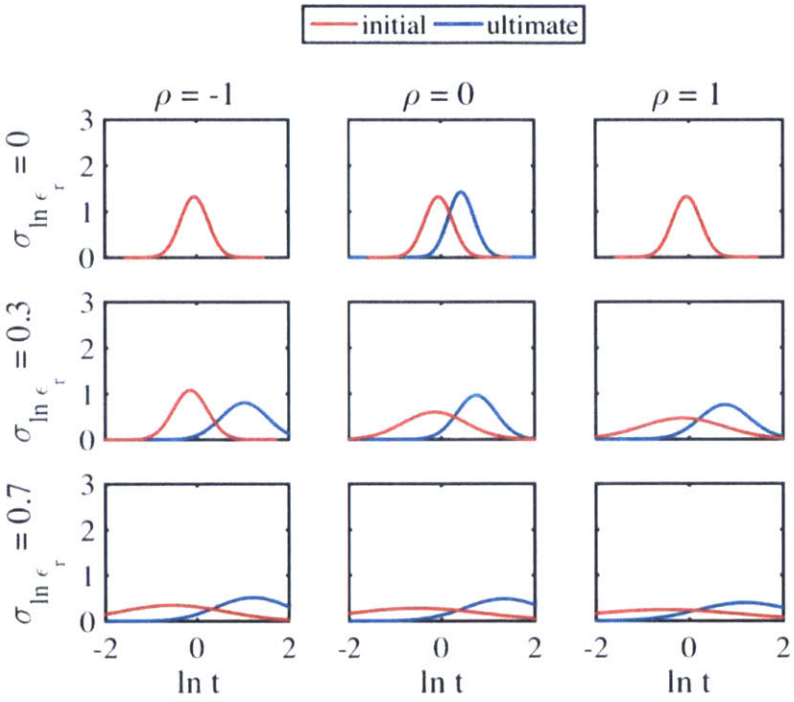

Figure C2: Same as **Figure C1** for the toughness $X = t$.

Chapter 5: The Effective Stiffness of Random Checkerboard Plates

The research and review presented in this chapter will be published in:

- L. S. Dimas, D. Veneziano, M.J. Buehler, *The Effective Stiffness of Random Checkerboard Plates*, In submission, 2015.

We investigate the elastic bulk stiffness E_{eff} of two-dimensional checkerboard specimens in which square tiles are randomly assigned to one of two component phases. This is a model system for a wide class of multi-phase polycrystalline materials such as granitic rocks and many ceramics. We study how the bulk stiffness is affected by different characteristics of the specimen (size relative to the tiles, stiff fraction, modulus contrast between the phases) and obtain analytical approximations to the probability distribution of E_{eff} as a function of these parameters. In particular we examine the role of percolation of the soft and stiff phases, a phenomenon that is important in polycrystalline materials and composites with inclusions. In small specimens, we find that the onset of percolation causes significant discontinuities in the effective modulus, whereas in large specimens the influence of percolation is smaller and gradual. The analysis is an extension of the elastic homogenization methodology presented in Chapter 2 which was devised for blocks with lognormal spatial variation of the modulus. Results are validated through Monte Carlo simulation. Compared with lognormal specimens with comparable first two moments, checkerboard plates have more variable effective modulus and are on average less compliant if there is prevalence of stiff tiles and more compliant if there is prevalence of soft tiles. These differences are linked to percolation.

5.1 Introduction

In Chapter 2 we considered the stochastic homogenization of n-dimensional rectangular blocks ($n = 1, 2,$ or 3) in which Young's modulus $E(x)$ varies spatially as an isotropic

lognormal random field. We expressed the log-modulus field $F(x) = \ln E(x)$ as the sum of the spatial average, marginal fluctuations along the coordinate axes ("main effects"), and interactions of order $2, \ldots, n$ ("ANOVA decomposition"). Then we obtained, exactly or in approximation, the random effects of the individual ANOVA terms and multiplicatively combined the component effects to approximate the joint distribution of the bulk elastic tensor of the block. A defining feature of this approach is that the contributions from the various ANOVA terms are analytically quantified. This feature is important when making sensitivity and reliability analyses and when designing or optimizing heterogeneous materials.

While some heterogeneous materials at certain length scales, like bone, nacre and concrete, display continuous spatial variation of their mechanical properties and may be represented through a lognormal model [106-109], other important classes of composites (like materials with inclusions or granular assemblies) have multimodal modulus distribution [4, 25, 110]. For example, random stiff inclusions are often used in reinforced polymers and multi-phase Voronoi tessellations have been used to represent collagen [111], granitic rocks [112], and other polycrystalline materials [113, 114]. It would be of interest to extend the homogenization approach of Chapter 2 to these classes of discrete heterogeneous materials.

A novel phenomenon in the homogenization of multi-phase materials relative to the lognormal case is percolation: when the softer phases percolate transversally to the direction of stretching, the body is very compliant, whereas longitudinal percolation of the stiffer phases causes an increase of the bulk modulus.

Here we study the elastic homogenization of what is arguably the simplest multi-phase granular material: a two-dimensional specimen partitioned into square tiles where a soft or stiff phase with known elastic modulus is randomly assigned to each tile. We call these "checkerboard materials", as depicted in **Figure 5.1**. While they are seldom found in nature, checkerboard materials allow one to investigate the role of percolation in a simple setting and constitute a model system for more complicated granular structures. Their

modulus distribution is binary and very different from a lognormal distribution. Therefore, checkerboard materials are a convenient test bed to gauge the generality of the ANOVA decomposition approach and make inroads into the complexities of multi-phase systems.

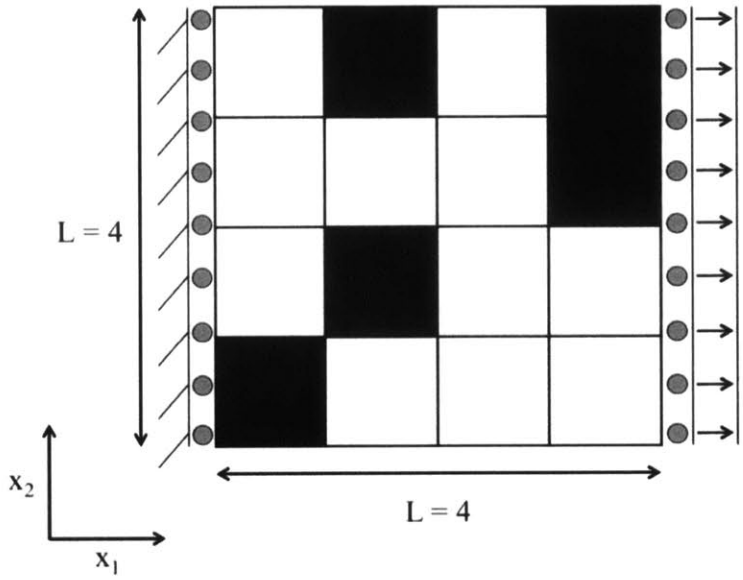

Figure 5.1: Illustration of checkerboard systems and boundary conditions. This is a model system for several polycrystalline systems such as granitic rocks and ceramic materials.

Checkerboard materials have received considerable interest in the heat and electron transport literature [115-119] and in percolation [119-122]. By contrast, we are not aware of any previous studies on elastic homogenization.

In extending the ANOVA decomposition technique to checkerboard materials, we address two related sets of questions:

1. How does the bulk modulus in tension depend on the various ANOVA components? What are the roles of percolation of the soft and stiff phases, the size of the specimen relative to the tiles, and the stiffness contrast between the phases? This line of inquiry into the factors that affect the bulk stiffness of checkerboard materials is pursued in Section 5.2;

2. Another set of questions address the distribution of the effective modulus E_{eff}: How can one approximate the distribution of E_{eff}? How does the distribution vary with the main controlling factors (the size of the specimen, the mean stiff fraction, and the stiffness contrast between the phases)? Section 5.3 builds on the findings of Section 5.2 to address these questions.

Section 5.4 uses Monte Carlo simulation to validate the analytical approximations of Sections 5.2 and 5.3. Section 5.5 compares results for checkerboard materials with those for lognormal modulus distribution with similar second moment properties. Section 5.6 summarizes our main contributions, highlights the key findings, and proposes directions for future research.

5.2 Factors that Influence the Effective Stiffness and the Role of Percolation

Consider a square specimen of side length L, partitioned into L^2 unit square tiles. Each tile is independently assigned to the stiff phase with probability p and the soft phase with probability $1-p$. Therefore the number of stiff tiles N has binomial distribution and the stiff fraction $f = N/L^2$ has mean value p and variance $p(1-p)/L^2$. Young's modulus E is 1 inside the soft tiles and e^{Δ} with $\Delta \geq 0$ inside the stiff tiles. The specimen is stretched in the x_1 direction, with zero tractions along the upper and lower sides and no shear stresses along the right and left sides; see **Figure 5.1**. We are interested in the distribution of the effective modulus E_{eff} for given $\{L, p, \Delta\}$.

A probabilistic analysis of E_{eff} is made in Section 5.3. In this section we control f rather than p and focus on understanding the roles played by the specimen size L, the stiff fraction f, the log-stiffness contrast Δ, and different components of the spatial variation of the modulus (see below for a definition of these components). For this purpose it is convenient to work with the log-modulus field $F(x_1, x_2) = \ln E(x_1, x_2)$ and log-effective

modulus $F_{eff} = \ln E_{eff}$. Notice that $F = 0$ inside the soft tiles, $F = \Delta$ inside the stiff tiles, and F_{eff} is a number between 0 and Δ.

5.2.1 Components of $F(x_1, x_2)$ and Their Effect on F_{eff}

To understand how the log-modulus field $F(x_1, x_2)$ affects F_{eff}, we make the ANOVA decomposition

$$F(x_1, x_2) = \overline{F} + \varepsilon_1(x_1) + \varepsilon_2(x_2) + \varepsilon_{12}(x_1, x_2) \tag{5.1}$$

where $\overline{F}$ is the average of F over the specimen, $\varepsilon_1(x_1)$ and $\varepsilon_2(x_2)$ are the main effects of x_1 and x_2, and $\varepsilon_{12}(x_1, x_2)$ is a second-order interaction term. The ε terms in Eq. 5.1 average to zero over each of their arguments. They are obtained from $F(x_1, x_2)$ and the averages $\overline{F}$, $\overline{F}_1(x_1) = \frac{1}{L}\int_0^L F(x_1, x_2)dx_2$, and $\overline{F}_2(x_2) = \frac{1}{L}\int_0^L F(x_1, x_2)dx_1$ as

$$\begin{aligned} \varepsilon_1(x_1) &= \overline{F}_1(x_1) - \overline{F}, \\ \varepsilon_2(x_2) &= \overline{F}_2(x_2) - \overline{F}, \\ \varepsilon_{12}(x_1) &= F(x_1, x_2) - \overline{F}_1(x_1) - \overline{F}_2(x_2) + \overline{F}. \end{aligned} \tag{5.2}$$

This is the same decomposition that was used in Chapter 2. An illustration of the decomposition for checkerboard specimens with side length $L = 4$ and 32 is shown in **Figure 5.2**.

By deleting the ε_{12}-term in Eq. 5.1, one obtains the first-order approximation

$$F_1(x_1, x_2) = \overline{F} + \varepsilon_1(x_1) + \varepsilon_2(x_2) \tag{5.3}$$

The lower-right panels in **Figure 5.2** show examples of this approximation. Note that in large specimens $F_1(x_1, x_2)$ is nearly uniform, whereas in small specimens it is highly

variable. Equation 5.3 corresponds to decomposable modulus fields in which $E(x_1, x_2)$ is the product of a function of x_1 and a function of x_2. For checkerboard materials $E(x_1, x_2)$ cannot be decomposable (ε_{12} cannot vanish), except in the limiting case of porous materials with zero soft-phase modulus. By contrast, other heterogeneous materials including those with lognormal modulus can have a decomposable E field.

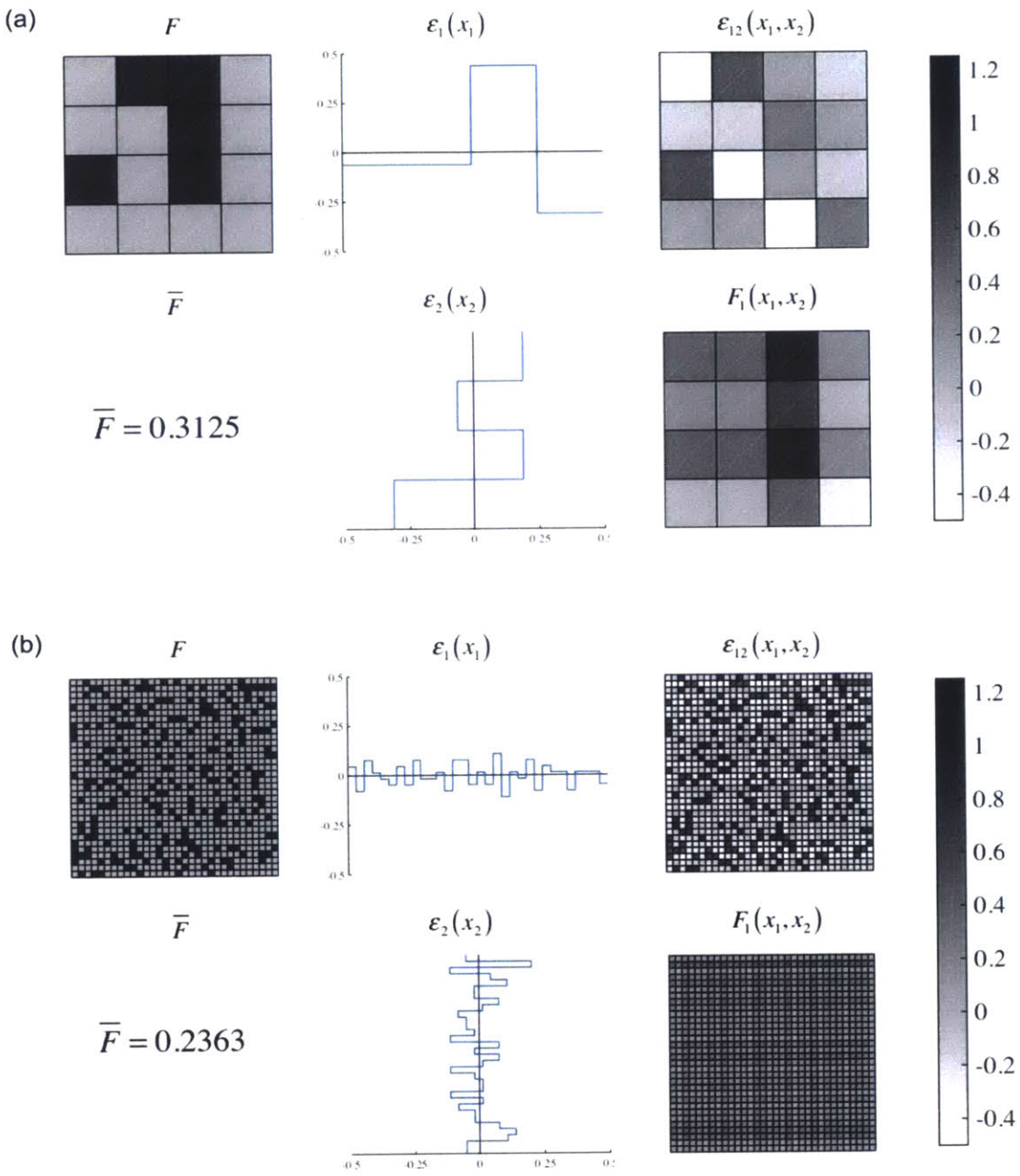

Figure 5.2: Examples of ANOVA decomposition of the log-modulus field. **a** $\{\boldsymbol{L}, \boldsymbol{p}, \boldsymbol{\Delta}\} = \{\mathbf{4}, \mathbf{0.5}, \mathbf{1}\}$ and **b** $\{\boldsymbol{L}, \boldsymbol{p}, \boldsymbol{\Delta}\} = \{\mathbf{32}, \mathbf{0.25}, \mathbf{1}\}$. $\overline{\boldsymbol{F}}$ is the spatial average of the log-modulus field, $\boldsymbol{\varepsilon_1}$ and $\boldsymbol{\varepsilon_2}$ are the marginal fluctuations in the $\boldsymbol{x_1}$- and $\boldsymbol{x_2}$-direction, respectively, $\boldsymbol{\varepsilon_{12}}$ is the second order fluctuation of $\boldsymbol{F}$, and $\boldsymbol{F_1} = \overline{\boldsymbol{F}} + \boldsymbol{\varepsilon_1} + \boldsymbol{\varepsilon_2}$ is the first-order approximation of the modulus field $\boldsymbol{F}$.

Our strategy is to first calculate the log-effective modulus $F_{eff,1}$ under the first-order approximation in Eq. 5.3 and then modify $F_{eff,1}$ to account for the second-order

fluctuation term $\varepsilon_{12}(x_1, x_2)$. One can easily obtain $F_{eff,1}$ since $\varepsilon_1(x_1)$ and $\varepsilon_2(x_2)$ contribute additive terms equal to the log of the harmonic average of $e^{\varepsilon_1(x_1)}$ and the log of the arithmetic average of $e^{\varepsilon_2(x_2)}$, respectively. Therefore, denoting by $\langle g(x)\rangle_q = \left(\frac{1}{L}\int_0^L [g(x)]^q dx\right)^{1/q}$ the q-norm of a function $g(x)$ in $[0, L]$, $F_{eff,1}$ is given by

$$F_{eff,1} = \ln\langle E(x_1, x_2)\rangle_0 + \ln\langle e^{\varepsilon_1(x_1)}\rangle_{-1} + \ln\langle e^{\varepsilon_2(x_2)}\rangle_1 \tag{5.4}$$

where the first term on the right hand side of Eq. 5.4 is the spatial average $\overline{F}$. An interesting feature of Eq. 5.4 is that the first-order fluctuations $\varepsilon_1(x_1)$ and $\varepsilon_2(x_2)$ do not interact, in the sense that their effects on $F_{eff,1}$ are additive and independent.

The next step is to modify Eq. 5.4 to account for the interaction term $\varepsilon_{12}(x_1, x_2)$. This is a difficult task because:

1. Even the direct effect of ε_{12}, by which we mean the effective log-modulus under $F(x_1, x_2) = \varepsilon_{12}(x_1, x_2)$, cannot be found analytically, and
2. While the first-order fluctuations ε_1 and ε_2 do not interact with each other, ε_{12} interacts with ε_1 and ε_2; therefore it is not sufficient to find the direct effect of ε_{12}. The basic reason for the interaction is that the effective modulus depends on the geometry of the soft and stiff phases (in particular how the soft and stiff tiles connect to form clusters and whether the clusters percolate) and these geometric features depend in a complicated way on all three ε terms.

The approach we take is to add to $F_{eff,1}$ a term $F_{eff,12}$ that includes the direct effect of ε_{12} as well as the interactions. For any simulated log-modulus field $F(x_1, x_2)$, we extract the fluctuations $\varepsilon_1(x_1)$ and $\varepsilon_2(x_2)$ using Eq. 5.2 and obtain $F_{eff,12}$ by subtracting $F_{eff,1}$ in Eq. 5.4 from the numerically calculated effective log-modulus F_{eff}.

To ease interpretation and compare with the first-order effects in Eq. 5.4, we express $F_{eff,12}$ as $\ln\langle g(x_1,x_2)\rangle_{q_{12}}$, the log of some q_{12}-norm of some function g related to $F(x_1,x_2)$. The obvious choice $\ln g = \varepsilon_{12}$ has two drawbacks: 1. Due to the interaction of ε_{12} with ε_1 and ε_2, no q_{12}-norm of such function is an accurate predictor of $F_{eff,12}$, and 2. The use of ε_{12} is not convenient for the probabilistic analysis in Section 5.3. After consideration of various alternatives, we have chosen $\ln g = F - \overline{F}$. In large specimens, $F - \overline{F} = \varepsilon_{12}$. In small specimens, $F - \overline{F}$ results in a more accurate and analytically more convenient predictor of $F_{eff,12}$ than ε_{12}. For example, **Figure 5.3** compares the values of q_{12} that match the observed log-moduli $F_{eff,12}$ in simulated specimens with $L = 4$, $\square = 4$ and variable f, for the two g functions mentioned above. While the trend with f is similar, the choice $\ln g = F - \overline{F}$ produces a predictor with lower dispersion.

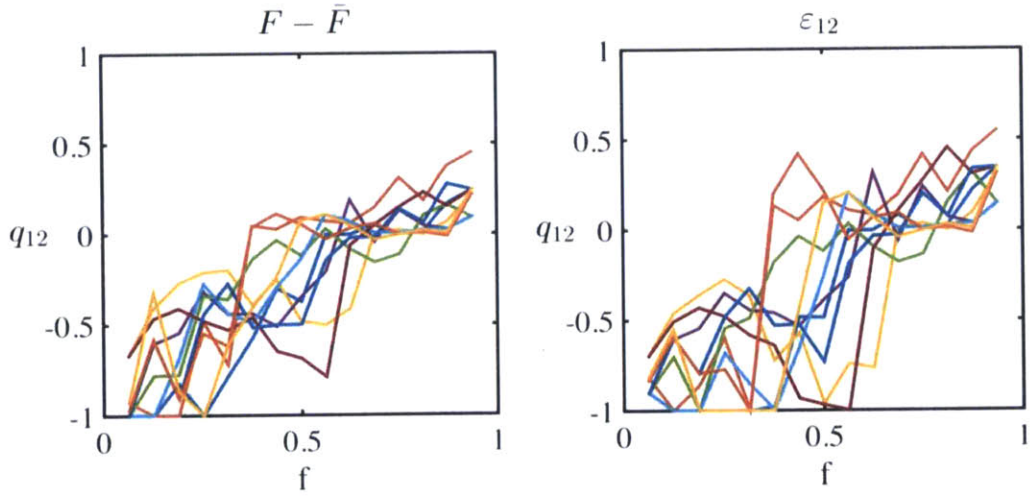

Figure 5.3: Comparison of q_{12} values for $\ln g = F - \overline{F}$ and $\ln g = \varepsilon_{12}$ when $L = 4$, $\Delta = 4$ and the stiff volume fraction f progressively increases from **0** to **1** in **1/16** increments.

With these considerations, we express the effective log-modulus as

$$F_{eff} = \ln\langle E(x_1,x_2)\rangle_0 + \ln\langle e^{\varepsilon_1(x_1)}\rangle_{-1} + \ln\langle e^{\varepsilon_2(x_2)}\rangle_1 + \ln\langle e^{F(x_1,x_2)-\overline{F}}\rangle_{q_{12}} \tag{5.5}$$

Notice that q_{12} in Eq. 5.5 is random (see scatter in **Figure 5.3**), with a distribution that depends on the specimen size L, the stiff fraction f, and the log-modulus contrast Δ. A model for the distribution of q_{12} is presented in Section 5.2.3.

The relative importance of the various terms in Eq. 5.5 depends to a large extent on the size of the specimen L. To illustrate, we consider a small specimen ($L = 4$) and a large specimen ($L = 32$), fix the log-modulus contrast Δ to 4, and through numerical simulation find the contribution of each term on the right hand side of Eq. 5.5 as the stiff volume fraction f progressively increases from 0 to 1 in $1/16$ increments. Notice that for $L = 4$ a $1/16$ increment of f corresponds to adding just one stiff tile at a time, whereas for $L = 32$ the same increment corresponds to adding 64 stiff tiles (in large specimens, adding one stiff tile at a time would be computationally very onerous). For each specimen size, we simulate 10 independent stiff-phase sequences. The results are presented in **Figure 5.4** using the following notation: ε_1 and ε_2 denote the main effects of $\varepsilon_1(x_1)$ and $\varepsilon_2(x_2)$, ε_{12} is F_{eff} under $F(x_1, x_2) = \varepsilon_{12}(x_1, x_2)$ (this is the direct effect of $\varepsilon_{12}(x_1, x_2)$), and "$int$" is the contribution to F_{eff} from the interaction between the main effects and the second-order fluctuations. Therefore, the sum "$\varepsilon_{12} + int$" corresponds to the last term in Eq. 5. Next we comment in some detail on **Figure 5.4**.

Small Specimen ($L = 4$)

Noticeable features of **Figure 5.4a** are:

- In the limiting cases $f = 0$ and $f = 1$, the modulus is spatially uniform; therefore all the □ terms in Eq. 1 vanish and so do their effects on F_{eff}. The effects of the □ terms are maximum and most variable for f around $0.4 - 0.5$;
- The contributions to F_{eff} from the different □ and int terms have similar orders of magnitude. In particular, it would be inaccurate to ignore the interaction effect; and
- F_{eff} and its components are not smooth functions of f, but display significant discontinuities and variability from simulation to simulation.

The jumps in the $F_{eff}(f)$ curves are related to percolation, a phenomenon to which we devote a separate subsection below.

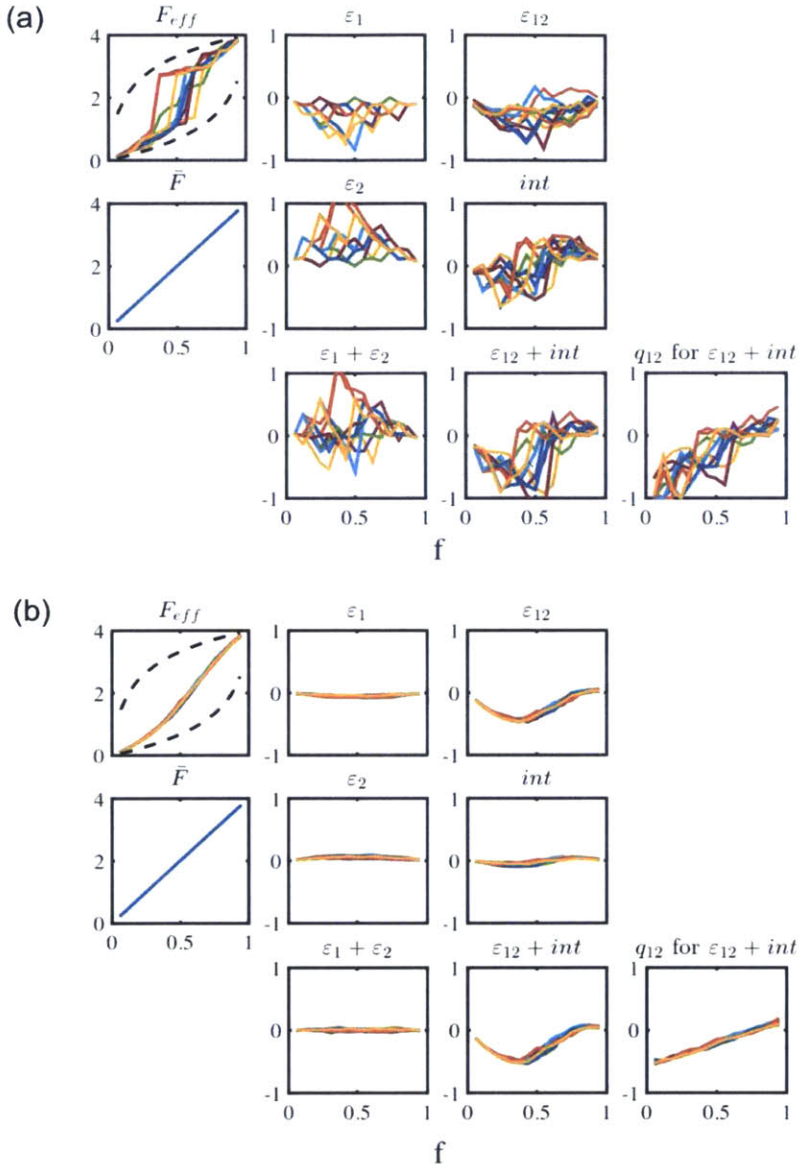

Figure 5.4: Contribution of various ANOVA components to the total effective log-stiffness $\boldsymbol{F_{eff}}$ for **a** $\boldsymbol{L = 4}$ and **b** $\boldsymbol{L = 32}$. In each case $\boldsymbol{\Delta = 4}$. Through numerical simulation we find the contribution of each term on the right hand side of Eq. 5.5 as the stiff volume fraction $\boldsymbol{f}$ progressively increases from **0** to **1** in **1/16** increments. See text for an explanation of the different components.

Large Specimens ($L = 32$)

In large specimens, the component contributions to F_{eff} are very different; see **Figure 5.4b**. When $L = 32$, the main effects are negligible and ε_{12} is very close to $F(x_1, x_2) - \overline{F}$. The effective log-stiffness is determined almost entirely by the spatial average $\overline{F}$, with

a secondary contribution from ε_{12}. The contributions from ε_1 and ε_2 are small and opposite in sign and virtually cancel each other.

Another important feature of large specimens is that the dependence of F_{eff} on the stiff fraction f is smooth and nearly identical in different simulations. The reason is that, as far as the effective modulus is concerned, specimens of size $L = 32$ are already close to the ergodic limit $L \to \infty$ under which F_{eff} becomes a deterministic function of f and Δ. The absence of significant discontinuities in the $F_{eff}(f)$ relationship is an interesting feature of elastic percolation, which we address below.

5.2.2 The Role of Percolation

An important stiffening mechanism in checkerboard materials is the formation of percolating stiff clusters. As was noted above, the effect of percolation changes drastically with the specimen size: in small specimens F_{eff} displays large discontinuities at certain values of the volume fraction f, whereas in large specimens F_{eff} is a smooth function of f; see top-left (F_{eff}) panels in **Figures 5.4a** and **5.4b**. To better understand this phenomenon, we consider the formation of two types of percolating clusters:

- Clusters made of only nearest neighbors (tiles that share one side). Using standard percolation notation, e.g. [122], we refer to this as NN-percolation (NN for nearest-neighbor); and
- Clusters formed by nearest and next-nearest neighbors, hence by tiles that share either one side or one vertex. We refer to this as $(NN + NNN)$-percolation (NNN for next-nearest neighbor).

Other neighborhood definitions are possible, but the two mentioned above are the most influential ones on the effective stiffness of checkerboard specimens. As is well known [122], in square lattices the $(NN + NNN)$ and NN percolation thresholds are $f_{NN+NNN} = 0.407$ and $f_{NN} = 0.593$, respectively.

Percolation in Small Specimens ($L = 4$)

Figure 5.5 shows how F_{eff} evolves with f in three different simulations. Also shown are the first $(NN + NNN)$ and NN percolation clusters, respectively highlighted in blue and red (the same color coding identifies the occurrence of these clusters in the plots of F_{eff} versus f). The vertical dashed lines in the F_{eff} plots correspond to the theoretical percolation thresholds 0.407 and 0.593. Stiff tiles are in black. The gray tile is the last stiff tile added to form each cluster. Notice that for the first simulation the NN and $(NN + NNN)$ percolating clusters coincide.

One can see that for small specimens NN-percolation is a significant stiffening mechanism that produces large discontinuities in the $F_{eff}(f)$ curve, whereas $(NN + NNN)$-percolation has a less dramatic effect. Also notice that for the present log-modulus contrast $\Delta = 4$, the value of F_{eff} at NN-percolation is around 3 when the cluster includes a full row of stiff tiles acting as a bar in tension (first two simulations) and around 2.5 if the cluster includes en-echelon connections (last simulation). In the latter case, as f increases and "longitudinal bars" form, the effective modulus experiences significant additional jumps; see arrows in the lower-right panel of **Figure 5.5**.

A complementary perspective is obtained by starting from a completely stiff material ($f = 1$) and progressively decreasing f until transversal $(NN + NNN)$ and NN percolating clusters of the soft-phase occur. The two perspectives are equivalent, in that the formation of $(NN + NNN)$ and NN percolating stiff clusters in the longitudinal direction respectively coincides with the formation of NN and $(NN + NNN)$ soft percolating clusters in the transversal direction.

The large jumps associated with percolation of the stiff and soft phases separate two branches of the $F_{eff}(f)$ curve: a lower branch where transversal soft percolation occurs and an upper branch where longitudinal stiff percolation occurs. The value of f at which the transition takes place is random, but often close to the theoretical percolation

thresholds of 0.407 and 0.593. These features of small specimens become more pronounced as Δ increases or L decreases.

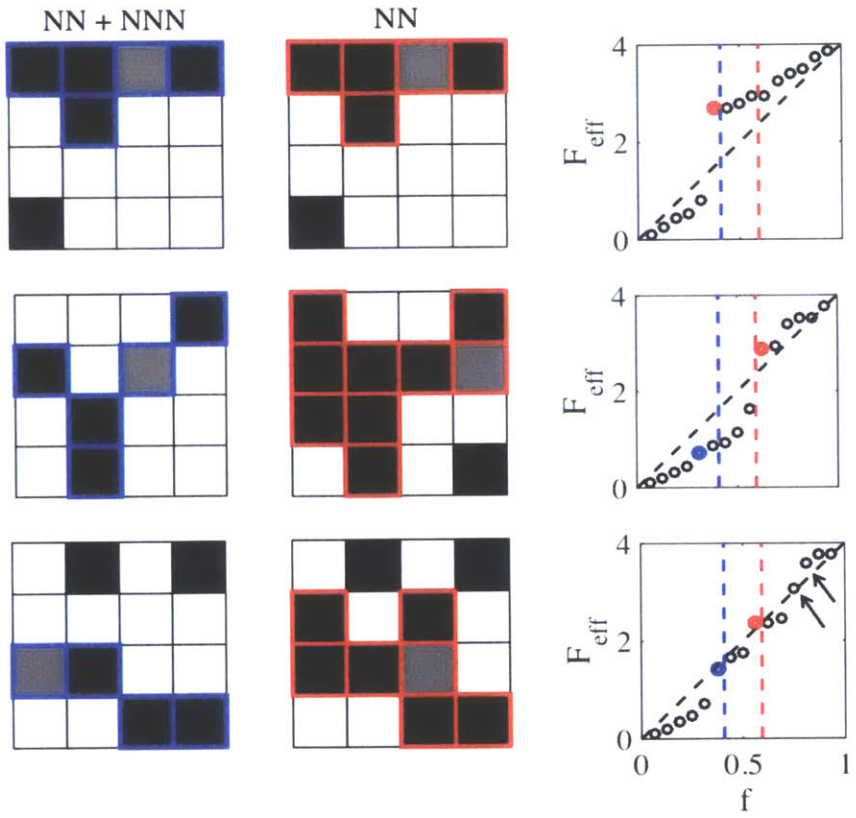

Figure 5.5: Three simulations of $F_{eff}(f)$ for systems with $L = 4$ and $\Delta = 4$. The first two columns show the first $(NN + NNN)$ and NN percolating clusters highlighted in blue and red, respectively. The points along the $F_{eff}(f)$ trajectory at which these percolating clusters form are shown with matching colors. The vertical dashed lines indicate the theoretical percolation thresholds.

Percolation in Large Specimens ($L = 32$)

Figure 5.6 is analogous to **Figure 5.5**, but refers to a large specimen with $L = 32$. In this case, for given f, F_{eff} is insensitive to the geometric arrangement of the stiff tiles. This is why we show the function $F_{eff}(f)$ for only one realization. F_{eff} varies smoothly with f and percolation has a gradual stiffening effect with no well-defined threshold. The jumps at the onset of NN and $(NN + NNN)$ percolation are barely visible. To our knowledge this feature of large-scale percolation has not been reported for other physical transport phenomena like electric conductivity and fluid or heat flow. This is partly because

previous studies of percolation in checkerboard systems have focused on the case of infinite material property contrast, when one of the phases is non-conducting. It is likely that also the difference between the elastic problem and other flow problems plays a role. For example, in the elastic case with large L and Δ the effective modulus depends on the degree of static determinacy of the stiff percolating cluster under the given boundary conditions. This degree increases gradually as more stiff tiles are included.

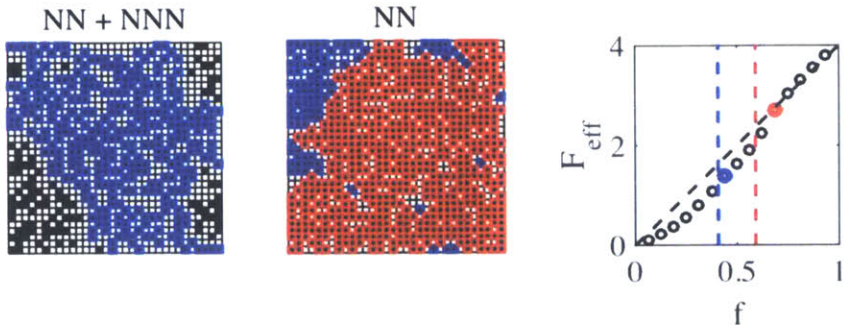

Figure 5.6: Same as **Figure 5.5** for $L = 32$, the $F_{eff}(f)$ plots are almost deterministic; hence we display only on simulation.

5.2.3 Modeling the Exponent q_{12} in Eq. 5.4

To complete the model of F_{eff} one needs to estimate the averaging exponent q_{12} in Eq. 5.4 as a function of $\{L, f, \Delta\}$. The lower-right panels of **Figure 5.4** show how q_{12} depends on f for a log-modulus contrast $\Delta = 4$ and specimens of size $L = 4$ and 32. Since q_{12} exhibits a far more regular behavior for $L = 32$ than for $L = 4$, we begin by seeking a model for $(q_{12}|L = 32, f, \Delta)$, applicable to large specimens.

Using the same format as **Figure 5.4, Figure 5.7a** shows simulations of the function $q_{12}(f)$ for $L = 32$ and $\Delta = \{1,2,3,4\}$. An interesting first observation is that, for all Δ, q_{12} exhibits near-linear dependence on f. This is in sharp contrast to the constant value $q_{12,LN} = -0.25$ in the case of lognormal modulus [36] and the constant values of q for the first three terms in Eq. 1 ($q_{\overline{F}} = 0$ for $\overline{F}$, $q_1 = -1$ for $\varepsilon_1(x_1)$, and $q_2 = 1$ for $\varepsilon_2(x_2)$). A qualitative explanation is that when f is small the soft phase percolates transversally and q_{12} is negative (softening effect), whereas for high f the stiff phase percolates

longitudinally and q_{12} is positive (stiffening effect). The horizontal dashed lines in **Figure 5.7a** indicate the value $q_{LN,12} = -0.25$. For all Δ (and L), the present q_{12} values are close to -0.25 at approximately $f = 0.5$ (for this value of f the second-order term ε_{12} has symmetrical distribution around zero, which is also the case when F is normal).

Another feature of **Figure 5.7a** is that the slope of $q_{12}(f)$ is nearly proportional to Δ. Using least-squares fitting, we obtain the following model of $E[q_{12}]$ for $L = 32$:

$$E[q_{12}|L = 32, f, \Delta] = -0.25 + 0.20\Delta(f - 0.5). \tag{5.6}$$

Equation 5.6, with the constant 0.20 replaced with a suitable function $c(L)$, is an accurate model for $E[q_{12}]$ over all specimen sizes. Least-squares fitting to the simulations in **Figure 5.7b** for $L = \{4,8,16,32\}$ gives the c values in the left panel of **Figure 5.7c**. Using $c(L) = \left(0.18 + \frac{0.57}{L}\right)$ (red curve in left panel of **Figure 5.7c**), we obtain the final model

$$E[q_{12}|L, f, \Delta] = -0.25 + \left(0.18 + \frac{0.57}{L}\right)\Delta(f - 0.5). \tag{5.7}$$

The black straight lines in **Figure 5.7b** are plots of this function.

In small specimens, one must also model the scatter of $(q_{12}|L, f, \Delta)$ around the mean value. As **Figures 5.4** and **5.7b** show, the scatter depends on L, but is insensitive to f and Δ. Also, the scatter vanishes in the large-specimen limit $L \to \infty$. The right panel of **Figure 5.7c** shows empirical standard deviations $\sigma_{q_{12}}$ from the simulations in **Figure 5.7b** and the least squares hyperbolic fit

$$\sigma_{q_{12}|L,f,\Delta} = \frac{0.74}{L}. \tag{5.8}$$

The distribution of $(q_{12}|L, f, \Delta)$ may be taken as normal.

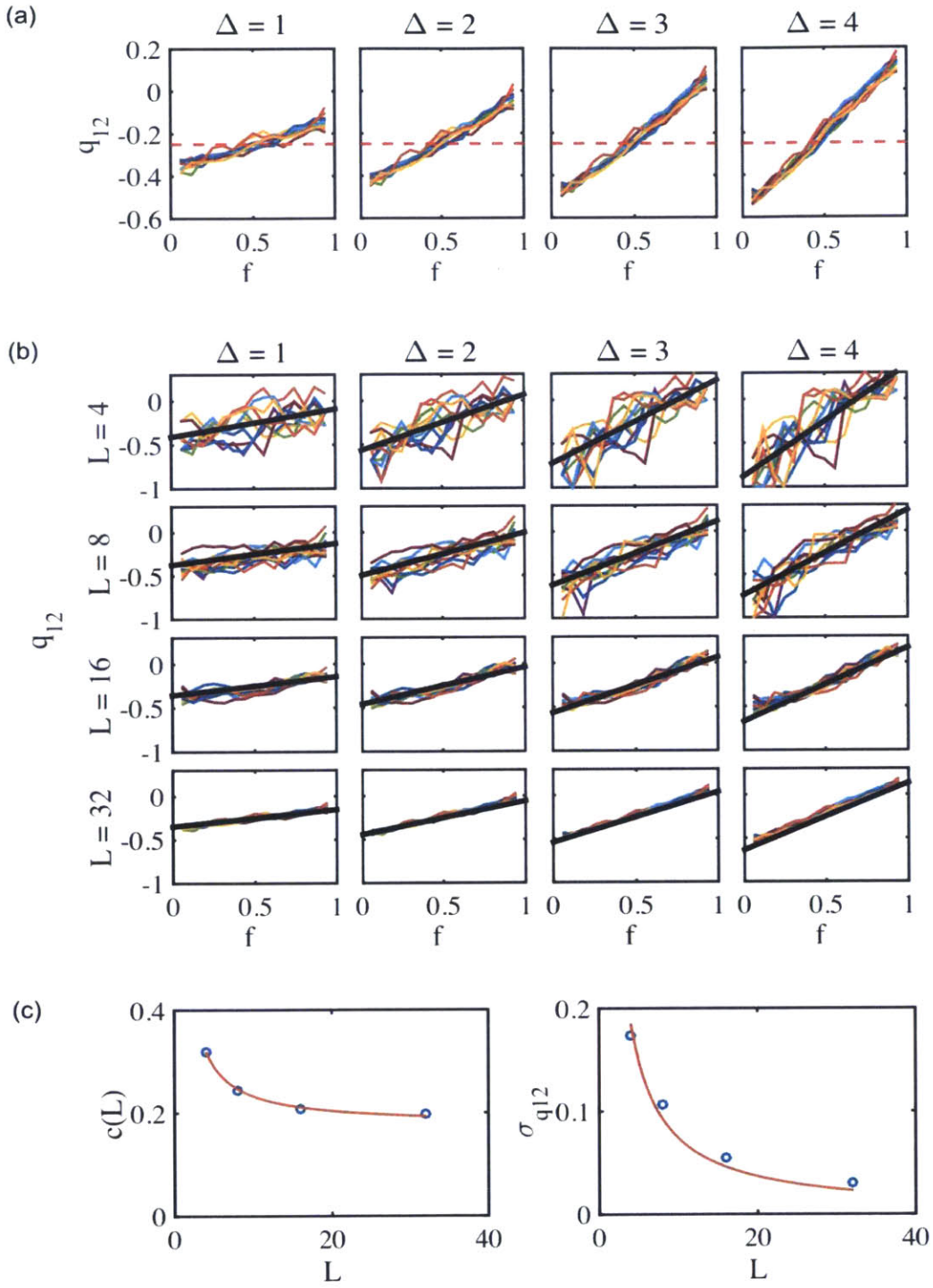

Figure 5.7: a Dependence of q_{12} on f_s for $L = 32$ and $\Delta = \{1, 2, 3, 4\}$. **b** Dependence of q_{12} on f for $L = \{4, 8, 16, 32\}$ and $\Delta = \{1, 2, 3, 4\}$ along with regression lines from Eq. 5.7. **c** Values of $c(L)$ in Eq. 5.6 for $L = \{4, 8, 16, 32\}$ and values of $\sigma_{q_{12}}(L)$ for $L = \{4, 8, 16, 32\}$, with least squares fits.

5.3 Probability Distribution of the Effective Modulus

Next we seek an analytical approximation to the distribution of F_{eff} for given specimen size L, stiff-phase probability p, and log-modulus contrast Δ. Uncertainty on $(E_{eff}|L,p,\Delta)$ is contributed by two sources: variability of the stiff fraction f given p, which is easy to quantify, and variability of the spatial arrangement of the stiff tiles given f, whose effect on E_{eff} is much more complex.

The approximation we propose is based on the assumption that the four terms on the right hand side of Eq. 5.5 have independent normal distributions. The assumption of normality is justified by the fact that these terms are obtained through averaging operations on the F values. By virtue of the central limit theorem their distribution is close to normal, at least for large specimens.

In practice, one can just replace the binary log-modulus field $F(x_1,x_2)$ with a normal random field having the same first two moments and then use the method presented in Chapter 2 for lognormal modulus fields. The mean value m_F and variance σ_F^2 are

$$\begin{aligned} m_F &= F_0 + p\Delta, \\ \sigma_F^2 &= \frac{\Delta^2}{L^2} p(1-p). \end{aligned} \tag{5.9}$$

A complicating factor is that the correlation function of F is non-isotropic and non-homogeneous, whereas the analysis in Chapter 2 considers isotropic fields. We make an isotropic representation of F by randomly translating and rotating the tile mesh. Random translation produces a homogeneous field whose correlation function is obtained by noting that the log-moduli at two points separated by distance r in some direction θ are identical if the points belong to the same tile and independent if the points are in different tiles. It follows that the correlation $\rho_F(r,\theta)$ equals the probability that the points belong to the same tile, which is also the overlap area between a unit square and the same unit square translated by (r,θ). Simple geometric reasoning gives

$$\rho_F(r,\theta) = \begin{cases} (1-|r\cos\theta|)(1-|r\sin\theta|), & \text{for } |r\cos\theta|<1 \text{ and } |r\sin\theta|<1 \\ 0, & \text{otherwise} \end{cases} \tag{5.10}$$

Finally we obtain the isotropic approximation by randomly rotating the field, which corresponds to averaging $\rho_F(r,\theta)$ over θ:

$$\rho_F(r) = \frac{2}{\pi}\int_0^{\pi/2} \rho_F(r,\theta)\, d\theta. \tag{5.11}$$

The accuracy of this and other approximations is verified in Section 5.4 using Monte Carlo simulation. An alternative isotropic approximation for the correlation function is obtained by replacing the unit square tiles with unit-area discs, i.e. by using the overlap area between two such discs with centers at distance r. The results from the two approaches are nearly identical.

The normal approximation method we have just described works well for the first three terms in Eq. 5.5, i.e. it gives an accurate estimate of the distribution of $F_{eff,1}$ in Eq. 5.4. For the contribution from ε_{12} (last term in Eq. 5.5), the analysis in Chapter 2 assumed a deterministic effect derived under large-specimen conditions, but this is not satisfactory for checkerboard specimens on two accounts: 1. Also for large checkerboard specimens, the deterministic effect of ε_{12} differs from the case of lognormal modulus (recall from Section 5.2 that in the lognormal case the large-specimen value of q_{12} is -0.25, whereas for checkerboard materials q_{12} depends in important ways on the stiff fraction and the modulus contrast); 2. For small specimens and intermediate values of p, the value of q_{12} in checkerboard materials is highly variable due to uncertainty on the presence/absence of different percolation clusters. Therefore, for the last term in Eq. 5.5 we develop a different stochastic approximation, as explained below.

As shown in Eq. 5.5, in checkerboard materials the additive effect of ε_{12} on F_{eff} may be written as $\ln\langle e^{F(x_1,x_2)-\overline{F}}\rangle_{q_{12}}$, where $[F(x_1,x_2)-\overline{F}]$ and q_{12} are random. In the Supporting Information, we use properties of the binary field $e^{F(x_1,x_2)-\overline{F}}$ to express this contribution in terms of the control parameters f and Δ and the random variable q_{12},

$$\ln\langle e^{F(x_1,x_2)-\overline{F}}\rangle_{q_{12}} = \begin{cases} -f\Delta + \dfrac{1}{q_{12}}\ln[fe^{q_{12}\Delta} + (1-f)], & q_{12} \neq 0 \\ 0 & q_{12} = 0 \end{cases} \tag{5.12}$$

Then we linearize Eq. 5.12 around the mean values of q_{12} and f and use the fact that q_{12} and f may be taken as normal with moments given in Eqs. 5.7 and 5.8 and in the beginning of Section 5.2 to obtain a normal approximation to the distribution of $\ln\langle e^{F(x_1,x_2)-\overline{F}}\rangle_{q_{12}}$. The approximating distribution of F_{eff} is normal, with mean value and variance given by the sum of the mean values and variances of $F_{eff,1}$ and $\ln\langle e^{F(x_1,x_2)-\overline{F}}\rangle_{q_{12}}$.

5.4 Numerical Validation

We validate the analytical results using Monte Carlo simulation. For each simulated modulus field (spatial distribution of stiff and soft tiles), we find the bulk modulus with a finite element model developed in MATLAB. Section 5.4.1 describes the numerical model and Section 5.4.2 compares numerical results with theoretical predictions.

5.4.1 Numerical Model

The difficulty of numerically analyzing checkerboard systems with large property contrast has been widely reported and studied in the context of electric conductivity and heat conduction [123-125]. The problem arises mainly when stiff (conducting) tiles meet at a corner: when Δ is large, the stiffness of the soft tiles is negligible and a singularity arises with a finite load transferred through a point [123]. Various specialized meshing

schemes have been proposed to produce accurate results for conductivity contrasts as large as 10^7 [123, 124]. While powerful, these approaches are complicated and are not pursued here. Rather, we limit the modulus contrast to a factor of about 50 ($\Delta = 4$) and overcome the challenge of large localized stresses by using refined finite-element discretizations.

For $\Delta = 4$, numerical results accurate to within 2% are obtained by using a 256×256 grid of quadratic nine-node elements. For $\Delta = 1$ and 2, this accuracy level is achieved or surpassed with a 128×128 grid; see Supporting Information. The size of the largest systems ($L = 32$) is considerable ($> 500{,}000$ nodes) and as we are interested in validating the theoretical results over a wide range of $\{L, p, \Delta\}$, we must limit the number of Monte Carlo simulations for each parameter combination (on a Dell Precision T5500 with an Intel Xeon 5600 series processor, each of the largest simulations takes approximately 90 seconds). We run 1,000 Monte Carlo simulations for each parameter combination and investigate a total of 64 combinations.

5.4.2 Validation Runs

In Section 5.2 we derived single-value estimates of $(F_{eff}|L, f, \Delta)$ (the true effective modulus under given (L, f, Δ) is random and the analytical expressions should be seen as approximations of the mean value) and in Section 5.3 we obtained normal approximations to the distribution of $(F_{eff}|L, p, \Delta)$. Here we compare both types of analytical predictions with numerical results for $L = \{4,8,16,32\}$, $p = \{0.1,0.3,0.6,0.9\}$, and $\Delta = \{2,4\}$ (results for $\Delta = \{1,3\}$ are in the Supporting Information).

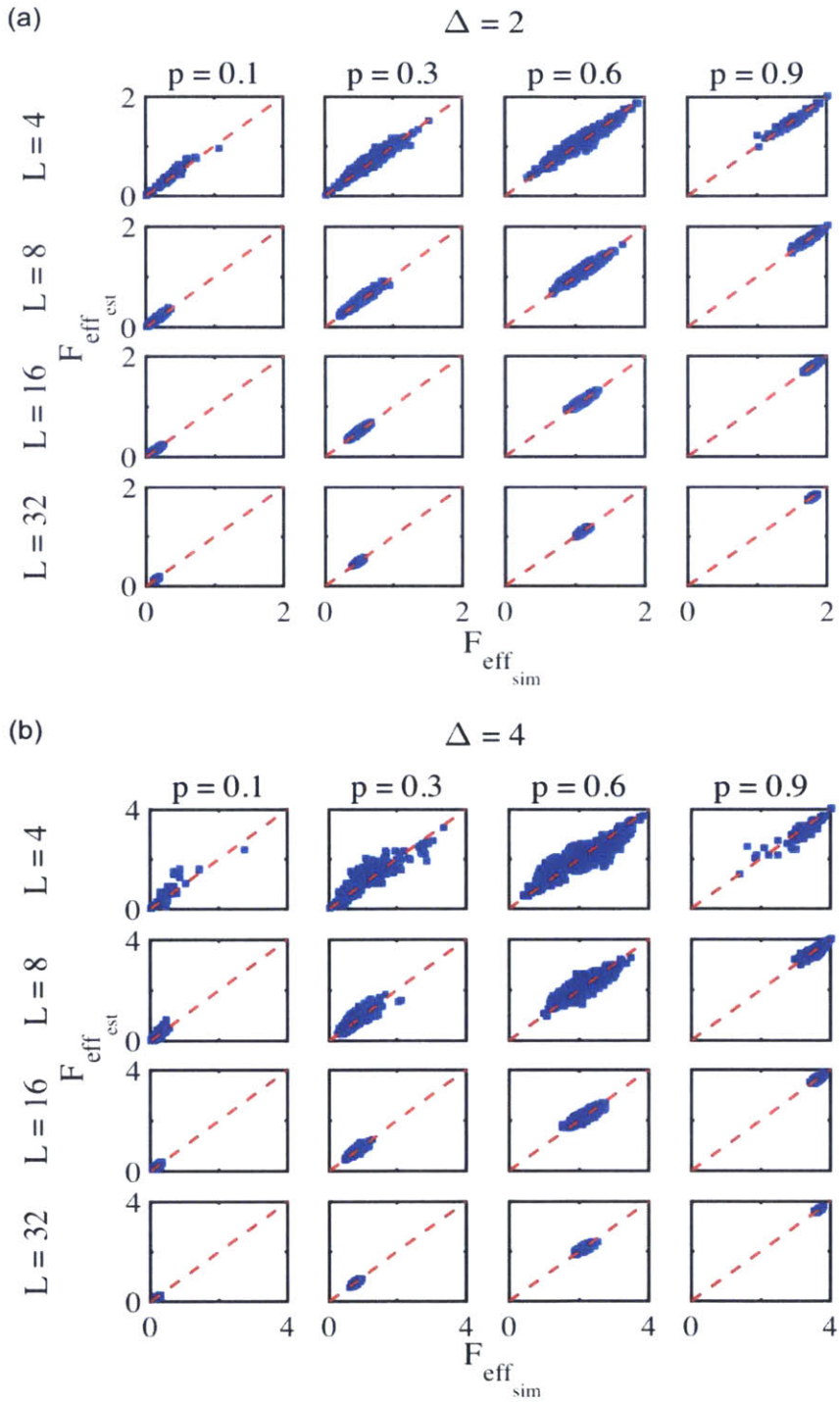

Figure 5.8: Scatter plots of single-value-predicted and simulated F_{eff} for $L = \{4, 8, 16, 32\}$, $f = \{0.1, 0.3, 0.6, 0.9\}$ and $\Delta = \{2, 4\}$.

Single-value Estimates of F_{eff}

Figure 5.8 shows scatterplots of simulated F_{eff} and single-value predictions.

We control p, and the stiff volume fraction f is a random variable. The single-value predictions of F_{eff} are calculated using Eq. 5.7 with the realized values of f. Although there is scatter, especially for small specimens with large Δ and intermediate values of p, the point estimates are nearly unbiased. The scatter is due to the fact that, as explained in Section 5.2.3, the mean values of q_{12} in Eq. 5.7, which are used to produce the single-value estimates, do not depend on the specific arrangement of the stiff tiles; rather they describe the average effect of the second-order term ε_{12} for given (L, f, Δ). In small specimens, the true effective stiffness depends on the specific arrangement of the stiff tiles, producing the scatter in **Figure 5.8**. In larger specimens, the effect of ε_{12} is insensitive to the arrangement of the stiff tiles (see Section 5.2) and the scatter is much reduced.

Distribution of F_{eff}

Figure 5.9 compares the numerical and approximate analytical cumulative distributions of F_{eff} for $L = \{4,8,16,32\}$, $p = \{0.1,0.3,0.6,0.9\}$, and $\Delta = \{2,4\}$.

Figure 5.9a shows that for $\Delta = 2$ the estimator is accurate for all L and p. Since F_{eff} is bounded between 0 and Δ, the approximating normal distributions have been doubly-censored by setting negative values to 0 and values above Δ to Δ. Also for $\Delta = 4$ the agreement is quite good; see **Figure 5.9b**. The small discrepancies for $L = 4$ are mainly due to a shorter-than-normal lower tail in the empirical distribution and "kinks" associated with percolation effects, which the analytical approximation does not treat in detail. For example, the sharp edge observed for $\{L = 4, p = 0.6\}$ at about $F_{eff} = 2.7$ marks the divide between specimens in which all four rows contain at least one soft tile and specimens in which only three rows contain one or more soft tiles. The first two moments are always accurately predicted.

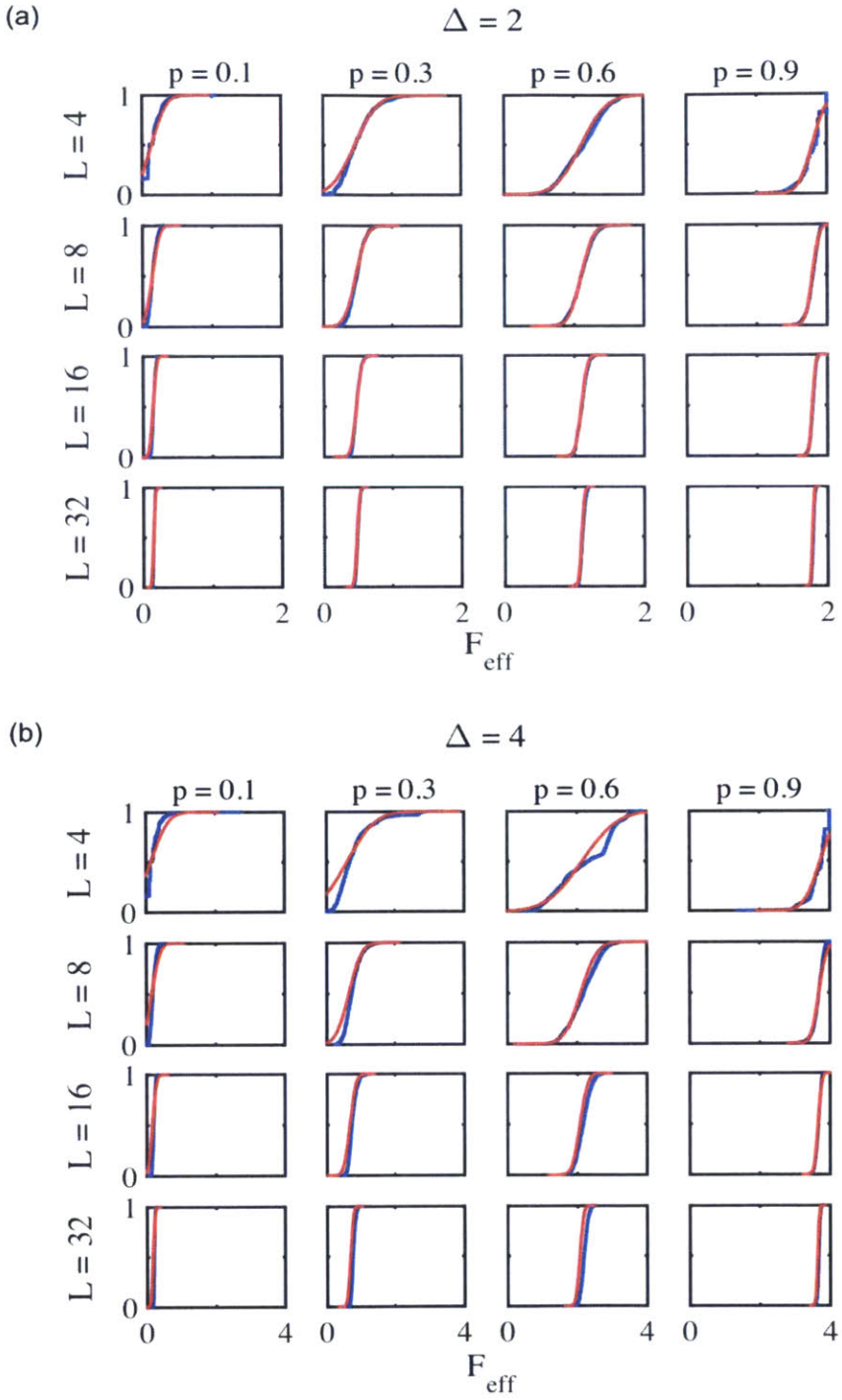

Figure 5.9: Comparison of approximate analytical (red) and empirical (blue) cumulative distributions $\boldsymbol{F_{eff}}$ for $\boldsymbol{L} = \{\mathbf{4}, \mathbf{8}, \mathbf{16}, \mathbf{32}\}$, $\boldsymbol{p} = \{\mathbf{0.1}, \mathbf{0.3}, \mathbf{0.6}, \mathbf{0.9}\}$ and $\boldsymbol{\Delta} = \{\mathbf{2}, \mathbf{4}\}$.

5.5 Comparison Between Checkerboard and Lognormal Materials

It is interesting to compare the compliance of checkerboard specimens with that of lognormal specimens with similar modulus variability. Here we make the comparison under ergodic conditions (i.e. for specimens that are large relative to the log-modulus correlation distance, in the checkerboard case just relative to the tile size). The reason for this choice is that in ergodic specimens the log-modulus field is the sum of only two terms, the spatial average $\bar{F}$ and the second-order fluctuation ε_{12}, and the effective modulus is $e^{\bar{F}}$ times some q_{12}-norm of $e^{\varepsilon_{12}}$. We consider the checkerboard and lognormal specimens to have comparable modulus variability if they share the mean value m_E (without loss of generality, we set $m_E = 1$) and log-variance σ_F^2. Notice that for large specimens m_E controls the spatially integrated "total stiffness"; hence we compare the effective modulus when the same total stiffness has different random spatial distribution.

In the lognormal case the marginal distribution of the modulus and the effective modulus are completely defined by $(m_E = 1, \sigma_F^2)$. In checkerboard specimens, the same quantities depend also on the stiff fraction f (which under the present ergodic conditions equals p). Specifically, it is easy to show that the modulus of the soft phase E_0 and the log-modulus contrast Δ (which together with f define the marginal distribution) are given by

$$E_0 = \frac{1}{fe^{\Delta} + (1-f)},$$
$$\Delta = \frac{\sigma_F}{\sqrt{f(1-f)}}, \tag{5.14}$$

Notice that Δ is proportional to σ_F and that for any given σ_F, Δ is symmetrical around $f = 0.5$ (where it is minimum) and diverges for $f = 0,1$.

For lognormal specimens $q_{12} = -0.25$ and the log-effective modulus is $F_{eff} = -\frac{5}{8}\sigma_F^2$ [36]. The corresponding quantities for the checkerboard specimen depend on σ_F^2 and f:

q_{12} is calculated from Eq. 5.7 (due to ergodicity, q_{12} is deterministic) and $F_{eff} = \overline{F} + \ln\langle e^{F(x_1,x_2)-\overline{F}}\rangle_{q_{12}}$, with $\overline{F} = (1-f)\ln E_0 + f(\ln E_0 + \Delta)$, E_0 given by Eq. 5.14, and $\ln\langle e^{F(x_1,x_2)-\overline{F}}\rangle_{q_{12}}$ given by Eq. 5.12.

Figure 5.10 shows F_{eff} as a function of σ_F^2. For the checkerboard specimen, three stiff fractions are considered: $f = 0.1, 0.5, 0.9$. As described in Section 5.2.4, the stiff fraction affects the log-effective stiffness of ergodic checkerboard specimens through two mechanisms: 1. the averaging exponent q_{12} (see Eq. 5.7) and 2. the marginal distribution of the modulus. To understand whether the differences in F_{eff} between lognormal and checkerboard specimens is due mainly to q_{12} or the shape of the marginal distribution, **Figure 5.10** shows also $F_{eff} = 1/2(q_{12}-1)\sigma_F^2$, the log-effective modulus under lognormal marginal distribution using the q_{12} value from Eq. 5.7. These hybrid values are given by the dashed lines. For $f = 0.5$, $q_{12} = -0.25$; hence the green dashed line gives also F_{eff} for lognormal specimens. Notice that:

- The effective stiffness is comparable when $f = 0.5$. Checkerboard specimens are softer than lognormal specimens when $f < 0.5$ and are stiffer when $f > 0.5$;
- When f is close to either 0 or 1 and σ_F^2 is large, F_{eff} for checkerboard specimens is very different from the lognormal value. This divergence is due to the dependence of Δ on σ_F and f (see comments on Eq. 14); and
- For $f \neq 0.5$, the difference between the checkerboard and lognormal cases is due mainly to the shape of the marginal distribution and to a lesser extent the generalized averaging exponent q_{12}. Therefore the modulus distribution beyond just the first two moments is of critical importance to the bulk elastic properties of composite materials.

To appreciate the difference in the marginal distribution of the log-modulus F, **Figure 5.10** shows lognormal/checkerboard comparisons for $\sigma_F^2 = 0.25$ and $f = \{0.1, 0.5, 0.9\}$. Notice that when f is small, the system consists of isolated rigid inclusions in a soft matrix. The inclusions deform minimally, the stresses are nearly uniform, and the

effective stiffness E_{eff} is close to the harmonic average $\langle e^{F(x)} \rangle_{-1}$. When f is large, the system consists of isolated pore inclusions in a stiff matrix. The pores deform with the matrix, the strain field is near uniform, and the effective stiffness is closer to the arithmetic average $\langle e^{F(x)} \rangle_{1}$.

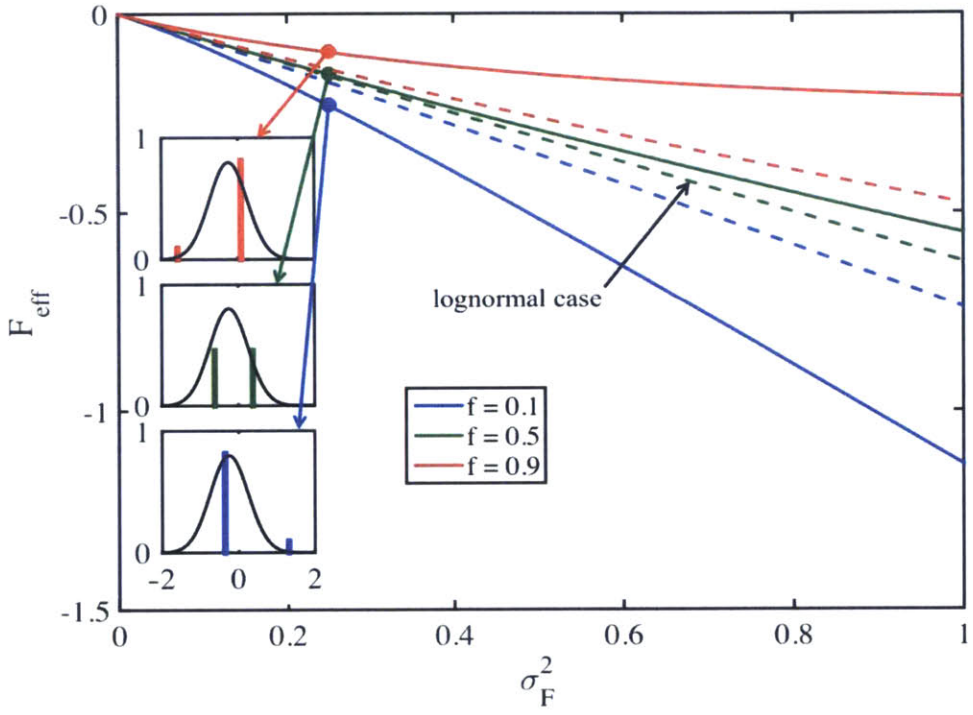

Figure 5.10: Dependence of $\boldsymbol{F_{eff}}$ on $\boldsymbol{\sigma_F^2}$ for large checkerboard and lognormal specimens with $\boldsymbol{m_E = 1}$. For checkerboard materials, results are presented for three values of the stiff fraction $\boldsymbol{f}$. Checkerboard results are shown as solid lines. The dashed lines give hybrid results when the exponent $\boldsymbol{q_{12}}$ is from checkerboard analysis but the marginal distribution of the modulus is assumed to be lognormal. The dashed green line is also the log-effective stiffness in the lognormal case. Small panels compare the checkerboard (binary) and normal marginal distribution of $\boldsymbol{F}$ for $\boldsymbol{\sigma_F^2 = 0.25}$ and $\boldsymbol{f = \{0.1, 0.5, 0.9\}}$.

5.6 Conclusions

We have extended the elastic homogenization approach reported in Chapter 2, which was originally developed for lognormal Young's modulus fields E, to two-phase checkerboard materials in which E has binary distribution. Checkerboard materials may be viewed as a simple model system for a wide class of multi-phase composites.

Important new factors in the elastic homogenization of checkerboard (and other multi-phase) materials are the longitudinal percolation of the stiff phase and the transversal percolation of the soft phase. A further distinction is based on the definition of neighboring cells in percolation clusters. Two basic neighborhood concepts are the sharing of one side (NN percolation) and the sharing of either one side or one vertex ($NN + NNN$ percolation), but other neighborhood definitions are also possible. These various forms of percolation make the stiffening or softening effects of percolation quite complex and difficult to quantify.

If one decomposes the log-modulus field $F(x_1, x_2) = \ln E(x_1, x_2)$ as shown in Eq. 5.1, then one can express the effect of each term on the right hand side as some q-norm of the Young's modulus E or of some component of modulus fluctuation. As shown by Eq. 5.5, the q values associated with $\overline{F}$, $\varepsilon_1(x_1)$ and $\varepsilon_2(x_2)$ are deterministic and equal 0, -1 and 1, respectively. This is true for all heterogeneous materials. On the other hand, the value of q_{12} for $\varepsilon_{12}(x_1, x_2)$ depends on the nature of the modulus heterogeneity. For two-dimensional specimens with lognormal modulus fluctuations, $q_{12} = -0.25$. By contrast, in checkerboard materials q_{12} is neither constant nor deterministic. Its mean value varies as an approximately linear function of the stiff fraction f, with a slope that increases as the log-modulus contrast Δ increases; see Eq. 5.7. For $f = 0.5$ (equal number of soft and stiff tiles), $E[q_{12}] \approx -0.25$ as in the lognormal case. Values above/below -0.25 are associated with stiff/soft percolation. The stochasticity of q_{12} is largely due to the variability of the stiff-fraction levels at which different types of percolation occur.

The complexities of percolation are especially prevalent in checkerboard specimens that are small relative to the size of the tiles. In large specimens, the effect of percolation is gradual and nearly deterministic (in this case Eq. 5.7 gives q_{12} rather than $E[q_{12}]$).

Based on this understanding of what affects the bulk modulus of checkerboard specimens, we have developed simple analytical approximations to the distribution of E_{eff}. A basic assumption on which the approximations are based is that the terms on the right hand side of Eq. 5.5 are independent normal. This assumption is strictly valid for

very large specimens, for which the approximations are especially accurate. For small specimens, the approximating lognormal distribution is smoother than the distributions of E_{eff} from simulation, but the first two moments of $\ln E_{eff}$ are captured very well.

Our analysis unveils interesting characteristics of the bulk stiffness of checkerboard systems and important differences with lognormal systems:

1. In small specimens longitudinal (transversal) percolation of stiff (soft) tiles is the most significant stiffening (softening) mechanism.
2. In large specimens (with finite modulus contrast) percolation has a gradual stiffening/softening effect and there is no well-defined threshold.
3. The effective stiffness of ergodic checkerboard and lognormal systems is comparable when the stiff fraction $f = 0.5$. Checkerboard specimens are softer than lognormal specimens when $f < 0.5$ and stiffer when $f > 0.5$;
4. For $f \neq 0.5$, the difference between the ergodic checkerboard and lognormal cases is due mainly to the shape of the marginal distribution and to a lesser extent the generalized averaging exponent q_{12}. The shape of the marginal distribution is especially influential for large σ_F.
5. The mean of F_{eff} is insensitive to L (to the size of the tiles for a specimen of fixed dimension), while the variance of F_{eff} increases with decreasing tile size. Considering the relationship between the first two moments of lognormal and associated normal variables, one concludes that if one is interested in reducing the coefficient of variation of E_{eff} one should use smaller tiles, whereas larger tiles increase the mean value of E_{eff}.

This work could be extended in several ways, including the following:

1. Checkerboard systems with more than two phases: The first-order log-modulus field F_1 could still be approximated using a moment-matched normal log-modulus model, whereas the second-order effect $F_{eff,12}$ would be affected by a multitude

of percolation thresholds associated with different phases and different neighborhood definitions;

2. Three-dimensional checkerboard systems stretched in the x_1 direction: Following Chapter 2, the 3D ANOVA decomposition of F includes the spatial average, three marginal fluctuations, three second-order fluctuations and one third-order fluctuation. The generalized averaging exponents q associated with the spatial average $\overline{F}$, the marginal fluctuations $\varepsilon_1(x_1)$, $\varepsilon_2(x_2)$ and $\varepsilon_3(x_3)$, and the second-order term $\varepsilon_{23}(x_2, x_3)$ are deterministic and equal 0, -1, 1, 1, and 1, respectively. The effect of the other two second-order fluctuations and the third order interaction could be dealt with in analogy with the present analysis of ε_{12};
3. Granular materials with grains forming random tessellations and two or more phases. Also in this case one could approximate the first-order log-stiffness F_1 using results for the lognormal case. Percolation should have similar effects as for checkerboard systems, although with different critical stiff fractions. Due to the more irregular geometry, the effects of percolation are expected to be more gradual than for checkerboard materials;
4. Finally, one could study the effect of percolation in greater detail. We have found that in large specimens with a modulus contrast factor up to 50, the effective stiffness depends in a smooth way on the stiff volume fraction f. By contrast, small specimens display sharp discontinuities associated with different types of percolation. It would be interesting to study the onset of these phenomena and in particular what controls the transition from sharp to smooth percolation effects in checkerboard and other granular materials.

Supporting Information

Part A: Derivation of Eq. 5.12

The field $\ln g = F - \overline{F}$ has binary marginal distribution, with probability $(1-f)$ at $F_0 - \overline{F} = -f\Delta$ and probability f at $F_1 - \overline{F} = (1-f)\Delta$. Therefore, the q_{12} moment of $g = e^{F-\overline{F}}$ is

$$E[g^{q_{12}}] = fe^{q_{12}(1-f)\Delta} + (1-f)e^{-q_{12}f\Delta} = e^{-q_{12}f\Delta}[fe^{q_{12}\Delta} + (1-f)] \tag{5.A1}$$

and the q_{12}-norm of g is given by

$$\langle g \rangle_{q_{12}} = (E[g^{q_{12}}])^{1/q_{12}} = \begin{cases} e^{-f\Delta}[fe^{q_{12}\Delta} + (1-f)]^{1/q_{12}} & q_{12} \neq 0 \\ 1, & q_{12} = 0 \end{cases} \tag{5.A2}$$

Taking the logarithm on both sides of Eq. 5.A2 gives the expression in Eq. 5.12.

Part B: Accuracy of Numerical Experiments

To investigate the accuracy of the numerical analysis in Section 4 we compare results with variously refined meshes. We find that systems with stiff fraction $f = 0.5$ cause the most numerical issues (many corner contacts between stiff tiles) and for each combination of $L = \{4,8,16,32\}$ and $\Delta = \{1,2,3,4\}$ investigate ten randomly simulated arrangements of stiff tiles with $f = 0.5$. An important controlling variable in the accuracy of the numerical results is the number of discretization elements per tile. We denote the number of elements in each coordinate direction by n_{el} and find F_{eff} for each stiffness field and each parameter combination for $n_{el}/L = \{1,2,4,8,16\}$. The results are plotted in the top panel of **Figure 5.B1** and in each case the log-effective stiffness if normalized by the value of F_{eff} when $n_{el}/L = 16$ (this normalization is motivated by the fact that the curves tend to plateau around $n_{el}/L = 8$). Note that in **Figure 5.B1** we plot the average discretization error across the ten randomly simulated arrangements of stiff tiles for each

combination of n_{el}/L, L, and Δ. We approximate the exact value of F_{eff} as the value calculated with $n_{el}/L = 16$ and obtain the following simple model for the numerical bias β_{disc} of F_{eff} due to the discretization,

$$\beta_{disc}(\Delta, L, n_{el}) = 1 + 0.01 \cdot \Delta \ln L \cdot e^{-1.5e^{-0.3\Delta}\cdot\frac{n_{el}}{L}}, \tag{5.B1}$$

where $F_{eff,numerical}(\Delta, L, n_{el}) = \beta_{disc}(\Delta, L, n_{el}) \cdot F_{eff,true}$. The lines in the bottom panel of **Figure 5.B1** are lines of Eq. 5.B1.

Part C: Numerical Validation for $\Delta = \{1, 3\}$

Figure 5.C1 complements **Figure 5.8** in the paper by showing scatterplots of simulated F_{eff} and single-value predictions for $\Delta = \{1,3\}$. As in **Figure 5.8**, the theoretical predictions are nearly unbiased and strongly correlated with the simulation values, especially for $\Delta = 1$.

Similarly, **Figure 5.C2** complements **Figure 5.9** by comparing the theoretical and simulation cumulative distributions of F_{eff} for $\Delta = \{1,3\}$. As in **Figure 5.9**, the agreement between the two distributions is quite good.

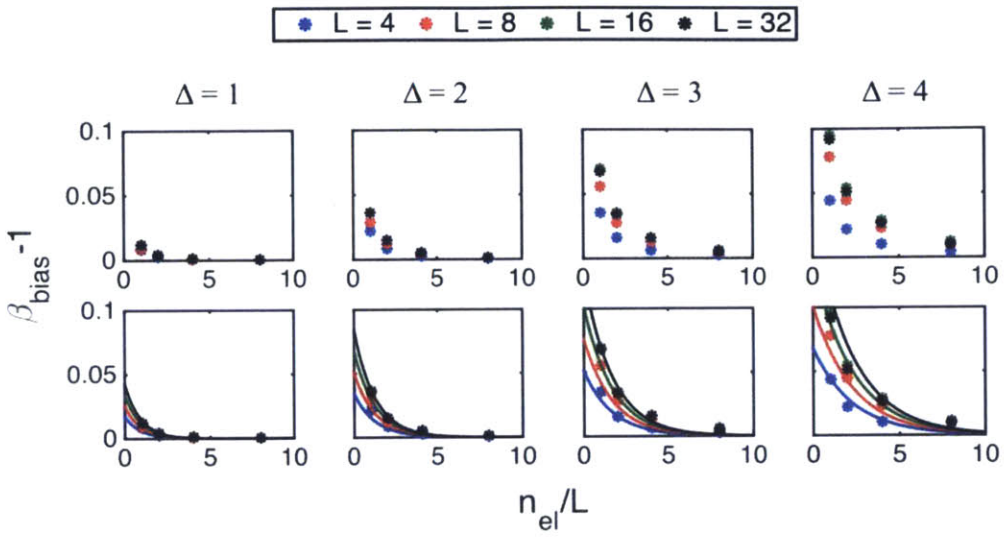

Figure 5.B1: For each value of L and Δ we simulate ten modulus fields with $f = 0.5$ and calculate F_{eff} numerically with 5 different discretizations of quadratic nine-node elements; $\frac{n_{el}}{L} = \{1,2,4,8,16\}$. The displayed data points indicate the average values of the numerical error across the ten simulated fields for each parameter combination. The values of F_{eff} are normalized by F_{eff} at $\frac{n_{el}}{L} = 16$. The bottom plot displays curves of the fitted bias model, which agrees well with the data across all parameter values.

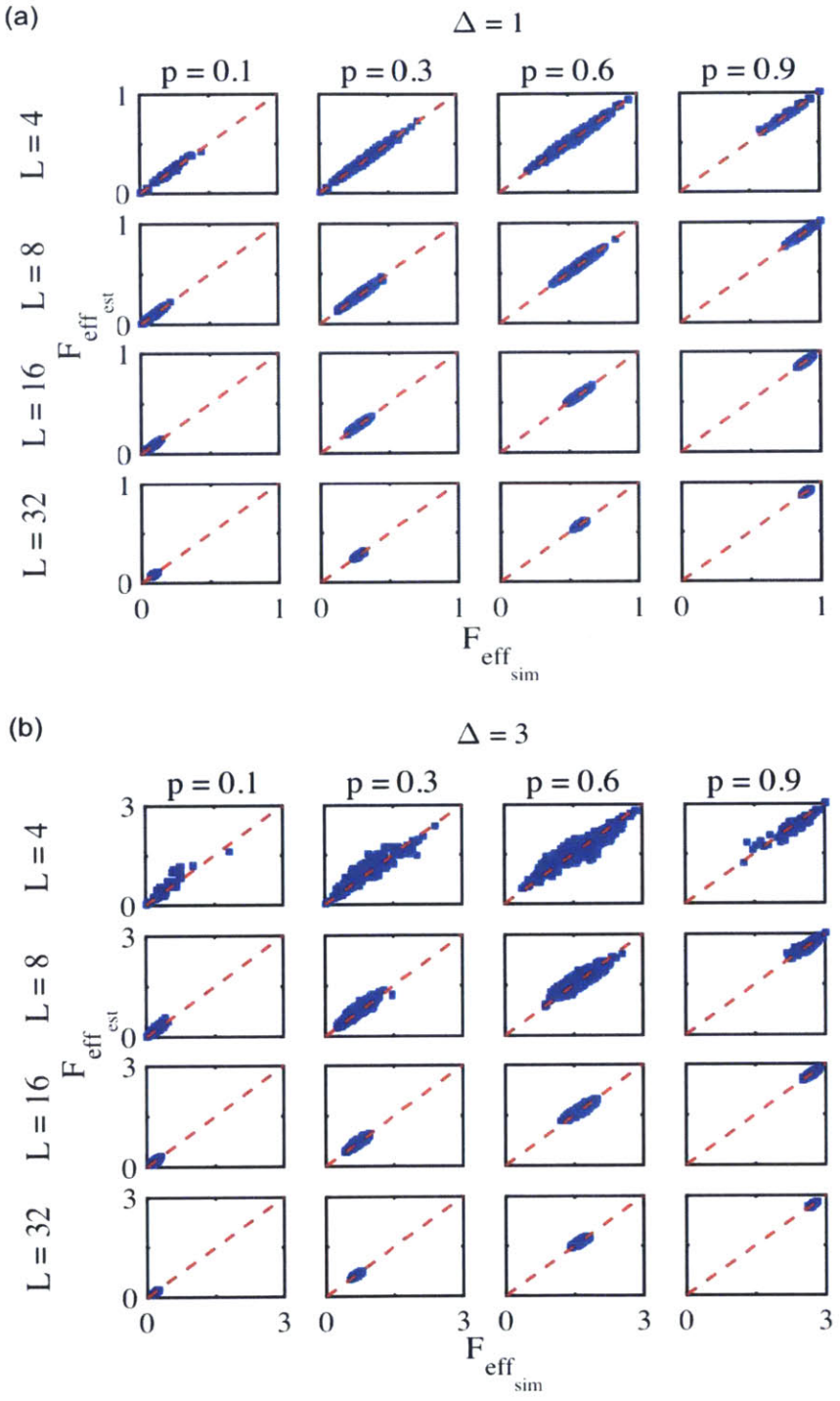

Figure 5.C1: Scatter plots of single-value-predicted and simulated F_{eff} values for $L = \{4,8,16,32\}$, $f = \{0.1,0.3,0.6,0.9\}$ and $\Delta = \{1,3\}$.

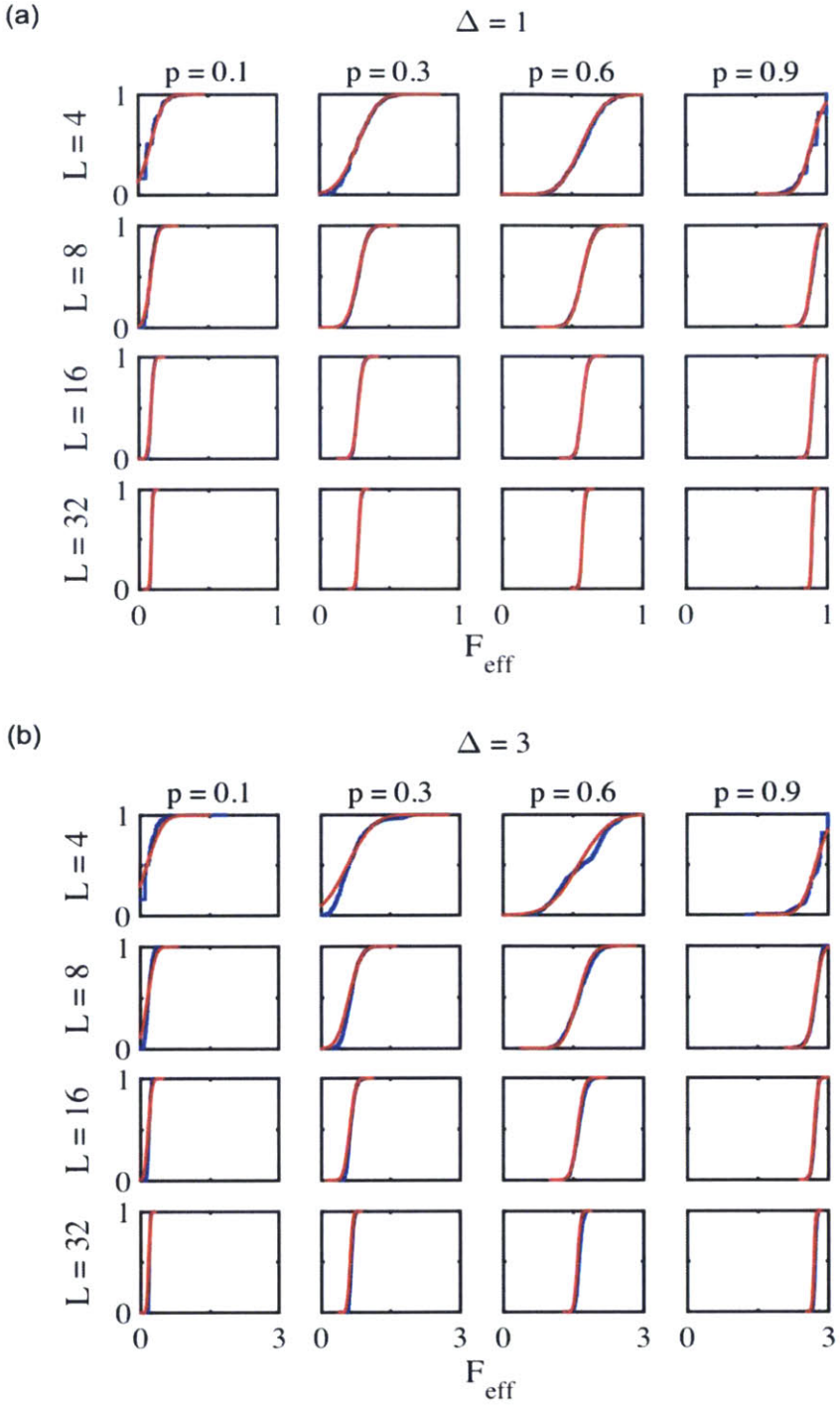

Figure 5.C2: Comparison of approximate analytical (red) and empirical (blue) cumulative distributions of F_{eff} for $L = \{4,8,16,32\}$, $p = \{0.1,0.3,0.6,0.9\}$ and $\Delta = \{1,3\}$.

Chapter 6: The Effective Stiffness of Multi-Phase Composites with Random Inclusions

6.1 Introduction

The class of multi-phase composites with random inclusions covers a wide range of materials. For example nacre, ceramic-metal composites, reinforced polymers, fiber-composites, and laminated composites all fall under this broad umbrella description. The spatial arrangement of the composite can be deterministic with each phase having random material properties, the material properties of the various phases can be deterministic and arranged randomly in space, or both the material properties and the spatial arrangement can be random. Furthermore, the inclusions can the same or different different shapes. Determining the effective stiffness of such multi-phase composites is a classical elastic homogenization problem and has been studied extensively. Some popular approaches include Maxwell-type approximations [48, 49] based on the classical work by Maxwell [38] on electrical conductivity and magnetism, implicit self-consistent approximations [50-53], and differential effective-medium approximations [54, 55] based on the work of Bruggeman on conductivity approximations [56].

Maxwell-type approximations consider systems with dilute inclusions and find the effective elasticity tensor by approximating the stress/strain field as the superposition of the stress/strain field due to each individual inclusion. These approximations are thus most accurate in the dilute inclusion limit. Implicit self-consistent approximations determine the effective elasticity tensor such that the incremental elasticity contribution of each individual phase averages to zero and does not consider the specific spatial arrangement of the inclusions. Differential effective-medium approximations evaluate the effective properties by considering the differential contribution of each individual phase sequentially in the dilute inclusion limit [1]. These methodologies are thus not suitable when inclusions form large clusters.

In this chapter we consider the effective stiffness of one simple type of multi-phase composites with random inclusions. We adopt the same approach as in Chapter 2. An advantage of our methodology is that it treats the spatial distribution of the modulus field explicitly and should be accurate for a large range of volume fractions of the stiffer inclusions.

We consider square specimens of side length L and finite thickness t with matrix of stiffness E_0. Square inclusions of thickness $t_I \ll t$ are distributed randomly according to a homogeneous Poisson process; see **Figure 6.1**. Without loss of generality we set $E_0 = 1$. The Young's modulus $E(x_1, x_2, x_3)$ is approximated as a two-dimensional field $E(x_1, x_2)$ obtained by averaging $E(x_1, x_2, x_3)$ in the x_3-direction.

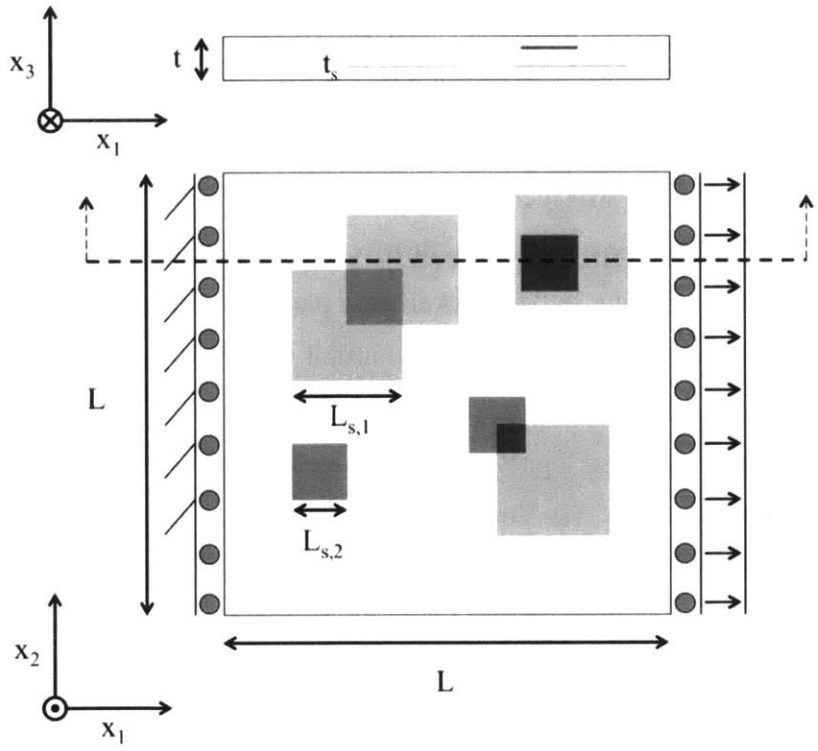

Figure 6.1: Illustration of composite system and boundary conditions.

Consider first the case of composites with one type of inclusion with stiffness E_1 and side length L_{I_1}. At a spatial location (x_1, x_2) at which a single inclusion of this type is present

in the (out-of-plane) x_3-direction, a fraction $\frac{t-t_I}{t}$ of the material has stiffness 1 and a fraction $\frac{t_I}{t}$ has stiffness E_1. Hence at that location

$$E(x_1, x_2) = 1 + \frac{t_I}{t}(E_1 - 1). \tag{6.1}$$

We let $\Delta_1 = \frac{t_I}{t}(E_1 - 1)$ and call Δ_1 the effective stiffness contrast of inclusions of type 1. At a spatial location (x_1, x_2) where N inclusions of type 1 overlap $E(x_1, x_2) = 1 + N\Delta_1$. If multiple types of inclusions are present, their stiffnesses also combine additively in the same way. When the locations of the inclusions form a Poisson point process, the Young's modulus $E(x_1, x_2)$ is a filtered Poisson point process. In our model we can have inclusions of different types (with different sizes and stiffnesses), but for each individual type the shape, size and stiffness are deterministic.

When the volume fraction of stiff inclusions p is small, inclusions do not overlap and the Young's modulus field has binary marginal distribution (if there is only one inclusion type) and characteristics similar to the checkerboard plates studied in Chapter 5. As the volume fraction of the stiff inclusions p tends to infinity, the Young's modulus field tends to a normal with a coefficient of variation that approaches 0. For low coefficient of variation, normal and associated lognormal fields have the same statistical characteristics. Therefore as p tends to infinity, the Young's modulus field tends to be lognormal. One concludes that depending on the value of p, the Young's modulus field lies between the lognormal fields considered in Chapter 2 and the binary fields considered in Chapter 5. This model is thus a good candidate for investigating the applicability of the ANOVA approach devised in Chapter 2 to non-lognormal multi-phase systems.

In the following sections we present the stochastic model and the analytical approach (Section 6.2), validate our analytical results (Section 6.3), and conclude by highlighting key findings and proposing directions for future research.

6.2 Stochastic Model and Probability Distribution of the Effective Modulus

First, we present the stochastic model and then discuss the analytical approach employed to approximate the probability distribution of E_{eff}.

6.2.1 Stochastic Model

We consider a square plate with side length L, thickness t, and stiffness 1, within which M types of square inclusions of infinitesimal thickness t_I, side lengths $L_I = \{L_{I_1}, L_{I_1}, \dots, L_{I_M}\}$, average volume fractions $p = \{p_1, p_2, \dots, p_M\}$, and effective stiffness contrasts $\Delta = \{\Delta_1, \Delta_2, \dots, \Delta_M\}$ are distributed uniformly and independently. When the locations of the inclusions form a Poisson point process, the Young's modulus is a filtered Poisson point process,

$$E(x_1, x_2) = 1 + \sum_{i=1}^{M} \sum_{n_i=1}^{N_i} h_i\left[(x_1, x_2), \left(x_1^{n_i}, x_2^{n_i}\right)\right]. \tag{6.2}$$

with filtering function,

$$h_i\left[(x_1, x_2), \left(x_1^i, x_2^i\right)_n\right] = \begin{cases} \Delta_i, & \left|x_1 - x_1^{n_i}\right| \le L_{s_i}/2 \text{ and } \left|x_2 - x_2^{n_i}\right| \le L_{s_i}/2 \\ 0, & \text{otherwise} \end{cases} \tag{6.3}$$

and $\left(x_1^{n_i}, x_2^{n_i}\right)$ the center point of inclusion n_i. We consider the specimen stretched in the x_1-direction, with zero tractions along the upper and lower sides and no shear stresses along the right and left sides; see **Figure 6.1**.

In **Figure 6.2** we show example stiffness field realizations for three-phase composites with side length $L = 16$, inclusion sizes $L_s = \{4,8\}$, effective stiffness contrasts $\Delta =$

{9,4} and average inclusion densities **a** $p = \{0.5,0.5\}$ and **b** $p = \{2.5,2.5\}$. The modulus field in **Figure 6.2b** is not far from lognormal.

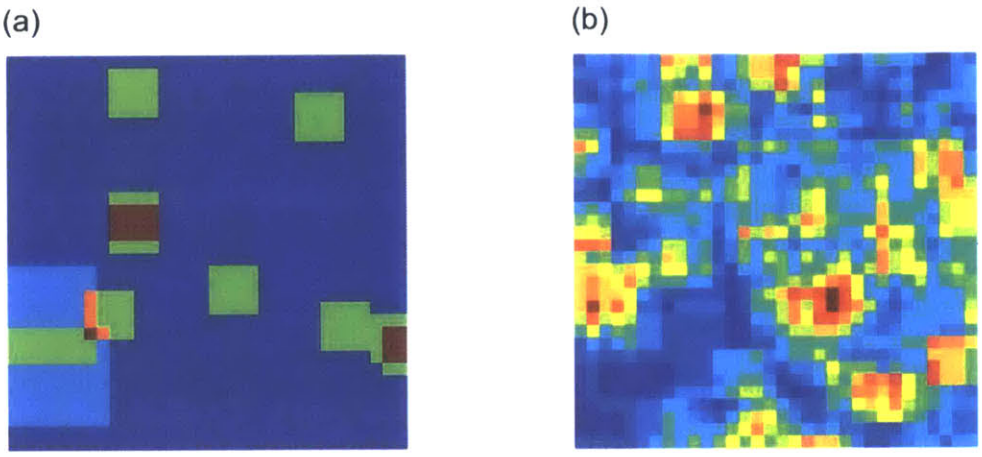

Figure 6.2: Realizations of the composite modulus field for three-phase systems. The specimens are of size $\boldsymbol{L = 32}$, with inclusions of sizes $\boldsymbol{L_s = \{4,8\}}$, stiffness contrasts $\boldsymbol{\Delta = \{10,5\}}$, and densities **a** $\boldsymbol{p = \{0.2,0.2\}}$ **b** $\boldsymbol{p = \{2.5,2.5\}}$.

6.2.2 Probability Distribution of the Effective Modulus

We seek the probability distribution of the effective modulus E_{eff} for a given specimen size L, inclusion sizes L_I, inclusion densities p, and effective stiffness contrasts Δ.

Following Chapter 2, we make an ANOVA decomposition of the log-modulus field $F = \ln E(x)$

$$F(x_1, x_2) = \overline{F} + \varepsilon_1(x_1) + \varepsilon_2(x_2) + \varepsilon_{12}(x_1, x_2) \tag{6.4}$$

where $\overline{F}$ is the average of F over the specimen, $\varepsilon_1(x_1)$ and $\varepsilon_2(x_2)$ are the marginal fluctuations in the x_1- and x_2-direction, and $\varepsilon_{12}(x_1, x_2)$ is a second-order interaction term. We approximate each term as independent normal, consider its contribution to F_{eff} and add the contributions to find the distribution of the effective log stiffness F_{eff}. The assumption of normality is justified by the fact that these terms are obtained through

averaging operations on the F field and by the central limit theorem their distribution is close to normal.

Except for the assumption of normality, the contributions of the first three terms are captured exactly. The spatial average $\overline{F}$ contributes to F_{eff} with a term equal to the arithmetic average of $F(x_1, x_2)$ and the marginal fluctuations $\varepsilon_1(x_1)$ and $\varepsilon_2(x_2)$ contribute to F_{eff} with terms equal to the log of the harmonic average of $e^{\varepsilon_1(x_1)}$ and the log of the arithmetic average of $e^{\varepsilon_2(x_2)}$ respectively. As in Chapter 2, we approximate the effect of $\varepsilon_{12}(x_1, x_2)$ as deterministic.

Similarly to Chapter 5 we estimate the distribution of F_{eff} by replacing the true log-modulus $F(x_1, x_2)$ field with a normal random field having the same first two moments and then applying the framework of Chapter 2 for lognormal modulus fields.

There is no analytical expression for the mean value m_F or the variance σ_F^2 of the exact log-modulus field $F(x_1, x_2) = \ln E(x_1, x_2)$. Thus we evaluate these moments numerically. The mean value m_E and variance σ_E^2 of the Young's modulus $E(x_1, x_2)$ for a system with M types of inclusions are given by,

$$\begin{aligned} m_E &= 1 + \sum_{i=1}^{M} p_i(\Delta_i + 1), \\ \sigma_E^2 &= \sum_{i=1}^{M} p_i(\Delta_i + 1). \end{aligned} \tag{6.5}$$

The correlation function of $E(x_1, x_2)$ can be found from properties of filtered Poisson point processes. In the limit of small p the variance of $E(x_1, x_2)$ is small and in the limit of large p, the modulus field is close to normal (the statistics of lognormal fields approach those of normal fields when the coefficient of variation approaches 0) and thus we approximate the correlation function of F as the correlation function of E. The validity of this and other approximations is evaluated in Section 3.

We first consider the correlation function of a system with a single type of inclusion. The approach in Chapter 2 applies to isotropic correlation functions. Therefore, to use that approach, we approximate the square inclusions with side length L_s as circular inclusions with radius $R = L_l/\sqrt{\pi}$. An alternative approach would be to develop the correlation for square inclusions and then obtain an isotropic approximation by randomly rotating the field. We later show that the two approaches give very similar results.

Following Matern [79], the, isotropic correlation function of a two-dimensional filtered Poisson point process with circular inclusions of radius R is given by,

$$\rho_E(r) = \begin{cases} 1 - \frac{2}{\pi}\left[r'\sqrt{1-r'^2} + \sin^{-1}(r')\right], & if\ r' = \frac{r}{2R} \leq 1 \\ 0, & otherwise. \end{cases} \tag{6.6}$$

Eq. 6.6 follows from to the area of the intersection of discs of radius R separated by a distance r. The correlation function obtained from considering square inclusions and then randomly rotating the field is very similar to Eq. 6.6.

In systems with several types of inclusions in which the inclusions are placed independently, the total covariance function is found by adding the individual covariance functions. The compound correlation function thus becomes a weighted average of the individual correlation functions $\rho_{E_i}(r)$,

$$\rho_E(r) = \frac{1}{\sigma_E^2}\sum_{i=1}^{M} \sigma_{E_i}^2 \rho_{E_i}(r). \tag{6.7}$$

With the moments as given, the distribution of F_{eff} is obtained as in Chapter 2 (equations and derivations are not repeated here).

6.3 Numerical Model and Validation

We validate our theoretical results with Monte Carlo simulation. To simulate the modulus fields we draw a Poisson random number of inclusions for each phase i according to the intensity p_i. The inclusions are then distributed uniformly and independently throughout the specimen and, as explained in Section 6.2, their moduli combine additively in regions in which they overlap.

For each simulated modulus field, we solve the mechanical problem using a finite element code in MATLAB. We discretize the system with a 128×128 mesh of linear four node elements and in experiments not shown here we show that with this discretization the numerical accuracy of our results is adequate.

To validate the approach of Section 6.2 we compare numerical results with theoretical predictions in systems with different values of L_I, Δ, and p and both one and two inclusion phases. In all cases the system size is $L = 32$ and the numerical results are based on 10,000 Monte Carlo simulations for the two-phase (one inclusion phase) systems and 1,000 Monte Carlo simulations for the three-phase (two inclusion phases) systems. The results are presented in **Figure 6.3**. Panels **a** and **b** show results for composites with one inclusion phase, $\Delta = 4$ and $L_I = 2$ and 4 respectively and panel **(c)** shows results for composites with two inclusion phases, $L_I = \{4,8\}$ and $\Delta = \{9,4\}$. In all cases we consider a wide range of inclusion densities p. In the two-phase system we consider $p = \{0.1,0.3,0.6,1,2,5\}$ and in the three phase system $p = \{0.1,0.1; 0.1,0.5; 0.1,2; 0.5,0.1; 0.5,0.5; 0.5,2; 2,0.1; 2,0.5; 2,2\}$. Thus the validation covers systems with a range of inclusion sizes in the low, intermediate, and high inclusion density regimes. **Figure 6.3** shows that the theoretical predictions are accurate for all parameter combinations.

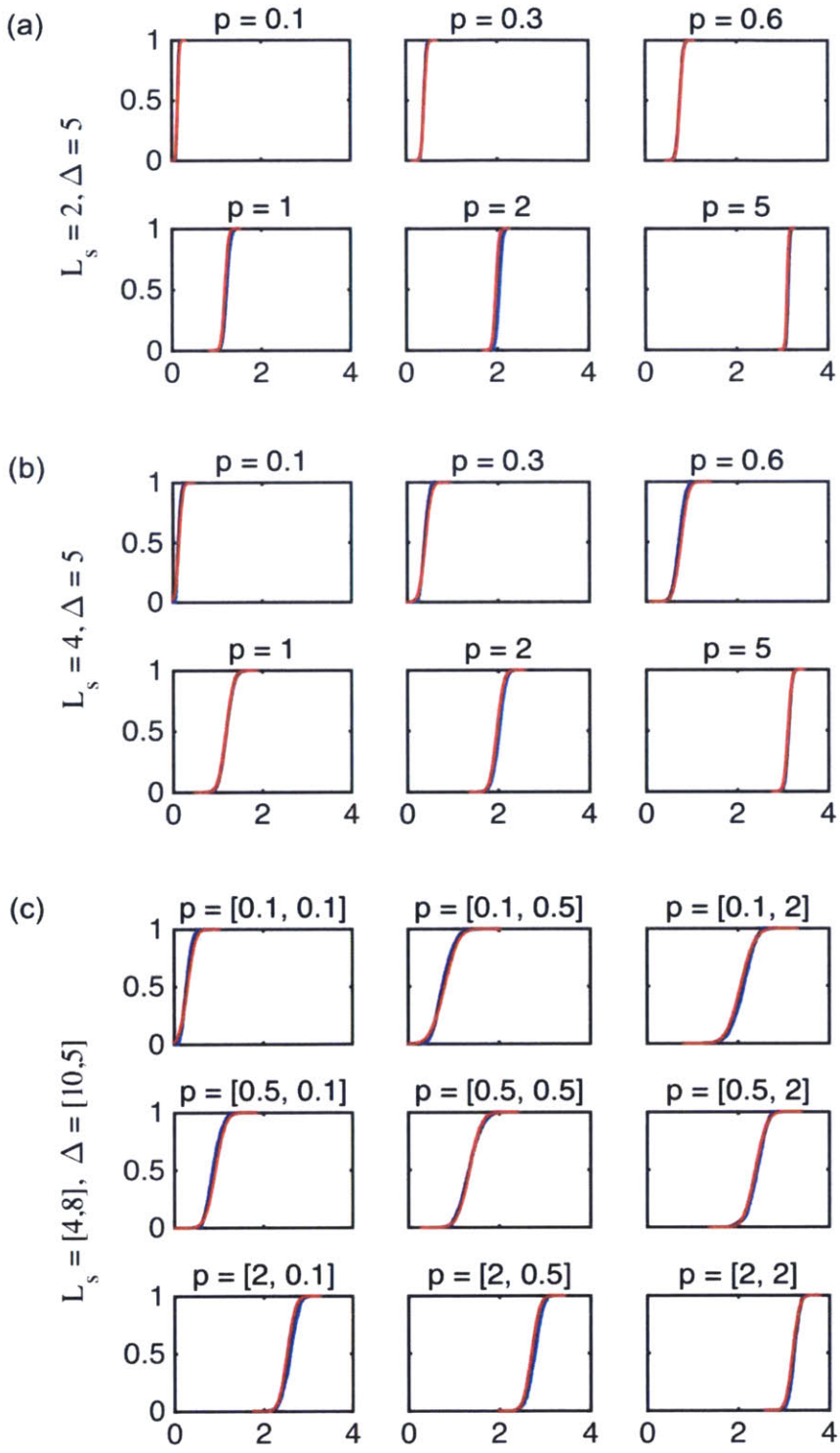

Figure 6.3: Comparison of approximate analytical (red) and numerical (blue) cumulative distributions of F_{eff} for $L = 32$ **a** $L_s = 2, \Delta = 5, p = \{0.1, 0.3, 0.6, 1, 2, 5\}$, **b** $L_s = 4, \Delta = 5, p = \{0.1, 0.3, 0.6, 1, 2, 5\}$, and **c** $L_s = \{4, 8\}, \Delta = \{10, 5\}, p = \{0.1, 0.1; 0.1, 0.5; 0.1, 2; 0.5, 0.1; 0.5, 0.5; 0.5, 2; 2, 0.1; 2, 0.5; 2, 2\}$.

6.4 Conclusions

We extended the homogenization approach of Chapter 2, which was originally developed for lognormal Young's modulus fields E, to multi-phase composite materials in which Young's modulus is modeled as a filtered Poisson point process. We approximate the log-modulus F as normal and decompose it into four ANOVA components, for which the effect on $F_{eff} = \ln E_{eff}$ is found either analytically or in approximation following the method of Chapter 2. We validated the results through extensive Monte Carlo simulation across a wide range of system parameters for both two- and three-phase composites and observed good agreement between theory and experiments. In contrast to Chapter 5, the ANOVA approach of Chapter 2 generalizes well to this class of composite systems, without any modification. Importantly the effect of the second order ANOVA component is well approximated as a deterministic ergodic term. The FPPP allows stiff regions to overlap, avoiding nearest-neighbor percolating clusters as those observed in Chapter 5, and this is likely an important reason why the second order interaction does not have a more dominant effect on the bulk stiffness. Our analysis provides evidence of the methodology presented in Chapter 2 as a general methodology valid also for systems with non-lognormal Young's modulus.

Possible extensions of this work include:

1. Three-dimensional composites with three-dimensional inclusions stretched in the x_1-direction. In a 3D system one could still assume that the moduli of inclusions combine additively when marked points of the FPPP overlap (although this could no longer be motivated by the homogenization argument presented here). Alternatively, one could consider a coverage model in which overlapping inclusions retain their original modulus, a thinning model in which overlapping inclusions are thrown away or a replacement model in which the arrangement of the inclusions is reshuffled until no overlap occurs. Each of these strategies

influence the first and second moments of F and suitable approximations would have to be found for these separately. With the first and second moments given the distribution of F_{eff} could be found analogously to in Chapter 2 for $n = 3$.

2. Interfaces may greatly affect the mechanical behavior of a composite. Their inclusion in stochastic material models poses several challenges (realistic representation, numerical analysis, treatment of uncertainty). One could start with simple systems (e.g. inclusions with simple geometry) and develop random homogenization strategies whereby each inclusion (plus interface) is replaced by an effective inclusion with homogeneous but random mechanical properties, thus converting materials with interfaces to equivalent random materials without interfaces. The latter can be treated as in this paper.
3. Fiber-reinforced materials may also be studied. Fiber-reinforced composites pose conceptually different problems and may require entirely different strategies. One possibility is to model the stiffness $E(x)$ as a compound Poisson field (or a compound non-Poisson field, to model the often-occurring clustering of fibers). It may then be possible to derive the second-moment properties of the modulus using theoretical results for integrals of such compound random fields and from that second-moment characterization approximate the distribution of the bulk moduli.

Chapter 7: Summary and Outlook

Random heterogeneities influence the bulk mechanical properties of materials in complex ways that depend on the property considered, the nature of the heterogeneity, the Euclidean dimension of the specimen, etc. Standard ways to evaluate the distribution of the bulk properties involve Monte Carlo simulation and numerical analysis. In this study we devised analytical methods to investigate the following problems:

- The bulk stiffness of one-, two-, and three-dimensional rectangular blocks in which Young's modulus varies spatially as a lognormal field (Chapter 2);
- The bulk strength of 1 and 2-dimensional rectangular blocks in which Young's modulus varies spatially as a lognormal field (Chapter 3);
- The bulk strength of one and two-dimensional rectangular blocks in which the Young's modulus and the local strength vary spatially as lognormal fields (Chapter 4);
- The bulk stiffness of two-dimensional random checkerboard plates (Chapter 5); and
- The bulk stiffness of two-dimensional plates with multi-phase inclusions in which the Young's modulus varies as a filtered Poisson Point Process (Chapter 6).

As described in Chapter 1 and illustrated in **Figure 1.3** these are idealized models for real material systems. They were chosen in part due to analytical convenience and in part to capture fundamentally different types of heterogeneity and material properties. Continuous variations in microstructural features such as for example the varying mineral degree of mineralization in bone or and the varying degree of hydration in cement paste could cause continuous variations in local mechanical properties similar to those of the lognormal fields considered here. Random checkerboard systems give an idealized description of a wide class of polycrystalline materials. Finally, many materials (reinforced polymers, particulate composites, etc.) are composed of a softer matrix phase

with randomly distributed inclusions of different shapes, sizes, and local mechanical characteristics.

In all cases we validate our analytical models with extensive Monte Carlo simulations and numerical analysis. For the numerical analysis we use a finite element model developed in MATLAB for the elastic and the initial strength problem and a discrete lattice model developed in Python for the ultimate strength problem. Beyond the computational cost of simulating fracture propagation, we encounter few numerical issues in analyzing the lognormal and filtered Poisson point process systems. The main difficulties are calculating the effective modulus of checkerboard materials. The difficulties arise mainly when stiff tiles meet at a corner: when the stiffness contrast between the soft and stiff phases is large, the stiffness of the soft tiles is negligible and a singularity arises with a finite load transferred through a point. We address the issue by using refined finite element discretizations, limiting the stiffness contrast (to 50), and estimating the bias induced by using not sufficiently refined discretizations. To deal with larger stiffness contrasts in a more computationally efficient manner one would need to use a different approach. This is left as a possible future extension.

Below we first summarize the main technical findings of this work. We then discuss the general applicability of our results before we conclude with discussing some possible topics for future research.

7.1 Main Technical Findings

In Chapter 2 we studied the effective elastic moduli of one-, two-, and three-dimensional rectangular blocks when the log Young's modulus $F(x) = \ln E(x)$ varies spatially as a normal random field. We used an ANOVA decomposition to express $F(x)$ as a constant plus a number of first- and higher-order fluctuation terms, analyzed the effect of each ANOVA term, and developed analytical approximations to the distribution of the effective elastic tensor as a combination of these effects. The analytical results were then

used to explore the dependence of the distribution of the log effective elasticity tensor on various geometric parameters and probabilistic characteristics. In all cases we observed a softening in the mean effective log-moduli induced by the heterogeneity. In most cases the log-moduli have similar variance and are highly correlated; hence in many cases one could assume perfect dependence, reducing the computational task to evaluating the mean values and the common variance of the log- moduli. Exceptions to this second rule involve moduli that depend significantly on different averages of the exponentiated first-order fluctuations of $F(x)$, for example the shear and transverse bulk modulus of highly elongated specimens.

In Chapter 3 we built upon the models and analysis strategy in Chapter 2 to study the distribution of fracture strength characteristics of notched one-dimensional rods and two-dimensional plates in which the log-Young's modulus varies spatially as an isotropic normal field. We consider materials in which the crack initiates or propagates when the maximum longitudinal strain at the edge of a crack tip exceeds a threshold value. We found that the strengths at fracture initiation display a complex behavior relative to their values under uniform modulus: The heterogeneities generally increase the mean value, whereas the median value is lower or higher depending on the Euclidean dimension of the specimen and the quantity considered (the elongation U, the load L, and the toughness T). Specifically, gains in the median occur for U and T, whereas the median of L is lower than in the uniform case.

In 2D specimens crack arrest increases the strengths at ultimate failure relative to the values at fracture initiation. This effect is modest for the ultimate load, but is important for the ultimate elongation and toughness. In specimens with limited variations of the modulus field we observed crack arrest mechanisms similar to those in laminates and composites with periodically varying modulus: crack arrest occurs as the fracture propagates towards higher modulus regions and the magnitude of the effect is controlled by the modulus contrast. As the variability of the modulus field increases, low modulus valleys appear. Fracture tends to propagate along these valleys, limiting the effectiveness of crack arrest and giving rise to different fracture patterns than those observed in

laminated composites with periodic modulus variation. The dispersion of the fracture strength parameters is smaller in the 2D than the 1D case and for 2D specimens decreases somewhat from initial fracture to ultimate failure conditions.

In Chapter 4 we extended the analysis of Chapter 3 to include the effect of random fracture strain. Specifically, we analyzed the distribution of the elongation, load and toughness at fracture initiation and ultimate failure for notched 1D rods and 2D plates when Young's modulus (stiffness) and the local fracture strain (material resistance) vary as isotropic lognormal fields. We found that whether the initial strengths on average are weakened or strengthened by heterogeneity of the failure strain largely depends on whether one reasons in arithmetic or log scale. When the log-modulus and the log-strength are positively correlated, heterogeneity of the material strength tends to increase the mean values at fracture initiation. The opposite is true when the random fields are negatively correlated. In 2D specimens, increasing the randomness of the material strength makes crack- arrest events more frequent and increases the ratio between ultimate and initial strengths. When the modulus and material strength have low spatial correlation, randomness of the material strength can significantly increase the effect of crack arrest, causing ultimate failure to be a more predictable and less brittle failure mode than fracture initiation.

In Chapter 5 we extended the elastic homogenization approach of Chapter 2 to random two-phase checkerboard materials in which the Young's modulus has binary distribution. Important new factors in the elastic homogenization of checkerboard (and other multi-phase) materials are the longitudinal percolation of the stiff phase and the transversal percolation of the soft phase. The effects of percolation are especially complex in checkerboard specimens that are small relative to the size of the tiles. The percolation effects make the ANOVA approach less accurate due to the complex interactions between the first and second order ANOVA components. However, by fitting a model for these complex interactions to data generated through Monte Carlo simulation we obtain results that are accurate over a wide range of system parameters.

Our analysis gives interesting insights into the effective stiffness of this class of composite system. In small specimens longitudinal (transversal) nearest neighbor percolation of the stiff (soft) tiles is the most significant stiffening (softening) mechanism whereas, next-nearest neighbor percolation has a less pronounced effect. By contrast, in large specimens (with finite modulus contrast) percolation has a gradual stiffening/softening effect and there is no well-defined threshold. Another interesting finding is that the effective stiffness of large checkerboard systems with stiff volume fraction $f = 0.5$ is comparable to that of lognormal systems with the same first two moments. Checkerboard specimens are softer than lognormal specimens when $f < 0.5$ and stiffer when $f > 0.5$. For $f \neq 0.5$, the difference between the large checkerboard and lognormal cases is due mainly to the shape of the marginal distribution, which in turn is related to the occurrence of percolation. For a checkerboard specimen of fixed dimension the mean of the log-effective stiffness is insensitive to the size of the tiles for a specimen of fixed dimension, while the variance of the log-effective stiffness increases with increasing tile size. Considering the relationship between the first two moments of lognormal and associated normal variables, we concluded that if one is interested in reducing the coefficient of variation of the bulk stiffness one should use smaller tiles, whereas larger tiles increase the mean value of the bulk stiffness.

In Chapter 6, we extended the methodology of Chapter 2 to a class of random multi-phase composites with non-lognormal marginal distribution of Young's modulus. Specifically, we considered square plates with inclusions in which the Young's modulus varies in space as a filtered Poisson point process (FPPP). In contrast to Chapter 5, the ANOVA approach of Chapter 2 with the FPPP process replaced with a lognormal process with the same first two moments produces accurate results.

This body of work provides insights into the elasticity and fracture mechanics properties of materials with different random heterogeneities. Its main limitations are the idealized models used in the study and the exclusion of more complex heterogeneities.

7.2 General Findings

With the specific accomplishments of this work as background, one may reflect on the applicability of the approaches and results to heterogeneous materials of practical importance, their usefulness for design and optimization, and the combinations of materials and bulk property of interest that call for significant extensions. We start with stiffness homogenization problems and then consider the assessment of bulk fracture strength.

Elastic Homogenization

Our first and most fundamental contribution on elastic homogenization is the analytical prediction of the joint probability distribution of the elastic tensor for one-, two-, and three-dimensional rectangular blocks when the local Young's modulus varies spatially as a lognormal random field. As detailed in the previous subsection, this includes insights on how the mean values, variances and correlation coefficients of the effective longitudinal and shear moduli vary with the Euclidean dimension and aspect ratios of the block and the parameters of the lognormal modulus field.

An important question is whether the same approach and results apply to other classes of heterogeneous materials. Specifically, one may question whether, in general, calculating the exact second-moment properties of the local modulus and then assuming lognormal distribution produces accurate results (we call this the "lognormal approximation"). This is an important question, both theoretically and for practical application, because few real synthetic and natural materials display lognormal modulus. The two classes of non-lognormal materials we have analyzed (checkerboard materials and materials with Poisson inclusions made of stiffer phases) provide interesting validation cases: checkerboard materials have a binary marginal distribution that is very different from lognormal and varies with the stiff volume fraction, while materials made of a matrix with Poisson stiff inclusions have a marginal distribution that evolves from binary (or discrete with few possible values) to lognormal as the density of inclusions increases from zero to infinity.

The analysis of the above non-lognormal cases has produced interesting insights:

- In general, the lognormal approximation is accurate (especially for materials with inclusions), making us speculate that it may be an acceptable approach for a wide class of heterogeneous materials. Of course, further validation work is necessary to assess the limits of this conclusion. Applicability of the lognormal approximation would make the methodology an important tool for material design. For example, our methodology allows one to predict the mean and variance of the effective stiffness from the mean value, variance and characteristic length scale of heterogeneity. By controlling the latter parameters, one can realize materials to satisfy target reliability requirements.

- The study of (small-size) checkerboard materials revealed that in certain multi-phase cases percolation reduces the accuracy of the lognormal approximation and requires an extension of the methodology. Percolation is a complex phenomenon due in part to the difficulty to analytically determine its effects on the bulk moduli and in part to the many forms of percolation: soft versus stiff percolation, different definitions of neighborhood with different associated stiffening or softening effects of percolating clusters, the fact that the formation of a percolating cluster may in itself have little effects on the bulk modulus (as the stiff volume fraction increases beyond the percolation threshold, the cluster increases its density and connectivity, with the consequence that the bulk modulus experiences a steady increase).

- To account for percolation in checkerboard materials, we had to modify the analysis developed for lognormal systems. We expect the modified approach to work well also for more general granular materials made of two or more phases. Also fiber reinforced materials are subjected to percolation, but are more difficult to analyze (also in a deterministic context). For example, a percolating cluster made of fibers would contribute to the effective stiffness in different ways

depending on the stiffness contrast with the embedding matrix, the curvature of the fibers, the nature and stiffness of the junctions between fibers etc. For these systems it is not clear under which conditions the lognormal approximation remains accurate.

- Another microstructural feature that often influences the bulk elasticity of actual materials (concrete, rock) but was not considered in this work is the presence of micro- and or macro-cracks. Cracks are difficult to study analytically, as their effect on the bulk elasticity depends in a complicated way on their orientation and the boundary conditions. For example, a single crack orientated perpendicularly to the loading direction softens a specimen in tension (the load acts to open the crack) but not in compression (load acts to close the crack). When several cracks are present, the resulting stress field under a given loading condition is a result of a complex interaction of the network of cracks.

Fracture Strengths

For materials with lognormal modulus and/or strength (expressed as a failure strain threshold), we also developed methods to determine the probability distribution of various bulk strength measures (elongation, load, fracture toughness) at fracture initiation and at ultimate specimen failure. Some of the findings are: (1) Decreasing the correlation length of the lognormal modulus makes the bulk properties more predictable, promotes crack arrest, and increases the ultimate fracture strengths; (2) Large fluctuations in the local material properties, in particular the local material strength, also promote crack arrest and are a second toughening mechanism; (3) Of course the fracture path tends to follow low-stiffness or low-strength "valleys" and high-strain ridges. This creates a complex interplay between the stiffness and strength of the material, especially when these two properties are correlated. Interestingly, crack-arrest effects, which are responsible for the increase in strength from initial to ultimate failure, are negatively correlated with the initial strength (if the crack tip where fracture initiates is in a relatively soft or weak region, it is likely that the fracture path will go through stiffer and stronger regions, with a compensatory effect on the ultimate strength). Therefore, in

general, the ultimate strengths have less statistical dispersion (are more accurately predictable) than the initial strengths. In addition, the ultimate strengths are less sensitive to the correlation between the local Young's modulus and material strength.

These results are necessarily less universal than those on the bulk elasticity because strength (especially at fracture initiation) depends to a large extent on local weaknesses and stress concentrations, which are highly dependent on the specific nature of the heterogeneities and defects in a material. For example, in Chapter 6 we found that the bulk stiffness of a system with square Poisson inclusions can be accurately approximated by assuming the inclusions to be circular. However, the stress field around a square inclusion is very different from that around a circular inclusion, with significant effects on the initial strength and fracture path. Also, the nature of crack propagation is fundamentally different in specimens with continuous (say lognormal) and discontinuous modulus and strength properties. In the discontinuous case, cracks may preferentially travel along interfaces and the interface behavior, which has not been considered here, has great significance.

While these considerations reduce the range of applicability of the results under lognormality assumptions, experimental evidence indicates that certain natural materials such as bone exhibit lognormal like variations in the local elastic modulus. As shown with nanoindentation and atomic force microscopy, at micrometer lengthscales the indentation modulus of bone varies spatially in an essentially continuous way. This feature is true also of other materials. If failure is determined by the elastic properties at the mesoscale (for example due to plastic phenomena at smaller scales), then the lognormal results could be used to explain at least certain fracture characteristics of such materials. Indeed, as was pointed out in Chapters 3 and 4, the predictions of our lognormal model are consistent with numerical and experimental findings on the fracture behavior of bone. Furthermore, while we do not expect the lognormal fracture results to have quantitative validity for multi-phase systems, we expect them to have at least qualitative predictive power.

As the mechanical model becomes more complex (multiple phases, stress concentrations, defects like micro-cracks and weak interfaces...), analytical treatment of the strength problem becomes increasingly problematic. In that case, the lognormal results can be used as a reference against which to assess strength results obtained through simulation.

7.3 Future Extensions

Finally we include some discussion on future extensions of our work. Possible future extensions include both relatively straightforward generalizations and the study of more fundamentally different homogenization problems. Among the straightforward extensions are:

1. Systems with continuous, but non-lognormal, variations of Young's modulus. One could follow an approach of the type in Chapter 6 to see whether the ANOVA approach with lognormal approximations yields accurate results;
2. Multi-phase systems with non-overlapping inclusions. One could first generate Poisson inclusions and then either redistribute or throw away overlapping inclusions. In either case one would have to adjust the first and second moments of the log-modulus to reflect the non-overlap condition;
3. Three-dimensional checkerboard systems stretched in the x_1-direction. In this case the bulk stiffness depends on three second-order and one third-order ANOVA component. Their interactions with the marginal fluctuations could be dealt with the single second order interaction in 2D;
4. Granular materials with grains forming random tessellations and two or more phases. Percolation should have effects similar to those in checkerboard systems, although with different critical stiff fractions. Due to the more irregular geometry, the effects of percolation are expected to be more gradual than for checkerboard materials.

More elaborate extensions of this work include:

1. A detailed study of percolation. We have found that in large checkerboard specimens with a modulus contrast factor up to 50, the effective stiffness depends in a smooth way on the stiff volume fraction. By contrast, small specimens display sharp discontinuities associated with different types of percolation. It would be interesting to study the onset of these phenomena and in particular what controls the transition from sharp to smooth percolation effects in checkerboard and other granular materials. As explained in Chapter 5 this extension would require a different numerical solver to efficiently deal with the stress singularities at corner contacts between the stiff tiles as explained in Chapter 5;
2. Fiber-reinforced composites pose conceptually different problems and may require entirely different strategies. An important difference of these systems is the local anisotropy of the Young's modulus field. Such systems may experience percolation, which could affect the bulk stiffness in complicated ways. One possibility is to model the stiffness $E(x)$ as a filtered Poisson field (or a filtered non-Poisson field, to model the often-occurring clustering of fibers). It may then be possible to derive the second-moment properties of the modulus using theoretical results for integrals of such random fields and from that second-moment characterization approximate the distribution of the bulk moduli. The current finite element model only allows for quadrilateral elements and would have to be revised to accurately describe the interaction between the fibers and the matrix;
3. Interfaces may greatly affect the mechanical behavior of a composite. Their inclusion in stochastic material models poses several challenges (realistic representation, numerical analysis, treatment of uncertainty). One could start with simple systems (e.g. inclusions with simple geometry) and develop random homogenization strategies whereby each inclusion (plus interface) is replaced by an effective inclusion with homogeneous but random mechanical properties, thus converting materials with interfaces to equivalent random materials without interfaces;

4. The study of fracture in random multi-phase composites (for example the models with inclusions studied in Chapter 6. In systems with inclusions and large discrete jumps in the local Young's modulus the fracture is likely to travel along interfaces. In addition to requiring a more accurate description of the interface properties and the challenges of an analytical treatment, such problems might require a different numerical approach. The current discrete lattice model has been shown to accurately predict crack propagation in systems with smoothly varying mechanical properties, but is relatively untested for systems with sharp discontinuities of material properties. The discretization might favor certain directions of crack propagation and thus misrepresent the fracture process.

7.4 References:

[1] S. Torquato, Random heterogeneous materials: microstructure and macroscopic properties. Vol. 16. 2002: Springer.

[2] S. Igarashi, V. Kawamura, A. Watanabe, 2004, Analysis of cement pastes and mortars by a combination of backscatter-based SEM image analysis and calculations based on the Powers model, Cement Concrete Comp, 26(8),977-85,10.1016/j.cemconcomp.2004.02.031

[3] L. Addadi, S. Weiner, 1997, Biomineralization - A pavement of pearl, Nature, 389(6654),912-&,Doi 10.1038/40010

[4] H. S. Gupta, U. Stachewicz, W. Wagermaier, P. Roschger, H. D. Wagner, P. Fratzl, 2006, Mechanical modulation at the lamellar level in osteonal bone, J Mater Res, 21(8),1913-21,Doi 10.1557/Jmr.2006.0234

[5] J. Aizenberg, J. C. Weaver, M. S. Thanawala, V. C. Sundar, D. E. Morse, P. Fratzl, 2005, Skeleton of Euplectella sp.: Structural hierarchy from the nanoscale to the macroscale, Science, 309(5732),275-8,Doi 10.1126/Science.1112255

[6] F. Barthelat, H. Tang, P. D. Zavattieri, C. M. Li, H. D. Espinosa, 2007, On the mechanics of mother-of-pearl: A key feature in the material hierarchical structure, J Mech Phys Solids, 55(2),306-37,Doi 10.1016/J.Jmps.2006.07.007

[7] P. Fratzl, H. S. Gupta, F. D. Fischer, O. Kolednik, 2007, Hindered crack propagation in materials with periodically varying Young's modulus - Lessons from biological materials, Adv Mater, 19(18),2657-+,Doi 10.1002/Adma.200602394

[8] H. J. Gao, B. H. Ji, I. L. Jager, E. Arzt, P. Fratzl, 2003, Materials become insensitive to flaws at nanoscale: Lessons from nature, P Natl Acad Sci USA, 100(10),5597-600,Doi 10.1073/Pnas.0631609100

[9] K. Okumura, P. G. de Gennes, 2001, Why is nacre strong? Elastic theory and fracture mechanics for biocomposites with stratified structures, Eur Phys J E, 4(1),121-7

[10] M. E. Waddoups, Eisenman.Jr, B. E. Kaminski, 1971, Macroscopic Fracture Mechanics of Advanced Composite Materials, J Compos Mater, 5(Noct),446-&,Doi 10.1177/002199837100500402

[11] J. M. Whitney, R. J. Nuismer, 1974, Stress Fracture Criteria for Laminated Composites Containing Stress-Concentrations, J Compos Mater, 8(Jul),253-65,Doi 10.1177/002199837400800303

[12] S. Kumar, X. Y. Li, A. Haque, H. J. Gao, 2011, Is Stress Concentration Relevant for Nanocrystalline Metals?, Nano Lett, 11(6),2510-6,Doi 10.1021/Nl201083t

[13] T. Zhang, X. Y. Li, S. Kadkhodaei, H. J. Gao, 2012, Flaw Insensitive Fracture in Nanocrystalline Graphene, Nano Lett, 12(9),4605-10,Doi 10.1021/Nl301908b

[14] M. Y. He, J. W. Hutchinson, 1989, Crack Deflection at an Interface between Dissimilar Elastic-Materials, Int J Solids Struct, 25(9),1053-67

[15] A. Zak, M. Williams, 1963, Crack Point Stress Singularities at a Bi-Material Interface, J Appl Mech, 30(1),142-3

[16] B. J. F. Bruet, J. H. Song, M. C. Boyce, C. Ortiz, 2008, Materials design principles of ancient fish armour, Nat Mater, 7(9),748-56,Doi 10.1038/Nmat2231

[17] J. D. Currey, 2005, Materials science - Hierarchies in biomineral structures, Science, 309(5732),253-4,Doi 10.1126/Science.1113954
[18] P. Fratzl, R. Weinkamer, 2007, Nature's hierarchical materials, Prog Mater Sci, 52(8),1263-334,Doi 10.1016/J.Pmatsci.2007.06.001
[19] S. Kamat, X. Su, R. Ballarini, A. H. Heuer, 2000, Structural basis for the fracture toughness of the shell of the conch Strombus gigas, Nature, 405(6790),1036-40
[20] M. A. Meyers, P. Y. Chen, A. Y. M. Lin, Y. Seki, 2008, Biological materials: Structure and mechanical properties, Prog Mater Sci, 53(1),1-206,Doi 10.1016/J.Pmatsci.2007.05.002
[21] J. Y. Rho, L. Kuhn-Spearing, P. Zioupos, 1998, Mechanical properties and the hierarchical structure of bone, Med Eng Phys, 20(2),92-102
[22] M. J. Jaasma, H. H. Bayraktar, G. L. Niebur, T. M. Keaveny, 2002, Biomechanical effects of intraspecimen variations in tissue modulus for trabecular bone, J Biomech, 35(2),237-46,Doi 10.1016/S0021-9290(01)00193-2
[23] L. S. Dimas, T. Giesa, M. J. Buehler, 2014, Coupled continuum and discrete analysis of random heterogeneous materials: Elasticity and fracture, J Mech Phys Solids, 63(481-90,Doi 10.1016/J.Jmps.2013.07.006
[24] K. Tai, M. Dao, S. Suresh, A. Palazoglu, C. Ortiz, 2007, Nanoscale heterogeneity promotes energy dissipation in bone, Nat Mater, 6(6),454-62,Doi 10.1038/Nmat1911
[25] S. Younis, Y. Kauffmann, L. Bloch, E. Zolotoyabko, 2012, Inhomogeneity of Nacre Lamellae on the Nanometer Length Scale, Crystal Growth & Design,10.1021/cg3007734
[26] G. E. Fantner, T. Hassenkam, J. H. Kindt, J. C. Weaver, H. Birkedal, L. Pechenik, J. A. Cutroni, G. A. G. Cidade, G. D. Stucky, D. E. Morse, P. K. Hansma, 2005, Sacrificial bonds and hidden length dissipate energy as mineralized fibrils separate during bone fracture, Nat Mater, 4(8),612-6,Doi 10.1038/Nmat1428
[27] F. Hang, H. S. Gupta, A. H. Barber, 2014, Nanointerfacial strength between non-collagenous protein and collagen fibrils in antler bone, J R Soc Interface, 11(92),Artn 20130993
Doi 10.1098/Rsif.2013.0993
[28] Y. Hu, V. Birman, A. Deymier-Black, A. G. Schwartz, S. Thomopoulos, G. M. Genin, 2015, Stochastic Interdigitation as a Toughening Mechanism at the Interface between Tendon and Bone (vol 108, pg 431, 2015), Biophys J, 108(5),1306-,Doi 10.1016/J.Bpj.2015.01.027
[29] F. Hang, A. H. Barber, 2011, Nano-mechanical properties of individual mineralized collagen fibrils from bone tissue, J R Soc Interface, 8(57),500-5,Doi 10.1098/Rsif.2010.0413
[30] H. M. Yao, M. Dao, D. Carnelli, K. S. Tai, C. Ortiz, 2011, Size-dependent heterogeneity benefits the mechanical performance of bone, J Mech Phys Solids, 59(1),64-74,10.1016/j.jmps.2010.09.012
[31] M. J. Mayo, W. D. Nix, 1988, A Micro-Indentation Study of Superplasticity in Pb, Sn, and Sn-38 Wt-Percent-Pb, Acta Metall Mater, 36(8),2183-92,Doi 10.1016/0001-6160(88)90319-7

[32] S. G. Erickson, D. V. Wiltschko, 1991, Spatially Heterogeneous Strength in Thrust-Fault Zones, J Geophys Res-Solid, 96(B5),8427-39,Doi 10.1029/91jb00248
[33] W. Weibull, A statistical theory of the strength of materials1939: Generalstabens litografiska anstalts förlag.
[34] S. A. Mirza, J. G. Macgregor, 1979, Variability of Mechanical-Properties of Reinforcing Bars, J Struct Div-Asce, 105(5),921-37
[35] J. B. Wachtman, 1967, Mechanical Properties of Ceramics - an Introductory Survey, Am Ceram Soc Bull, 46(8),756-+
[36] D. Veneziano, Computational fluid and solid mechanics 20032003: Elsevier.
[37] L. Rayleigh, 1892, LVI. On the influence of obstacles arranged in rectangular order upon the properties of a medium, The London, Edinburgh, and Dublin Philosophical Magazine and Journal of Science, 34(211),481-502
[38] J. C. Maxwell, A treatise on electricity and magnetism1873, Oxford,: Clarendon press.
[39] A. Einstein, *Eine neue bestimmung der moleküldimensionen*, 1905, Buchdruckerei KJ Wyss.
[40] M. J. Beran, Statistical continuum theories. Monographs in statistical physics and thermodynamics,1968, New York,: Interscience Publishers. xv, 424 p.
[41] M. Kachanov, I. Sevostianov, Effective Properties of Heterogeneous Materials. Vol. 193. 2013: Springer.
[42] S. Nemat-Nasser, M. Hori, Micromechanics : overall properties of heterogeneous materials. North-Holland series in applied mathematics and mechanics1993, Amsterdam ; New York: North-Holland. xx, 687 p.
[43] E. Sanchez-Palencia, A. Zaoui, International Centre for Mechanical Sciences., Homogenization techniques for composite media : lectures delivered at the CISM International Center for Mechanical Sciences, Udine, Italy, July 1-5, 1985. Lecture notes in physics1987, Berlin ; New York: Springer-Verlag. ix, 397 p.
[44] J. P. Watt, G. F. Davies, R. J. O'Connell, 1976, The elastic properties of composite materials, Rev. Geophys. Space Phys, 14(4),541-63
[45] R. M. Christensen, K. H. Lo, 1979, Solutions for effective shear properties in three phase sphere and cylinder models, J Mech Phys Solids, 27(4),315-30
[46] J. R. Willis, 1982, Properties of Composites, Advances in applied mechanics, 21(1
[47] Z. Hashin, 1983, Analysis of composite materials—a survey, J Appl Mech, 50(3),481-505
[48] G. J. Weng, 1984, Some Elastic Properties of Reinforced Solids, with Special Reference to Isotropic Ones Containing Spherical Inclusions, Int J Eng Sci, 22(7),845-56,Doi 10.1016/0020-7225(84)90033-8
[49] T. Mori, K. Tanaka, 1973, Average Stress in Matrix and Average Elastic Energy of Materials with Misfitting Inclusions, Acta Metall Mater, 21(5),571-4,Doi 10.1016/0001-6160(73)90064-3
[50] B. Budiansky, 1965, On the elastic moduli of some heterogeneous materials, J Mech Phys Solids, 13(4),223-7

[51] R. Hill, 1965, Theory of Mechanical Properties of Fibre-Strengthened Materials .3. Self-Consistent Model, J Mech Phys Solids, 13(4),189-&,Doi 10.1016/0022-5096(65)90008-6
[52] R. Hill, 1965, A Self-Consistent Mechanics of Composite Materials, J Mech Phys Solids, 13(4),213-&,Doi 10.1016/0022-5096(65)90010-4
[53] J. E. Gubernatis, J. A. Krumhansl, 1975, Macroscopic Engineering Properties of Polycrystalline Materials - Elastic Properties, J Appl Phys, 46(5),1875-83,Doi 10.1063/1.321884
[54] R. McLaughlin, 1977, A study of the differential scheme for composite materials, Int J Eng Sci, 15(4),237-44
[55] S. Boucher, 1974, On the effective moduli of isotropic two-phase elastic composites, J Compos Mater, 8(1),82-9
[56] D. Bruggeman, 1935, Berechnung verschiedener physikalischer Konstanten von heterogenen Substanzen. I. Dielektrizitätskonstanten und Leitfähigkeiten der Mischkörper aus isotropen Substanzen, Annalen der physik, 416(8),665-79
[57] R. Ghanem, P. D. Spanos, 1990, Polynomial Chaos in Stochastic Finite-Elements, J Appl Mech-T Asme, 57(1),197-202,Doi 10.1115/1.2888303
[58] G. Stefanou, 2009, The stochastic finite element method: Past, present and future, Comput Method Appl M, 198(9-12),1031-51,Doi 10.1016/J.Cma.2008.11.007
[59] E. Vanmarcke, M. Grigoriu, 1983, Stochastic Finite-Element Analysis of Simple Beams, J Eng Mech-Asce, 109(5),1203-14
[60] M. F. Ngah, A. Young, 2007, Application of the spectral stochastic finite element method for performance prediction of composite structures, Compos Struct, 78(3),447-56,Doi 10.1016/J.Compstruct.2005.11.009
[61] M. F. Pellissetti, R. G. Ghanem, 2000, Iterative solution of systems of linear equations arising in the context of stochastic finite elements, Adv Eng Softw, 31(8-9),607-16,Doi 10.1016/S0965-9978(00)00034-X
[62] F. Yamazaki, M. Shinozuka, G. Dasgupta, 1988, Neumann Expansion for Stochastic Finite-Element Analysis, J Eng Mech-Asce, 114(8),1335-54
[63] L. Huyse, M. A. Maes, 2001, Random field modeling of elastic properties using homogenization, J Eng Mech-Asce, 127(1),27-36,Doi 10.1061/(Asce)0733-9399(2001)127:1(27)
[64] M. Ostojastarzewski, C. Wang, 1989, Linear Elasticity of Planar Delaunay Networks - Random Field Characterization of Effective Moduli, Acta Mech, 80(1-2),61-80,Doi 10.1007/Bf01178180
[65] W. A. Curtin, 1997, Toughening in disordered brittle materials, Phys Rev B, 55(17),11270-6,Doi 10.1103/Physrevb.55.11270
[66] M. Sahimi, S. Arbabi, 1993, Mechanics of Disordered Solids .3. Fracture Properties, Phys Rev B, 47(2),713-22,Doi 10.1103/Physrevb.47.713
[67] M. Grigoriu, M. T. A. Saif, S. Elborgi, A. R. Ingraffea, 1990, Mixed-Mode Fracture Initiation and Trajectory Prediction under Random Stresses, Int J Fracture, 45(1),19-34,Doi 10.1007/Bf00012607
[68] H. O. Madsen, S. Krenk, N. C. Lind, Methods of structural safety. Dover ed2006, Mineola, NY: Dover Publications. vi, 407 p.
[69] M. Shinozuka, G. Deodatis, 1988, Response Variability of Stochastic Finite-Element Systems, J Eng Mech-Asce, 114(3),499-519

[70] S. R. Arwade, G. Deodatis, 2011, Variability response functions for effective material properties, Probabilist Eng Mech, 26(2),174-81,Doi 10.1016/J.Probengmech.2010.11.005
[71] K. Teferra, S. R. Arwade, G. Deodatis, 2012, Stochastic variability of effective properties via the generalized variability response function, Comput Struct, 110(107-15,Doi 10.1016/J.Compstruc.2012.07.005
[72] K. Teferra, S. R. Arwade, G. Deodatis, 2014, Generalized variability response functions for two-dimensional elasticity problems, Comput Method Appl M, 272(121-37,Doi 10.1016/J.Cma.2014.01.013
[73] D. Veneziano, A. Tabaei, 2001, Analysis of variance method for the equivalent conductivity of rectangular blocks, Water Resour Res, 37(12),2919-27,Doi 10.1029/2000wr000051
[74] M. Ostoja-Starzewski, 1998, Random field models of heterogeneous materials, Int J Solids Struct, 35(19),2429-55,Doi 10.1016/S0020-7683(97)00144-3
[75] L. Graham-Brady, 2010, Statistical characterization of meso-scale uniaxial compressive strength in brittle materials with randomly occurring flaws, Int J Solids Struct, 47(18-19),2398-413,Doi 10.1016/J.Ijsolstr.2010.04.034
[76] J. A. Ma, I. Temizer, P. Wriggers, 2011, Random homogenization analysis in linear elasticity based on analytical bounds and estimates, Int J Solids Struct, 48(2),280-91,Doi 10.1016/J.Ijsolstr.2010.10.004
[77] M. Shinozuka, 1987, Structural Response Variability, J Eng Mech-Asce, 113(6),825-42
[78] K. Karhunen, Zur spektraltheorie stochastischer prozesse1946: Suomalainen tiedeakatemia.
[79] B. Matérn, 1960, Spatial variation, meddelanden fran statens skogsforskningsinstitut, Lecture Notes in Statistics, 36(21
[80] T. S. Cook, F. Erdogan, 1972, Stresses in Bonded Materials with a Crack Perpendicular to Interface, Int J Eng Sci, 10(8),677-&,Doi 10.1016/0020-7225(72)90063-8
[81] A. Romeo, R. Ballarini, 1995, A crack very close to a bimaterial interface, J Appl Mech-T Asme, 62(3),614-9,Doi 10.1115/1.2895990
[82] F. Delale, F. Erdogan, 1983, The Crack Problem for a Non-Homogeneous Plane, J Appl Mech-T Asme, 50(3),609-14
[83] F. Erdogan, A. C. Kaya, P. F. Joseph, 1991, The Crack Problem in Bonded Nonhomogeneous Materials, J Appl Mech-T Asme, 58(2),410-8,Doi 10.1115/1.2897201
[84] J. W. Hutchinson, Z. Suo, 1992, Mixed-Mode Cracking in Layered Materials, Adv Appl Mech, 29(63-191
[85] S. Rahman, B. N. Rao, 2002, Probabilistic fracture mechanics by Galerkin meshless methods - part II: reliability analysis, Comput Mech, 28(5),365-74,Doi 10.1007/S00466-002-0300-8
[86] B. N. Rao, S. Rahman, 2002, Probabilistic fracture mechanics by Galerkin meshless methods - part I: rates of stress intensity factors, Comput Mech, 28(5),351-64,Doi 10.1007/S00466-002-0299-X

[87] R. M. Reddy, B. N. Rao, 2008, Stochastic fracture mechanics by fractal finite element method, Comput Method Appl M, 198(3-4),459-74,Doi 10.1016/J.Cma.2008.08.014
[88] G. Mayer, 2005, Rigid biological systems as models for synthetic composites, Science, 310(5751),1144-7,Doi 10.1126/Science.1116994
[89] T. L. Anderson, Fracture mechanics : fundamentals and applications. 3rd ed2005, Boca Raton, FL: Taylor & Francis. 621 p.
[90] J. W. Eischen, 1987, Fracture of Nonhomogeneous Materials, Int J Fracture, 34(1),3-22
[91] A. A. Griffith, 1921, The phenomena of rupture and flow in solids, Philosophical transactions of the royal society of london. Series A, containing papers of a mathematical or physical character, 221(163-98
[92] V. M. Zolotarev, One-dimensional stable distributions. Vol. 65. 1986: American Mathematical Soc.
[93] J. E. Bolander, S. Saito, 1998, Fracture analyses using spring networks with random geometry, Eng Fract Mech, 61(5-6),569-91,Doi 10.1016/S0013-7944(98)00069-1
[94] W. A. Curtin, H. Scher, 1990, Brittle-Fracture in Disordered Materials - a Spring Network Model, J Mater Res, 5(3),535-53
[95] G. N. Hassold, D. J. Srolovitz, 1989, Brittle-Fracture in Materials with Random Defects, Phys Rev B, 39(13),9273-81
[96] E. Schlangen, E. J. Garboczi, 1997, Fracture simulations of concrete using lattice models: Computational aspects, Eng Fract Mech, 57(2-3),319-32,Doi 10.1016/S0013-7944(97)00010-6
[97] P. M. Duxbury, P. L. Leath, 1994, Failure Probability and Average Strength of Disordered-Systems, Physical Review Letters, 72(17),2805-8,Doi 10.1103/Physreviett.72.2805
[98] P. L. Leath, P. M. Duxbury, 1994, Fracture of Heterogeneous Materials with Continuous Distributions of Local Breaking Strengths, Phys Rev B, 49(21),14905-17,Doi 10.1103/Physrevb.49.14905
[99] H. J. Herrmann, A. Hansen, S. Roux, 1989, Fracture of Disordered, Elastic Lattices in 2 Dimensions, Phys Rev B, 39(1),637-48,Doi 10.1103/Physrevb.39.637
[100] I. J. Beyerlein, S. L. Phoenix, 1997, Statistics of fracture for an elastic notched composite lamina containing Weibull fibers .2. Probability models of crack growth, Eng Fract Mech, 57(2-3),267-99,Doi 10.1016/S0013-7944(97)00013-1
[101] S. Roux, D. Vandembroucq, F. Hild, 2003, Effective toughness of heterogeneous brittle materials, Eur J Mech a-Solid, 22(5),743-9,Doi 10.1016/S0997-7538(03)00078-0
[102] A. Chudnovsky, B. Kunin, 1987, A Probabilistic Model of Brittle Crack Formation, J Appl Phys, 62(10),4124-9,Doi 10.1063/1.339128
[103] L. Dearcangelis, S. Redner, H. J. Herrmann, 1985, A Random Fuse Model for Breaking Processes, J Phys Lett-Paris, 46(13),L585-L90
[104] G. Lilliu, J. G. M. van Mier, 2003, 3D lattice type fracture model for concrete, Eng Fract Mech, 70(7-8),927-41,Pii S0013-7944(02)00158-3
Doi 10.1016/S0013-7944(02)00158-3

[105] N. Dalén, L.-G. Hellström, B. Jacobson, 1976, Bone mineral content and mechanical strength of the femoral neck, Acta Orthopaedica, 47(5),503-8
[106] M. S. Cheung, W. C. Li, 2003, Probabilistic fatigue and fracture analyses of steel bridges, Struct Saf, 25(3),245-62,Pii S0167-4730(02)00067-X
Doi 10.1016/S0167-4730(02)00067-X
[107] P. Geyskens, A. Der Kiureghian, P. Monteiro, 1998, Bayesian prediction of elastic modulus of concrete, J Struct Eng-Asce, 124(1),89-95,Doi 10.1061/(Asce)0733-9445(1998)124:1(89)
[108] S. Hiratsuka, Y. Mizutani, M. Tsuchiya, K. Kawahara, H. Tokumoto, T. Okajima, 2009, The number distribution of complex shear modulus of single cells measured by atomic force microscopy, Ultramicroscopy, 109(8),937-41,Doi 10.1016/J.Ultramic.2009.03.008
[109] M. Balland, N. Desprat, D. Icard, S. Fereol, A. Asnacios, J. Browaeys, S. Henon, F. Gallet, 2006, Power laws in microrheology experiments on living cells: Comparative analysis and modeling, Phys Rev E, 74(2),Artn 021911
Doi 10.1103/Physreve.74.021911
[110] F. J. Ulm, M. Vandamme, C. Bobko, J. A. Ortega, 2007, Statistical indentation techniques for hydrated nanocomposites: Concrete, bone, and shale, J Am Ceram Soc, 90(9),2677-92,DOI 10.1111/j.1551-2916.2007.02012.x
[111] S. Nachtrab, S. C. Kapfer, C. H. Arns, M. Madadi, K. Mecke, G. E. Schroder-Turk, 2011, Morphology and Linear-Elastic Moduli of Random Network Solids, Adv Mater, 23(22-23),2633-+,10.1002/adma.201004094
[112] R. Soulie, E. Merillou, O. Romain, T. Djamchid, R. Ghazanfarpour, 2007, Modeling and rendering of heterogeneous granular materials: Granite application, Comput Graph Forum, 26(1),66-79,DOI 10.1111/j.1467-8659.2007.00949.x
[113] Z. G. Fan, Y. G. Wu, X. H. Zhao, Y. Z. Lu, 2004, Simulation of polycrystalline structure with Voronoi diagram in Laguerre geometry based on random closed packing of spheres, Comp Mater Sci, 29(3),301-8,10.1016/j.commatsci.2003.10.006
[114] S. Kumar, S. K. Kurtz, 1994, Simulation of Material Microstructure Using a 3d Voronoi Tessellation - Calculation of Effective Thermal-Expansion Coefficient of Polycrystalline Materials, Acta Metallurgica Et Materialia, 42(12),3917-27,Doi 10.1016/0956-7151(94)90170-8
[115] J. B. Keller, 1987, Effective conductivity of periodic composites composed of two very unequal conductors, Journal of mathematical physics, 28(10),2516-20
[116] S. Kirkpatrick, 1973, Percolation and Conduction, Rev Mod Phys, 45(4),574-88,Doi 10.1103/Revmodphys.45.574
[117] R. Landauer. *Electrical conductivity in inhomogeneous media.* in *Electrical transport and optical properties of inhomogeneous media.* 1978. AIP Publishing.
[118] P. Sheng, 1980, Theory for the Dielectric Function of Granular Composite Media, Physical Review Letters, 45(1),60-3,Doi 10.1103/Physrevlett.45.60
[119] P. Sheng, R. V. Kohn, 1982, Geometric Effects in Continuous-Media Percolation, Phys Rev B, 26(3),1331-5,Doi 10.1103/Physrevb.26.1331
[120] L. Berlyand, K. Golden, 1994, Exact Result for the Effective Conductivity of a Continuum Percolation Model, Phys Rev B, 50(4),2114-7,Doi 10.1103/Physrevb.50.2114

[121] Y. Chen, C. A. Schuh, 2009, Effective transport properties of random composites: Continuum calculations versus mapping to a network, Phys Rev E, 80(4),Artn 040103
Doi 10.1103/Physreve.80.040103
[122] K. Malarz, S. Galam, 2005, Square-lattice site percolation at increasing ranges of neighbor bonds, Phys Rev E, 71(1),Artn 016125
Doi 10.1103/Physreve.71.016125
[123] S. A. Berggren, D. Lukkassen, A. Meidell, L. Simula, 2001, A new method for numerical solution of checkerboard fields, Journal of Applied Mathematics, 1(4),10.1155/s1110757x01000316
[124] J. Helsing, 2011, The effective conductivity of arrays of squares: Large random unit cells and extreme contrast ratios, J Comput Phys, 230(20),7533-47,Doi 10.1016/J.Jcp.2011.05.032
[125] G. W. Milton, The theory of composites. Cambridge monographs on applied and computational mathematics2002, Cambridge ; New York: Cambridge University Press. xxviii, 719 p.

7.2 List of Figures

Figure 1.1: a Synthetic random heterogeneous materials. From top to bottom: Cement paste, fiber reinforced cermet, and an interpenetrating three-phase cermet composed of boron carbide (black regions), aluminum (white regions), and another ceramic phase (gray regions). b Natural random heterogeneous materials. From top to bottom: Fontainebleau sandstone, cellular structure of cancellous bone, and 'stack-of-coins' structure of aragonite crystals that make up gastropod nacre. Adapted and reprinted from [1-3] with permission of Springer, Elsevier and the Natura Publishing Group. 13

Figure 1.2: 2D interpolated color plot of the reduced indentation modulus, showing both a clear modulation along the lines of the lamellae inside an osteon, as well as regions of much lower moduli where the osteocyte lacunae and Haversian systems are present. Adapted and reprinted from [4] with permission of Cambridge University Press. 14

Figure 1.3: Examples of random fields from the a lognormal, b checkerboard, and c random inclusion models considered in this thesis. 20

Figure 2.1: Realizations of 2D normal log-stiffness fields with a simple exponential correlation kernel for normalized correlation lengths of (a) 0.125 and (b) 0.5..... 24

Figure 2.2: (a) 1D rod. Comparison of theoretical (red) and numerically predicted distributions (blue) of F1 for $r0/L = 0.125$, $\sigma F = 0.3$ and correlation function e-r/r0 or e-r/r0^2 . (b) Comparison of theoretical and simulated distributions of the 2D elastic tensor for a rectangular block with parameters $L2/L1 = 100$, $r0/L1 = 2$, $\sigma F = 0.5$ and correlation function e-r/r0. (c) Similar comparison for a cubic specimen with $r0/L = 0.25$, $\sigma F = 0.3$ and correlation function e-r/r0. 37

Figure 2.3: Normalized mean and standard deviation of the effective Young's modulus of a 1D rod as a function of the dimensionless specimen length L/r0, for correlation functions e-(r/r0) and e-(r/r0)2 . As $L/r0 \to \infty$ the mean value tends to the deterministic ergodic limit, while the standard deviation tends to 0. 39

Figure 2.4: Parameters of the effective elastic tensor of a 2D rectangular block as a function of the aspect ratio L2/L1 and the normalized correlation distance r0/L1. The correlation function is e-r/r0. The correlation coefficients are shown for σF = 0.5. The longitudinal, square-like and transversal regimes are indicated in the lower left panel..... 40

Figure 2.5: Parameters of the effective tensor for a 3D rectangular block with side lengths L1 = L2 = L and L3 as a function of the aspect ratio L3/L and the normalized correlation distance r0/L1. The correlation function is e-r/r0. The correlation coefficients are for σF = 0.5. The plate-like, cube-like, and elongated regimes are indicated in the center low panel. 43

Figure 3.1: (a) Specimen geometry and (b) measures of fracture strength for 1D rods and 2D plates. In the 1D rods the modulus varies only in the x1-direction and in 2D plates there are modulus variations both along the x1-direction and x2-direction... 71

Figure 3.2: Scatterplot and correlation coefficient between strain energy release rate at fracture initiation GI, c and initial toughness modulus TI. One thousand Monte Carlo simulations of a 2L × L specimen in which the log-modulus field Fx is normal with double exponential correlation function, standard deviation σF = 0.3, and correlation length r0 = 0.5L..... 72

Figure 3.3: (a) Log-log scatterplots of ultimate strength XU versus initial strength XI for X = u, l, and t, 1000 Monte Carlo simulations of a square specimen with unit side length. The log-modulus Fx is normal with simple exponential correlation function ρFr, standard deviation σF = 0.3 and correlation length r0 = 0.125. The red lines indicate fitted 10^{th} , 50^{th} , and 90^{th} percentiles prior to censoring. (b) Probability PlnXU = lnXI as a function of lnXI based on the fitted models. 78

Figure 3.4: Example fracture paths and corresponding load elongation curves for notched square specimens with unit side length. The log-modulus Fx is a normal field with simple exponential correlation function ρFr, correlation length r0 = 0.125, and standard deviation a σF = 0.3 b σF = 0.3 c σF = 0.7. The number '1' indicates the location of the initial crack tip and '2' indicates the last crack-arrest event. Specimen a fails upon initial crack propagation while both b and c exhibit crack arrest..... 82

Figure 3.5: Comparison of analytical fracture strength distributions (red) with histograms from Monte Carlo simulations (blue). a initial strengths for a rod of unit length, and b initial strengths for a square plate with unit side length, and c ultimate strengths for a square plate of unit side length. Simulation of 10,000 samples in cases (a,b) and 1,000 samples in case c. In all cases the log-modulus field Fx is normal with simple exponential correlation function ρFr, standard deviation $\sigma F = 0.3$, and correlation length $r0 = 0.125$. 84

Figure 3.6: Parameters of the initial fracture strength distributions for 1D rods as a function of the normalized correlation length $r0/L$. Blue and red curves show results for simple- and double-exponential correlation functions. 86

Figure 3.7: Same as Figure 3.6 for square plates. 88

Figure 3.8: Mean (solid lines) and median values (dashed lines) of the initial fracture strengths for 1D rods and 2D squares as a function of the normalized correlation length $r0/L$. Blue and red curves show results for simple- and double- exponential correlation functions. 89

Figure 3.9: Parameters of the regression model in Eq. 3.10 for square specimens with unit side length. Normal log-modulus Fx with simple exponential correlation function ρFr, standard deviation $\sigma F = 0.3,0.5,0.7$ and correlation length $r0 = 0.125,0.25,0.5,1$. Parameters are fitted by maximum likelihood to 250 Monte Carlo simulations. 92

Figure 3.10: Marginal distributions of the normalized initial and ultimate log-fracture strengths for $\sigma F = 0.5$ and $r0 = 0.125,0.25,0.5,1$ 93

Figure 4.1: a Specimen geometry and b fracture strength measures for 1D rods and 2D plates. The definitions are identical to in Chapter 3. 103

Figure 4.2: Square specimen. a Log-log scatterplots of the ultimate strength XU versus the initial strength XI for X = u, l, and t from 1000 Monte Carlo simulations. The log-modulus Fx and log-strength $\ln\varepsilon rx$ are normal with simple exponential spatial correlation function with correlation length $r0/L = 0.125$, standard deviations $\sigma F = \sigma\ln\varepsilon r = 0.3$, and correlation $\rho = -1$ between Fx and $\ln\varepsilon rx$ for any given x. The red lines are fitted 10^{th}, 50^{th}, and 90^{th} percentiles prior to censoring. b Probability

PlnXU > lnXI as a function of lnXI based on the fitted models, for deterministic and random strength. 112
Figure 4.3: Comparison of analytical fracture strength distributions (red) with histograms from Monte Carlo simulations (blue). a Initial strengths for a rod, b initial strengths for a square plate, and c ultimate strengths for a square plate. Simulation of 10,000 samples in cases (a,b) and 1,000 samples in case c. Randomness of Fx and lnεrx is the same as in Figure 4.2 114
Figure 4.4: Correlation coefficients of the log-strengths and log-effective modulus in 1D rods with high spatial correlation of the modulus and failure strain ($r0/L \gg 1$). Correlation between a log-strength pairs and b log-strength and the log-effective modulus for different ρ and select values of $c = \sigma F/\sigma \ln \varepsilon r$. 120
Figure 4.5: Parameters of the regression model in Eq. 4.13 for the elongation $X = u$ of a square specimen. Fx and lnεrx have exponential spatial correlation function with correlation length $r0/L = 0.125,0.25,1$, standard deviations $\sigma F = 0.3$ and $\sigma \ln \varepsilon r = 0,0.3,0.7$ and correlation $\rho = -1,0,1$. In each case, the parameters are fitted to 100 Monte Carlo simulations. 121
Figure 4.6: Marginal distributions of the normalized initial and ultimate log elongation lnu for $r0/L = 0.125$, $\sigma F = 0.3$, $\rho = -1,0,1$, and $\sigma \ln \varepsilon r = 0,0.3,0.7$. 124
Figure 5.1: Illustration of checkerboard systems and boundary conditions. This is a model system for several polycrystalline systems such as granitic rocks and ceramic materials. 134
Figure 5.2: Examples of ANOVA decomposition of the log-modulus field. a $L, p, \Delta = 4,0.5,1$ and b $L, p, \Delta = 32,0.25,1$. F is the spatial average of the log-modulus field, $\varepsilon 1$ and $\varepsilon 2$ are the marginal fluctuations in the x1- and x2-direction, respectively, $\varepsilon 12$ is the second order fluctuation of F, and $F1 = F + \varepsilon 1 + \varepsilon 2$ is the first-order approximation of the modulus field F 138
Figure 5.3: Comparison of q12 values for lng = F-F and lng = $\varepsilon 12$ when $L = 4$, $\Delta = 4$ and the stiff volume fraction f progressively increases from 0 to 1 in 1/16 increments. 140
Figure 5.4: Contribution of various ANOVA components to the total effective log-stiffness Feff for a $L = 4$ and b $L = 32$. In each case $\Delta = 4$. Through numerical

simulation we find the contribution of each term on the right hand side of Eq. 5.5 as the stiff volume fraction f progressively increases from 0 to 1 in 1/16 increments. See text for an explanation of the different components. 142
Figure 5.5: Three simulations of Fefff for systems with L = 4 and Δ = 4. The first two columns show the first NN + NNN and NN percolating clusters highlighted in blue and red, respectively. The points along the Fefff trajectory at which these percolating clusters form are shown with matching colors. The vertical dashed lines indicate the theoretical percolation thresholds. 145
Figure 5.6: Same as Figure 5.5 for L = 32, the Fefff plots are almost deterministic; hence we display only on simulation. 146
Figure 5.7: a Dependence of q12 on fs for L = 32 and Δ = 1,2,3,4. b Dependence of q12 on f for L = 4,8,16,32 and Δ = 1,2,3,4 along with regression lines from Eq. 5.7. c Values of cL in Eq. 5.6 for L = 4,8,16,32 and values of σq12L for L = 4,8,16,32, with least squares fits. 148
Figure 5.8: Scatter plots of single-value-predicted and simulated Feff for L = 4,8,16,32, f = 0.1,0.3,0.6,0.9 and Δ = 2,4. 153
Figure 5.9: Comparison of approximate analytical (red) and empirical (blue) cumulative distributions Feff for L = 4,8,16,32, p = 0.1,0.3,0.6,0.9 and Δ = 2,4. 155
Figure 5.10: Dependence of Feff on σF2 for large checkerboard and lognormal specimens with mE = 1. For checkerboard materials, results are presented for three values of the stiff fraction f. Checkerboard results are shown as solid lines. The dashed lines give hybrid results when the exponent q12 is from checkerboard analysis but the marginal distribution of the modulus is assumed to be lognormal. The dashed green line is also the log-effective stiffness in the lognormal case. Small panels compare the checkerboard (binary) and normal marginal distribution of F for σF2 = 0.25 and f = 0.1,0.5,0.9. 158
Figure 6.1: Illustration of composite system and boundary conditions. 169
Figure 6.2: Realizations of the composite modulus field for three-phase systems. The specimens are of size L = 32, with inclusions of sizes Ls = 4,8, stiffness contrasts Δ = 10,5, and densities a p = 0.2,0.2 b p = 2.5,2.5. 172

Figure 6.3: Comparison of approximate analytical (red) and numerical (blue) cumulative distributions of Feff for L = 32 a Ls = 2, Δ = 5, p = 0.1,0.3,0.6,1,2,5, b Ls = 4, Δ = 5, p = 0.1,0.3,0.6,1,2,5, and c Ls = 4,8, Δ = 10,5, p = 0.1,0.1; 0.1,0.5; 0.1,2; 0.5,0.1; 0.5,0.5; 0.5,2; 2,0.1; 2,0.5; 2,2. 176

7.3 List of Tables

Table 2.1: ANOVA fluctuation terms and their associated variances for n = 2 and n = 3. 28

Table 4.1: Values of the first and second moments of the initial logged strengths lnXI and initial unlogged strengths XI under the limiting conditions of low spatial correlation r0/L ≪ 1 (the log-modulus and log-strength are ergodic and the log-effective stiffness Feff is deterministic, Feff = -σF2) and high spatial correlation r0/L ≫ 1 (the log-modulus and log-strength are spatially uniform and Feff = F*). 117